

Design and Development of Lithium-
Sulphur Batteries: *Operando* Studies using
X-ray Absorption Spectroscopy

by

Nanami Yokota

A thesis submitted to the University of Kent as part of the
requirement in the subject of Chemistry for the degree of

Doctor of Philosophy

Department of School of Physical Sciences

August 2018



Contents

| | |
|---|-----------|
| List of Figures..... | 6 |
| List of Tables..... | 17 |
| List of Abbreviations..... | 18 |
| Declarations..... | 20 |
| Acknowledgements..... | 21 |
| Abstract..... | 22 |
| Chapter 1..... | 24 |
| Literature Review..... | 24 |
| 1.1 General Introduction..... | 24 |
| 1.1.1 Battery characteristics..... | 26 |
| 1.2 Li-ion batteries..... | 26 |
| 1.3 Post Li-ion batteries..... | 27 |
| 1.4 Fundamentals of Li-S batteries..... | 31 |
| 1.5 Challenges and improvements of Li-S technologies..... | 35 |
| 1.5.1 Positive electrode..... | 35 |
| 1.5.2 Negative electrode..... | 39 |
| 1.6 Electrolyte..... | 43 |
| 1.6.1 Electrolyte systems..... | 44 |
| 1.7 Characterisation techniques of Li-S cells..... | 47 |
| 1.7.1 Ex-situ measurement..... | 48 |
| 1.7.2 In situ/operando measurement..... | 48 |
| 1.8 Aim of the thesis..... | 49 |
| 1.9 References..... | 51 |
| Chapter 2..... | 64 |

| | |
|--|-----------|
| Materials and Methods | 64 |
| 2.1 Material synthesis | 64 |
| 2.1.1 Cathode preparations..... | 64 |
| 2.1.2 Electrolyte preparations | 66 |
| 2.1.3 Separator preparations..... | 66 |
| 2.1.4 Coin cell configuration..... | 66 |
| 2.2 Material characterisations..... | 67 |
| 2.2.1 Laboratory electrochemical characterisation methods | 67 |
| 2.2.2 X-Ray Diffraction (XRD)..... | 68 |
| 2.2.3 Synchrotron radiation..... | 69 |
| 2.2.4 X-ray Absorption Spectroscopy (XAS)..... | 70 |
| 2.3 XAS measurements..... | 75 |
| 2.3.1 XMaS instrument..... | 76 |
| 2.3.2 Soft X-ray spectroscopy | 77 |
| 2.3.3 Beamline set-up..... | 78 |
| 2.4 Operando cell preparation | 80 |
| 2.4.1 Slurry coating for operando cells | 80 |
| 2.4.2 Operando cell configuration | 81 |
| 2.5 Benchmark test of operando cell..... | 82 |
| 2.5.1 Electrochemical performance of operando cell..... | 82 |
| 2.5.2 XAS resolution of operando cell..... | 84 |
| 2.6 Sulphur K-edge reference samples | 85 |
| 2.6.1 S K-edge reference compounds | 85 |
| 2.6.2 Preparation of polysulphide..... | 86 |
| 2.6.3 Reference compounds; S ₈ , Li ₂ S, Li ₂ S ₄ | 86 |
| 2.6.4 Qualitative analysis of S ₈ , Li ₂ S ₄ , and Li ₂ S..... | 88 |
| 2.6.5 References compounds– oxidised sulphur | 90 |
| 2.7 Data analysis | 90 |
| 2.8 Conclusions | 91 |
| 2.9 References | 92 |

| | |
|---|------------|
| Chapter 3..... | 100 |
| Effects of Electrolytes..... | 100 |
| 3.1 Introduction | 100 |
| 3.2 Material preparations..... | 105 |
| 3.2.1 Electrode preparations | 105 |
| 3.2.2 Electrolyte preparations | 106 |
| 3.3 Material characterisations..... | 108 |
| XRD measurements..... | 108 |
| 3.4 Electrochemical measurements..... | 109 |
| 3.4.1 Electrochemical performances of S+AB+PVP electrode in various electrolyte systems | 112 |
| 3.4.2 Summary of electrochemical observations | 121 |
| 3.5 Visual examinations of the transparent cells | 122 |
| 3.6 Operando sulphur K-edge XAS analysis..... | 126 |
| 3.6.1 Operando cell | 126 |
| 3.6.2 Validation of sulphur cathode and electrolytes..... | 127 |
| 3.6.3 Operando measurement | 135 |
| 3.6.4 Radical polysulphides | 153 |
| 3.7 Conclusions | 155 |
| 3.8 References | 156 |
| Chapter 4..... | 165 |
| Sulphur Cathodes with Inorganic Additives | 165 |
| 4.1 Introduction | 165 |
| 4.2 Material preparations..... | 169 |
| 4.2.1 Electrode preparations | 169 |
| 4.3 Material characterisations..... | 170 |
| XRD measurements..... | 170 |
| 4.4 Electrochemical measurements..... | 173 |

| | | |
|--|--|------------|
| 4.4.1 | LiTDI/TEGDME | 174 |
| 4.4.2 | LiTDI/TEGDME/LiNO ₃ | 177 |
| 4.5 | XAS analysis..... | 181 |
| 4.5.1 | S K-edge XANES – Pristine spectrum of each cell..... | 182 |
| 4.5.2 | Operando XAS analysis | 185 |
| 4.5.3 | High-energy region | 209 |
| 4.6 | Conclusions | 213 |
| 4.7 | References | 215 |
| Chapter 5 | | 220 |
| Electrically Conducting Polymer Additives | | 220 |
| 5.1 | Introduction | 220 |
| 5.2 | Material preparations..... | 225 |
| 5.2.1 | Synthesis of polymer additives for sulphur composites..... | 225 |
| 5.2.2 | Electrode preparations | 226 |
| 5.3 | Material characterisations..... | 227 |
| 5.4 | Electrochemical measurements..... | 231 |
| 5.4.2 | Operando XAS analysis | 235 |
| 5.5 | Conclusions | 248 |
| 5.6 | References | 250 |
| Chapter 6 | | 256 |
| Conclusions and Future Work | | 256 |
| 6.1 | Conclusions | 256 |
| 6.2 | Future work..... | 258 |
| Appendix | | 260 |
| A-1 | List of chemicals used | 260 |

| | |
|---|-----|
| A-2 Second discharge and charge cycle of TiO ₂ @S cell for operando double-edge experiment | 262 |
| A-3 Post-mortem XAS measurements | 263 |
| A-3.1 Sample preparation | 263 |
| A-3.2 Beamline set up | 264 |
| A-3.2 Results | 265 |
| A-4 References..... | 266 |

List of Figures

| | |
|--|----|
| Figure 1-1. Comparison of different secondary batteries in terms of volumetric and gravimetric energy density.. | 25 |
| Figure 1-2. Schematic of a typical Li-ion battery..... | 27 |
| Figure 1-3. Bar graph compares the theoretical and practical specific energy of gasoline, Li-ion, Li-S, and Li-air batteries..... | 28 |
| Figure 1-4. An illustration of a non-aqueous Li-air battery, typically composed of a lithium anode, electrolyte containing lithium salt and organic solvent, and a porous O_2^- cathode made with carbon particles. | 29 |
| Figure 1-5. A schematic illustration of a Li-S cell..... | 31 |
| Figure 1-6. Typical voltage profile of Li-S cell..... | 32 |
| Figure 1-7. CV curve of a sulphur cathode scanned during the initial cycle at a scan rate of 0.03 mV s^{-1} | 34 |
| Figure 1-8. Initial discharge-charge voltage profile of Li-S battery cycled in $LiNO_3$ -free electrolyte. The cathode consists of S+AB+PVP (65:25:15 weight ratio). The electrolyte consists of 1 M LiTFSI in DOL/DME. This cell can only deliver an initial coulombic efficiency of 21.5 % due to the ‘infinite’ charging phenomenon..... | 40 |
| Figure 1-9. Schematic of dendrite growth within Li-S battery..... | 41 |
| Figure 2-1. Schematic diagrams of the S+AB+PVP cathode synthesis steps. (a) A photograph of slurry coated on Al current collector sheet using a doctor blade and (b) cathode discs cut into 12.7 mm. | 65 |
| Figure 2-3. Schematic diagram of 2016 coin cell configuration..... | 67 |
| Figure 2-4. Schematic illustration of Bragg condition. | 69 |

| | |
|--|----|
| Figure 2-5. (a) X-ray is absorbed, and a core electron is excited from the atom. Relaxation state by (b) fluorescence X-ray emission and (c) Auger electron emission..... | 71 |
| Figure 2-6. XAS spectra of TiO ₂ showing the XANES and EXAFS regions, as well as the inset showing the pre-edge region in XANES. The inset shows an expanded view of the XANES region. | 72 |
| Figure 2-7. A schematic of EXAFS process representing the origin of EXAFS oscillations, where 'A' represents the absorbing atom and 'N' represents the neighbouring atom..... | 73 |
| Figure 2-8. An illustration of a typical apparatus for XAS measurements..... | 74 |
| Figure 2-9. An overview of XAS experiment set-up at XMaS..... | 76 |
| Figure 2-10. Schematic of a double crystal monochromator. | 77 |
| Figure 2-11. Experimental set up for <i>operando</i> XANES measurement (S K-edge and Ti K-edge) conducted at XMaS beamline (BM28) at the ESRF. | 79 |
| Figure 2-12. A photo of a coin cell sample mounted on the electrically connected sample stage. | 79 |
| Figure 2-13. Schematic illustration of X-ray transparent cathode preparation..... | 80 |
| Figure 2-14. Schematic diagram and a photograph the of X-ray transparent <i>operando</i> coin cell configuration. | 81 |
| Figure 2-15. Discharge/charge curves of sulphur electrode cycled using <i>operando</i> cell (dotted lines) and conventional coin cell (solid lines). | 83 |
| Figure 2-16. Discharge/charge profiles of sulphur electrodes cycled in conventional CR2016 cell (black line) and <i>operando</i> cell after 5 days of storage (dotted red line). Both cells are cycled in the same electrolyte (LiTDI/TMS) at a rate of 0.1 C between 1.3 – 2.8 V. | 84 |

| | |
|---|-----|
| Figure 2-17. Raw S K-edge XANES spectra of Mylar-film compared to LiTDI/TEGDME cell at the pristine state. | 85 |
| Figure 2-18. S K-edge XANES spectra of reference compounds; S ₈ , Li ₂ S, and Li ₂ S ₄ . The spectra of Li ₂ S and Li ₂ S ₄ are offset for clarity by 0.8 and 1.6 units, respectively..... | 86 |
| Figure 2-19. Schematic illustration of the S K-edge XANES; the pre-edge and the main-edge region corresponding to terminal sulphur and internal sulphur, respectively. | 88 |
| Figure 2-20. XANES spectra of reference compounds – Na ₂ S ₂ O ₃ , Na ₂ SO ₃ ²⁻ , and FeSO ₄ . The spectra are shown offset for clarity. | 90 |
| Figure 3-1. Structures of lithium salts used in this study, (a) LiTFSI and (b) LiTDI. ... | 104 |
| Figure 3-2. XRD patterns of pure AB, S+AB powder after heating, and pure sulphur. | 108 |
| Figure 3-3. (a) CV profiles of the S+AB+PVP cathode cycled in LiTFSI/DOL:DME/LiNO ₃ electrolyte, recorded by scanning rate of 0.1 mV s ⁻¹ between 1.3 – 2.8 V, (b) an expanded view of the cathodic peaks in the potential range between 1.95 V and 2.50 V, (c) an expanded view of the anodic peaks, and (d) CV profiles of another cell recorded at the same scanning rate between potential window of 1.8 – 2.8 V. | 110 |
| Figure 3-4. Electrochemical analysis of S+AB+PVP cathode in LiTFSI/DOL:DME/LiNO ₃ electrolyte cycled at a rate of 0.1 C. (a) Galvanostatic discharge and charge curves, and (b) Cycling performance and Coulombic efficiency..... | 111 |
| Figure 3-5. CV curves of sulphur electrode of 1 M LiTFSI in different solvents recorded at a scan rate of 0.1 mV s ⁻¹ ; (a) DOL:DME, (b) TEGDME:DOL, (c) TEGDME, and (d) TMS. | 113 |
| Figure 3-6. Electrochemical performances of S+AB+PVP electrode in various electrolyte systems with LiTFSI and LiTDI salt, and with/without LiNO ₃ . (a) (b) | |

| | |
|--|-----|
| The first discharge/charge curves, (c) (d) the 20 th cycle, (e) (f) Cycling performances, and (g) (h) show the coulombic efficiencies. | 115 |
| Figure 3-7. Discharge/charge curves for S+AB+PVP electrode cycled at a C-rate of 0.1 C in (a) LiTFSI/DOL:DME, (b) LiTDI/DOL:DME, and (c) LiTDI/DOL:DME/LiNO ₃ electrolytes..... | 119 |
| Figure 3-8. Discharge/charge curves from 1st to 6th cycle of S+AB+PVP electrode using 7M LiTFSI/DOL:DME electrolyte cycled at a rate of 0.1 C between 1.3 – 2.8 V. Inset shows the CV response of this cell scanned at a rate of 0.1 mV s ⁻¹ . | 120 |
| Figure 3-9. The appearance of transparent cells immediately after the cell assembly. (a) LiTFSI/DOL:DME/LiNO ₃ and (b) LiTFSI/TEGDME:DOL/LiNO ₃ | 123 |
| Figure 3-10. Visual examination of the LiTFSI/DOL:DME/LiNO ₃ cell. | 124 |
| Figure 3-11. Visual examination of the LiTFSI/TEGDME:DOL/LiNO ₃ cell. | 125 |
| Figure 3-12. S K-edge XANES spectra of the sulphur electrode (S+AB+PVP) and S ₈ reference compound..... | 128 |
| Figure 3-13. Normalised S K-edge XANES spectra of the LiTFSI/DOL:DME/LiNO ₃ electrolyte and the LiTFSI/DOL:DME/LiNO ₃ cell at the pristine state..... | 129 |
| Figure 3-14. Normalised S K-edge XANES spectra of the pure LiTDI/TMS electrolyte and the LiTDI/TMS cell at the pristine state. | 130 |
| Figure 3-15. S K-edge XANES spectra of the LiTDI/DOL:DME cell at the pristine state compared to Li ₂ S ₄ reference compound. The spectra are shown offset for clarity..... | 131 |
| Figure 3-16. Raw XANES spectra of pure LiTDI/TEGDME/LiNO ₃ electrolyte compared with the LiTDI/TEGDME cell at the pristine state, validating that the LiTDI/TEGDME/LiNO ₃ electrolyte does not contain any sulphur species. . | 133 |

- Figure 3-17.** Sulphur K-edge XANES spectra of the LiTDI/TEG cell at the pristine state (red line) compared with Na₂S₂O₃ reference (green line) and the air-exposed cell (blue line). The spectra are shown offset for clarity..... 134
- Figure 3-18.** (a) *Operando* XANES spectra of the LiTFSI/DOL:DME/LiNO₃ cell and (b) corresponding experimental voltage profile during the initial discharge (green line) and following charge (orange line)..... 135
- Figure 3-19.** *Operando* measurement of the LiTFSI/DOL:DME cell. (a) Discharge and charge profile of the measured cell at a 0.1 C rate. The symbols on the voltage curve indicate the point where the XANES spectra were collected. (b) S K-edge XANES spectra collected during the initial discharge. Spectrum number 0 corresponds to the pristine spectrum collected before applying the current to the cell. The inset represents the area ratio of the main-edge to the pre-edge which guides the chain length of polysulphide species exist in the sample, and (c) S K-edge XANES spectra collected during the charging process..... 137
- Figure 3-20.** Normalised S K-edge XANES spectra set of (a) LiTFSI/DOL:DME/LiNO₃ cell and (b) LiTFSI/DOL:DME cell..... 138
- Figure 3-21.** *Operando* measurement of the LiTDI/DOL:DME cell. (a) Discharge/charge curve of the cell cycled at the 0.1 C rate, and the normalised S K-edge XANES spectra set during the initial (b) discharge and (c) charge processes..... 140
- Figure 3-22.** A series of *operando* XANES spectra of the LiTDI/DOL:DME cell demonstrating spectral changes during the (a) discharge and (b) charge. Time between each measurement was about 15 min, the spectra are shown offset for clarity. Reference spectra of FeSO₄ (black line) is shown for comparison. Indication of stable features at the higher energy region confirms that beam-damaged sulphur is absent. 142

| | |
|--|-----|
| Figure 3-23. <i>Operando</i> measurement for the LiTDI/TMS cell. (a) Discharge/charge curve of the cell cycled at the 0.1 C rate. (b) Waterfall plot of the S K-edge XANES spectra..... | 143 |
| Figure 3-24. Normalised S K-edge XANES spectra set of the LiTDI/TMS cell during the first discharge. The inset shows the calculated area ratio of the main/pre-edge peak..... | 144 |
| Figure 3-25. Normalised S K-edge XANES spectra dataset during the first charge of the LiTDI/TMS cell. The inset shows the evolution of the main/pre-edge area ratio. | 146 |
| Figure 3-26. Normalised S K-edge spectra of LiTDI/TMS cell at the pristine state and end of the charging process, with the inset showing the raw spectra to show the direct concentration of sulphur species present in the sample..... | 147 |
| Figure 3-27. <i>Operando</i> measurement for the LiTDI/TEGDME cell. (a) Galvanostatic curve for the first discharge at the 0.1 C rate, followed by the charge at the 0.05 C. (b) waterfall plot of the S K-edge XANES spectra. (c) Plot of the calculated area ratio of the main/pre-edge peak..... | 149 |
| Figure 3-28. Normalised S K-edge spectra collected during <i>operando</i> measurement of the (a) initial discharge of the LiTDI/TEGDME cell. (b) XANES spectra collected during the following charge. | 150 |
| Figure 3-29. (a) Normalised and (b) raw S K-edge XANE spectra of LiTDI/TEGDME at the pristine state and charged state. | 152 |
| Figure 3-30. Sulphur K-edge spectra; the region before the pre-edge shows no peaks of radical species..... | 154 |
| Figure 4-1. Reactivity of different MXs with lithium polysulphides as a function of redox potentials vs Li/Li ⁺ | 167 |
| Figure 4-2. XRD patterns of prepared composites. (a) V ₂ O ₅ @S, (b) TiO ₂ @S, (c) SnO ₂ @S, (d) CuS@S, and (e) CuO@S. | 170 |

- Figure 4-3.** Electrochemical performances of sulphur composite electrodes with different MX additives assembled in LiTDI/TEGDME electrolyte cycled at the 0.1 C rate. (a) Discharge/charge curves and (b) Cycling performances and coulombic efficiencies. 174
- Figure 4-4.** Electrochemical performances of sulphur composite electrodes with different MX additives assembled in LiTDI/TEGDME/LiNO₃ electrolyte cycled at a current rate of 0.1 C. (a) The first discharge/charge curves. (b) Cycling performances and coulombic efficiencies. 177
- Figure 4-5.** Galvanostatic discharge/charge curves of pure S electrode and MX@S electrodes cycled in LiTDI/TEGDME/LiNO₃ electrolyte at a constant current rate of 0.1 C. (a) Pure sulphur electrode, (b) V₂O₅@S cathode, (c) SnO₂@S cathode, (d) TiO₂@S cathode, (e) CuS@S cathode, and (f) CuO@S cathode. . 179
- Figure 4-6.** S K-edge XANES spectra of (a) TiO₂@S, SnO₂@S, and CuS@S cells, (b) CuO@S and V₂O₅@S cells, all at the pristine state, and (c) S₈ and Li₂S₄ reference compounds (offset for clarity). 184
- Figure 4-7.** *Operando* XANES dataset for the TiO₂@S cell. (a) Voltage profile for the first cycle with dots indicating the points where XAS spectra were collected and labelled from 1 – 17. This cell is cycled at a constant rate of 0.1 C. (b, c) XANES spectra of the S K-edge during the first discharge and charge processes, respectively, corresponding to the labels in the voltage profile, and spectrum number 0 indicating the pristine spectrum (offset for clarity). (d) Data points correspond to the energy position of the main-edge of each spectrum, (e) plot of the maximum intensity of the main-edge (normalised), (f) area ratio of the main/pre-edge, and (g) waterfall graph of S K-edge XANES spectra to show a clear image of the pre-edge evolution. 186
- Figure 4-8.** Normalised S K-edge XANES spectra set without offset. (a) During the initial discharge and (b) during the initial charge. The inset show an expanded view of the isosbestic points. 191

Figure 4-9. Sulphur K-edge XANES spectra of Li_2S reference compound and end of the initial discharge of the $\text{TiO}_2@\text{S}$ cell cycled at 0.1 C rate (offset for clarity).192

Figure 4-10. Normalised Ti K-edge XANES spectra of two references: Ti_2O_3 , Ti(III) and anatase- TiO_2 , Ti(IV). The inset shows an expanded view of the pre-edge area..... 194

Figure 4-11. *Operando* XANES of the $\text{TiO}_2@\text{S}$ cell measured at 0.1 C rate. (a) Voltage profile for the first discharge and charge. The points at which measurements were collected are marked with dots of corresponding colour on each point and labeled 1 to 11. The corresponding normalised XANES spectra for; (b, c) the initial discharge and (c) charge. The S K-edge spectra are shown in the left panels, and the right panels represents the Ti K-edge spectra. 197

Figure 4-12. Ti K-edge XANES spectra of Ti_2O_3 (Ti^{3+}) reference, $\text{TiO}_2@\text{S}$ cell at the pristine, and discharged to 1.4 V state. The inset shows the expanded view of the pre-edge region..... 198

Figure 4-13. *Operando* XANES dataset for the $\text{V}_2\text{O}_5@\text{S}$ cell. (a) Voltage profile for the first cycle with dots indicating the points where XAS spectra were collected and labelled from 1 – 23. (b) Normalised S K-edge XANES spectra during the first discharge and (c) charge, corresponding to the labels in the voltage profile, and the spectrum number 0 indicating the pristine state of the cell. (d) Waterfall graph of XANES to show a clear image of the evolution of the pre-edge. (e) Plot of the calculated area ratio of the main/pre-edge... 200

Figure 4-14. Raw spectra (not normalised) of the pristine state and the charged state of $\text{V}_2\text{O}_5@\text{S}$ electrode..... 203

Figure 4-15. *Operando* XANES dataset for the $\text{CuO}@\text{S}$ cell. (a) Voltage profile for the first cycle with dots indicating the points where XAS spectra were collected and labelled from 1 – 19. This cell is cycled at a constant rate of 0.1 C. (b) Plot of the calculated area ratio of the main/pre-edge. (c) Normalised S K-edge XANES spectra collected during first discharge and (d) charge,

| | |
|---|-----|
| corresponding to the labels in the voltage profile. The pristine spectrum is labelled as spectrum number 0. | 204 |
| Figure 4-16. <i>Operando</i> XANES dataset for the SnO ₂ @S cell. (a) Voltage profile for the first cycle with dots indicating the points where XAS spectra were collected and labelled from 1 – 22. This cell is cycled at a constant rate of 0.1 C. (b) Plot of the calculated area ratio of the main/pre-edge. (c, d) Normalised XANES spectra for S K-edge during first discharge and charge, respectively, corresponding to the labels in the voltage profile, and spectrum number 0 indicating the pristine spectrum..... | 206 |
| Figure 4-17. <i>Operando</i> XANES dataset for the CuS@S cell. (a) Voltage profile for the first cycle with dots indicating the points where XAS spectra were collected and labelled from 1 - 21, (b) Plot of the calculated area ratio of the main/pre-edge. (c, d) Normalised XANES spectra for S K-edge during first discharge and charge, respectively, corresponding to the labels in the voltage profile, and spectrum number 0 indicating the pristine spectrum. | 208 |
| Figure 4-18. Expanded view of the higher energy region of normalised S K-edge XANES spectra. (a, b) TiO ₂ @S and (c, d) V ₂ O ₅ @S, during the first discharge and charge, respectively. (e, f) CuO@S..... | 209 |
| Figure 4-19. S K-edge XANES spectra of reference compounds – Na ₂ S ₂ O ₃ , NaSO ₃ , and FeSO ₄ (offset for clarity). | 210 |
| Figure 5-1. Chemical structure of PANI. | 221 |
| Figure 5-2. Chemical structure of PEDOT:PSS. | 223 |
| Figure 5-3. FTIR spectrum of dried PEDOT:PSS. | 227 |
| Figure 5-4. XRD spectrum of dried PEDOT:PSS. | 228 |
| Figure 5-5. FTIR pattern of synthesised PANI..... | 229 |
| Figure 5-6. XRD patterns of pure sulphur, pure AB, PANI-AB@S, and AB@S composite. | 231 |

- Figure 5-7.** Galvanostatic cycling curves for the as-prepared electrodes cycled at a rate of 0.1 C using the electrolyte composed of 1 M LiTFSI and 0.25 M LiNO₃ in DOL:DME (1:1 by volume). (a) AB@S, (b) PANI-AB@S cells. (c) PEDOT:PSS-AB@S cells. 232
- Figure 5-8.** Normalised S K-edge XANES spectra of the binder-free AB@S cell in the pristine state and S₈ reference compound. The inset shows the pristine state of the PANI-@S cell and PEDOT:PSS-AB@S cell..... 237
- Figure 5-9.** *Operando* XANES spectra dataset for the AB@S electrode cycled at the 0.1 C rate in LiTFSI/DOL:DME/LiNO₃ electrolyte. (a) Galvanostatic discharge/charge curve for the initial cycle with labels 1 – 8 indicating the points at which XANAES spectra were started to record. (b) Normalised S K-edge spectra collected during discharge corresponding to these labels including the pristine spectrum (labelled as 0). The inset showing the calculated main/pre-edge area ratio for each spectrum. 238
- Figure 5-10.** Normalised S K-edge XANES spectra set collected during the charging process of the AB@S cell..... 240
- Figure 5-11.** (a) *Operando* galvanostatic discharge curve of PANI-AB@S cell at a rate of 0.1 C plotted as a function of time, the dots indicate the points where the XANES spectra were collected. (b) *Operando* sulphur K-edge XANES spectra obtained during the initial discharge process of the PANI-AB@S cell with the inset showing the calculated main/pre-edge area ratio for each spectrum..... 242
- Figure 5-12.** Sulphur K-edge XANES spectra obtained during the initial charge process of the PANI-AB@S cell..... 244
- Figure 5-13.** (a) Discharge curve for *operando* measurements of the PEDOT:PSS-AB@S cell at a 0.05 C rate with dots indicating the point at XANES spectra are collected. (b) S K-edge XANES spectra with offset collected during *operando* measurement, and (c) selected spectra without offset to clearly show the

| | |
|--|-----|
| peak intensities. (d) Plot of the calculated main/pre-edge area ratio for each spectrum..... | 245 |
| Figure 5-14. Sulphur K-edge XANES spectra of the PEDOT:PSS-AB@S cell at the pristine state and the discharged state compared with pure PEDOT:PSS reference compound..... | 247 |
| Figure 5-15. Schematic image of effects of PANI and PEDOT:PSS additives on the sulphur cathode. | 248 |
| Figure A-1. <i>Operando</i> XANES measurement of the TiO ₂ @S cell at 0.1 C rate. (a) Voltage profile for the second discharge and charge. Normalised XANES spectra for both the S K-edge (left panels) and the Ti K-edge (right panels) for (b) the second discharge (labelled as 12 - 16), and (c) the second charge (labelled as 17 - 22). | 262 |
| Figure A-2. Preparation steps for post-mortem samples..... | 263 |
| Figure A-3. Ti K-edge XAS set up at beamline B18 at DLS..... | 265 |
| Figure A-4. (a) Typical voltage profile of TiO ₂ @S for the first cycle with labels of various (de)lithiated states (1 - 6) for samples used in <i>ex situ</i> XAS measurements, and (b) <i>ex situ</i> Ti K-edge XANES spectra of TiO ₂ @S cathodes. | 266 |

List of Tables

| | |
|---|-----|
| Table 2-1. List of beamline specifications. | 75 |
| Table 3-1. Basic properties of organic solvents tested for this study. | 103 |
| Table 3-2. List of electrolyte compositions examined in this study. (a) 1 M LiTFSI used as the lithium salt and (b) 1 M LiTDI used as the lithium salt. All combinations have been studied both with and without LiNO ₃ | 107 |
| Table 3-3. List of electrolyte compositions measured by <i>operando</i> XAS. | 127 |
| Table 4-1. Redox potentials of the MX additives studied in this work and the initial discharge capacities of each MX@S cycled using LiTDI/TEGDME and LiTDI/TEGDME/LiNO ₃ electrolytes. (* indicates the higher capacity compared between an electrolyte with and without LiNO ₃)..... | 173 |
| Table 4-2. List of additives tested using XAS measurements | 182 |
| Table 4-3. A summary of the pre-edge detection in different MX@S electrodes at OCV after storage..... | 183 |
| Table 5-1. FTIR spectrum peak assignments for PEDOT:PSS | 228 |
| Table 5-2. FTIR spectrum peak assignments for emeraldine PANI | 230 |
| Table A-1. List of chemicals and materials used | 260 |

List of Abbreviations

| | |
|-------------------|---|
| AB | Acetylene black |
| BF ₄ | Tetrafluoroborate |
| CE | Coulombic efficiency |
| CV | Cyclic voltammetry |
| DLS | Diamond Light Source |
| DMC | Dimethyl carbonate |
| DME | 1,3-dimethoxyethane |
| DOL | 1,3-dioxolane |
| EC | Ethylene carbonate |
| ESRF | European Synchrotron Radiation Facility |
| EXAFS | Extended X-ray Absorption Fine Structure |
| FTIR | Fourier transform infrared spectroscopy |
| LCF | Linear combination fit analysis |
| Li-S | Lithium sulphur |
| LiBETI | Lithium bis(pentafluorethenesulphonyl) amide |
| LiFSI | Lithium bis(fluorosulphonyl) imide |
| LiNO ₃ | Lithium nitrate |
| LiTDI | Lithium 4,5-dicyano-2-(trifluoromethyl)imidazole |
| LiTf | Trifluoromethansulphonate |
| LiTFSA | Lithium bis(trifluoromethanesulphonyl) amide |
| LiTFSI | Lithium bis(trifluoromethane) sulphonamide |
| NiMH | nickel-metal hydride |
| NMP | N-methyl-2-pyrrolidone |
| OCV | open circuit voltage |
| PANI | Polyaniline |
| PEDOT:PSS | Poly(3,4-ethylenedioxythiophene) polystyrene sulphonate |
| PVDF | Poly(vinylidene difluoride) |
| PVP | Polyvinylpyrrolidone |
| SEI | Solid electrolyte interphase |
| SEM | Scanning electron microscopy |

| | |
|--------|--------------------------------------|
| TEGDME | Tetraethylene glycol dimethyl ether |
| TEM | Transmission electron microscopy |
| TMS | Tetramethylene sulphone |
| UV-VIS | Ultraviolet-visible spectroscopy |
| XANES | X-ray absorption near edge structure |
| XAS | X-ray Absorption spectroscopy |
| XPS | X-ray Photoelectron Spectroscopy |
| XRD | X-ray diffraction |

Declarations

I, Nanami Yokota, hereby certify that this thesis has been written by me and confirm that the work presented in this thesis is my own. This work has not been previously submitted for any academic degree.

Nanami Yokota

August 2018

Acknowledgements

First of all, I would like to express my deep gratitude to my supervisor Dr. Maria Alfredsson, for her continuous support during my years at the University of Kent.

Special thanks to the ESRF BM28 XMaS beamline scientists, Dr. Paul Thompson, Dr. Oier Bikondoa, and Dr. Laurence Bouchenoire for their enormous contribution to the XANES work. I would also like to thank Dr. Giannantonio Cibir, B18 beamline scientist at the DLS. Further acknowledgements go to Professor Alan Chadwick, and Dr. Silvia Ramos for their help during beamtime.

I am extremely grateful for the TU Delft Frans Ooms, Professor Erik Kelder for their amazing support and supply of their materials and access to facilities.

I would like to thank to my PhD student colleagues in the Maira Alfredsson's group, Matteo Paul Hogan, Jimmel Stewart, Marcus Bertuzzo, Sally Pang, and Dr. Rebecca Tannary who have helped me during my PhD.

Finally, I would like to thank all my family and friends who support me during my studies.

Abstract

Advanced power sources are urgently needed to meet the ever-increasing demand of modern society, especially battery requirements for extended-range electric vehicles and grid energy storage applications. [1] However, current rechargeable lithium-ion batteries are not able to fulfil the demand for future energy demands.

The Li-S batteries represent a very promising electrochemical system for these applications that offers high theoretical capacity of 1673 mAh g⁻¹, low material cost, and relative safety. [2] Despite these attractive advantages, Li-S batteries are still hindered from large scale commercialisation, due to a number of challenges. [3] The major concern is thought to be caused by the shuttle effect, originating from the dissolution of cathode species into the electrolyte and migration towards the anode, where they react with the lithium metal, resulting in loss of active sulphur material. [4] This leads to poor cycling stability, low Coulombic efficiency, and Li corrosion. The sulphur cathode undergoes very complicated reaction step during cell cycling but the complete reaction mechanisms are still not established.

Herein, an *operando* XAS technique is employed to gain deep insights into the mechanism of Li-S cell reaction. This measurement technique offers the advantage to be element specific that is sensitive to oxidation states and chemical bonding of the atoms of interest. XAS in the S K-edge region is a powerful tool for the detection of the reaction product of Li-S batteries. The fingerprint analysis consisting of a comparison of XAS spectra between different sulphur species and measured data is helpful for distinguishing different species exist in the cell during the battery operation.

Operando measurements were performed utilising a modified *operando* cell specifically designed for X-ray experiments and provide accurate information of electrochemical process. The design and specification of the *operando* cell are described in chapter 2.

The objective of chapter 3 was to investigate the differences in the sulphur reaction mechanisms in variation of the electrolyte compositions including Li salts, solvent systems, and LiNO₃ additive. The S K-edge XANES measurements demonstrated that

the electrolyte compositions influence the self-discharge rate and the conversion reaction mechanisms of sulphur chemistry.

Chapter 4 systematically investigated the function of inorganic metallic additives on sulphur electrodes with the aim of redox-shuttle suppression, catalytic activities, self-discharge mitigations, and adsorption of polysulphides. This chapter highlights the unique *operando* XAS measurements of the S and Ti K-edges using a single test cell. This revealed details about the response of the TiO₂ and S chemistry during lithiation and de-lithiation. Reversibility of the oxidation states of TiO₂ was demonstrated. Additionally, the importance of the *operando* analysis is demonstrated by comparison with the post-mortem analysis.

Chapter 5 demonstrates the environmentally friendly and cost-effective fabrication method of sulphur electrodes. Potential hazardous material is eliminated from the sulphur electrode system and replaced with conductive polymers, PANI and PEDOT:PSS, and their cell performances were investigated using *operando* XAS technique.

Chapter 1

Literature Review

1.1 General Introduction

Energy demand is increasing worldwide linked to rising world population. It is also linked to our daily life styles; relying on constant access to electricity, making renewable energy sources as important in the future, as in the present.

We currently heavily rely on fossil fuels, e.g., coal, crude oil, and natural gas as the primary energy sources. However, fossil fuels are limited and not sustainable. Burning of fossil fuels also lead to CO₂ emissions that pollute our natures, creating global warming. We, thus, need to reduce our reliance on fossil fuels adopting alternative clean and renewable energy sources, including solar and wind power. However, to work effectively, these energy sources are uncontrollable and heavily relying on the weather or climate. There is also an absolute need of advanced energy storage system that can utilise the energy when excess is produced and then be able to release it back on demand in order to provide a constant power supply. [5] This is where batteries can be a solution, owing to its ability to electrochemically store and release energy in a controllable fashion.

The performance of the battery can be estimated by comparing a range of properties summarised in **Figure 1-1**. Batteries are divided into two classes; primary and secondary batteries. Primary batteries are non-rechargeable and designed as a disposable battery. Those batteries are assembled in the charged state and the reaction runs only once until exhausted and then discarded; resultant products not arranged to allow the reaction to run in inverse. [6] The most common primary batteries are alkaline battery, zinc-manganese battery, and carbon-zinc battery.

Secondary batteries are rechargeable batteries that generally have lower energy storage capability than primary batteries. [6] The chemistry of a secondary battery is different from a primary battery. Rechargeable cells can be fabricated in either the

charged or discharged state and reversible reactions take place. [7] Currently, the most common secondary battery technology available on market are lead acid (Pb-acid), nickel cadmium (Ni-Cd), nickel metal hydride (Ni-MH), and Lithium-ion (**Figure 1-1**). Ni-MH was used in the first hybrid electrical vehicle (HEV) application and invaded the primary alkaline battery market due to its relatively high energy capacity and light weight. [8][9] However, Ni-MH deteriorates the cell performance at low temperature, [10] leading to low rate capability and low coulombic efficiency (CE). [11] Li-ion batteries are currently the most popular portable electronics. They have also been a demand for application in electrical vehicles (EVs) and HEVs, but the future development needs better specifications. Lithium-sulphur (Li-S) batteries are one type of secondary batteries researched for its potential applications in automotive industry as could improve the performance compared to Li-ion technologies. Li-S system can be considered as a potential alternative to traditional Li-ion batteries and, will therefore, be discussed under post Li-ion batteries in this thesis.

The aim of this thesis is to understand the atomistic properties of Li-S batteries using *operando* X-ray absorption spectroscopy (XAS) techniques in combination with electrochemical measurements.

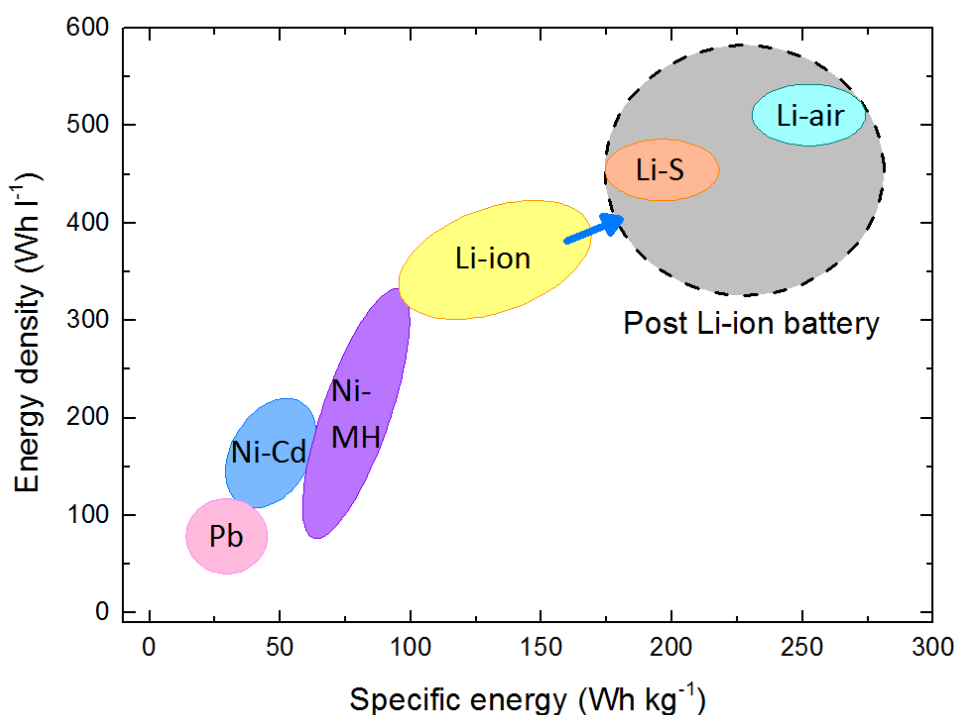


Figure 1-1. Comparison of different secondary batteries in terms of volumetric and gravimetric energy density. Reproduced from [12].

1.1.1 Battery characteristics

This section provides an introduction to the terminology often used in this thesis to describe batteries. [13]

- The term 'specific energy', expressed in Wh kg^{-1} corresponds to the energy of battery per unit mass, whereas the 'energy density' measures energy of battery per unit volume.
- In Li-S system, voltage polarisation is ascribed to the concentrated polarisation during Li_2S nucleation from long-chain polysulphides. [14] This happens because of the low electric and ionic conductivity of the elemental sulphur and intermediate species, which elevate the internal resistance of the battery. Electronic and ionic conductivity are significantly important for the efficient movement of electrons and ions during battery cycling. [15]

Voltage polarisation is typically observed at the joint section between the high and low discharge plateaus. Also, can be recognised by the large difference in current plateaus between discharge and charge.

- Internal resistance: the resistance within the battery. With increasing internal resistance, efficacy of reduction kinetics decreases, and thermal stability is lowered as more of the energy is converted to heat.
- Open-circuit voltage (OCV): the voltage of the battery when no current is applied.
- Cut-off voltage is the low end of the voltage window, defines the minimum voltage to which the battery is allowed to discharge.
- Coulombic efficiency (CE): describes the charge efficiency compared to the prior discharge. In Li-S battery, low CE is mainly related to the redox shuttle reaction, which is translated into excessive charging capacity.

1.2 Li-ion batteries

Li-ion batteries were commercially launched by Sony in 1991. [16] It has quickly replaced the Ni-MH batteries and become one of the most successful and fastest growing modern electrochemistry used for mobile applications, such as, portable electronics and automotive applications. [6][17][18] Li-ion batteries hold great promise, benefiting from being lighter and smaller, as well as demonstrating higher energy density than Pb-acid, Ni-Cd, and Ni-MH systems. [11]

A traditional Li-ion battery consists of two electrodes, the positive (cathode) and the negative (anode) electrodes, separated by an electrolyte, which is a medium for ion transfer between the two electrodes. Reversible chemical reactions at both electrodes are required (Figure 1-2).

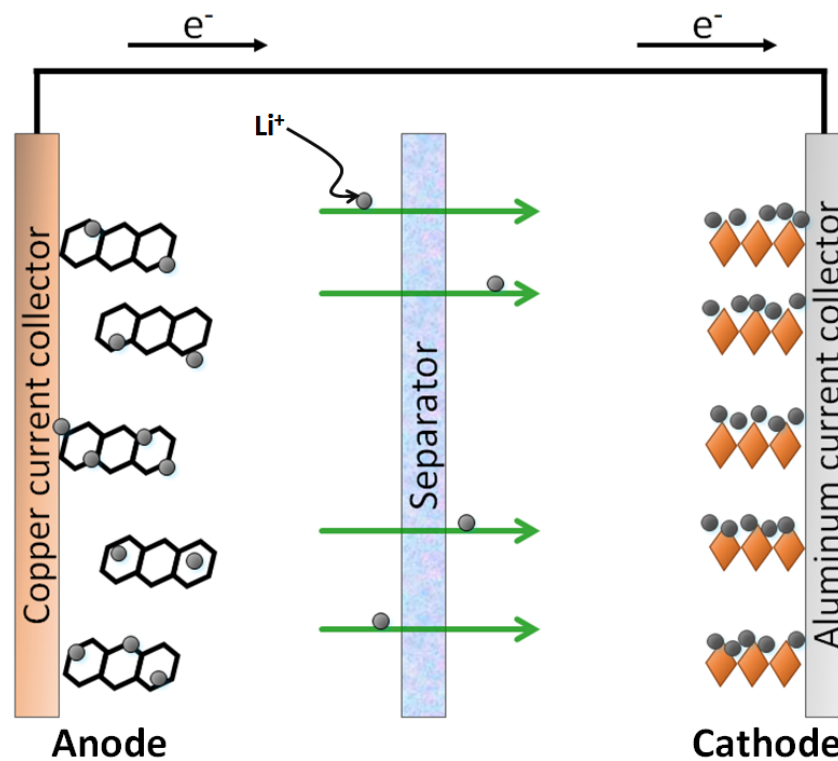


Figure 1-2. Schematic of a typical Li-ion battery. Graph reproduced from [19].

1.3 Post Li-ion batteries

Despite the great progress achieved over the years, the energy density of Li-ion technologies currently available on the market will not be able to satisfy the demands by all future applications e.g., extended range of electric vehicles, heavy duty and grid applications. [19][20] Recently, researchers have engaged in developing various types of “next-generation” post lithium-ion batteries whose feasibility and performance still need to be explored. [21]

The theoretical specific energy associated with the current Li-ion cells, applied in recent electric vehicles, can only achieve a specific energy of $\sim 450 \text{ Wh kg}^{-1}$, which is an order of magnitude lower than that of gasoline (octane) at $\sim 13000 \text{ Wh kg}^{-1}$. [19] Two

promising candidates, Li-S and Li-air systems, can instead deliver a theoretical specific energy of $\sim 2600 \text{ Wh kg}^{-1}$ and $\sim 11000 \text{ Wh kg}^{-1}$, respectively (**Figure 1-3**). [22][23]

Considering that gasoline only have a practical specific energy of 1700 Wh kg^{-1} , both Li-S and Li-air are closer to the expected value than Li-ion that demonstrate a practical specific energy of 250 Wh kg^{-1} compared to 650 and 950 Wh kg^{-1} , for Li-S and Li-air batteries, respectively. The goals of the next generation Li-ion batteries are, therefore, reachable. Moreover, the use of sulphur as a cathode material has the great advantage of being both abundant and low cost, compared to the conventional Li-ion battery materials. [2]

In the following section, Li-air battery is briefly introduced and after that, an overview of the fundamentals of Li-S batteries is described, with details on the recent progress of various elements, such as, lithium anodes, sulphur cathodes, and electrolytes.

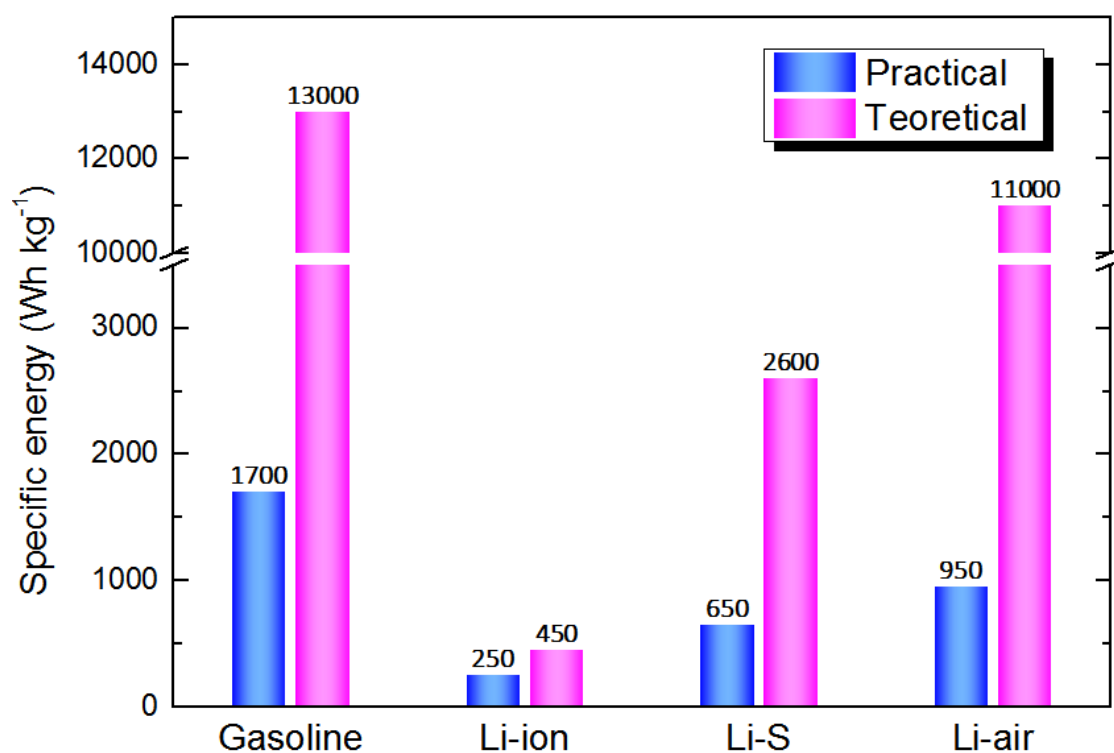


Figure 1-3. Bar graph compares the theoretical and practical specific energy of gasoline, Li-ion, Li-S, and Li-air batteries. Graph reproduced from [23][24].

Li-air battery

Based on excess Li^+ ion supply from the Li anode and a progressive flux of O_2 through the cathode, the Li-air electrochemical reaction offers a remarkable theoretical specific energy of $\sim 11,000 \text{ Wh kg}^{-1}$, which is identical to the value of gasoline. [19][25] There are four types of lithium-air batteries, based on the electrolyte used; (i) aqueous electrolytic, (ii) aprotic/non-aqueous electrolytic, (iii) mixed/hybrid electrolytic, and (iv) solid-state electrolytic. Among which the non-aqueous Li-air battery system has been the most studied one, due to its higher theoretical energy density than other types (**Figure 1-4**). [24] All the four systems listed above use metallic lithium as the anode and O_2 gas as the cathode.

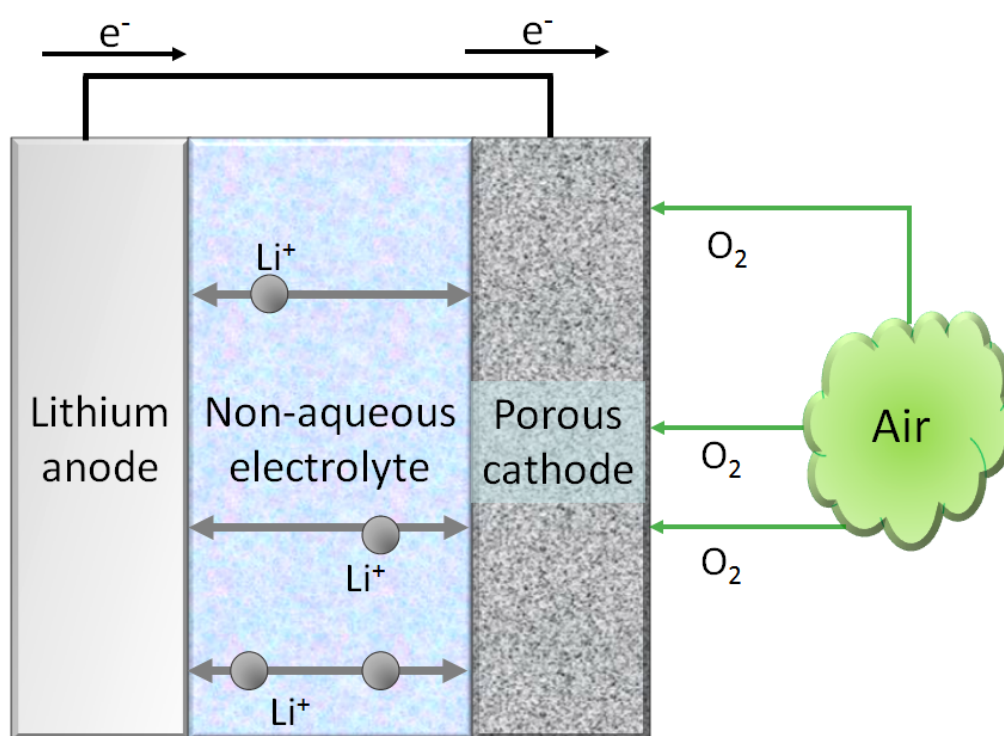


Figure 1-4. An illustration of a non-aqueous Li-air battery, typically composed of a lithium anode, electrolyte containing lithium salt and organic solvent, and a porous O_2^- cathode made with carbon particles. Graph reproduced from [19][24][26].

Current Li-air batteries are still in the experimental stages, and practical application of this technology is limited because of poor cycling performance and low energy efficiency. These limiting parameters arise from its design; (1) insufficient electric

conductivity of Li_2O_2 and unstable cycling due to slow Li^+ diffusion coefficient, (2) evaporation of electrolyte during cycling which severely shorten the cycle life, [26][27] (3) potential risks of fire and explosion due to the concept of combining Li metal and O_2 gas, particularly when a flammable liquid electrolyte is employed, [25] and (4) limited depths of discharge potential applied to prevent ubiquitous side reactions. In addition, unsatisfactory understanding of the fundamentals of chemical reactions, such as, catalytic reactions. Those challenges still take a longer time to be resolved, therefore, the commercialisation of Li-air batteries is still relatively far, unless a major breakthrough is to be reported.

Li-S battery

Instead, Li-S batteries are expected to proceed to full commercialisation further than Li-air batteries. [28] The industrial interest in Li-S battery has increased from few dedicated research companies. Currently, the UK based company 'OXIS Energy' holds more than 100 patents on Li-S batteries. An USA based company 'Sion Power' has a manufactured 350 Wh kg^{-1} Li-S battery sold into the unmanned aerial vehicle (UAV) market. [29] In addition, Li-S cells are already available in a number of niche applications. [3]

Li-S battery is expected to deliver a specific capacity of 1673 mAh g^{-1} and offers high theoretical specific energy of 2600 Wh kg^{-1} when fully discharged, far greater than current Li-ion batteries. [30] Additionally, sulphur is an abundant element, therefore, inexpensive and environmentally friendly, making it particularly attractive for a low-cost system. [4][31]

1.4 Fundamentals of Li-S batteries

A classic Li-S cell is composed of a sulphur-based cathode and a metallic lithium anode, separated by a separator soaked into an organic electrolyte, as illustrated in **Figure 1-5**. The Li-S batteries operates by reversible reaction of sulphur to form series of polysulphide species through a multistep redox reaction.

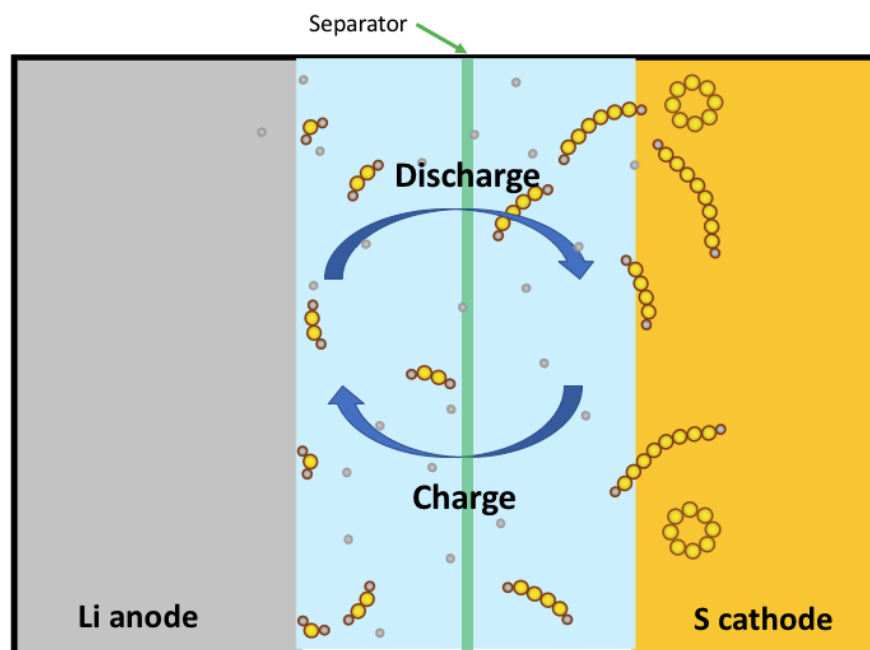


Figure 1-5. A schematic illustration of a Li-S cell. Graph reproduced from [32].

Despite its promising attributes, there are several unresolved drawbacks with the Li-S system, which have limited its practical applications, e.g., Li-S cell still suffers from low energy utilisation and efficiency.

Herein, the limiting factors of Li-S batteries are described, and different approaches for improvements of Li-S cells previously done are described. This thesis deals with the issues in the Li-S system. Efforts has been made to improve the cathode and the electrolyte compositions.

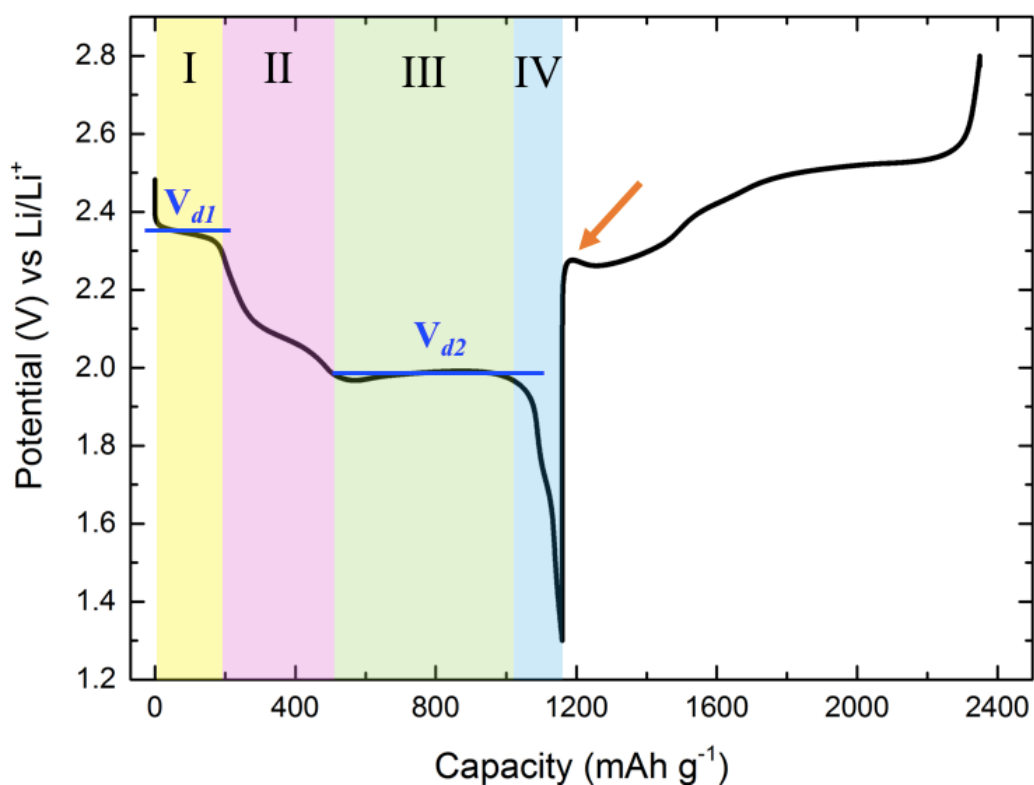


Figure 1-6. Typical voltage profile of Li-S cell. Graph reproduced from [33].

The Li-S cell is based on conversion reactions (between $S_8 \leftrightarrow Li_2S$) rather than on intercalation. [34] Li-S cell operation begins by a discharge process because of the absence of Li ions at the sulphur cathode when the cell is assembled. Hence the cell is originally in a charged state. **Figure 1-5** illustrates the working mechanism of Li-S batteries during cycling and **Figure 1-6** displays the typical galvanostatic discharge/charge profile. A Li-S cell undergoes solid \rightarrow liquid \rightarrow solid transitions involving dissolution precipitation, [35] which is completely different electrochemical reactions to other conventional lithium ion battery systems (e.g, $LiCoO_2$ and $LiMn_2O_4$) and makes Li-S batteries difficult to control. [7] The overall redox couple of a Li-S battery can be simply described by **Equation(1-1)**;

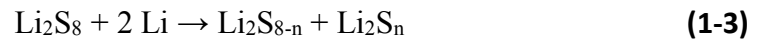


In practice, the actual discharge and charge processes are extremely complex with numerous side reactions co-existing simultaneously. Moreover, there are numbers of publications suggesting different reaction equations and the real reaction mechanisms are still not fully established. Currently, it is generally accepted that the discharge process follows four stages;

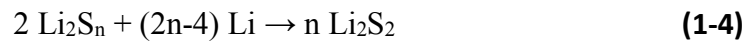
Stage I: Sulphur existing as elemental cyclooctasulphur (cyclo-S₈) is reduced by two electrons to form dianionic long-chain polysulphide intermediates (Li₂S₈) expressed by **Equation (1-2)** with a first potential plateau appearing at about 2.3 V, denoted as a high voltage plateau, V_{d1} in **Figure 1-6**. The formed Li₂S₈ dissolves into the liquid electrolyte activating the residual sulphur to become contact with Li⁺-ions.



Stage II: The chain lengths of the dissolved Li₂S₈ are reduced to medium/short-chain polysulphides (Li₂S_x, 4<X≤6) expressed by **Equation (1-3)**. The battery experiences a gradual potential decrease during this stage and the electrolyte becomes more viscous due to the increase in the concentration of dissolved polysulphides.



Stage III: In the beginning of stage III, the cell is saturated with long-chain polysulphides. Medium/short-chain polysulphides are further reduced to form insoluble Li₂S₂ and Li₂S, showing a second plateau at about 2.1 V (denoted as low voltage plateau, V_{d2} in **Figure 1-6**), contributing to the major capacity of the Li-S battery. [37] This reaction can be expressed by **Equation (1-4)** and **Equation (1-5)**, and these two reactions are competing with each other. [33]



Stage IV: Further reduction of Li₂S₂ to Li₂S is associated with a voltage decrease, which is defined by **Equation (1-6)**.



The reverse reactions occur during the charging process, starting with a voltage drop linked to oxidation of Li₂S₂ and Li₂S, indicated by an arrow in **Figure 1-6**. [33] This forms soluble polysulphides, which generate the conversion reaction and diffusion to the cathode to be re-activated.

The chemistry behind these voltage plateaus can be further investigated by understanding CV curves, from which each peak represents a chemical reaction.

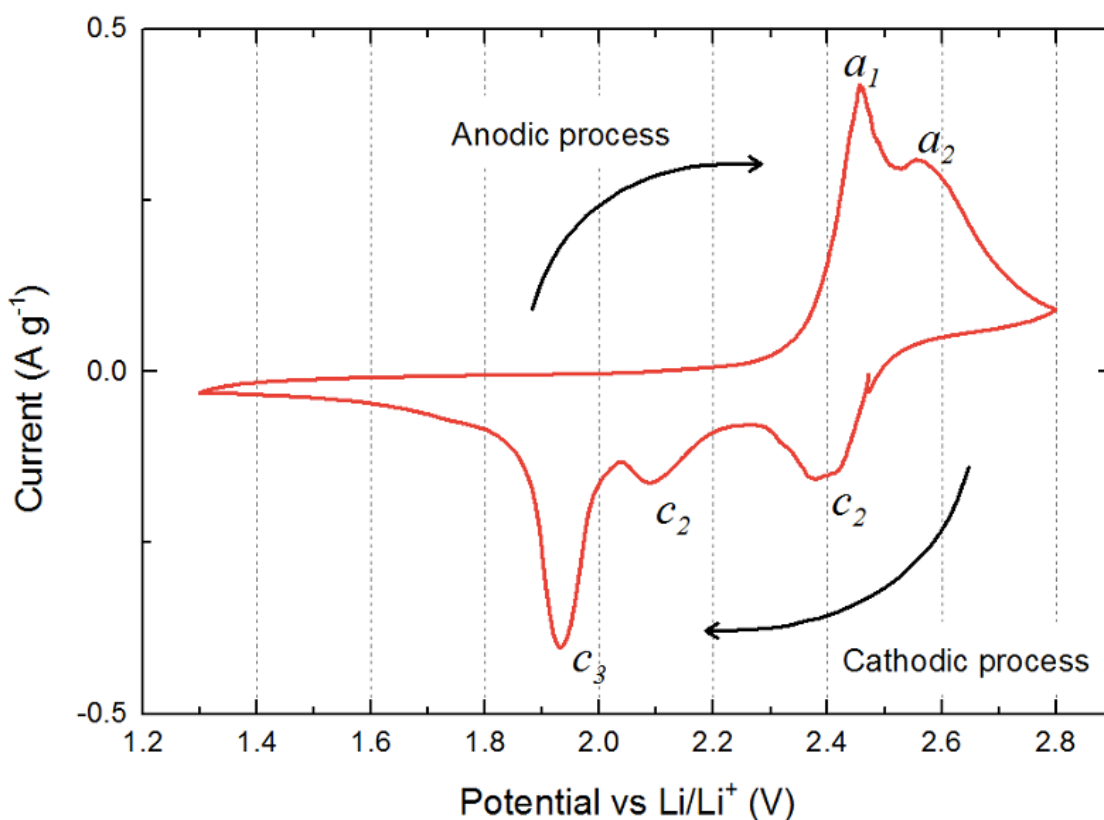


Figure 1-7. CV curve of a sulphur cathode scanned during the initial cycle at a scan rate of 0.03 mV s^{-1} .

A typical CV profile of a Li-S cell is represented in **Figure 1-7**. Three cathode current peaks are located at about 2.4, 2.1 and 1.9 V, denoted as *c*₁, *c*₂, and *c*₃, corresponding to Stage I, II, and II in **Figure 1-6**, respectively. The *c*₂ peak can often be overlapped with the *c*₃ peak, depending on the type of electrolyte and scan rate. [38] During the oxidation process, two anodic current peaks are located about 2.5 and 2.6 V (denoted as *a*₁ and *a*₂, respectively) partially overlaid with each other, where peak *a*₁ corresponds to the oxidation of $\text{Li}_2\text{S}/\text{Li}_2\text{S}_2$ and peak *a*₂ accounts for the further oxidation to S_8 . [39] Again, different cell composition (electrolyte and electrode design) and different scan rate may result in overlapping peaks representing these peaks as a single broad peak. [40]

1.5 Challenges and improvements of Li-S technologies

Despite the progress with Li-S cell and the understanding of the reaction mechanisms, there are still a number of factors causing rapid capacity fading, including dissolution of active material in form of polysulphides leading to diffusional loss of active sulphur. Other issues are associated with the insulating nature of sulphur and reaction products.

1.5.1 Positive electrode

This subsection describes the unsolved issues surrounding the sulphur cathodes.

- 1) Low conductivity of sulphur and reaction products formed during cell operation. [35]

Sulphur has both low electronic conductivity ($\sim 5 \times 10^{-30} \text{ S cm}^{-1}$ at room temperature) and poor ionic diffusivity leading to poor electrochemical utilisation. [41][42][43][44] Thus, the sulphur electrode requires supporting electronically conductive additives, typically carbon. [45] As polysulphides are formed, they are dissolved into the electrolyte and leaves remaining sulphur exposed to the carbon so the reduction reaction of sulphur progressively moves forward. [33] Therefore, we cannot completely exclude formation of polysulphides as they can act as redox mediator species to improve the kinetics of the electrochemical reaction. [46][47][48]

- 2) Polysulphide dissolution into the electrolyte [49]

The polar nature of long chain lithium polysulphides and non-polar carbons do not engage in strong interaction. [4] Common solvents used in Li-S electrolytes show polar properties, allowing strong interactions with the long-chain polysulphide. The intermediate polysulphide formed during the battery operation, therefore, dissolves into the electrolyte. Dissolved lithium polysulphides can migrate through the separator to the anode side, where they are further reduced to solid precipitates ($\text{Li}_2\text{S}_2/\text{Li}_2\text{S}$). [50] Some of which remain on the Li anode side and do not participate in further reactions, leading to the loss of active materials. Also, some of the polysulphides remain dissolved in the electrolyte, and do not precipitate back onto the cathode as lithium sulphides instead becoming electrochemically irreversible (detached). [51] As a result, poor discharge capacity and rapid capacity fade are often observed during cycling. [35] This cyclic process is known as the 'shuttle' phenomenon of Li-S batteries and severely

shorten the battery life. [52][53] The dissolution and distribution of sulphur species heavily depends on the nature and volume of the electrolyte, the current density (expressed as C-rate), and the composition and architecture of the sulphur electrode. [54]

3) Large volumetric expansion and morphological change [55]

Sulphur particles experience large volume expansion and shrinkage (up to 80 %) upon discharge and charge processes. [56] This causes irreversible morphological pulverisation in the cathode and breaks the electrical connection between active materials, leading to fast capacity decay. [20][57][58]

4) Self-discharge phenomenon

The self-discharge poses a large obstacle for the practical application of Li-S batteries. The main cause of self-discharge in Li-S batteries is the fact that the active material dissolves in the electrolyte during storage time, while there are no current applied over the cell (OCV). This causes side reactions between the sulphur in the cathode and lithium ion present in the electrolyte. The soluble polysulphides gradually diffuse out of the cathode, reducing the amount of active sulphur in the electrode. Consequently, the discharge capacity is lowered.

To address these issues, extensive efforts have been devoted to improving the sulphur cathode structure and composition. The ideal sulphur electrode should meet the following requirements: (i) Provide adequate room for polysulphides to diffuse and reverse evenly, [32] (ii) controlled surface area for sulphur-electrolyte contact to minimise polysulphide dissolution and side reactions, (iii) sufficient space to accommodate sulphur volume expansion, (iv) a minimal conductive pathway to facilitate both ion and electron transport to enable high-rate chemical transformations of sulphur active materials, [56][59][60][61] (v) large conductive surface area for insulating solid lithium sulphides deposition, in order to retain the morphology of electrodes, [62] and (vi) an interconnected and closed architecture for polysulphides containment. This section describes recent achievements on sulphur cathode materials.

1) Host materials

A large part of the research undertaken on Li-S batteries is devoted to control the dissolution, diffusion, and redox mechanisms of polysulphides at the cathode and is becoming the kernel of advanced electrode design. The group led by Nazar pioneered the concept of a high-ordered, mesoporous carbon sulphur cathode in 2009, enabling insulating sulphur to maintain a close contact with the conductive carbon framework. [50] This work contributed to the rapid development in the field of Li-S batteries and increased the number of publications progressing in the understanding of Li-S batteries based on the analysis of sulphur cathodes. [63][64] A number of carbon frameworks, such as, carbon nanotubes, [65][66] carbon nanofibers, 2D carbon sulphur structures based on graphene materials, [67] as well as 3D materials including porous and hollow carbon spheres have become popular strategies to develop the electrode architecture for Li-S batteries. [68]

2) Conductive polymer additives

Another approach to solve the problems is to use electrically conductive polymers, such as, poly3,4-ethylenedioxythiophene (PEDOT), [69] polyaniline (PANI), [70] polypyrrole (PPY), [71] and polythiophene (PT) [72] to encapsulate the sulphur particles within the cathode. Conductive polymers are promising materials for sulphur cathodes due to; promoting electronic conduction; elastic and flexible properties, which can accommodate the sulphur volume expansion; and large variety of functional groups that offers effecting binding sites for lithium polysulphides, therefore, serving as physical barriers to the diffusional loss of active sulphur out of the electrodes. [50][73]

3) Inorganic host materials

The recent trend has been towards the employment of inorganic host materials including metal oxides, nitrides and sulphides to confine lithium polysulphides within the cathode via strong chemical bonding. A more detailed explanation of this concept can be found in Chapter 5.

4) Alternatives to sulphur cathodes

As an alternative to sulphur cathodes, the employment of fully lithiated Li_2S as a starting material is becoming a possible option, with a high theoretical capacity of 1166 mAh g^{-1} . The advantage of fully lithiated sulphur, Li_2S can be paired with different kinds of lithium metal-free materials, such as, Si, Ge, and Sn. Such materials can be pre-lithiated and employed as the source of lithium, which eliminates the use of the Li metal. Hence, disadvantages arising from metallic lithium such as dendrite formation and safety concerns can be eliminated. [63] Unlike sulphur, Li_2S exists in fully expanded state, therefore, undergoes volumetric contraction during its initial delithiation process instead of expansions in the case of S_8 cathodes, preventing structural damage to the cathode. Moreover, the higher melting point of Li_2S allows material modification at a high temperature and surface coating can be more stable.

Despite the number of advantages over sulphur, it has some disadvantages to overcome. Li_2S still suffers from poor ionic and electronic conductivities and has very large particle sizes. [74] It is also highly sensitive towards moisture and air, therefore, Li_2S cathode fabrication requires to be in an argon atmosphere. [75] In addition, it shows poor performance during prolonged cycling due to dissolution of lithium polysulphide intermediates, which hinders the practical applications of Li_2S cathodes. In attempts to overcome this problem, Zheng and co-workers successfully developed *in situ* formed Li_2S /microporous carbon, which delivered a specific capacity of 650 mAh g^{-1} after 900 cycles with a CE close to 100 % at 0.1 C rate. [76]

5) Lithium polysulphide catholytes

Another approach that recently has become attractive is to use the soluble lithium polysulphide (so-called catholyte) as a replacement to the solid cathode. [73][74] Such configuration provides a facile dispersion and homogeneous distribution of active sulphur in the conductive matrix and eliminates the initial transition step from solid to liquid conversion, potentially engaging to a faster reaction. As a consequence, high utilisation of the sulphur active material is achieved. [35] Recently, the Manthiram group demonstrated the use of a lithium superionic conductor (LiSICON) solid membrane as a cation-selective electrolyte for catholyte batteries, which successfully stabilises the ionic conductivity of the cell during electrochemical process. [78] As Li_2S

and catholytes have not been studied as a starting material in this thesis it will not be further discussed.

1.5.2 Negative electrode

Li metal is commonly used as a negative electrode in the Li-S systems. Working with pure Li metal as the anode is associated with various difficulties compared to intercalation materials used in Li-ion batteries, including safety issues. It is very complicated to stabilise the Li anode in Li-S cells due to double damage from an uncontrolled growth of 'Li dendrite' and side reactions between the Li metal and polysulphides during operation. [79]

(1) Polysulphide shuttle

Soluble polysulphides formed during the cell reaction can migrate to the anode side through the separator and react with the Li metal by being reduced to lithium sulphides ($\text{Li}_2\text{S}_2/\text{Li}_2\text{S}$) at the Li surface. During the charge process, these lithium sulphides are converted to lithium polysulphides. However, this reaction is difficult due to the insulating nature and low solubilities of $\text{Li}_2\text{S}_2/\text{Li}_2\text{S}$. Abnormally high charge capacity ('infinite' charge phenomenon) appears making it difficult to reach complete oxidation of polysulphides into elemental sulphur resulting in extremely low CE value (**Figure 1-8**). [52][80] Moreover, diffusive anion transport of polysulphides opposes to the electron transport also contributes to the infinite charging phenomenon. [81] During the charging plateau, the redox shuttle reaction is a competing process with the re-oxidation of short-chain polysulphides to long-chain polysulphides.

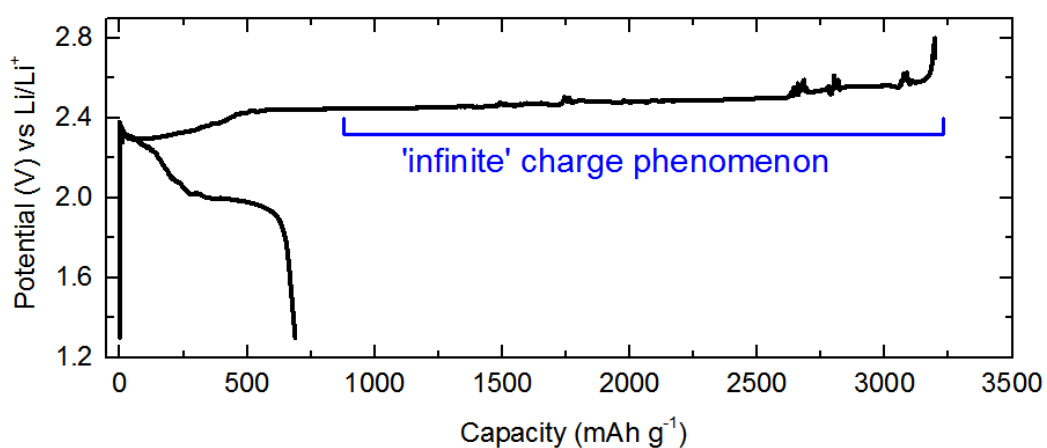


Figure 1-8. Initial discharge-charge voltage profile of Li-S battery cycled in LiNO_3 -free electrolyte. The cathode consists of S+AB+PVP (65:25:15 weight ratio). The electrolyte consists of 1 M LiTFSI in DOL/DME. This cell can only deliver an initial coulombic efficiency of 21.5 % due to the ‘infinite’ charging phenomenon.

(2) Non-uniform solid electrolyte interphase (SEI) formation

The highly reactive nature of lithium metal easily forms an SEI layer, which contentiously causes irreversible side reactions with the electrolyte and blocks the lithium deposition on anode upon charging. [82] This also leads to the infinite charge phenomenon. Charging time for Li-S battery needs to be massively reduced to become an alternative for vehicle batteries when introduced to the market. [83]

(3) Li dendrites

Li dendrite originates from uneven stripping/plating of a lithium layer when the battery is discharged/charged. This grows over the repeated cycles eventually penetrating through the separator to reach the cathode. This causes an internal short circuit which may generate thermal runaway posing a severe safety hazard (**Figure 1-9**). [84] Also, dendrite growth leads to continuous breaking and reforming of the SEI layer, which further consumes Li metal, causing the low utilisation of the Li metal and the cell will eventually fail due to depletion of electrolyte and high impedance through the thick SEI. [85] Moreover, the dendrites could be detached and lose contact with the lithium anode, which become inactive, resulting in further loss of capacity. [35]

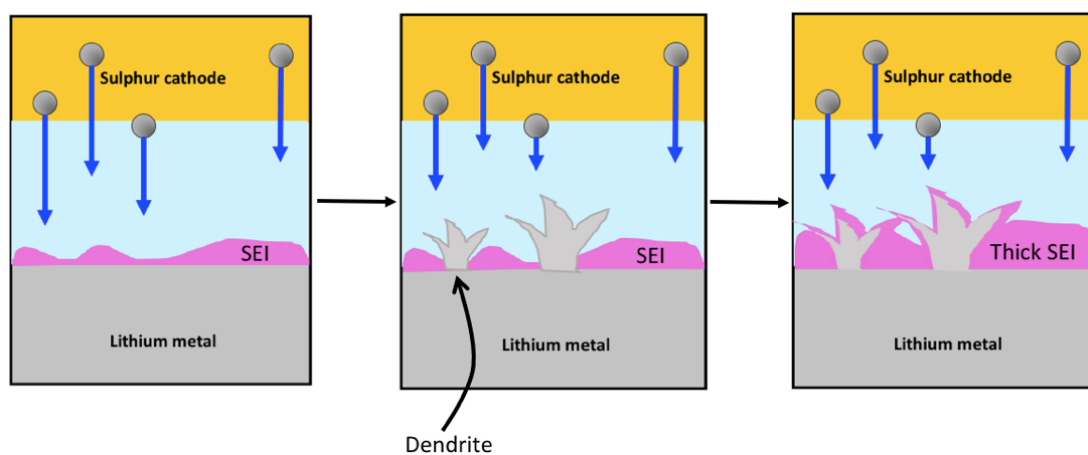


Figure 1-9. Schematic of dendrite growth within Li-S battery. Graph reproduced from [86]

Unlike the cathode, the Li anode has not gathered enough attention and number of publications are significantly smaller than the ones focused on the sulphur cathode, although it is directly involved in the parasitic reactions. [87] The behaviour of the Li anode holds a pivotal role when overcoming the challenges of Li-S systems. [88]

(1) LiNO_3 additive

A general approach to address the above-mentioned drawbacks is to modify the electrolyte system with the LiNO_3 additive. In 2008, Mikhaylik *et. al*, reported that the addition of LiNO_3 hinders the lithium polysulphide shuttle reaction achieving a Li-S battery with CE values of almost 100%. In the following year, the addition of LiNO_3 was found to enhance the rate of sulphur utilisation in the cathode. [89] These results gave a significant impact and LiNO_3 has become the most-used additive in electrolyte solutions in Li-S batteries. [90]

However, the mechanism for this improvement is still not fully understood. [91] The current understanding on the function is that the presence of LiNO_3 in the electrolyte plays different roles at the Li anode and sulphur cathode. [92] At the anode side, reduction of LiNO_3 by Li metal directs deposition of the nonreactive passivation layer (LiNO_3 -induced SEI film) on the surface of Li anode. Based on a comprehensive XPS and FTIR data, Aurbach and co-workers identified the passivation layer as Li_xNO_y . [89] This layer protects the lithium anode exposed to dissolved polysulphides and thereby

diminishes the shuttle reaction, thus improving the cycling performance of Li-S cells. [30][38][88][90][93][94] Later on, Xiong *et al.* proposed the mechanism for the SEI formation on Li metal using the XPS and SEM techniques. [87] They claimed that the passivation film continues to grow during cycling due to the strong oxidative nature of LiNO₃. Hence, the Li metal progressively consumes LiNO₃ and results in a thick layer of SEI film and deposit substantial debris on the Li metal. [31][95]

On the cathode side, LiNO₃ is instead irreversibly reduced at potentials below 1.6 V, the discharge process and the resultant products may accumulate on the carbon surface causing adverse effect on the reversibility of the sulphur electrode. [57][92] This can easily be handled by raising the cut-off voltage, although the capacity needs to be compromised by narrowing the voltage window. [38] Addition of LiNO₃ raises the safety issues due to the strong oxidative nature of LiNO₃. [33][82][87] Continuous cycling exhausts the NO₃⁻ group, leaving the cathode composition similar to the black gunpowder. Therefore, LiNO₃ should not be relied too heavily upon in the future. [14]

Against these adverse effects of the LiNO₃ salt, the Zhang group designed a LiNO₃-free electrolyte system, demonstrating a successful Li-S pouch cell achieving the specific energy of 350 Wh kg⁻¹ at the 0.05 C rate. This is so far the best Li-S performance reported in the absence of the LiNO₃ salt in the electrolyte. [14] The single solvent of DOL containing 2 M LiTFSI was used as the electrolyte and this observed an excellent reversibility of lithium anode benefiting from low solubility and low permeability of polysulphide along with high conductivity of Li⁺. Using pure DOL as the solvent was found to contributed to lithium anode protection.

(2) Li anode protection

Several groups have been developing different pathways to protect the lithium anode. Yang *et al.* proposed the pre-treatment of Li metal by crown-ether containing electrolytes, forming a polymer-like film on the surface of Li metal. This film can selectively permeabilise the Li⁺-ions while blocking the polysulphide access to the Li anode. [96] Wen and co-workers demonstrated the fabrication of Li₃N protective layers on the surface of the Li anode via *in situ* reaction between Li and N₂ gas. [82] The Cui group pioneered the synthesis of an anode composed of molten lithium infused into 3D 'lithiophilic' layered graphene oxide. [97] Jin *et al.* proposed the

fabrication of 3D current collector composed of carbon nanotubes connected to an ultrathin graphite foam via carbon-carbon covalent bonds, which can be used for both the lithium anode and sulphur cathode. [98] A drawback is that these sophisticated anode synthesis methods are both complicated and costly.

(3) Elimination of Li metal

An alternative to lithium metal anode, silicon is considered as a promising anode material for Li-S batteries due to its high theoretical capacity of 3580 mAh g⁻¹. [99] Although the silicon suffers from large volume change during lithiation and delithiation, it can be solved by employment of nanosized Si. [100] To employ Si as an anode, prelithiation is required. Yang *et al.*, proposed a lithium metal-free battery consisting of a Li₂S mesoporous carbon composite cathode and a silicon nanowire anode. [101] Cui and co-workers successfully proved the concept of pre-lithiated silicon nanowire anode, paired with a sulphur cathode. [102] However, this approach still needs further improvements regarding to the insufficient supply of Li-ions and uncontrolled voltage of the electrodes. [103]

1.6 Electrolyte

It is widely accepted that the solvent holds a key role in the electrochemical performance of the Li-S system. [104] The electrolyte design is a dominant factor to manipulate dissolution, diffusion of polysulphide and subsequent shuttle reactions. [37][105] The soluble polysulphides are highly reactive with the carbonate-based electrolytes via nucleophilic reactions and generally excluded as potential solvents. [106] Hence, common solvents used for other Li-ion batteries are chemically incompatible with Li-S cells. [107][108] Thus, the choice of the electrolyte solvents in Li-S cells are mainly limited to ether-based electrolytes, such as, 1,3-Dioxolane (DOL), 1,2-Dimethoxyethane (DME), and Tetraethylene glycol dimethyl ether (TEGDME). [109][110] Currently, the most commonly used electrolyte for Li-S cells is 1M LiTFSI in DOL/DME with small amount of LiNO₃. However, the ether solvents are highly volatile and flammable, posing serious safety concerns on the practical applications of Li-S batteries. [111]

For the successful operation of a Li-S battery, the electrolyte should satisfy many criteria; (i) good ionic conductivity ($10^{-3} \sim 10^{-2} \text{ S cm}^{-1}$ at ambient temperature), (ii) good polysulphide solubility, but low polysulphide permeability through the separator (iii) low viscosity, (iv) electrochemical stability, (v) chemical stability with lithium anode and in the presence of polysulphide dianions and anions radicals, and (vi) low volatility, low flammability, and low toxicity to ensure the safety. [109]

High ionic conductivity is crucial for the electrolyte as for any other electrochemical cells, high efficiency of ion transportation between the electrodes is essential. [112] Electrolytes for Li-S cells should also hold a suitable degree of polysulphide solubility. Dissolution of polysulphide brings the reaction forward, therefore, complete prevention of polysulphide dissolution will largely reduce the utilisation of sulphur. Hence, the solubility of polysulphide should need to be carefully tuned. [107]

To surmount these obstacles, various modifications have been developed. Electrolytes can be optimised by changing the solvents, salts, and additives and there is a wide variety of choices available. [14]

1.6.1 Electrolyte systems

In this section we start by giving an introduction of solvents used in the electrolyte systems for Li-S batteries, followed by an introduction to various salts currently researched in the field of Li-S batteries.

(1) Ether-based solvents

Ethers are not commonly used in other Li-ion batteries as they decompose at high potentials ($\sim 4.0 \text{ V vs Li/Li}^+$), but could be used in Li-S batteries as these are not cycled above 3 V vs Li/Li^+ . [113] Among the wide variety of ether choices, chain-ether, such as, DME, DOL, TEGDME, polyethylene glycol dimethyl ethers (PEGDME), and tetrahydrofuran (THF) are commonly used in Li-S systems owing to its excellent polysulphide solubility, which contributes to a series of polysulphide chemical reactions as well as electrode reactions of polysulphides. [50][114]

Barchasz and co-workers reported that a single solvent of TEGDME contributes to an excellent electrochemical performance in Li-S batteries among a series of ether-based solvents. This is because TEGDME has a relatively high donor number, which has been

associated with more solvating O atoms in its structure, enabling to dissolve and dissociate the Li salt and polysulphides well. [115] However, it is difficult to achieve all the above-mentioned requirements of the electrolyte for the Li-S system with the use of a single solvent. Therefore, mixed solvents, binary as well as ternary mixtures, have become popular choices to design Li-S electrolytes. It was later found that a mixture of TEGDME and DOL solvent in the volume ratio of 25:75 provides a high ionic conductivity electrolyte with good polysulphide solvation ability. [113] Thus, it is concluded that the solvation ability is a key factor to achieve high battery performance. [116]

(2) Sulphone-based solvents (EMS, TMS, MiPS)

Further, there have been a few reports on sulphone-based electrolytes, such as, tetramethylene sulphone (TMS) [117] and ethyl methyl sulphone (EMS). [118] TMS has excellent advantages of low volatility, low toxicity, and high safety compared to ether-based solvents, while EMS offers high ionic conductivity due to its low viscosity property. [112] In the work of Yoon *et al.* TMS was found to have low donor ability, which prevents dissolution of S_8 into the electrolyte. Combining the sulphone-based and ether-based solvent is also common for Li-S electrolytes. [119] A binary solvent mixture, TMS/DME electrolyte containing 1 M LiTFSI combined with sulphur-multi walled carbon nanotube cathode achieved stable electrochemical performance. [120]

(3) Carbonate-based solvents (Ethylene carbonate (EC), Dimethyl carbonate (DMC), Propylene carbonate (PC))

Although carbonate-based solvents are chemically incompatible with most sulphur cathodes, they are occasionally used if sulphur is strongly confined in a porous host, which avoids the formation of long chain polysulphides, thus eliminating the strong nucleophilic reaction of dissolved polysulphides with the electrolyte. For example, Xin and co-workers demonstrated that small S_{2-4} molecules confined in carbon micropores paired with a carbonate-based electrolyte (1M $LiPF_6$ in EC/DMC (1:1 wt %)) exhibited the initial discharge capacity of 1670 mAh g^{-1} at 0.1 C, retaining over 1000 mAh g^{-1} after 200 cycles. [121] They claimed that the active small sulphur allotropes (S_2 , S_3 , and S_4) are confined in microporous carbon with the pore size smaller than the diameter of

a S_8 ring, which excluded the transition between S_8 and S_4^{2-} during cell cycling. [121] Although the real state and the true mechanism for this material are still unclear. [31]

Instead the Zheng group have prepared a sulphur cathode suitable for a carbonate-based electrolyte (1M $LiPF_6$ in EC/DMC (1:1 wt %)). Based on a composite design of copper-stabilised sulphur-microporous carbon. They obtained a specific capacity of more than 600 mAh g^{-1} after 500 cycles and the average CE value close to 100%. [55]

(4) Choice of Li salt

The Li-salt is the source of Li^+ in the electrolyte. [112] To achieve the desired Li-S cell performance, lithium salts should be compatible with the electrolyte solvents. Good solubility and high dissociation ability are essential to obtain good ionic conductivity. Moreover, they need to be chemically and electrochemically stable, as well as thermally stable.

Currently or potentially used Li salts in Li-S battery includes; LiTFSI, $LiClO_4$, $LiPF_6$, LiTDI, $LiNO_3$, LiBOB, LiBETI, and LiTf (see Table of abbreviation in **Appendix A-1**). Among these, LiTFSI and LiTf are presently the norms as both of those satisfy the requirements mentioned above. It is worth pointing out that LiTf is not a suggested salt for most of other Li-ion batteries, as the Al current collector starts to corrode at 2.8 V in LiTf electrolytes. Nonetheless, this should not be a problem with Li-S cell as it is normally cycled below 2.8 V vs Li/Li^+ .

The importance of the lithium salt is often overlooked and there are only a few studies focused on the effect of lithium salt alone. [112] Different studies use different compositions of lithium salt, solvents, and concentrations, which makes it difficult to compare the effect of individual lithium salts between the work of different researchers. [112] However, there are few studies where the lithium salt is the only variable and all other parameter consistent. Ueno *et al.* analysed the difference in a series of equimolar mixtures of glyme solvents (triglyme and tetraglyme) and lithium salts (LiTFSI, LiBETI, LiTf, and $LiNO_3$), [122] while Han *et al.* measured the counter anion effects of common Li salts (Tf^- , $TFSI^-$, FSI^- , and TDI^-) when dissolved in DOL/DME solvents with various concentrations. [123]

In the work of Ueno *et al.*, a heavy redox shuttle was observed when LiNO_3 and LiTf are paired with the triglyme solvent. Attempts were made at the molecular level to explain the poor performance of this electrolyte; the strong interaction between NO_3^- and OTf^- anions was suggested as a result of slightly less stable $[\text{Li}(\text{triglyme})]^+$ complex. Hence, lithium polysulphide species are highly solubilised in the electrolyte thereby causing unfavourable redox reactions. Additionally, BF_4 was found to decompose in the presence of polysulphides and LiNO_3 showed an irreversible reduction at the composite cathode during the discharge.

Han *et al.* claimed that anion plays an important role in SEI layer formation as well as the dissolution of polysulphide species. The higher mobility anion, such as, TFSI^- increases the concentration of anions in the electrolyte causing salt decomposition with the formation of thick SEI layer as a result. On the other hand, lower mobility anion, such as, Tf^- can accelerate the undesired polysulphide dissolution due to the strong interaction between anions and polysulphides. In this aspect, the TDI^- anion has relatively low mobility and weaker interaction with polysulphides and exhibited the better cell performance.

On the other hand, Gao *et al.* measured the impacts of three different Li salts; LiCF_3SO_3 , LiPF_6 , and LiClO_4 in TEGDME solvent and claimed that the electrochemical behaviour is virtually the same and the choice of lithium salt had no significant effect. [118]

The concentration of the Li-salt is also proven to influence the Li-S cell performance. Hu *et al.* reported that the use of a non-aqueous liquid 'Solvent-in-Salt' electrolyte with ultrahigh salt concentration, composed of 7 M LiTFSI in DOL/DME (1:1 by volume), controls both the thickness of a SEI layer and lithium deposition, therefore, protects the lithium anode against the dendrite growth, resulting in better cell performance. Additionally, the cell shows excellent cycling performance in a wide temperature range down to -20°C . [79]

1.7 Characterisation techniques of Li-S cells

The discharge and charge of Li-S cells involve complicated multistep processes and the precise state of sulphur reaction and the true mechanism is still a subject to debate, and may not even be the same in different Li-S cell compositions. [31][124][125]

Characterisation techniques of Li-S cell applied in previous studies are briefly described here and detailed explanations can be found in Chapter 2 for the methods used in this study.

1.7.1 Ex-situ measurement

Most electrochemical cell investigation techniques are conducted via post-mortem (ex-situ) analysis to presume the electrochemical mechanism. [126] Unfortunately, it is difficult to obtain accurate information using ex-situ techniques due to the following reasons:

- (1) Sulphur can be stable only for a short time under high vacuum because of its low melting point and high vapour pressure at ambient temperature.
- (2) *Ex situ* samples are extracted from cells cycled at the desired potential and those samples generally require post-treatment, for instance, washing away the electrolyte to obtain a clean sample for XRD measurement may result in changed properties. There is also a chance of the material exposed to air, which disturbs the accuracy of the measurement because sulphur intermediate products are highly sensitive to the external environment and spontaneous reaction may occur during or before the measurement.
- (3) The high solubility of polysulphides in the electrolyte makes it difficult to exactly detect and track with conventional methods.
- (4) Sulphur cathodes may be metastable and may not be stable when electrically disconnected. Therefore, the relaxation time between material extraction and measurement may reduce the accuracy of the characterisation.

1.7.2 In situ/operando measurement

In situ/operando characterisation give more unambiguous information of the electrochemical reaction process under real working conditions, which eliminates the artefacts from additional treatment steps. [125][127] *In situ* measurements involve the materials cycled in desired cells and stopped during the measurement, which is carried out directly inside the cell at OCV. The term '*operando*' refers to a continuous measurement of the cell without disturbing the battery reaction.

The intermediate products formed during Li-S cell cycling are highly sensitive to water and oxygen. Also, the chain lengths of polysulphide species are sensitive towards complex equilibria in solution. Therefore, mechanistic analysis operated during the Li-S cycling brings significant advantages of obtaining an accurate information of the nature of the electrochemical processes. [128] However, *operando* measurements are also associated with few drawbacks. For *in situ/operando* characterisations, compromises may have to be made between having standard electrochemistry during measurement and the characterisation limitations due to cell configurations. [129] For example, characterisation using X-ray requires an X-ray transparent cell, which may affect the electrochemistry of the battery and alteration may be required in the cell compositions, hence, measurements cannot be carried out under the real working conditions. Designing a cell configuration to achieve both standard electrochemistry and *in situ/operando* measurement is crucial to obtain accurate results.

1.8 Aim of the thesis

This chapter introduced the field of batteries and the gap between the current battery technology and future energy storage demands. More specifically, the fundamentals of the Li-S technologies are explained, including current understanding of the cell operation mechanisms, recent progress, technical obstacles, and material developments of this system.

The aim of this thesis is to better understand the Li-S operation system and sulphur reaction mechanisms using *operando* synchrotron radiation XAS techniques. For this purpose, advanced electrode and electrolyte materials for Li-S batteries are fabricated and the behaviour of the sulphur reaction products are analysed under real operating conditions. The following chapter 2 describes material synthesis and characterisation techniques employed for this study, including the design of X-ray transparent Li-S cell. In chapter 3 various electrolytes were investigated to better understand the influence of the electrolyte systems towards sulphur reactions. Effects of lithium salt, organic solvents, and the LiNO₃ additive are discussed. Chapter 4 presents the modification of the sulphur cathode using several inorganic metallic additives, which offers the adsorption of polysulphide intermediates as well as additional specific capacity. Chapter 5 investigates the possibility of the replacement of an insulating binder with

conductive polymer additives to facilitate in a similar fashion as well as providing the architecture for sulphur and polysulphide confinement within the cathode. Additionally, binder-free electrodes are investigated that eliminates the safety concern originating from potentially hazardous material. The electrodes in chapter 5 are fabricated using an environmentally friendly method replacing hazardous NMP solution with methanol.

1.9 References

- [1] Q. Zhang, Y. Wang, Z. W. Seh, Z. Fu, R. Zhang, and Y. Cui, "Understanding the Anchoring Effect of Two-Dimensional Layered Materials for Lithium-Sulfur Batteries," *Nano Lett.*, vol. 15, no. 6, pp. 3780–3786, 2015.
- [2] Y. Yang, G. Yu, J. J. Cha, H. Wu, M. Vosgueritchian, Y. Yao, Z. Bao, and Y. Cui, "Improving the Performance of Lithium - Sulfur Batteries by Conductive Polymer Coating," *ACS Nano*, vol. 5, no. 11, pp. 9187–9193, 2011.
- [3] T. Cleaver, P. Kovacic, M. Marinescu, T. Zhang, and G. Offer, "Perspective—Commercializing Lithium Sulfur Batteries: Are We Doing the Right Research?," *J. Electrochem. Soc.*, vol. 165, no. 1, pp. A6029–A6033, 2018.
- [4] Q. Pang, X. Liang, C. Y. Kwok, and L. F. Nazar, "Review—The Importance of Chemical Interactions between Sulfur Host Materials and Lithium Polysulfides for Advanced Lithium-Sulfur Batteries," *J. Electrochem. Soc.*, vol. 162, no. 14, pp. A2567–A2576, 2015.
- [5] I. Hadjipaschalis, A. Poullikkas, and V. Efthimiou, "Overview of current and future energy storage technologies for electric power applications," *Renew. Sustain. Energy Rev.*, vol. 13, no. 6–7, pp. 1513–1522, 2009.
- [6] M. Winter and R. J. Brodd, "What Are Batteries , Fuel Cells , and Supercapacitors ? What Are Batteries , Fuel Cells , and Supercapacitors ?," *Chem. Rev.*, vol. 104, no. 10, pp. 4245–4270, 2004.
- [7] J. B. Goodenough and K.-S. Park, "The Li-Ion Rechargeable Battery: A Perspective," *J. Am. Chem. Soc.*, vol. 135, pp. 1167–1176, 2013.
- [8] K. A. Smith, "Electrochemical Control of Lithium-Ion Batteries," *IEEE Control Syst.*, vol. 30, no. 2, pp. 18–25, 2010.
- [9] K. Young and S. Yasuoka, "Capacity Degradation Mechanisms in Nickel/Metal Hydride Batteries," *Batteries*, vol. 2, no. 1, p. 3, 2016.
- [10] B. Pierozynski, "On the low temperature performance of nickel-metal hydride (NiMH) batteries," *Int. J. Electrochem. Sci.*, vol. 6, no. 4, pp. 860–866, 2011.
- [11] J. Liu, C. Xu, Z. Chen, S. Ni, and Z. Xiang, "Progress in aqueous rechargeable batteries," *Green Energy Environ.*, vol. 3, no. 1, pp. 20–41, 2017.
- [12] J.-M. Tarascon and M. Armand, "Issues and challenges facing rechargeable lithium batteries," *Nature*, vol. 414, no. 6861, pp. 359–367, 2001.

- [13] M. E. V. Team, "A Guide to Understanding Battery Specifications," *Current*, no. December, pp. 1–3, 2008.
- [14] C. Qu, Y. Chen, X. Yang, H. Zhang, X. Li, and H. Zhang, "LiNO₃-free electrolyte for Li-S battery: A solvent of choice with low Ksp of polysulfide and low dendrite of lithium," *Nano Energy*, vol. 39, no. June, pp. 262–272, 2017.
- [15] B. W. Byles, N. K. R. Palapati, A. Subramanian, and E. Pomerantseva, "The role of electronic and ionic conductivities in the rate performance of tunnel structured manganese oxides in Li-ion batteries The role of electronic and ionic conductivities in the rate performance of tunnel structured manganese oxides in Li-ion batte," *APL Mater.*, vol. 4, p. 046108, 2016.
- [16] G. E. Blomgren, "The Development and Future of Lithium Ion Batteries," *J. Electrochem. Soc.*, vol. 164, no. 1, pp. A5019–A5025, 2017.
- [17] J. Conder, R. Bouchet, S. Trabesinger, C. Marino, L. Gubler, and C. Villevieille, "Direct observation of lithium polysulfides in lithium-sulfur batteries using *operando* X-ray diffraction," *Nat. Energy*, vol. 2, p. 17069, 2017.
- [18] A. S. Arico, P. Bruce, B. Scrosati, J.-M. Tarascon, and W. van Schalkwijk, "Nanostructured Materials for Advanced Energy Conversion and Storage Devices," *Nat. Mater.*, vol. 4, pp. 366–377, 2005.
- [19] K. Amine, R. Kanno, and Y. Tzeng, "Rechargeable lithium batteries and beyond: Progress, challenges, and future directions," *MRS Bull.*, vol. 39, no. 5, pp. 395–401, 2014.
- [20] J. Yan, X. Liu, M. Yao, X. Wang, T. K. Wafle, and B. Li, "Long-Life, High-Efficiency Lithium-Sulfur Battery from a Nanoassembled Cathode," *Chem. Mater.*, vol. 27, no. 14, pp. 5080–5087, 2015.
- [21] Yan Yu, Xiaobo Ji, and Hongjin Fan, "Post lithium ion batteries for emerging energy storage technologies," *Green Energy Environ.*, vol. 3, no. 1, p. 1, 2018.
- [22] Z. W. Seh, J. Sun, Y. Sun, and Y. Cui, "A highly reversible room-temperature sodium metal anode," *ACS Cent. Sci.*, vol. 1, no. 8, pp. 449–455, 2015.
- [23] D. Lin, Y. Liu, and Y. Cui, "Reviving the lithium metal anode for high-energy batteries," *Nat. Nanotechnol.*, vol. 12, no. 3, pp. 194–206, 2017.
- [24] M. A. Rahman, X. Wang, and C. Wen, "A review of high energy density lithium-air battery technology," *J. Appl. Electrochem.*, vol. 44, no. 1, pp. 5–22, 2014.

- [25] N. Bonnet-Mercier, R. A. Wong, M. L. Thomas, A. Dutta, K. Yamanaka, C. Yogi, T. Ohta and H. R. Byon, "A structured three-dimensional polymer electrolyte with enlarged active reaction zone for Li-O₂ batteries," *Sci. Rep.*, vol. 4, p. 7127, 2014.
- [26] D. Geng, N. Ding, T. S. A. Hor, S. W. Chien, Z. Liu, D. Wu, X. Sun, and Y. Zong, "From Lithium-Oxygen to Lithium-Air Batteries: Challenges and Opportunities," *Adv. Energy Mater.*, vol. 6, no. 9, pp. 1–14, 2016.
- [27] S. A. Freunberger, Y. Chen, Z. Peng, J.M. Griffin, L.J. Hardwick, F. Barde, P. Novak, and P.G. Bruce, "Reactions in the Rechargeable Lithium-O₂ Battery with Alkyl Carbonate Electrolytes," *J. Am. Chem. Soc.*, vol. 133, pp. 8040–8047, 2011.
- [28] G. Lampič, G. Gotovac, H. Geaney, and C. O. Dwyer, "Comparing the Suitability of Lithium Ion, Lithium Sulfur and Lithium Air Batteries for Current and Future Vehicular Applications," 2016.
- [29] G. Settanni, Z. Jiajia, S. Tongchuan, S. Susanne, L. Katharina, S. Friederike, and M. Volker, "Protein corona composition of PEGylated nanoparticles correlates strongly with amino acid composition of protein surface," *Energy Environ. Sci.*, no. 12, pp. 3477–3494, 2015.
- [30] A. Manthiram, Y. Fu, and Y. Su, "Challenges and Prospects of Lithium Sulfur Batteries," *Acc. Chem. Res.*, vol. 46, no. 5, pp. 1125–1134, 2013.
- [31] S. Zhang, K. Ueno, K. Dokko, and M. Watanabe, "Recent Advances in Electrolytes for Lithium-Sulfur Batteries," *Adv. Energy Mater.*, vol. 5, no. 16, p. 1500117, 2015.
- [32] X. Fan, W. Sun, F. Meng, A. Xing, and J. Liu, "Advanced chemical strategies for lithium-sulfur batteries: A review," *Green Energy Environ.*, vol. 3, no. 1, pp. 2–19, 2018.
- [33] S. S. Zhang, "Liquid electrolyte lithium/ sulfur battery : Fundamental chemistry, problems, and solutions," *J. Power Sources*, vol. 231, pp. 153–162, 2013.
- [34] M. K. Song, Y. G. Zhang, and E. J. Cairns, "A Long-Life, High-Rate Lithium/Sulfur Cell: A Multifaceted Approach to Enhancing Cell Performance," *Nano Lett.*, vol. 13, no. 12, pp. 5891–5899, 2013.
- [35] Z. W. Seh, Y. Sun, Q. Zhang, and Y. Cui, "Designing high-energy lithium–sulfur batteries," *Chem. Soc. Rev.*, vol. 45, no. 20, pp. 5605–5634, 2016.

- [36] Q. Pang, X. Liang, C. Y. Kwok, and L. F. Nazar, "Review—The Importance of Chemical Interactions between Sulfur Host Materials and Lithium Polysulfides for Advanced Lithium-Sulfur Batteries," *J. Electrochem. Soc.*, vol. 162, no. 14, pp. A2567–A2576, 2015.
- [37] S. S. Zhang, "Improved cyclability of liquid electrolyte lithium/sulfur batteries by optimizing electrolyte/sulfur ratio," *Energies*, vol. 5, no. 12, pp. 5190–5197, 2012.
- [38] S. S. Zhang, "Effect of Discharge Cutoff Voltage on Reversibility of Lithium/Sulfur Batteries with LiNO₃-Contained Electrolyte," *J. Electrochem. Soc.*, vol. 159, no. 7, pp. A920–A923, 2012.
- [39] J. Ma, Z. Fang, Y. Yan, Z. Yang, L. Gu, Y. S. Hu, H. Li, Z. Wang, and X. Huang, "Novel Large-Scale Synthesis of a C/S Nanocomposite with Mixed Conducting Networks through a Spray Drying Approach for Li-S Batteries," *Adv. Energy Mater.*, vol. 5, no. 16, 2015.
- [40] Z. Sun, J. Zhang, L. Yin, G. Hu, R. Fang, H. M. Cheng, and F. Li, "Conductive porous vanadium nitride/graphene composite as chemical anchor of polysulfides for lithium-sulfur batteries," *Nat. Commun.*, vol. 8, p. 14627, 2017.
- [41] W. Zhou, Y. Yu, H. Chen, and F. J. Disalvo, "Yolk-Shell Structure of Polyaniline-Coated Sulfur for Lithium-Sulfur Batteries," *J. Am. Chem. Soc.*, vol. 135, no. 135, pp. 16736–16743, 2013.
- [42] S. Moon, Y. H. Jung, W. K. Jung, D. S. Jung, J. W. Choi, and D. K. Kim, "Encapsulated monoclinic sulfur for stable cycling of Li-S rechargeable batteries," *Adv. Mater.*, vol. 25, no. 45, pp. 6547–6553, 2013.
- [43] Z. Liang, G. Zheng, W. Li, Z. W. Seh, H. Yao, K. Yan, D. Kong, and Y. Cui, "Sulfur Cathodes with Hydrogen Reduced Titanium Dioxide Inverse Opal Structure," *ACS Nano*, vol. 8, no. 5, pp. 5249–5256, 2014.
- [44] Y. Sun, S. Wang, H. Cheng, Y. Dai, J. Yu, and J. Wu, "Synthesis of a ternary polyaniline@acetylene black-sulfur material by continuous two-step liquid phase for lithium sulfur batteries," *Electrochim. Acta*, vol. 158, pp. 143–151, 2015.
- [45] L. Qie and A. Manthiram, "High-Energy-Density Lithium-Sulfur Batteries Based on Blade-Cast Pure Sulfur Electrodes," *ACS Energy Lett.*, vol. 1, no. 1, pp. 46–51, 2016.

- [46] A. Vizintin, L. Chabanne, E. Tchernychova, I. Arcon, L. Stievano, G. Aquilanti, M. Antonietti, T.-P. Fellingner, and R. Dominko, "The mechanism of Li₂S activation in lithium-sulfur batteries : Can we avoid the polysulfide formation?," *J. Power Sources*, vol. 344, pp. 208–217, 2017.
- [47] R. Dominko, A. Vizintin, G. Aquilanti, L. Stiveano, M. J. Helen, A. R. Munnangi, M. Fichtner, and I. Arcon, "Polysulfides Formation in Different Electrolytes from the Perspective of X-ray Absorption Spectroscopy," *J. Electrochem. Soc.*, vol. 165, no. 1, pp. A5014–A5019, 2018.
- [48] A. Berger, A. T. S. Freiberg, A. Siebel, R. Thomas, M. U. M. Patel, M. Tromp, H. A. Gasteiger, and Y. Gorlin, "The Importance of Chemical Reactions in the Charging Process of Lithium-Sulfur Batteries," *J. Electrochem. Soc.*, vol. 165, no. 7, pp. A1288–A1296, 2018.
- [49] K. Liao, P. Mao, N. Li, M. Han, J. Yi, P. He, Y. Sun, and H.S. Zhou, "Stabilization of polysulfides via lithium bonds for Li–S batteries," *J. Mater. Chem. A*, vol. 4, no. 15, pp. 5406–5409, 2016.
- [50] X. Ji, K. T. Lee, and L. F. Nazar, "A highly ordered nanostructured carbon-sulphur cathode for lithium-sulphur batteries," *Nat. Mater.*, vol. 8, no. 6, pp. 500–506, 2009.
- [51] R. Elazari, G. Salitra, A. Garsuch, A. Panchenko, and D. Aurbach, "Sulfur-impregnated activated carbon fiber cloth as a binder-free cathode for rechargeable Li-S batteries," *Adv. Mater.*, vol. 23, no. 47, pp. 5641–5644, 2011.
- [52] Y. V. Mikhaylik and J. R. Akridge, "Polysulfide Shuttle Study in the Li/S Battery System," *J. Electrochem. Soc.*, vol. 151, no. 11, pp. A1969–A1976, 2004.
- [53] Q. Wang, J. Jin, X. Wu, G. Ma, J. Yang, and Z. Wen, "A shuttle effect free lithium sulfur battery based on a hybrid electrolyte," *Phys. Chem. Chem. Phys.*, vol. 16, no. 39, pp. 21225–21229, 2014.
- [54] M. Cuisinier, C. Hart, M. Balasubramanian, A. Garsuch, and L. F. Nazar, "Radical or Not Radical: Revisiting Lithium-Sulfur Electrochemistry in Nonaqueous Electrolytes," *Adv. Energy Mater.*, vol. 5, no. 16, p. 1401801, 2015.
- [55] S. Zheng, Y. Feng, Z. Li, Y. Zhu, Y. Xu, C. Luo, J. Yang, and C. Wang, "Copper-stabilized sulfur-microporous carbon cathodes for Li-S batteries," *Adv. Funct. Mater.*, vol. 24, no. 26, pp. 4156–4163, 2014.

- [56] W. Li, Z. Liang, Z. Lu, H. Yao, Z. W. Seh, K. Yan, G. Zheng, and Y. Cui, "A Sulfur Cathode with Pomegranate-Like Cluster Structure," *Adv. Energy Mater.*, vol. 5, no. 16, p. 1500211, 2015.
- [57] F. Condi, D. Godoi, D. Wang, Q. Zeng, K. Wu, and I. R. Gentle, "Dependence of LiNO_3 decomposition on cathode binders in Li-S batteries," *J. Power Sources*, vol. 288, pp. 13–19, 2015.
- [58] Y. Yang, G. Zheng, and Y. Cui, "Nanostructured sulfur cathodes," *Chem. Soc. Rev.*, vol. 42, no. 7, pp. 3018–3132, 2013.
- [59] L. Li, T. A. Pascal, J. G. Connell, F. Y. Fan, S. M. Meckler, L. Ma, Y. M. Chiang, D. Prendergast, and B. A. Helms, "Molecular understanding of polyelectrolyte binders that actively regulate ion transport in sulfur cathodes," *Nat. Commun.*, vol. 8, no. 1, p. 2277, 2017.
- [60] O. Ogoke, G. Wu, X. Wang, A. Casimir, L. Ma, T. Wu and J. Lu, "Effective strategies for stabilizing sulfur for advanced lithium–sulfur batteries," *J. Mater. Chem. A*, vol. 5, no. 2, pp. 448–469, 2017.
- [61] G. Li, W. Cai, B. Liu, and Z. Li, "A multi functional binder with lithium ion conductive polymer and polysulfide absorbents to improve cycleability of lithium sulfur batteries," *J. Power Sources*, vol. 294, pp. 187–192, 2015.
- [62] G. Y. Zheng, Y. Yang, J. J. Cha, S. S. Hong, and Y. Cui, "Hollow Carbon Nanofiber-Encapsulated Sulfur Cathodes for High Specific Capacity Rechargeable Lithium Batteries," *Nano Lett.*, vol. 11, no. 10, pp. 4462–4467, 2011.
- [63] S. Chung, C. Chang, and A. Manthiram, "Progress on the Critical Parameters for Lithium – Sulfur Batteries to be Practically Viable," *Adv. Funct. Mater.*, vol. 28, p. 1801188, 2018.
- [64] H. J. Peng, J. Q. Huang, X. B. Cheng, and Q. Zhang, "Review on High-Loading and High-Energy Lithium–Sulfur Batteries," *Adv. Energy Mater.*, vol. 7, no. 24, pp. 1–54, 2017.
- [65] J. Guo, Y. Xu, and C. Wang, "Sulfur-Impregnated Disordered Carbon Nanotubes Cathode for Lithium Sulfur Batteries.pdf," pp. 4288–4294, 2011.
- [66] S. C. Han, M. S. Song, H. Lee, H.-S. Kim, H. J. Ahn, and J. Y. Lee, "Effect of Multiwalled Carbon Nanotubes on Electrochemical Properties of Lithium/Sulfur

- Rechargeable Batteries," *J. Electrochem. Soc.*, vol. 150, no. 7, pp. A889–A893, 2003.
- [67] B. Ding, C. Z. Yuan, L. F. Shen, G. Y. Xu, P. Nie, Q. X. Lai, and X. G. Zhang, "Chemically tailoring the nanostructure of graphene nanosheets to confine sulfur for high-performance lithium-sulfur batteries," *J. Mater. Chem. A*, vol. 1, no. 4, pp. 1096–1101, 2013.
- [68] K. Zhang, Q. Zhao, Z. Tao, and J. Chen, "Composite of sulfur impregnated in porous hollow carbon spheres as the cathode of Li-S batteries with high performance," *Nano Res.*, vol. 6, no. 1, pp. 38–46, 2013.
- [69] Y. Sun, Z. Wei, W. Li, and H. Yao, "In operando optical imaging of temporal and spatial distribution of polysulfides in lithium-sulfur batteries," *Nano Energy*, vol. 11, pp. 579–586, 2015.
- [70] G. Ma, Z. Wen, J. Jin, Y. Lu, X. Wu, M. Wu and C. Chen, "Hollow polyaniline sphere@sulfur composites for prolonged cycling stability of lithium-sulfur batteries," *J. Mater. Chem. A*, vol. 2, no. 27, pp. 10350–10354, 2014.
- [71] G. Ma, Z. Wen, J. Jin, Y. Lu, K. Rui, X. Wu, M. Wu, and J. Zhang "Enhanced performance of lithium sulfur battery with polypyrrole warped mesoporous carbon/sulfur composite," *J. Power Sources*, vol. 254, pp. 353–359, 2014.
- [72] F. Wu, J. Chen, R. Chen, S. Wu, L. Li, S. Chen, and T. Zhao, "Sulfur/ Polythiophene with a Core/ Shell Structure : Synthesis and Electrochemical Properties of the Cathode for Rechargeable Lithium Batteries," *J. Phys. Chem. C*, vol. 115, no. 13, pp. 6057–6063, 2011.
- [73] K. Park, J. H. Cho, J.-H. Jang, B.-C. Yu, A. T. De La Hoz, K. M. Miller, C. J. Ellison, and J. B. Goodenough, "Trapping lithium polysulfides of a Li-S battery by forming lithium bonds in a polymer matrix," *Energy Environ. Sci.*, vol. 8, no. 8, pp. 2389–2395, 2015.
- [74] M. R. Kaiser, X. Liang, H. K. Liu, S. X. Dou, and J. Z. Wang, "A methodical approach for fabrication of binder-free Li₂S-C composite cathode with high loading of active material for Li-S battery," *Carbon N. Y.*, vol. 103, pp. 163–171, 2016.
- [75] T. Takeuchi, H. Sakaebe, H. Kageyama, H. Senoh, T. Sakai, and K. Tatsumi, "Preparation of electrochemically active lithium sulfide-carbon composites using

- spark-plasma-sintering process," *J. Power Sources*, vol. 195, no. 9, pp. 2928–2934, 2010.
- [76] S. Zheng, Y. Chen, Y. Xu, F. Yi, Y. Zhu, Y. Liu, J. Yang and C. Wang, "In Situ Formed Lithium Sulfide/ Microporous Carbon Cathodes for Lithium-Ion Batteries," *ACS Nano*, vol. 7, no. 12, pp. 10995–11003, 2013.
- [77] X. Yu and A. Manthiram, "A class of polysulfide catholytes for lithium–sulfur batteries: energy density, cyclability, and voltage enhancement," *Phys. Chem. Chem. Phys.*, vol. 17, no. 3, pp. 2127–2136, 2015.
- [78] X. Yu, Z. Bi, F. Zhao, and A. Manthiram, "Hybrid Lithium-Sulfur Batteries with a Solid Electrolyte Membrane and Lithium Polysulfide Catholyte," *ACS Appl. Mater. Interfaces*, vol. 7, no. 30, pp. 16625–16631, 2015.
- [79] L. Suo, Y. S. Hu, H. Li, M. Armand, and L. Chen, "A new class of Solvent-in-Salt electrolyte for high-energy rechargeable metallic lithium batteries," *Nat. Commun.*, vol. 4, p. 1481, 2013.
- [80] S. jung Oh and W. young Yoon, "Effect of polypyrrole coating on Li powder anode for lithium-sulfur secondary batteries," *Int. J. Precis. Eng. Manuf.*, vol. 15, no. 7, pp. 1453–1457, 2014.
- [81] N. Ding, L. Zhou, C. Zhou, D. Geng, J. Yang, S. W. Chien, Z. Liu, M.-F. Ng, A. Yu, T. S. A. Hor, M. B. Sullivan, and Y. Zong, "Building better lithium-sulfur batteries: from LiNO₃ to solid oxide catalyst," *Sci. Rep.*, vol. 6, no. 1, p. 33154, 2016.
- [82] G. Ma, Z. Wen, M. Wu, C. Shen, Q. Wang, J. Jin, and X. Wu, "A lithium anode protection guided highly-stable lithium–sulfur battery," *Chem. Commun.*, vol. 50, no. 91, pp. 14209–14212, 2014.
- [83] M. Song, Y. Zhang, and E. J. Cairns, "A Long-Life, High-Rate Lithium/Sulfur Cell: A Multifaceted Approach to Enhancing Cell Performance," vol. 13, no. 12, pp. 5891–5899, 2013.
- [84] X. Pu, G. Yang, and C. Yu, "Safe and reliable operation of sulfur batteries with lithiated silicon," *Nano Energy*, vol. 9, pp. 318–324, 2014.
- [85] Z. W. Seh, J. Sun, Y. Sun, and Y. Cui, "A Highly Reversible Room-Temperature Sodium Metal Anode," vol. 6, 2015.
- [86] Y. Liu, Q. Liu, L. Xin, Y. Liu, F. Yang, E. A. Stach, and J. Xie, "Making Li-metal electrodes rechargeable by controlling the dendrite growth direction," *Nat. Energy*, vol. 2, no. 7, p. 17083, 2017.

- [87] S. Xiong, K. Xie, Y. Diao, and X. Hong, "Characterization of the solid electrolyte interphase on lithium anode for preventing the shuttle mechanism in lithium sulfur batteries," *J. Power Sources*, vol. 246, pp. 840–845, 2014.
- [88] S. Xiong, K. Xie, Y. Diao, and X. Hong, "Properties of surface film on lithium anode with LiNO_3 as lithium salt in electrolyte solution for lithium-sulfur batteries," *Electrochim. Acta*, vol. 83, pp. 78–86, 2012.
- [89] D. Aurbach, E. Pollak, R. Elazari, G. Salitra, C. S. Kelley, and J. Affinito, "On the Surface Chemical Aspects of Very High Energy Density, Rechargeable Li–Sulfur Batteries," *J. Electrochem. Soc.*, vol. 156, no. 8, pp. A694–A702, 2009.
- [90] M. Barghamadi, A. S. Best, A. I. Bhatt, A. F. Hollenkamp, Peter J. Mahon, M. Musameh, and T. R  ther, "Effect of LiNO_3 additive and pyrrolidinium ionic liquid on the solid electrolyte interphase in the lithium–sulfur battery," *J. Power Sources*, vol. 295, pp. 212–220, 2015.
- [91] S. S. Zhang, "A new finding on the role of LiNO_3 in lithium-sulfur battery," *J. po*, vol. 322, pp. 99–105, 2016.
- [92] S. S. Zhang, "Role of LiNO_3 in rechargeable lithium/sulfur battery," *Electrochim. Acta*, vol. 70, pp. 344–348, 2012.
- [93] K. Sun, D. Su, Q. Zhang, D. C. Bock, A. C. Marschilok, K. J. Takeuchi, E. S. Takeuchi, and H. Gan, "Interaction of CuS and Sulfur in Li-S Battery System," *J. Electrochem. Soc.*, vol. 162, no. 14, pp. A2834–A2839, 2015.
- [94] X. Liang, Z. Wen, Y. Liu, M. Wu, J. Jin, H. Zhang, and X. Wu, "Improved cycling performances of lithium sulfur batteries with LiNO_3 -modified electrolyte," *J. Power Sources*, vol. 196, no. 22, pp. 9839–9843, 2011.
- [95] T. A. Pascal, K. H. Wujcik, D. R. Wang, N. P. Balsara, and D. Prendergast, "Thermodynamic origins of the solvent-dependent stability of lithium polysulfides from first principles," *Phys. Chem. Chem. Phys.*, vol. 19, no. 2, pp. 1441–1448, 2017.
- [96] Y. B. Yang, Y. X. Liu, Z. Song, Y. H. Zhou, and H. Zhan, " Li^+ -Permeable Film on Lithium Anode for Lithium Sulfur Battery," *ACS Appl. Mater. Interfaces*, vol. 9, no. 44, pp. 38950–38958, 2017.

- [97] D. Lin, Y. Liu, Z. Liang, H. W. Lee, J. Sun, H. Wang, K. Yan, J. Xie, and Y. Cui, "Layered reduced graphene oxide with nanoscale interlayer gaps as a stable host for lithium metal anodes," *Nat. Nanotechnol.*, vol. 11, no. 7, pp. 626–632, 2016.
- [98] S. Jin, S. Xin, L. Wang, Z. Du, L. Cao, J. Chen, X. Kong, M. Gong, J. Lu, Y. Zhu, H. Ji, and R. S. Ruoff, "Covalently Connected Carbon Nanostructures for Current Collectors in Both the Cathode and Anode of Li–S Batteries," *Adv. Mater.*, vol. 28, no. 41, pp. 9094–9102, 2016.
- [99] H. Jha, I. Buchberger, X. Cui, S. Meini, and H. A. Gasteiger, "Li-S Batteries with Li₂S Cathodes and Si/C Anodes," *J. Electrochem. Soc.*, vol. 162, no. 9, pp. A1829–A1835, 2015.
- [100] J. Chen, M. Liu, J. Sun, and F. Xu, "Templated magnesiothermic synthesis of silicon nanotube bundles and their electrochemical performances in lithium ion batteries," *RSC Adv.*, vol. 4, no. 77, pp. 40951–40957, 2014.
- [101] Y. Yang, M. T. McDowell, A. Jackson, J. J. Cha, S. S. Hong, and Y. Cui, "New nanostructured Li₂S/Silicon rechargeable battery with high specific energy," *Nano Lett.*, vol. 10, no. 4, pp. 1486–1491, 2010.
- [102] N. Liu, L. Hu, M. T. Mcdowell, A. Jackson, and Y. Cui, "Prelithiated Silicon Nanowires as an Anode for Lithium Ion Batteries," *Energy Environ. Sci.*, vol. 5, no. 8, pp. 6487–6493, 2011.
- [103] M. Hagen, E. Quiroga-Gonzalez, S. Doerfler, G. Fahrner, J. Tuebke, M. J. Hoffmann, H. Althues, R. Speck, M. Krampfert, S. Kaskel, and H. Foell, "Studies on preventing Li dendrite formation in Li-S batteries by using pre-lithiated Si microwire anodes," *J. Power Sources*, vol. 248, pp. 1058–1066, 2014.
- [104] M. Cuisinier, P. E. Cabelguen, S. Evers, G. He, M. Kolbeck, A. Garsuch, T. Bolin, M. Balasubramanian, and L. F. Nazar, "Sulfur Speciation in Li–S Batteries Determined by *Operando* X-ray Absorption Spectroscopy," *J. Phys. Chemistry Lett.*, vol. 4, pp. 3227–3232, 2013.
- [105] X. Liu, J. Q. Huang, Q. Zhang, and L. Mai, "Nanostructured Metal Oxides and Sulfides for Lithium-Sulfur Batteries," *Adv. Mater.*, vol. 29, no. 20, p. 1601759, 2017.
- [106] T. Yim, M. S. Park, J. S. Yu, K. J. Kim, K. Y. Im, J. H. Kim, G. Jeong, Y. N. Jo, S. G. Woo, K. S. Kang, I. Lee, and Y. J. Kim, "Electrochimica Acta Effect of chemical

- reactivity of polysulfide toward carbonate-based electrolyte on the electrochemical performance of Li-S batteries,” *Electrochim. Acta*, vol. 107, pp. 454–460, 2013.
- [107] J. Chen, K. S. Han, W. A. Henderson, K. C. Lau, M. Vijayakumar, T. Dzwiniel, H. Pan, L. A. Curtiss, J. Xiao, K. T. Mueller, Y. Shao, and J. Liu “Restricting the Solubility of Polysulfides in Li-S Batteries Via Electrolyte Salt Selection,” *Adv. Energy Mater.*, vol. 6, no. 11, p. 1600160, 2016.
- [108] J. Park, K. Ueno, N. Tachikawa, K. Dokko, and M. Watanabe, “Ionic Liquid Electrolytes for Lithium – Sulfur Batteries,” 2013.
- [109] D. Chang, S. Lee, S. Kim, and H. Kim, “Binary electrolyte based on tetra (ethylene glycol) dimethyl ether and 1 , 3-dioxolane for lithium – sulfur battery,” *J. Power Sources*, vol. 112, pp. 452–460, 2002.
- [110] B. Jache, B. Mogwitz, F. Klein, and P. Adelhelm, “Copper sul fi des for rechargeable lithium batteries : Linking cycling stability to electrolyte composition,” *J. Power Sources*, vol. 247, pp. 703–711, 2014.
- [111] A. Benítez, D. Di Lecce, Á. Caballero, J. Morales, E. Rodríguez-Castellón, and J. Hassoun, “Lithium sulfur battery exploiting material design and electrolyte chemistry: 3D graphene framework and diglyme solution,” *J. Power Sources*, vol. 397, no. April, pp. 102–112, 2018.
- [112] J. Scheers, S. Fantini, and P. Johansson, “A review of electrolytes for lithium e sulphur batteries,” *J. Power Sources*, vol. 255, pp. 204–218, 2014.
- [113] F. Alloin, “Revisiting TEGDME/ DIOX Binary Electrolytes for Lithium / Sulfur Batteries : Importance of Solvation Ability and Additives,” *J. Electrochem. Soc.*, vol. 160, no. 3, pp. 430–436, 2013.
- [114] H. J. Yang and Y. Jung, “Effects of polysulfide nonsolvents on the electrochemical performance of Li-S batteries,” *Int. J. Electrochem. Sci.*, vol. 10, no. 11, pp. 9049–9055, 2015.
- [115] C. Barchasz, J. Leprêtre, S. Patoux, and F. Alloin, “Electrochimica Acta Electrochemical properties of ether-based electrolytes for lithium/sulfur rechargeable batteries,” *Electrochim. Acta*, vol. 89, pp. 737–743, 2013.
- [116] G. Li, Z. Li, B. Zhang, and Z. Lin, “Developments of Electrolyte Systems for Lithium-Sulfur Batteries: A Review,” *Front. Energy Res.*, vol. 3, pp. 1–12, 2015.

- [117] R. Dominko, R. Demir-Cakan, M. Morcrette, and J. M. Tarascon, "Analytical detection of soluble polysulphides in a modified Swagelok cell," *Electrochem. commun.*, vol. 13, no. 2, pp. 117–120, 2011.
- [118] J. Gao, M. a Lowe, Y. Kiya, and D. Abru, "Effects of Liquid Electrolytes on the Charge-Discharge Performance of Rechargeable Lithium / Sulfur Batteries : Electrochemical and *in Situ* X-ray Absorption Spectroscopic Studies," *J. Phys. Chem. C*, vol. 115, pp. 25132–25137, 2011.
- [119] V. S. Kolosnitsyn, E. V Karaseva, D. Y. Seung, and M. D. Cho, "Cycling a Sulfur Electrode : Effect of Physicochemical Properties of Electrolyte Systems," *Russ. J. Electrochem.*, vol. 39, no. 10, pp. 1089–1093, 2003.
- [120] S. Yoon, Y. H. Lee, K. H. Shin, S. B. Cho, and W. J. Chung, "Binary sulfone/ether-based electrolytes for rechargeable lithium-sulfur batteries," *Electrochim. Acta*, vol. 145, pp. 170–176, 2014.
- [121] S. Xin, L. Gu, N. H. Zhao, Y. X. Yin, L. J. Zhou, Y. G. Guo, and L. J. Wan "Smaller Sulfur Molecules Promise Better Lithium – Sulfur Batteries," *J. Am. Chem. Soc.*, vol. 134, pp. 18510–18513, 2012.
- [122] K. Ueno, J. W. Park, A. Yamazaki, T. Mandai, N. Tachikawa, K. Dokko and M. Watanabe, "Anionic Effects on Solvate Ionic Liquid Electrolytes in Rechargeable Lithium – Sulfur Batteries," *J. Phys. Chem. C*, vol. 117, no. 40, pp. 20509–20516, 2013.
- [123] K. S. Han, J. Chen, R. Cao, N. N. Rajput, V. Murugesan, L. Shi, H. Pan, J. G. Zhang, J. Liu, K. A. Persson, and K. T. Mueller "Effects of Anion Mobility on Electrochemical Behaviors of Lithium-Sulfur Batteries," *Chem. Mater.*, vol. 29, no. 21, pp. 9023–9029, 2017.
- [124] A. Fotouhi, D. Auger, L. O'Neill, T. Cleaver, and S. Walus, "Lithium-Sulfur Battery Technology Readiness and Applications—A Review," *Energies*, vol. 10, no. 12, p. 1937, 2017.
- [125] J. Tan, D. Liu, X. Xu, and L. Mai, "*In situ/operando* characterization techniques for rechargeable lithium-sulfur batteries: a review," *Nanoscale*, 2017.
- [126] Y. Ye, A. Kawase, M. K. Song, B. Feng, Y. S. Liu, M. A. Marcus, J. Feng, E. J. Cairns, J. Guo, and J. Zhu, "X-ray Absorption Spectroscopy Characterization of a Li/S Cell," *Nanomaterials*, vol. 6, no. 1, p. 14, 2016.

- [127] J. Nelson, S. Misra, Y. Yang, A. Jackson, Y. Liu, H. Wang, H. Dai, J. C. Andrews, Y. Cui and M. F. Toney, "In Operando X-ray Diffraction and Transmission X-ray Microscopy of Lithium Sulfur Batteries," *J. Am. Chem. Soc.*, vol. 134, pp. 6337–6343, 2012.
- [128] A. T. S. Freiberg, A. Siebel, A. Berger, S. M. Webb, Y. Gorlin, M. Tromp, and H. A. Gasteiger, "Insights into the Interconnection of the Electrodes and Electrolyte Species in Lithium-Sulfur Batteries Obtained Using Spatially Resolved *Operando* X-ray Absorption Spectroscopy and X-ray Fluorescence Mapping," *J. Phys. Chem. C*, vol. 122, pp. 5303–5316, 2018.
- [129] A. A. Franco, *Rechargeable Lithium Batteries From Fundamental to Applications*. Woodhead Publishing, 2015.

Chapter 2

Materials and Methods

This chapter demonstrates the experimental procedures, preparation of Li-S batteries, including sulphur composite cathode synthesis, slurry coating, electrolyte preparation, and battery analysis techniques used in this work. The list of materials and chemicals used are summarised in **Appendix A-1**.

2.1 Material synthesis

2.1.1 Cathode preparations

All sulphur cathode composites prepared in this thesis were synthesised via a hydrothermal method unless otherwise stated.

1. S + AB + PVP composite (used for **Chapter 3** and **4**)

Sulphur was melt-diffused into acetylene black carbon (AB), which is the most prevalent technique to prepare sulphur cathodes. The S+AB+PVP cathode was synthesised by following steps; (i) 70 wt% sulphur and 30 wt % AB were mixed using an agate mortar followed by heating in Teflon-lined autoclave at 155 °C for 12 hours, this mixture is hereby denoted as S+AB. (ii) NMP solution containing 6 % polyvinylpyrrolidone (PVP) (denoted by PVP-6) is prepared to use as a solvent to form a slurry. (iii) A slurry consisting of 85 wt. % of S+AB and 15 wt. % of PVP is prepared by using the desired amount of PVP-6 solution and stirred for about 16 hours for homogenisation. The final composition of S+AB+PVP (60:25:15 by mass ratio) were prepared. (iv) The slurry was coated on an aluminium current collector using a doctor-blade with a wet thickness of 180 µm. (v) The electrodes were dried under vacuum at 60° for about 16 hours to eliminate residual solvent and moisture (**Figure 2-1a**). (vi) The cathode sheet was cut into 12.7 mm size circles (**Figure 2-1b**) and stored in an argon-filled glove box until use. This is used as a reference cathode in **Chapter 3** and **4**.

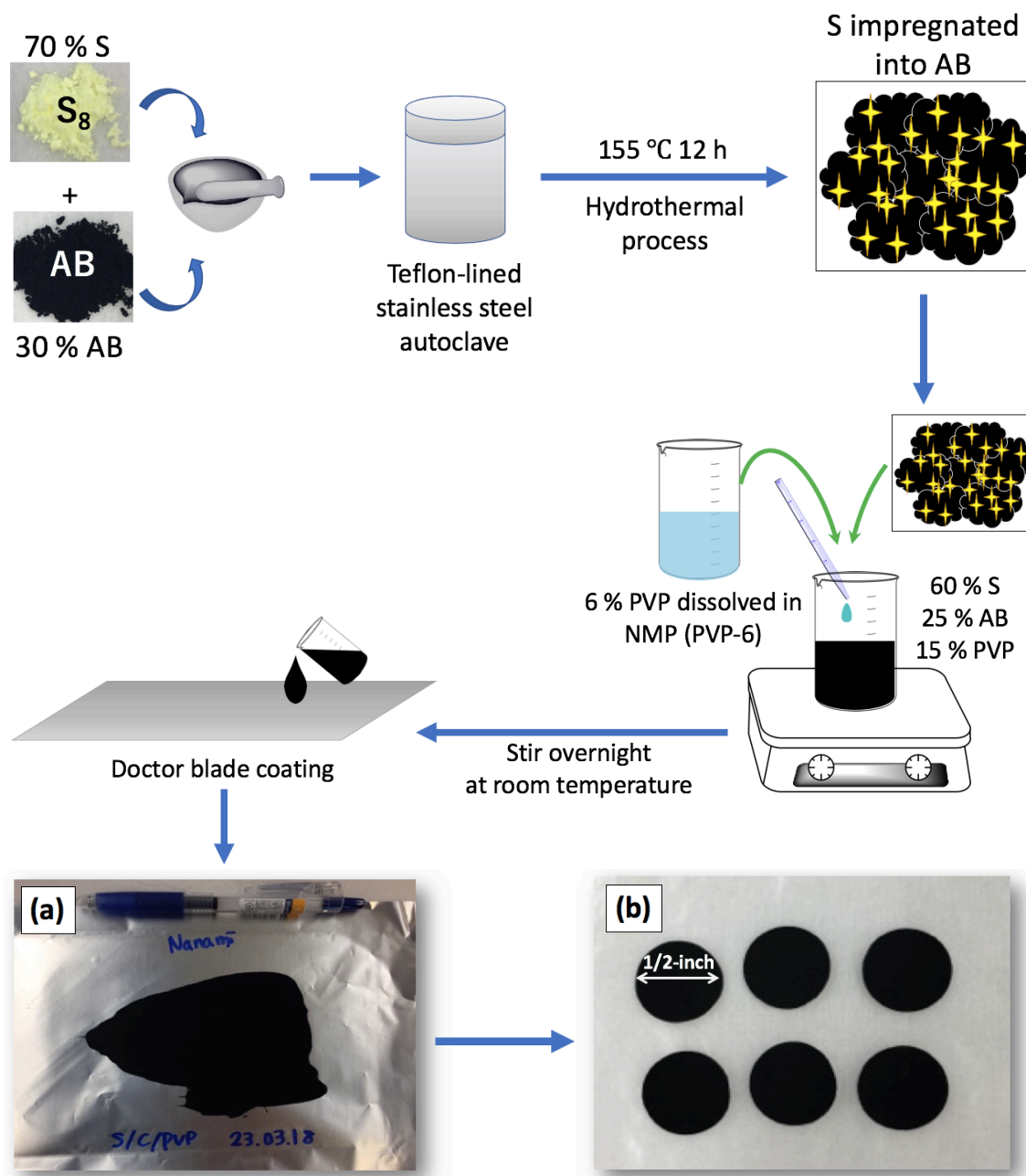


Figure 2-1. Schematic diagrams of the S+AB+PVP cathode synthesis steps. (a) A photograph of slurry coated on Al current collector sheet using a doctor blade and (b) cathode discs cut into 12.7 mm.

2. Sulphur cathodes with metal oxides (sulphide) additives (MX@S)

80 wt. % sulphur and 20 wt. % metal oxides or sulphide (MX) were mixed using an agate mortar followed by heating in Teflon-lined autoclave at 155 °C for 12 hours. A slurry consisting of 12:48:25:15 equals to MX: sulphur: AB: PVP is prepared by addition of the desired amount of AB and PVP-6 solution into the MX+S mixture and stirred for

about 16 hours to for homogenisation. The slurry coating method is the same as described above.

2.1.2 Electrolyte preparations

All electrolytes were prepared in an argon-filled glove box containing less than 0.5 ppm of oxygen and water. All lithium salts were dried under vacuum at 120 °C for 12 hours prior to use. The dried salts were dissolved at desired concentration in the electrolyte solvents and stirred for about 16 hours. In this thesis, each chapter uses different electrolyte systems. The details of the electrolyte compositions and concentrations are stated in each experiment.

2.1.3 Separator preparations

In this work all cells were assembled using glassfibre separators (purchased from Whatman GF/C, [2]). Separator was punched into 15.8 mm and dried under vacuum at 80 °C for 24 hours and kept under argon until use.

2.1.4 Coin cell configuration

All cell parts (top cap, 0.5 mm spacer, bottom case with gasket) were dried under vacuum at 80 °C for 24 hours before transferred into an argon-filled glove box (Mbraun; < 0.5 ppm O₂ and H₂O). Coin cells were assembled using a coin cell crimper purchased from MTI [3]. All Li foils used were cleaned with brush to remove oxidised layer and punched into 12.7 mm diameter prior to assembly into coin cells.

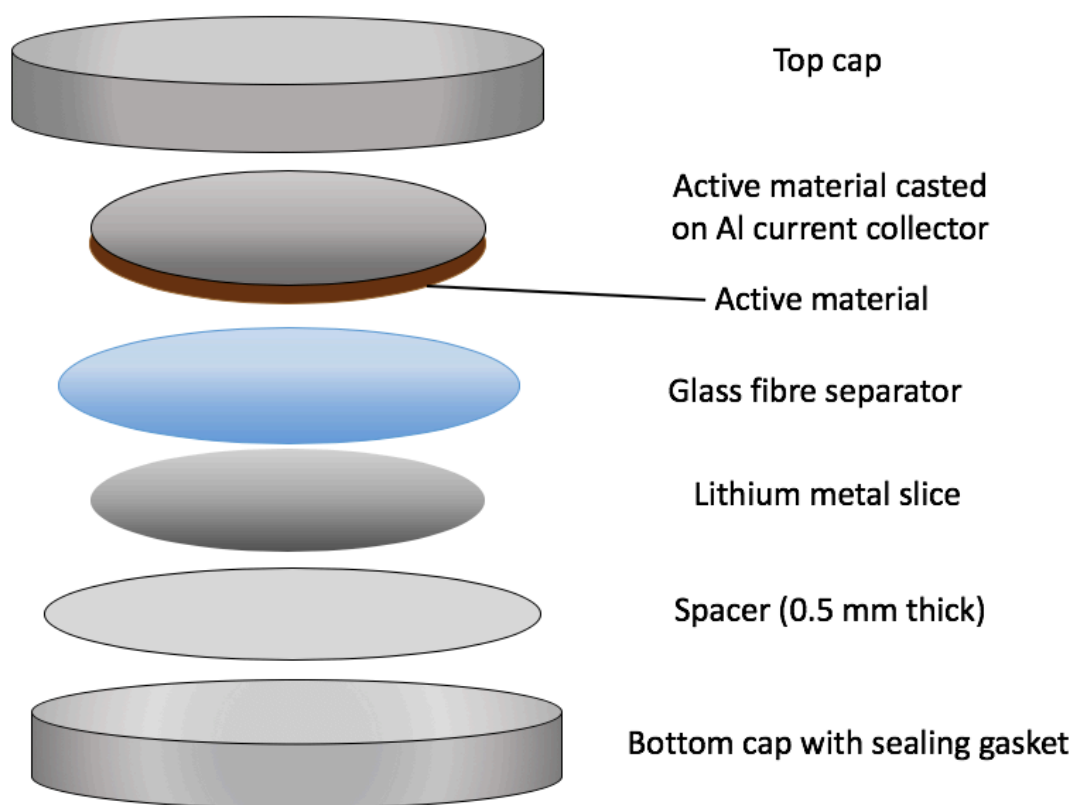


Figure 2-2. Schematic diagram of 2016 coin cell configuration.

2.2 Material characterisations

This section introduces the techniques employed to characterise the as-synthesised materials.

2.2.1 Laboratory electrochemical characterisation methods

Cycling voltammetry (CV) and galvanostatic charge/discharge were tested to evaluate the electrochemical performances of batteries. All measurements were carried out using Bio-Logic VMP-3 potentiostat (Bio-Logic) [4] or Maccor Battery Tester [5] at room temperature.

2.2.1.1 Cyclic Voltammetry (CV) curve

In CV measurements, a series of voltage is applied to the battery through the fixed voltage window at a constant scan rate. During the CV scan, the analyte is either reduced or oxidised, which produce currents and plotted as a function of voltage. This is called a cyclic voltammogram (CV), allowing acquisition of the cathodic and the anodic peaks which can be employed to investigate the redox potential of the

electrodes and electrolytes. In this study, we applied two-electrode cells consisting of a metallic Li and sulphur cathode in CR2016 coin cells for all CV measurements. [6]

2.2.1.2 Galvanostatic cycling (Discharge and Charge) curve

Galvanostatic discharge/charge curve is used to determine the practical capacity and cycle performance of the electrode materials. The specific capacity is generally expressed as mAh g⁻¹. When describing batteries, the term 'C-rate' is often used, which is a measure of the battery discharge (charge) rate relative to its maximum capacity. The C-rate of 1 (1 C) means to allow the cell to reach its theoretical amount of discharge capacity in one hour. [7] In this study, the applied C-rate was calculated based on the theoretical specific capacity of sulphur active material (Q = 1673 mAh g⁻¹) and stated for each experiment. From the galvanostatic discharge/charge curves, Coulombic efficiency (CE, %) can be calculated using **Equation (2-1)**:

$$CE (\%) = \frac{\text{Discharge (mAh g}^{-1}\text{)}}{\text{Charge (mAh g}^{-1}\text{)}} \times 100 \quad (2-1)$$

This gives the information about the degree of polysulphide shuttle. Lower than 100 % indicates the presence of redox shuttle occurring from the 'infinite' charge. The CE value higher than 100 % implies the incomplete charge (irreversible charge), therefore, leading to the capacity fade in following cycle.

2.2.2 X-Ray Diffraction (XRD)

X-Ray Diffraction (XRD) is a non-destructive method for determination of the structure of crystalline materials, providing information of spacing between atoms and orientation of crystals based on their diffraction pattern. The atomic planes of a crystal cause an incident beam of X-rays to interfere with one another as they leave the crystal, generating a diffracted ray called X-ray diffraction. The scattered X-ray undergoes constructive interference and observes a well-defined pattern of X-ray intensities, which satisfies the Bragg's law expressed by **Equation(2-2)**.

$$n\lambda = 2d_{hkl} \sin\theta \quad (2-2)$$

Where n is an integer (= 1), λ is the wavelength of the X-ray wave, d_{hkl} is the crystal plane spacing (d-spacing), and θ is the angle of incidence between the X-ray beam and the selected lattice plane. Each diffracted rays can be associated to the d-spacing which determines the crystal structure. [8]

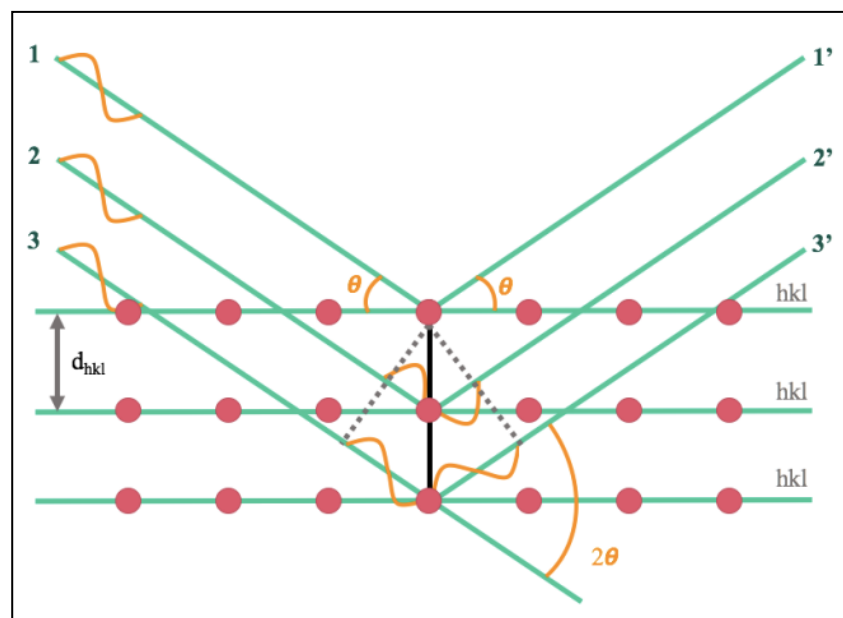


Figure 2-3. Schematic illustration of Bragg condition. Graph reproduced from [8].

2.2.2.1 Sample preparation for XRD measurement

XRD patterns were recorded using Rigaku MiniFlex equivalent with Cu K_{α} radiation. (See [9] for the specification of XRD instrument used.) Samples were finely ground using an agate mortar prior to the measurement. All samples were deposited on zero-background diffraction plate using some grease, and the patterns were acquired within the 10-80° (2θ) range, using a step size of 0.02°.

2.2.3 Synchrotron radiation

Synchrotron radiation is emitted when an electron beam is moving near the speed of light and forced to change its direction by the bending magnet. [10] Important properties of the synchrotron radiation are; high intensity, broad and continuous frequency range from infrared up to the hard X-ray region, high degree of polarisation, pulsed time structure, high brightness of the X-ray source due to small cross section, ultra-high vacuum environment and high beam stability. [11] The benefit of synchrotron X-ray is the tunability of the energy, which provides element specific information of local and each atomic species. [12] Also, synchrotron X-ray sources are highly intense, which give a trace amount detection sensitivity and measurements can be collected in shorter amount of time than when using conventional lab-based X-ray instruments. Therefore, for synchrotron-based method, the experiments can be

designed to take advantage of the penetrative power of X-rays to carry out *operando* measurements. [13]-[16]

2.2.4 X-ray Absorption Spectroscopy (XAS)

X-ray Absorption Spectroscopy (XAS) is a strong analytical tool to provide an element-specific probe of local electronic structure, which allow us to determine detailed information about the oxidation state, bonding configuration, and chemical environment around the excited atom without being interfered by other elements present in the sample. [13] Since XAS probes short range order, the state of the sample is not limited. The sample can be in an amorphous, liquid, or gas phase. [14] Therefore, XAS is predominantly advantageous for the Li-S battery material characterisation because during battery reaction of discharge and charge, the material undergoes structural transformations and can exist in crystalline, amorphous or even liquid phase. [15] In this thesis, benefits of the XAS technique was used to elucidate the reaction mechanism of the electrodes during the electrochemical process of the Li-S battery. Generally, for Li-ion battery materials, XAS measurements are done at the K-edge. The K-edge is due to 1s core level (a K-shell) absorption, which is suitable for measurement for elements with low atomic number and transition metals in the first row. The XAS technique is extensively applied to Li-ion battery materials to understand the mechanism of the electrochemical reaction in the material during cell operation. [16] XAS measures the absorption behavior of atom due to its chemical and physical state. Generally, the intensity of X-ray absorption is calculated according to Beer-Lambert law expressed by **Equation (2-3)**:

$$I = I_0 e^{-\mu t} \quad (2-3)$$

Where I is the intensity transmitted through the sample, I_0 refers to the intensity of the incident beam, μ is the absorption coefficient and t is the sample thickness.

The simple mechanism is displayed in **Figure 2-4**. When an X-ray photon is absorbed by an electron, one of the core electrons is excited to the continuum and leaves a core hole at the core level (**Figure 2-5a**). This vacancy leads to two types of relaxation process to lower the overall energy of the atom, either by emission of an X-ray fluorescence photon (**Figure 2-5b**) or Auger electron (**Figure 2-5c**).

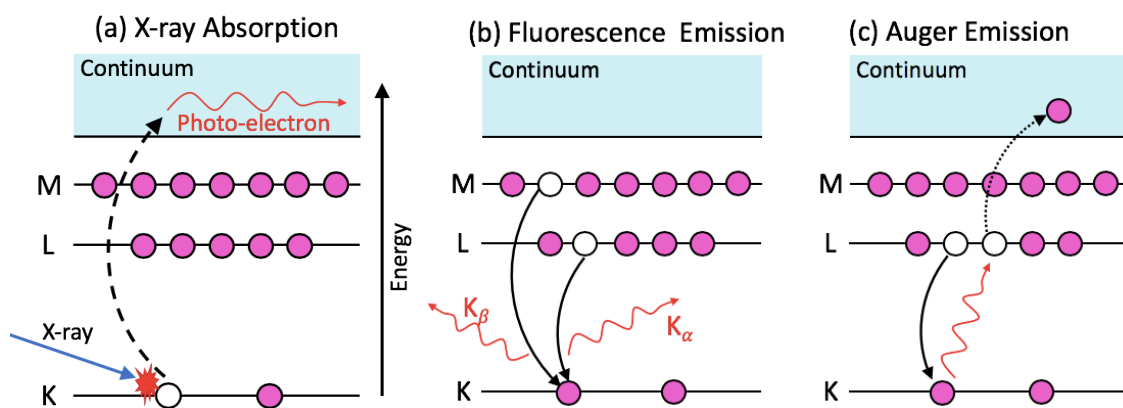


Figure 2-4. (a) X-ray is absorbed, and a core electron is excited from the atom. Relaxation state by (b) fluorescence X-ray emission and (c) Auger electron emission. Graph reproduced from [17].

In X-ray fluorescence, a higher energy electron fills the core hole, ejecting a photon of well-defined energy (**Figure 2-5b**). The fluorescence energy emitted during this process is characteristic of the atom. At the S K-edge, XANES spectra correspond to the $S\ 1s \rightarrow 3p$ orbital transition. [13] This is due to restriction of the lowest un-occupied antibonding states on the S atoms by dipole selection rules of $\Delta L = \pm 1$, $\Delta J = 0$ or ± 1 . [18] [35][58] When there is an excess energy, additional electron is emitted either from the same core level involved in the relaxation process or from different shells. This secondary ejected electron is called an Auger electron (**Figure 2-5c**). XAS measures these transitions from core electronic states of electrons to the excited states and the continuum as a function of the energy of the incident X-ray. The XAS spectrum is generally divided into two regions: (i) the X-ray absorption near edge structure (XANES) and (ii) the extended X-ray absorption fine structure (EXAFS) (see **Figure 2-6**). [18]

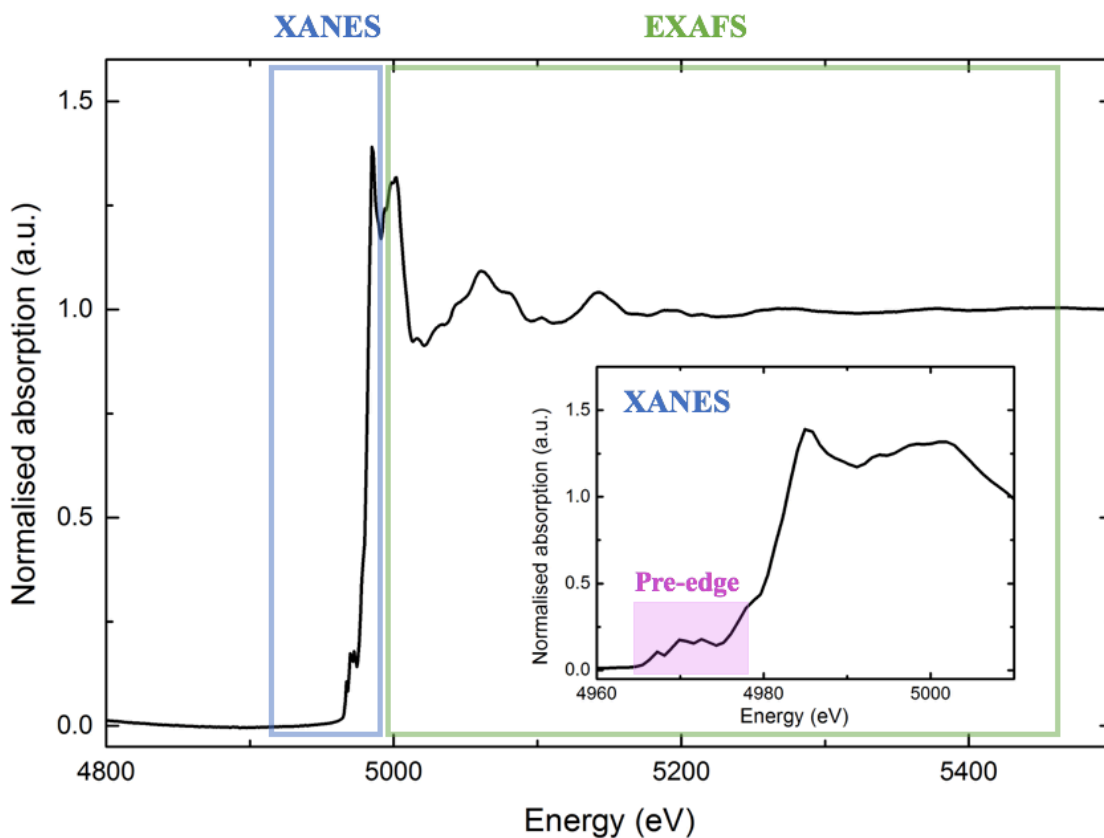


Figure 2-5. XAS spectra of TiO₂ showing the XANES and EXAFS regions, as well as the inset showing the pre-edge region in XANES. The inset shows an expanded view of the XANES region. Graph reproduced from [19].

2.2.4.1 XANES

The X-ray absorption near-edge structure (XANES) region is from about 20 eV below the edge position to about 50 eV above the absorption energy edge (E_0). XANES measurement provides information about coordination geometry, oxidation states, and density of states of the material. The edge energy increases with increasing atomic number and oxidation number due to higher charge of the nuclei, because the binding of the core electrons is tighter. It, thus require more energy to excite an electron. [14] Most importantly, multiple scattering (scattering involving several atoms) has to be considered while EXAFS is dominated by single-scattering. The multiple scattering depends on the interatomic distance, in which the photo-electron scatters from 2 or more atoms prior to returning to the absorbing atom. [17] Unlike the EXAFS region, XANES does not have a simple equation therefore used as a fingerprint to identify phases.

2.2.4.2 EXAFS

The extended X-ray absorption fine structure (EXAFS) region is from about 50 eV to about 1000 eV above the E_0 . The atomic arrangement of the neighboring atoms causes the oscillation of the absorption coefficient. EXAFS provides structural information such as bond distance of the nearest neighboring atoms and coordination spheres. The EXAFS oscillation result from the interference between the outgoing and back-scattered photoelectron from neighboring atoms in the molecule as presented in **Figure 2-7**. With the increasing scanning energy above the absorption-edge energy, the electrons entered to the continuum is backscattered off neighboring atoms. At a particular energy E_1 , the outgoing and the back-scattered X-rays are in phase, resulting in constructive interference, increasing the absorption coefficient. At a higher energy E_2 , the outgoing and backscattered waves are out of phase due to destructive interference, decreasing the absorption coefficient. [14][20] This modulates the energy-dependent fine structure of the absorption coefficient.

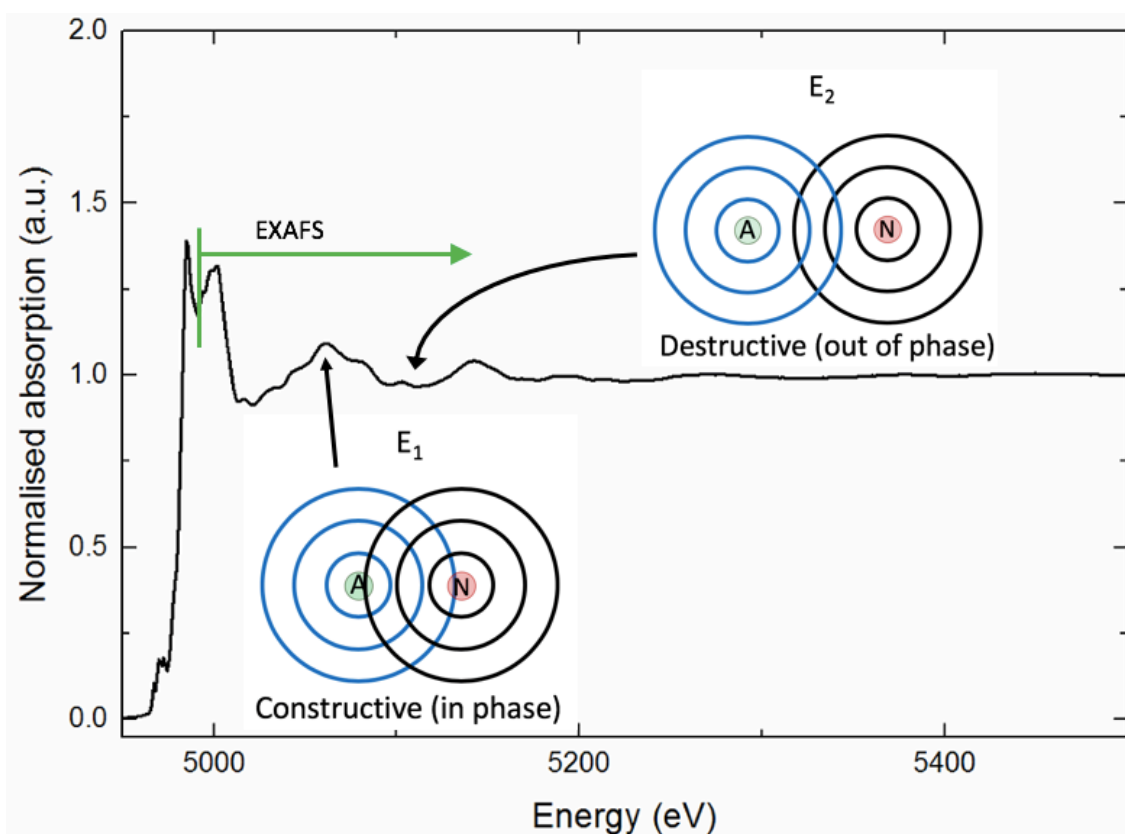


Figure 2-6. A schematic of EXAFS process representing the origin of EXAFS oscillations, where 'A' represents the absorbing atom and 'N' represents the neighbouring atom. Graph reproduced from [18][21].

XAS can be measured either by transmission or fluorescence mode. The basis of experimental geometry is displayed in **Figure 2-8**. Transmission or fluorescence measurements are processed depending on the sample thickness and concentration, and the energy region of interest. It also depends on the range of energy. For the sulphur K-edge, fluorescence is the preferred measurement setup because most of the energies will be absorbed by the time the beam goes through the sample.

2.2.4.3 Transmission measurement

Transmission-detection mode is the simple setup for XAS measurement. In a transmission measurement, the intensity of the X-ray beam is measured before and after a sample and the absorption coefficient is calculated by **Equation (2-4)**;

$$\mu(E)x = -\ln(I_0/I) \quad (2-4)$$

Where x is the sample thickness, I_0 is the X-ray intensity incident on a sample, and I is the intensity transmitted through the sample. [18][20]

2.2.4.4 Fluorescence measurement

In a fluorescence experiment, the incoming beam I_0 is measured using an ion chamber while monitoring the intensity of the X-ray fluorescence using energy dispersive Si solid state detector. [22] The absorption coefficient can be expressed by **Equation (2-5)**.

$$\mu(E) \propto I_f/I_0 \quad (2-5)$$

Where I_f is the intensity of a fluorescence line (electron emission). Generally, the sample is placed at 45° against the beam and the fluorescence detector oriented at 90° degree against the incoming beam (**Figure 2-7**). [17]

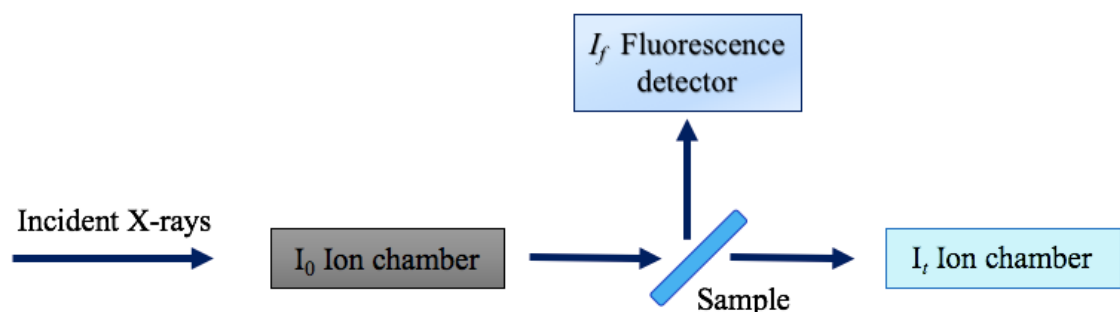


Figure 2-7. An illustration of a typical apparatus for XAS measurements.

2.2.4.5 Self-absorption (SA) correction

In fluorescence measurement, all matter attenuates the fluorescence intensity, hence, the XAS oscillations can be damped due to the self-absorption (SA) effects. The total absorption in the sample will be expressed by **Equation (2-6)**.

$$\mu_{tot}(E) = \mu_x(E) + \mu_{other}(E) \quad (2-6)$$

For concentrated samples, and are equivalent, thus XAS will be disturbed by the SA effects, which can alter the shape of the spectrum. [23] This is a common problem with sulphur samples, where measurement is taken in fluorescence mode in concentrated samples. [25]-[27] In principle, SA effects and distortion of XANES spectra can be avoided by dilution of sulphur concentration in samples and reducing the particle size of sulphur. [24] The low sulphur content and low sulphur loading, so-called ‘two lows’, considerably reduces the overall energy density per gram of the cathode that is not suitable for practical application. [25][26] During the discharge and charge processes, polysulphides are formed and dissolved into the electrolyte and vice versa. This can alter the concentration of sulphur species detected by the X-ray, therefore, even if a SA correction is applied, the concentration of sulphur species at the probed area cannot be determined precisely enough. [27] Additionally, the thickness of the sulphur electrode is expected to change due to the deposition of Li₂S and intermediate polysulphide species. [28] Therefore, in this study, SA correction was not applied in any of the samples and focused on a qualitative analysis of *operando* XANES spectra and the quantitative analysis of XANES spectra using linear combination fit (LCF) or principal components analysis (PCA) was not performed because the good fit was not obtained in most of the spectra.

2.3 XAS measurements

In this thesis, XAS experiment was conducted at two different beamlines, B18 at the Diamond Light Source (DLS) and BM28 at the ESRF. The basic operation specification of each beamlines are as listed in **Table 2-1**; [26][27]

Table 2-1. List of beamline specifications. [32]-[34]

| Beamline | B18, DLS | BM28, ESRF |
|--------------------|------------------------|-------------------------|
| Energy range (keV) | 2.05 - 35 | 2.4 - 15 |
| Energy resolution | 1.4 x 10 ⁻⁴ | 1.74 x 10 ⁻⁴ |

| | | |
|------------------------------|--|-------------------------------|
| Beam size (H x V) | 200 μ x 250 μ up to 1 mm x 1 mm | 500 μ m x 500 μ m |
| Flux at sample (@ 10 keV) | 1.3 x 10 ¹³ (300 mA) | 3 x 10 ¹² (200 mA) |

The experiment set up for B18 (DLS) is explained in **Appendix A-3**. The section below is focused on the set up for the beamline XMaS (X-ray Magnetic Scattering, BM28) at the European Synchrotron Radiation Facility (ESRF, Grenoble, France).

2.3.1 XMaS instrument

The beamline set-up at the XMaS beamline (BM28) at the ESRF is shown schematically in **Figure 2-9**, consisting of a double-crystal monochromator followed by a toroidal mirror. There is a total of three slits where the beam goes through. The slits control the width of the beam and its angular spread. The monochromator filters a narrow energy bandwidth from the X-ray source to a single desired wavelength. [31] The mirror is used for harmonic rejection to remove the harmonic contamination from the monochromator and vertical focusing, which greatly helps in performing low-energy measurements. [22] In our experiment, a double mirror harmonic rejection was used. [32]

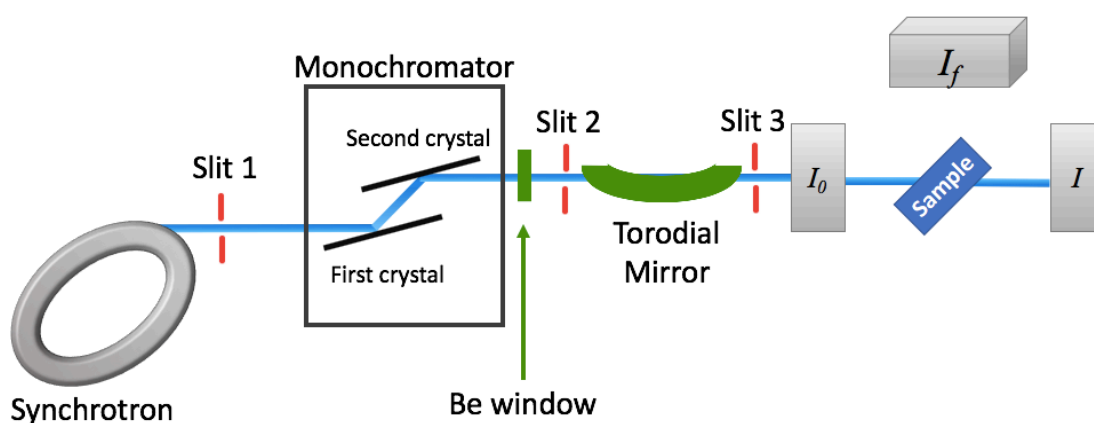


Figure 2-8. An overview of XAS experiment set-up at XMaS. [33]

For the S K-edge, EXAFS measurement would be very difficult, if not impossible. This is highly related to the energy adjustment system using a double crystal monochromator. The schematic for a double crystal monochromator is shown in **Figure 2-10**.

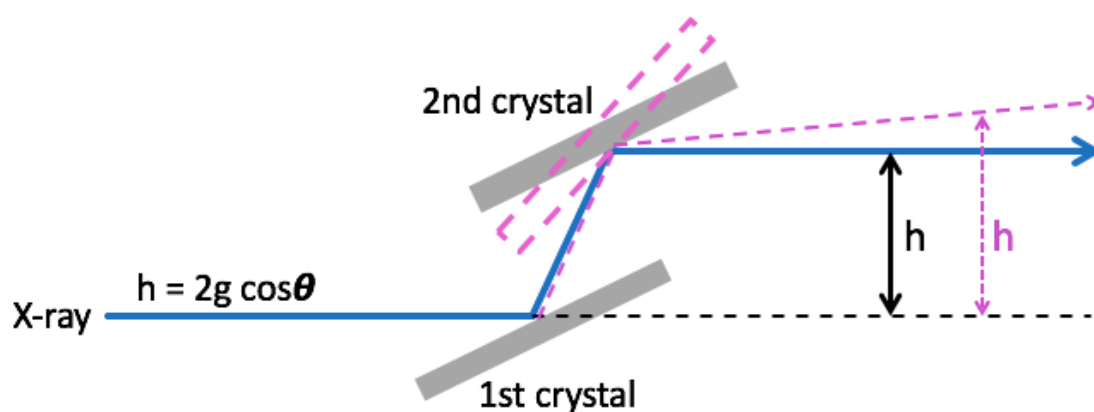


Figure 2-9. Schematic of a double crystal monochromator. Graph reproduced from [11].

Energy adjustment is done by rotation and vertical movement of the monochromator along the desired Bragg's angle corresponding to a given energy. The direction of the incident and exit beam remains constant while the vertical offset (h) between these two changes with energy according to **Equation (2-7)**. [11][23][36][37][38]

$$h = 2g \cos \theta \quad (2-7)$$

Where g is the distance between the two crystals and θ is the Bragg angle. At such lower energies of S K-edge (2.47 keV), the monochromator Bragg angle becomes a lot larger, hence the distance between the first and second crystal increases considerably, leading to a large vertical displacement of the beam after the monochromator (**Figure 2-10**). [22] Normally, to fit the EXAFS data, a k -range of $8 - 15 \text{ \AA}^{-1}$ is required, which makes the EXAFS measurements for the S K-edge is difficult, if not possible. In this thesis, EXAFS analysis have not been employed and only the XANES regions measurements were collected, which is sufficient to detect the type of sulphur species formed during the Li-S cell reaction. The narrow energy region of EXAFS collected after the XANES regions was only used for normalisation.

2.3.2 Soft X-ray spectroscopy

X-rays region are generally divided into two classes; soft X-ray and hard X-ray. Soft X-rays are assigned to the energy range typically less than 10 keV, whereas hard X-rays referred to the energy range of 10 – 200 keV. [34] Soft X-rays are located in between hard X-rays and extreme ultraviolet radiation (EUV), and probes core to valence transitions of K-edges of the so-called life-elements, such as, oxygen, nitrogen, carbon. [35] Recent work has shown that the XMaS beamline (BM28) at the ESRF can be a high

flux source for XAS in the 2 - 4 keV energy regime. There are only few beamlines available at those energies region. The K-edges of P, S, Cl, K, and Ca exists in this energy window. [22] A modular vacuum chamber made it possible to conduct such low energy K-edge studies (**Figure 2-10**). [22] This vessel fits within the Eulerian cradle, which allows the sample environment to be maintained under vacuum or pure helium atmosphere, as well as providing the ports for the fluorescence detector. To measure the S K-edge, it is essential to carry out the experiments in such conditions to minimise absorption and scattering from the atmosphere. XMaS beamline is facilitated with a Keytek detector, which is suitable for such a bespoke sample environment. [36]

For the fluorescence measurements, the choices of X-ray window materials are limited at the emission at these lower energies can easily absorbed. We have successfully designed a cell for this low energy regime using a thin Mylar film window. On the other hand, this means that vacuum cannot be used because the fragile Mylar film may break and cause evaporation of the electrolyte. Instead, the vessel chamber is filled with He gas. [32]

2.3.3 Beamline set-up

All *operando* XANES measurements were performed at the XMaS beamline (at the ESRF) [32] using a double crystal monochromator to adjust the energy at the S K-edge energy (2.47 keV) or the Ti K-edge energy (4.98 keV). The XAS measurements were performed in fluorescence mode mostly using a Ketek detector, unless otherwise stated. [22] A detector is placed in plane at 90° to the X-ray beam and a sample oriented at 45° to the incoming beam. [22] Reference compounds made into pellets and measured under vacuum of $\sim 10^{-6}$ mbar. Whereas all *operando* measurements were carried out at room temperature under constant He-gas flow. The measured coin cell samples were mounted on a sample holder which is equipped with a high precision XYZ-motorised mount and electrical cables (**Figure 2-12**).

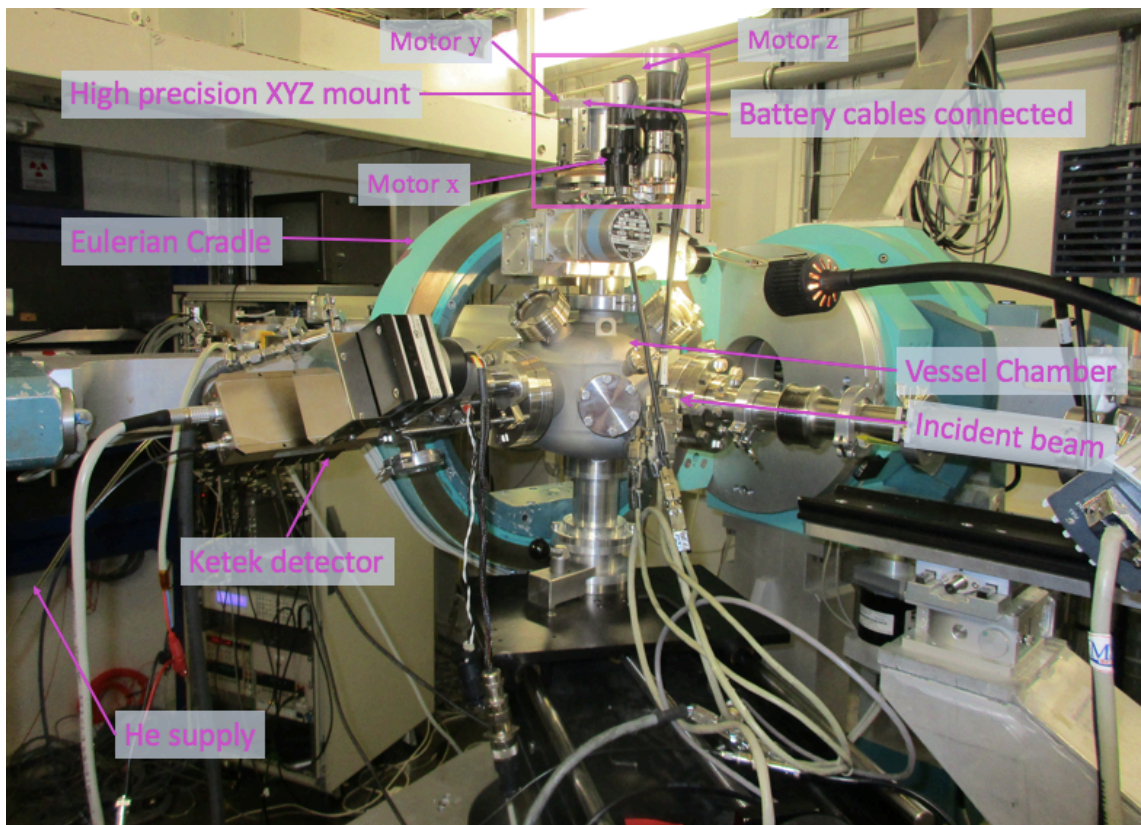


Figure 2-10. Experimental set up for *operando* XANES measurement (S K-edge and Ti K-edge) conducted at XMaS beamline (BM28) at the ESRF.

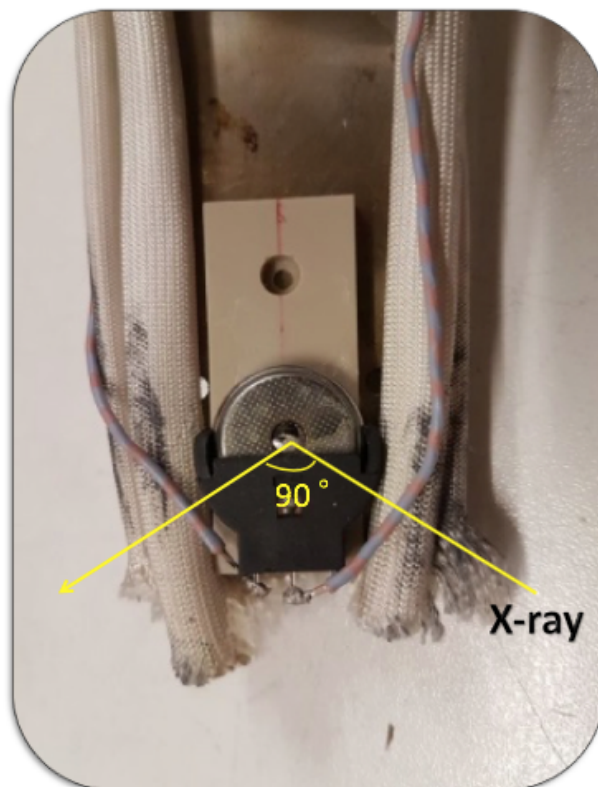


Figure 2-11. A photo of a coin cell sample mounted on the electrically connected sample stage.

2.4 *Operando* cell preparation

This section describes the X-ray transparent coin cell, which was especially designed for *operando* XAS measurements at BM28 at the ESRF. All procedure and fabrication methods described here are used in **Chapter 3** and **Chapter 4**. The X-ray transparent cell composition and fabrication method used for **Chapter 5** is described separately in **Section 5.2**.

2.4.1 Slurry coating for *operando* cells

In fluorescence detection mode the beam is reflected at the sample. This means that the beam goes through the Mylar window and sample twice. At such low energies of the sulphur K-edge (2.47 keV), the beam cannot go through an Al current collector, therefore, modification of the electrode was necessary. The slurry preparation procedures are the same as described in **Section 2.1.1**. The slurry coating method is modified to fabricate cathodes suitable for the XAS measurement. Prior to slurry coating, 2 mm diameter holes were punched through an aluminium sheet for the preparation of the current collector. Mylar films were placed underneath the pre-cut aluminium sheet to cover the holes during the coating process. A slurry was coated using a doctor-blade, as shown in **Figure 2-13**, using the wet thickness of 180 μm . The cathode sheet was dried at 60 °C under vacuum for about 16 hours and cut into 12.7 mm sized discs. The Mylar film on the back of the current collector were removed carefully and cathodes were kept in an argon-filled glove box until use.

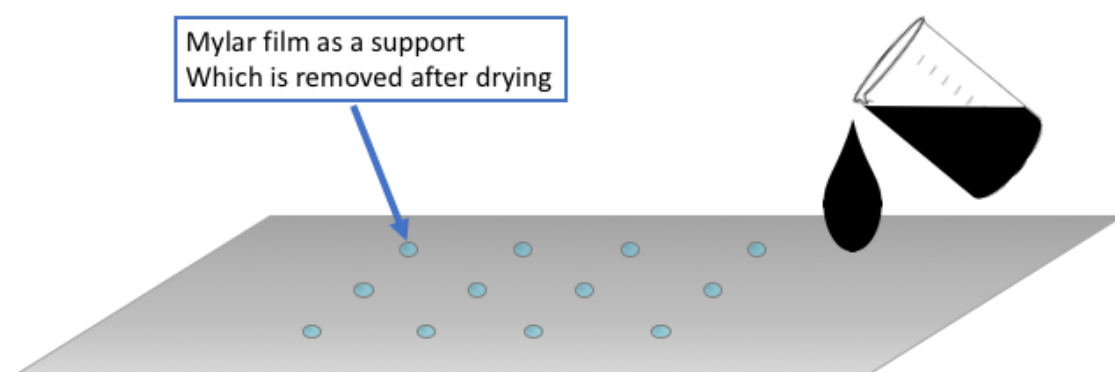


Figure 2-12. Schematic illustration of X-ray transparent cathode preparation.

In an argon-filled glove box, X-ray transparent *operando*, coin cells were assembled using Li foil as the anode, glass fibre as separator, and the as-prepared (window)

cathodes. The electrolytes used are different for each study and stated for each experiment. A stainless spacer (0.5 mm thickness) is placed between the Li metal and a bottom case to ensure good pressure within the cell. *Operando* coin cells were assembled in an argon-filled glove box utilising a coin cell crimper, unless otherwise stated. The configuration of the *operando* cell is described as below.

2.4.2 *Operando* cell configuration

As previously described, to undertake the S K-edge measurements at XMaS (ESRF) beamline, all measurements need to be done in a vessel chamber. This introduces limitation on the cell size, excluding a pouch cell design, which need to be large enough to ensure no electrolyte evaporation is taking place during cell assembly. A Swagelok cell is also excluded, as it cannot fit in the chamber. Instead, an X-ray transparent coin cell is designed, which is presented in **Figure 2-14**, including the overall cell design and the electrode arrangement.

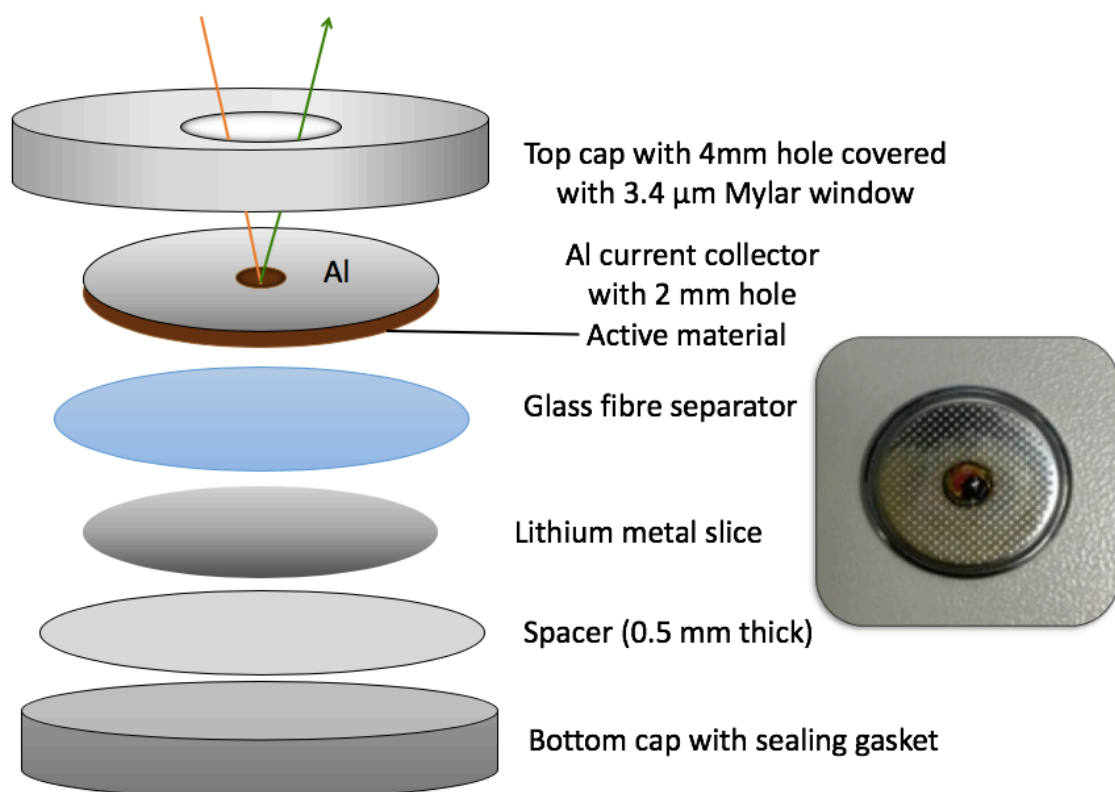


Figure 2-13. Schematic diagram and a photograph the of X-ray transparent *operando* coin cell configuration.

2.5 Benchmark test of *operando* cell

For a successful *operando* XAS measurement, the *operando* cell needs to achieve both (i) standard electrochemical behavior and (ii) X-ray access to the material of interest. These two important factors are examined and discussed below.

2.5.1 Electrochemical performance of *operando* cell

A benchmark analysis of *operando* coin cell was performed to test the reproducibility of the electrochemical performance. **Figure 2-15** compares the first discharge and charge profiles of conventional and X-ray transparent *operando* coin cell as a function of specific capacity. Both cells were tested under the same condition using the same slurry batch, at a rate of 0.1 C using electrolyte composed of 1M LiTFSI and 0.25 M LiNO₃ dissolved in DOL:DME (1:1 by volume). Voltage profile of *operando* coin cell resembles that of the conventional coin cell including the plateau voltages, demonstrating that the *operando* window modification to the coin cells does not alter the electrochemical performance of the cells. *In operando* cell achieved the first discharge capacity of 1036 mAh g⁻¹, whereas that of the conventional cell is 1074 mAh g⁻¹. We believe the slight capacity loss is due to reduced pressure of the coin cell where Mylar window is placed. From this test, we established the electrochemical performance retention of *in operando* coin cell is reminiscent of the conventional cells, hence modified coin cells are suitable for the *operando* XAS analysis.

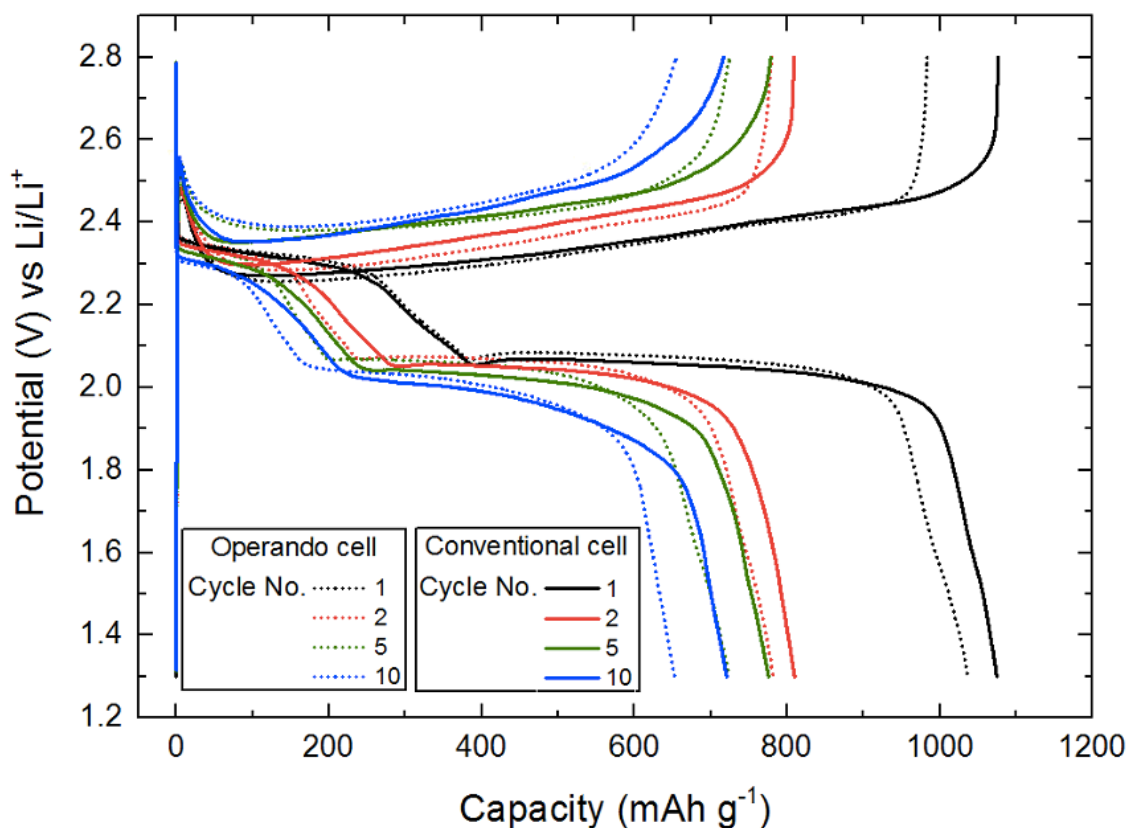


Figure 2-14. Discharge/charge curves of sulphur electrode cycled using *operando* cell (dotted lines) and conventional coin cell (solid lines).

Operando cells were assembled in-house at University of Kent and transferred to the beamline in argon atmosphere. The coin cell assembly process requires a special equipment (coin cell crimper), which means, it was not possible to build coin cells at the synchrotron facility. All cells were stored and cycled with equipment available at the ESRF. Generally, there were up to 5 days after cell assembly until the start of measurements. However, this should have not affected the electrochemistry of the cells, as the *operando* cell stored for 5 days demonstrated a standard electrochemistry behaviour, as shown in **Figure 2-15**, again compared with the fresh cells without an X-ray window. Both cells are assembled using the same electrolyte and the same sulphur electrode compositions. Both exhibited two discharge voltage plateaus with following single charge plateau, with capacities in acceptable difference.

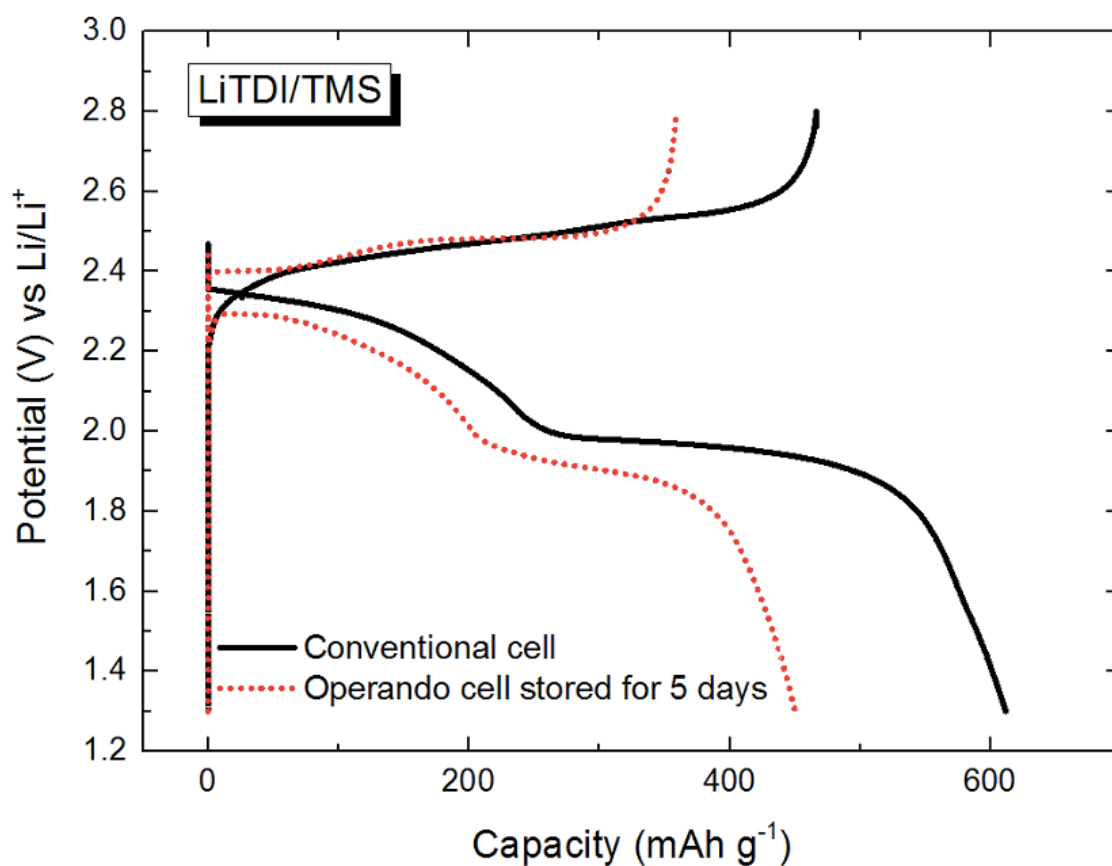


Figure 2-15. Discharge/charge profiles of sulphur electrodes cycled in conventional CR2016 cell (black line) and *operando* cell after 5 days of storage (dotted red line). Both cells are cycled in the same electrolyte (LiTDI/TMS) at a rate of 0.1 C between 1.3 – 2.8 V.

2.5.2 XAS resolution of *operando* cell

After confirming the electrochemical performance of the *operando* cell, we examined its resolution capability at the beamline. **Figure 2-17** represents the raw XANES spectra of Mylar film and sulphur cathode assembled in coin cell before applying a current. Here, we chose to display the raw spectra to prove the X-ray access to the material of interest. Raw spectrum provides the measure of the relative content of sulphur species in measured samples.

Since the beam goes through a Mylar window before detecting the sulphur cathode, Mylar window must not contain or be contaminated by any sulphur species as it interrupts the measurement of the active sulphur species. No sulphur peaks were

detected in the Mylar film, which successfully confirms the no sulphur contamination in the Mylar window.

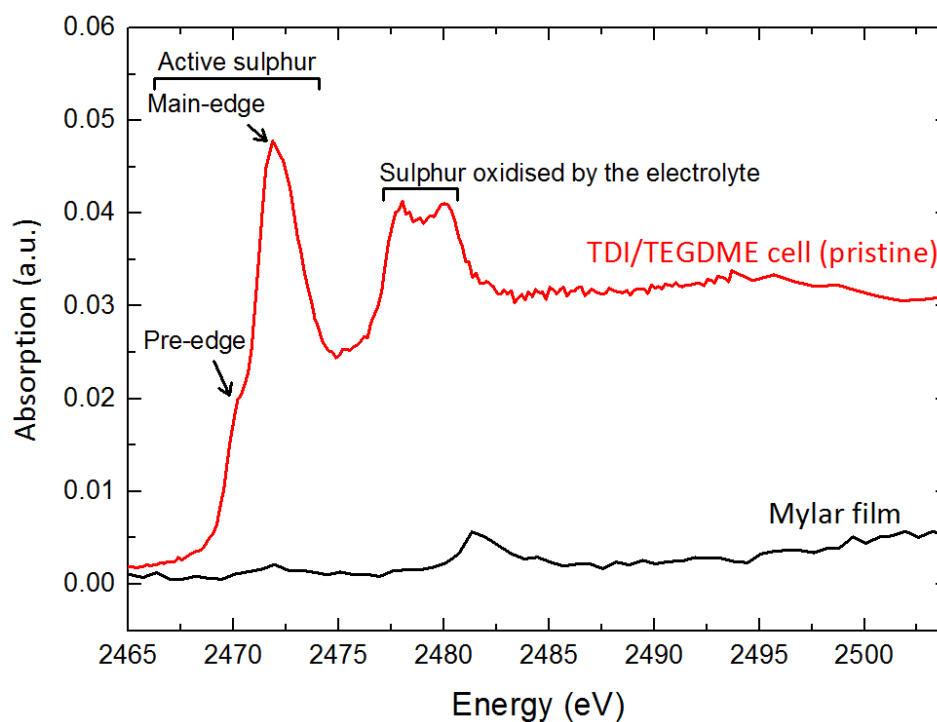


Figure 2-16. Raw S K-edge XANES spectra of Mylar-film compared to LiTDI/TEGDME cell at the pristine state.

2.6 Sulphur K-edge reference samples

2.6.1 S K-edge reference compounds

S K-edge XANES spectra for sulphur-containing reference compounds were collected using commercially available compounds, i.e., S_8 , $FeSO_4$, Na_2SO_3 , and $Na_2S_2O_3$. These reference compounds were diluted in PVP binder by grinding into a fine powder using an agate mortar. The diameter of 12.7 mm pellets were then made with the resultant mixture using a hydraulic press. The amount of material was calculated to optimise the signal to noise ratio using the Absorbix software. [37] Commercially available Li_2S (Sigma-Aldrich, stored in an argon-filled glovebox.) was mounted in an X-ray transparent *operando* coin cell without modification or dilution in a solvent. This was processed in argon atmosphere is due to moisture sensitivity of the compound. Polysulphide references were synthesised by stoichiometric mixing of S_8 and Li_2S described below.

2.6.2 Preparation of polysulphide

Polysulphide samples were prepared following the method established by Rauh *et al.* [38] Stoichiometric amounts of elemental sulphur and Li_2S calculated using **Equation (2-8)** were mixed for 24 hours in TEGDME at 50 °C, followed by centrifuging for 10 min at 5000 rpm. [39]–[44] However, only Li_2S_4 is discussed in this thesis for clarity, as all synthesised $\text{Li}_2\text{S}_{2-8}$ compounds displayed similar features in the XANES.



The resultant solutions were sealed in X-ray transparent *operando* coin cells for XANES measurement. All the operations were conducted under argon atmosphere with less than 0.5 ppm of H_2O and O_2 . The use of Li_2S_4 here represents fingerprint detection of the linear polysulphide chain contribution, as shown by **Figure 2-18**, which compares the S K-edge XANES spectra of three different references (S_8 , Li_2S_4 , and Li_2S) expected to form during Li-S cell cycling.

2.6.3 Reference compounds; S_8 , Li_2S , Li_2S_4

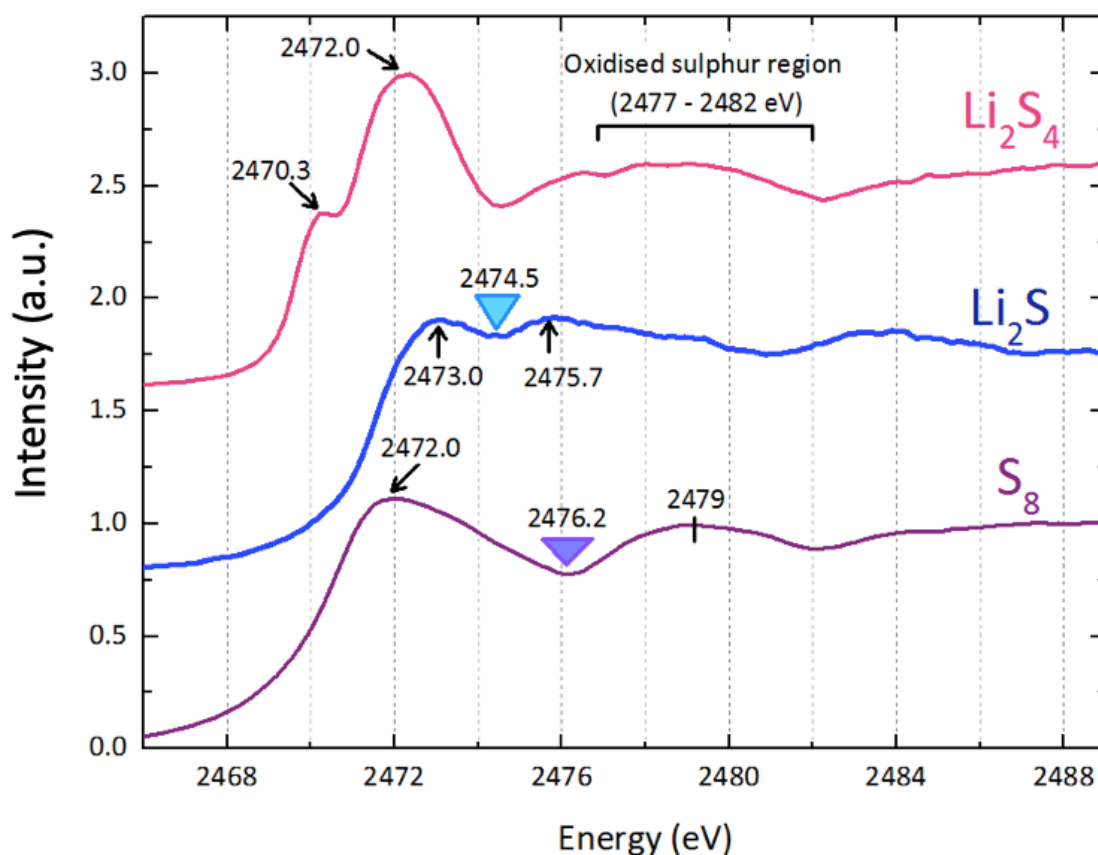


Figure 2-17. S K-edge XANES spectra of reference compounds; S_8 , Li_2S , and Li_2S_4 . The spectra of Li_2S and Li_2S_4 are offset for clarity by 0.8 and 1.6 units, respectively.

The elemental sulphur (S_8) exhibits a prominent peak at 2472.0 eV arising from 1s to unoccupied 3p transition, denoted as the main-edge, [45] together with a concave feature at 2476.2 eV and broad feature centred at about 2479 eV.

Li_2S is composed of two peaks at 2473.0 eV and 2475.7 eV, with a distinct concave feature in between these peaks at 2474.5 eV, which agree with other references in the literature. [39][46] Although Li_2S is in more reduced state than S_8 and Li_2S_4 , the ionic character of the Li-S bond result in two main peaks exist at higher energies than that observed in S_8 with its main-edge at 2472.0 eV. [47]

Lithium polysulphides (Li_2S_n), contain reduced form of sulphur atoms with an overall oxidation number of S^{2-} , characterised by the shoulder resonance at 2470.3 eV (denoted as the pre-edge), additional to the main-edge at 2472.0 eV. This shoulder clearly indicates the presence of a reduced form of sulphur in the sample. [46] After the main-edge, a notable concave shape is recognised at 2474.5 eV. The main- and the pre-edge resonances strongly depend on the local symmetry of sulphur atoms in the compound. [48] Coordination of sulphur atoms in polysulphide are mainly divided into two types; (i) terminal sulphur atoms placed at the end of the linear polysulphide chain and adjacent to a lithium atom [13][44][45] and (ii) internal sulphur atoms acting as a bridge between the terminal sulphur atoms (**Figure 2-19**). [39][51] Atom (i) and (ii) types are presented as the pre-edge and the main-edge, respectively. [51][52] These peak assignments agree well with previously published data. [7][17][57][35]

Additionally, it was confirmed that the reference compounds, S_8 , Li_2S , and Li_2S_4 do not exhibit any characteristic resonance after 2477 eV, whereas oxidised form of sulphur compounds ($S_2O_3^{2-}$, SO_3^{2-} , and SO_4^{2-}) involve distinct peaks at higher energy region (see **Figure 2-20**).

All features identified in this subsection of the thesis will be used in the following chapters to identify the different sulphur species that may appear in the electrodes at different stages of the cycling.

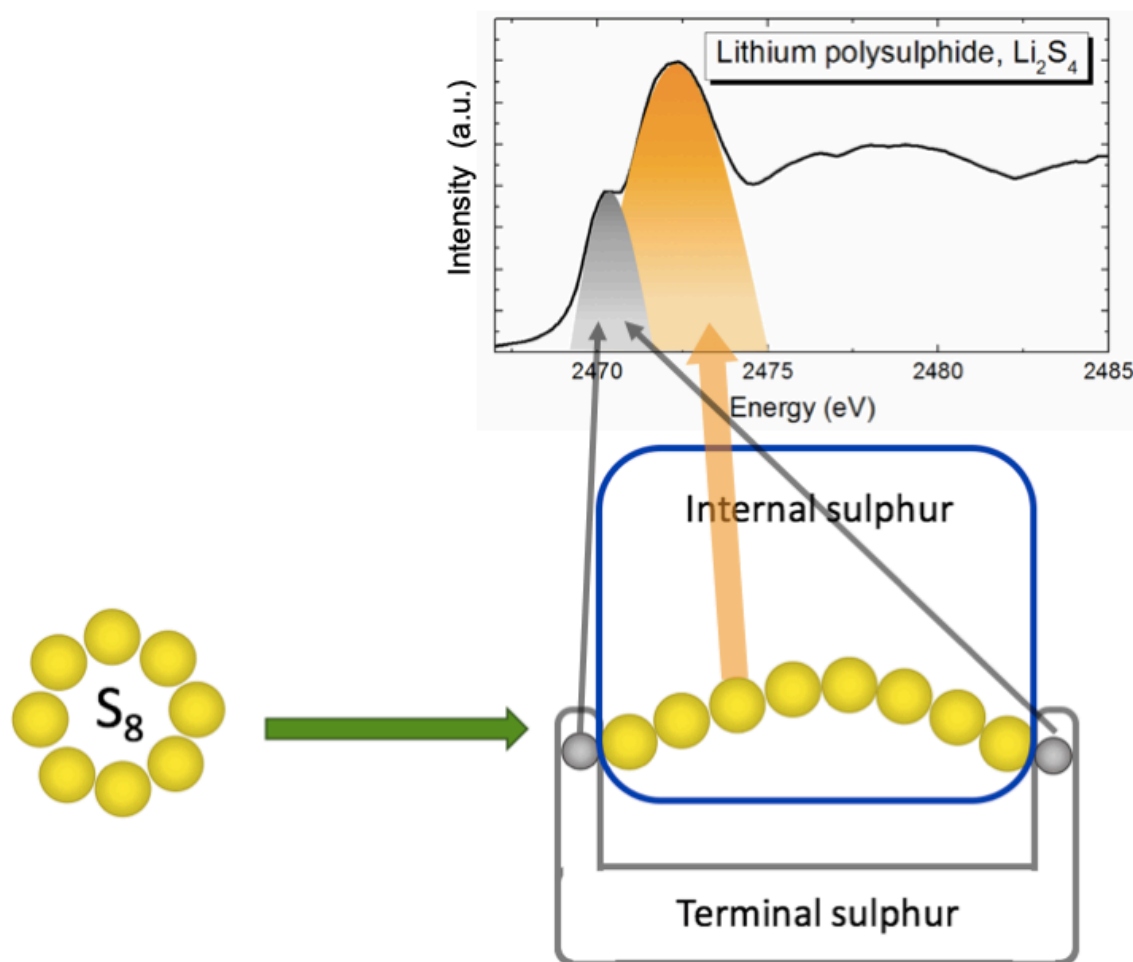


Figure 2-18. Schematic illustration of the S K-edge XANES; the pre-edge and the main-edge region corresponding to terminal sulphur and internal sulphur, respectively. [13]

2.6.4 Qualitative analysis of S_8 , Li_2S_4 , and Li_2S

The chain lengths of polysulphides can be identified by two methods based on the main and pre-edge features, i.e., by looking at (i) the absorption energy position of the main-edge and (ii) the ratio between the intensities (peak area) of the main/pre-edge resonances.

First-principles calculations by Pascal *et al*, has given a guideline to measure the chain length of different polysulphides based on the energy position of the pre-edge and the main-edge. [13] A linear polysulphide has more negatively charged terminal S atoms compared to internal S atoms. [51] It was found that there is a linear correlation between the peak splitting of the terminal and internal S atoms and partial atomic charge difference. In long-chain polysulphides, the charge is more distributed and lead to weak splitting of the internal and terminal S atoms, while in shorter polysulphide

chains, the charge is more localised leading to well-resolved peaks of the pre-edge and main-edge spectra. Thus, for internal S atoms (main-edge), the peak position shifts to higher absorption energy with decreasing S-S chain length, due to increased core-level binding offered by a decreased local valence electron density around the excited sulphur atoms. [13][58] Also, the main-edge signal will become smaller with decreasing chain-length of polysulphide, as the total proportion of the internal sulphur is smaller. Therefore, the area ratio between the main-edge and the pre-edge is proportional to the chain length of polysulphides. For example, long-chain polysulphide Li_2S_8 consists of 6 internal S atoms with 2 terminal S atoms adjacent to Li atoms. Therefore, the intensity of the main-edge would be much higher than that of the pre-edge. Thus, the main-edge to pre-edge area ratio reflects the relative population of sulphur atom types in a given sample, and this could be regarded as an estimate of the average polysulphide chain length. [59] However, this will not have a simple linear relationship when insoluble $\text{Li}_2\text{S}_2/\text{Li}_2\text{S}$ are involved in the reaction. [27] This is because the XANES spectrum of crystalline Li_2S has significantly different spectral features compared to those of linear-chain polysulphides and elemental sulphur. [28][40][41][47][62] This is because, these peaks are not arising from terminal and internal sulphur atoms, as there are no internal sulphur in Li_2S compounds, instead, these two peaks can be explained by the ionic character of the Li_2S bond. [47] Thus, *the area ratio of main/pre-edge can only be useful to indicate polysulphide chains, but not insoluble Li_2S .*

For an estimation of the number of intermediate states that exist in a reaction, an isosbestic point can be a useful identification tool. [63] Isosbestic point is the crossing point of a set of curves indicating the stoichiometric conversion of one species to another, which result from the fact that in a reaction the reactants and products have equal absorption coefficient at a specific energy, while the analytical concentration remains constant. [64] A clear isosbestic point indicates a two-step conversion reaction, whereas a nearly or imperfect isosbestic point means that the spectra are dominated by a two-step conversion reaction but are still affected by the presence of side reactions. [65]

2.6.5 References compounds– oxidised sulphur

Figure 2-19 shows the sulphur containing reference compounds $\text{Na}_2\text{S}_2\text{O}_3$, Na_2SO_3 , and FeSO_4 , to identify possible oxidised sulphur species formed during Li-S cell reaction. [55][66]

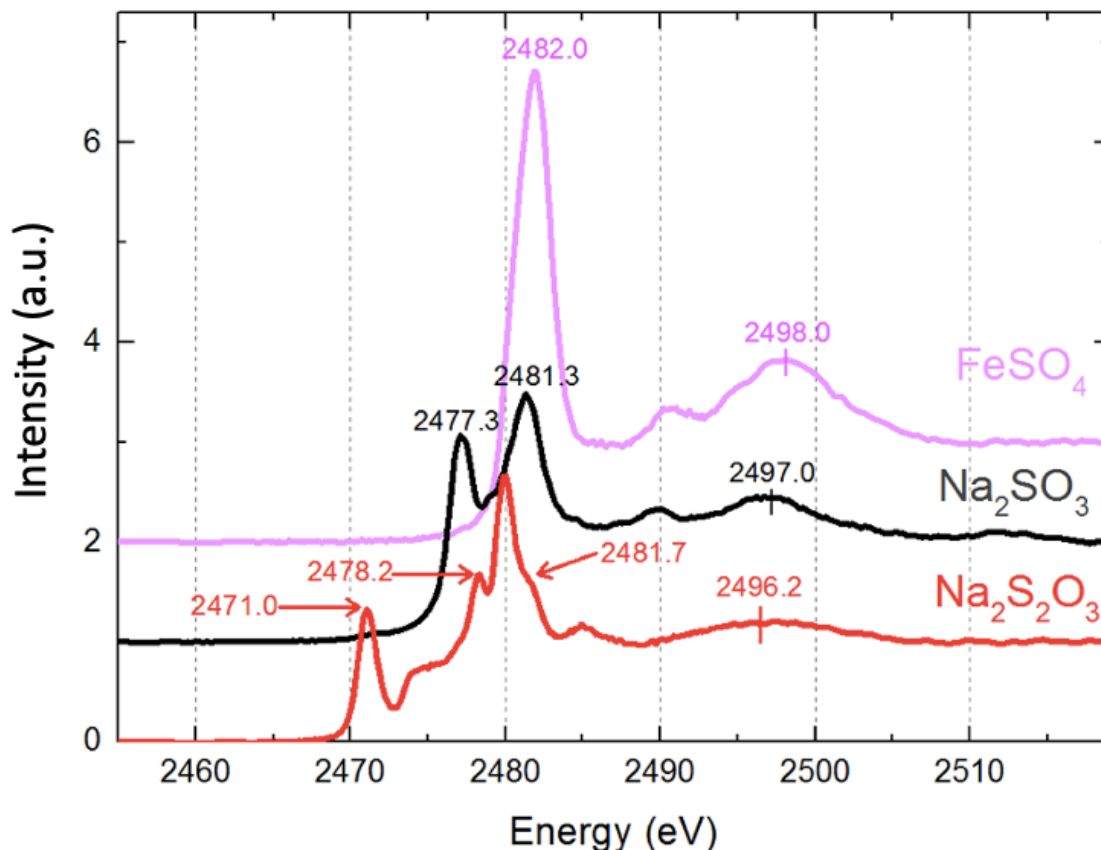


Figure 2-19. XANES spectra of reference compounds – $\text{Na}_2\text{S}_2\text{O}_3$, $\text{Na}_2\text{SO}_3^{2-}$, and FeSO_4 . The spectra are shown offset for clarity.

The distinct features of $\text{Na}_2\text{S}_2\text{O}_3$ (2478.2 eV and 2480.0 eV) [55][67], Na_2SO_3 (sharp peaks at 2477.3 eV and 2481.3 eV and broad feature at 2497 eV) [68], and FeSO_4 (dominant peak at 2482.0 eV and broad peak at 2498.0 eV) [69] are used to determine the oxidised sulphur products formed after the electrochemically active sulphur main-edge. These peak positions are in agreements with previous publications.

2.7 Data analysis

XANES data processing and analyses were conducted with the Athena program under the IFEFFIT package. [70] All collected XAS spectra were converted to $\mu(E)$ spectra using Equation (2-5), yielding the raw absorption spectra of the sulphur K-edge. These

raw spectra were then imported to the Athena software to process background subtraction and normalisation. The X-ray energy calibration was performed with an absorption measurement on pure sulphur in fluorescence-mode, where the peak was centroid to 2472.0 eV. [40][46] Depending on the focus of the spectral representation, whether it is on the concentration or the changes in the type of sulphur species, either the raw or the normalised spectra are displayed and indicated in each figure.

2.8 Conclusions

In this chapter, fabrication of the samples and experimental techniques are described. Also, the principle and overview of the characterisation techniques are explained, including laboratory-based XRD technique and the synchrotron radiation techniques.

For the rest of this study, XAS will be used as an analysis technique to qualitatively measure the reaction of sulphur in Li-S cells. In this work, X-ray transparent electrochemical cell was designed, with configuration allowing for measuring the S K-edge XAS spectra under fluorescence mode during cell cycling. We have used sulphur containing reference compounds (S_8 , Li_2S_4 , and Li_2S) to establish the possible intermediate products formed within the cell during cycling. The variety of the S K-edge spectral feature of the main/pre-edge area ratio, isosbestic points, and energy shift of the main-edge is discussed to give a guideline, which can be used to analyse the intermediate species formed during cell reaction.

2.9 References

- [1] “Celgard Li-ion Battery Separator Film (25um thickness x 85mm width x 60m Length) - EQ-bsf-0025-60C.” [Online]. Available: <https://www.mtixtl.com/separatorfilm-EQ-bsf-0025-60C.aspx>. [Accessed: 23-Aug-2018].
- [2] “Whatman® glass microfiber filters, Grade GF/F Grade GF/F circles, 47 mm, 100/pk | Sigma-Aldrich.” [Online]. Available: https://www.sigmaaldrich.com/catalog/product/aldrich/wha1825047?lang=en®ion=GB&gclid=CjwKCAjwvtnbBRA5EiwAcRvnph0J10-VWRYymZWICyBD-KwiKXSR6QwMgn0bB581TthNY_rj2Jr3BoCkBOQAvD_BwE. [Accessed: 23-Aug-2018].
- [3] “Disassembling Machine for All Button Cells of CR2016 , CR2025 & CR2032 - MSK-110D.” [Online]. Available: <https://www.mtixtl.com/CompactHydraulicCoinCellDisassemblingMachine-MSK-110D.aspx>. [Accessed: 23-Aug-2018].
- [4] “VMP3 Multichannel Workstation - ec-lab.” [Online]. Available: <https://www.ec-lab.co.uk/vmp3-multichannel-workstation.html>. [Accessed: 23-Aug-2018].
- [5] “MACCOR - Model 4200.” [Online]. Available: <http://www.maccor.com/Products/Model4200.aspx>. [Accessed: 23-Aug-2018].
- [6] V. S. Kolosnitsyn, E. V. Kuzmina, E. V. Karaseva, and S. E. Mochalov, “A study of the electrochemical processes in lithium-sulphur cells by impedance spectroscopy,” *J. Power Sources*, vol. 196, no. 3, pp. 1478–1482, 2011.
- [7] M. E. V. Team, “A Guide to Understanding Battery Specifications,” *Current*, no. December, pp. 1–3, 2008.
- [8] B. Barcikowski, S. Amendola, V. Marzun, G. Rehbock, C. Reichenberger, S. Zhang, D. Goekce, *Handbook of Laser Synthesis of Colloids*. 2016.
- [9] “Benchtop powder X-ray diffraction (XRD) instrument | Rigaku.” [Online]. Available: <https://www.rigaku.com/en/products/xrd/miniflex?gclid=CjwKCAjwvtnbBRA5EiwAcRvnpjw6H1->

apivMMWQ51b_MwvTeRcZLdYNWpRHHkApDrdiXv1r2uJ4R6RoCObwQAvD_Bw
E. [Accessed: 23-Aug-2018].

- [10] “What is a synchrotron?” [Online]. Available:
<https://www.esrf.eu/about/synchrotron-science/synchrotron>. [Accessed: 23-Aug-2018].
- [11] S. Mobilio, F. Boscherini, and C. Meneghini, “Synchrotron radiation: Basics, methods and applications,” *Synchrotron Radiat. Basics, Methods Appl.*, pp. 1–799, 2015.
- [12] F. M. Alamgir and S. Y. Lai, *Handbook of Solid State Batteries*. 2015.
- [13] T. A. Pascal K.H.Wujcik, J. Velasco-Velez, C. Wu, A.A.Teran, M. Kapilashrami, J.Cabana, J. Guo, M. Salmeron, N.Balsara and D. Prendergast, “X - ray Absorption Spectra of Dissolved Polysulfides in Lithium – Sulfur Batteries from First-Principles,” *J. Phys. Chem. Lett.*, vol. 5, pp. 1547–1551, 2014.
- [14] J. Yano and V. K. Yachandra, “X-ray absorption spectroscopy,” *Photosynth. Res.*, vol. 102, no. 2, pp. 241–254, 2009.
- [15] J. Mcbreen, “The application of synchrotron techniques to the study of lithium-ion batteries,” *J. Solid State Electrochem.*, vol. 13, no. 7, pp. 1051–1061, 2009.
- [16] E. C. Miller, R. M. Kasse, K. N. Heath, B. R. Perdue and M. F. Toney, Operando Spectromicroscopy of Sulfur Species in Lithium-Sulfur Batteries, *J. Electrochem. Soc.*, 165, pp. A6043–A6050, 2018.
- [17] M. Newville, “Fundamentals of XAFS,” *Rev. Mineral. Geochemistry*, vol. 78, no. 1, pp. 33–74, 2014.
- [18] J.E.Penner-Hann, “X-ray absorption spectroscopy,” vol. 102, no. 2, pp. 241–254, 2009.
- [19] J. Kowalska and S. DeBeer, “The role of X-ray spectroscopy in understanding the geometric and electronic structure of nitrogenase,” *Biochim. Biophys. Acta - Mol. Cell Res.*, vol. 1853, no. 6, pp. 1406–1415, 2015.
- [20] C. S. Schnorr and M. C. Ridgway, *X-Ray Absorption Spectroscopy of Semiconductors*, vol. 190. Springer Berlin Heidelberg, 2015.

- [21] C. T. Dillon, "Synchrotron Radiation Spectroscopic Techniques as Tools for the Medicinal Chemist: Microprobe X-Ray Fluorescence Imaging, X-Ray Absorption Spectroscopy, and," *Aust. J. Chem.*, vol. 65, no. 3, pp. 204–217, 2012.
- [22] P. B. J. Thompson, B. N. Nguyen, R. Nicholls, R. A. Bourne, J. B. Brazier, K. R. J. Lovelock, S. D. Brown, D. Wermeille, O. Bikondoa, C. A. Lucas, Thomas P. A. Hasee and M. A. Newton, "X-ray spectroscopy for chemistry in the 2-4 keV energy regime at the XMaS beamline: Ionic liquids, Rh and Pd catalysts in gas and liquid environments, and Cl contamination in γ -Al₂O₃," *J. Synchrotron Radiat.*, vol. 22, pp. 1426–1439, 2015.
- [23] G. Aquilanti, M. Giorgetti, R. Dominko, L. Stievano, I. Ar̄con, N. Novello, and L. Olivi, "Operando characterization of batteries using x-ray absorption spectroscopy: Advances at the beamline XAFS at synchrotron Elettra," *J. Phys. D. Appl. Phys.*, vol. 50, no. 7, p. 074001, 2017.
- [24] G. Almkvist, K. Boye, and I. Persson, "K-edge XANES analysis of sulfur compounds: An investigation of the relative intensities using internal calibration," *J. Synchrotron Radiat.*, vol. 17, no. 5, pp. 683–688, 2010.
- [25] H. Tamara, D. Susanne, H. Althues, and S. Kaskel, "Lithium e sulfur batteries : Influence of C-rate , amount of electrolyte and sulfur loading on cycle performance," vol. 268, pp. 82–87, 2014.
- [26] L.-X. Miao, W.-K. Wang, A.-B. Wang, K.-G. Yuan, and Y.-S. Yang, "A high sulfur content composite with core–shell structure as cathode material for Li–S batteries," *J. Mater. Chem. A*, vol. 1, no. 38, p. 11659, 2013.
- [27] R. Dominko, M. U. M. Patel, V. Lapornik, A. Vizintin, M. Kōzelj, N. N. Tūsar, I. Ar̄con, L. Stievano, and G. Aquilanti, "Analytical Detection of Polysulfides in the Presence of Adsorption Additives by Operando X-ray Absorption Spectroscopy," *J. Phys. Chem. C*, vol. 119, no. 33, pp. 19001–19010, 2015.
- [28] S. Waluś, G. Offer, I. Hunt, Y. Patel, T. Stockley, J. Williams, and R. Purkayastha, "Volumetric expansion of Lithium-Sulfur cell during operation – Fundamental insight into applicable characteristics," *Energy Storage Mater.*, vol. 10, pp. 233–245, 2018.

- [29] “[Online]
https://warwick.ac.uk/fac/cross_fac/xmas/impact/meetings/multiferroics/main/synchrotron/ [Accessed on 7/8/2018].”
- [30] “B18 Technical Information B18 Applications,” [Online] Available:
<https://www.diamond.ac.uk/Instruments/Spectroscopy/B18.html> [Accessed:
23-Aug-2018].
- [31] “Storage Rings as Synchrotron Radiation Sources.” [Online]. Available:
http://photon-science.desy.de/research/students__teaching/primers/storage_rings__beamlines/index_eng.html. [Accessed: 23-Aug-2018].
- [32] S. D. Brown, L. Bouchenoire, D. Bowyer, J. Kervin, D. Laundry, M.J. Longfield, D. Mannix, D. F. Paul, A. Stunault, P. Thompson, M. J. Cooper, C. A. Lucas, and W. G. Stirling, “The XMaS beamline at ESRF: Instrumental developments and high resolution diffraction studies,” *J. Synchrotron Radiat.*, vol. 8, no. 6, pp. 1172–1181, 2001.
- [33] “Beamline Details.” [Online]. Available:
https://warwick.ac.uk/fac/cross_fac/xmas/xmasbeamline/description.
[Accessed: 28-Aug-2018].
- [34] M. R. Kundu, S. M. White, N. Gopalswamy, and J. Lim, “Millimeter, Microwave, Hard X-Ray, and Soft X-Ray Observations of Energetic Electron Populations in Solar Flares,” *Astrophys. J. Suppl. Ser.*, vol. 90, no. February, pp. 599–610, 1994.
- [35] K. M. Lange and E. F. Aziz, “Electronic structure of ions and molecules in solution: A view from modern soft X-ray spectroscopies,” *Chem. Soc. Rev.*, vol. 42, no. 16, pp. 6840–6859, 2013.
- [36] F. T. H. E. President and F. T. H. E. President-elect, “XMaS Newsletter 2016,” vol. 10, no. 5, pp. 1–4, 2003.
- [37] M. Alain, M. Jacques, M.-B. Diane, and P. Karine, “MAX: Multiplatform Applications for XAFS,” *J. Phys. Conf. Ser.*, vol. 190, no. 1, p. 012034, 2009.
- [38] R. D. Rauh, F. S. Shuker, J. M. Marston, and S. B. Brummer, “FORMATION OF LITHIUM POLYSULFIDES IN APROTIC MEDIA,” vol. 39, no. September 1976, pp. 1761–1766, 1977.

- [39] Y. Gorlin, M.U.M. Patel, A. Freiberg, Q. He, M. Piana, M. Tromp, and H.A. Gasteiger, "Understanding the Charging Mechanism of Lithium-Sulfur Batteries Using Spatially Resolved Operando X-Ray Absorption Spectroscopy," *J. Electrochem. Soc.*, vol. 163, no. 6, pp. A930–A939, 2016.
- [40] M. Vijayakumar, N. Govind, E. Walter, S. D. Burton, A. Shukla, A. Devaraj, J. Xiao, J. Liu, C. Wang, A. Karim, and S. Thevuthasan, "Molecular structure and stability of dissolved lithium polysulfide species," *Phys. Chem. Chem. Phys.*, vol. 16, no. 22, pp. 10923–10932, 2014.
- [41] S. S. Zhang, "Improved cyclability of liquid electrolyte lithium/sulfur batteries by optimizing electrolyte/sulfur ratio," *Energies*, vol. 5, no. 12, pp. 5190–5197, 2012.
- [42] S. S. Zhang, "Effect of Discharge Cutoff Voltage on Reversibility of Lithium/Sulfur Batteries with LiNO₃-Contained Electrolyte," *J. Electrochem. Soc.*, vol. 159, no. 7, pp. A920–A923, 2012.
- [43] X. Tao, J. Wang, C. Liu, H. Wang, H. Yao, G. Zheng, Z. W. She, Q. Cai, W. Li, G. Zhou, C. Zu, and Y. Cui, "Balancing surface adsorption and diffusion of lithium-polysulfides on nonconductive oxides for lithium-sulfur battery design," *Nat. Commun.*, vol. 7, 2016.
- [44] G. Zhou, H. Tian, Y. Jin, X. Tao, B. Liu, R. Zhang, Z.W. Seh, D. Zhuo, Y. Liu, J. Sun, and J. Zhao, "Catalytic oxidation of Li₂S on the surface of metal sulfides for Li-S batteries," *Proc. Natl. Acad. Sci.*, vol. 114, no. 5, pp. 840–845, 2017.
- [45] J. Gao, M. a Lowe, Y. Kiya, and D. Abru, "Effects of Liquid Electrolytes on the Charge-Discharge Performance of Rechargeable Lithium / Sulfur Batteries : Electrochemical and *in situ* X-ray Absorption Spectroscopic Studies," *J. Phys. Chem. C*, vol. 115, pp. 25132–25137, 2011.
- [46] A. Vizintin, L. Chabanne, E. Tchernychova, I. Arcon, L. Stievano, G. Aquilanti, M. Antonietti, T.-P. Fellingner, and R. Dominko, "The mechanism of Li₂S activation in lithium-sulfur batteries : Can we avoid the polysulfide formation?," *J. Power Sources*, vol. 344, pp. 208–217, 2017.
- [47] Y. Gorlin, A. Siebel, M. Piana, T. Huthwelker, H. Jha, G. Monsch, F. Kraus, H. A. Gasteiger, and M. Tromp, "Operando Characterization of Intermediates

- Produced in a Lithium-Sulfur Battery," *J. Electrochem. Soc.*, vol. 162, no. 7, pp. A1146–A1155, 2015.
- [48] M. U. M. Patel, I. Arcon, G. Aquilanti, L. Stievano, G. Mali, and R. Dominko, "X-ray Absorption Near-Edge Structure and Nuclear Magnetic Resonance Study of the Lithium – Sulfur Battery and its Componentshttps.," *ChemPhysChem*, vol. 15, no. 5, pp. 894–904, 2014.
- [49] L. Li, T. A. Pascal, J. G. Connell, F. Y. Fan, S. M. Meckler, K. Ma, Y. M. Chaing, D. Prendergast, and B. A. Helms, "Molecular understanding of polyelectrolyte binders that actively regulate ion transport in sulfur cathodes," *Nat. Commun.*, vol. 8, no. 1, p. 2277, 2017.
- [50] M. Kavcic, K. Bucar, M. Petric, M. Zitnik, I. Arcon, R. Dominko, and A. Vizintin, "Operando Resonant Inelastic X-ray Scattering: An Appropriate Tool to Characterize Sulfur in Li-S Batteries," *J. Phys. Chem. C*, vol. 120, no. 43, pp. 24568–24576, 2016.
- [51] T. A. Pascal, C. D. Pemmaraju, and D. Prendergast, "X-ray spectroscopy as a probe for lithium polysulfide radicals," *Phys. Chem. Chem. Phys.*, vol. 17, no. 12, pp. 7743–7753, 2015.
- [52] K. H. Wujcik, T.A. Pascal, C.D. Pemmaraju, D. Devaux, W.C. Stolte, N.P. Balsara, and D. Prendergast, "Characterization of Polysulfide Radicals Present in an Ether-Based Electrolyte of a Lithium-Sulfur Battery during Initial Discharge Using *in situ* X-Ray Absorption Spectroscopy Experiments and First-Principles Calculations," *Adv. Energy Mater.*, vol. 5, p. 1500285, 2015.
- [53] G. Aquilanti, N. Giorgetti, R. Dominko, L. Stiveano, I. Arcon, N. Novello, and L. Olivi, "Operando characterization of batteries using x-ray absorption spectroscopy: Advances at the beamline XAFS at synchrotron Elettra," *J. Phys. D. Appl. Phys.*, vol. 50, no. 7, p. 074001, 2017.
- [54] R. Dominko, A. Vizintin, G. Aquilanti, L. Stiveano, M. J. Helen, A. R. Munnangi, M. Fichtner, and I. Arcon, "Polysulfides Formation in Different Electrolytes from the Perspective of X-ray Absorption Spectroscopy," *J. Electrochem. Soc.*, vol. 165, no. 1, pp. A5014–A5019, 2018.

- [55] A. T. S. Freiberg, A. Siebel, A. Berger, S. M. Webb, Y. Gorlin, M. Tromp, and H. A. Gasteiger, "Insights into the Interconnection of the Electrodes and Electrolyte Species in Lithium-Sulfur Batteries Obtained Using Spatially Resolved *Operando* X-ray Absorption Spectroscopy and X-ray Fluorescence Mapping," *J. Phys. Chem. C*, vol. 122, pp. 5303–5316, 2018.
- [56] A. Berger, A. T. S. Freiberg, A. Siebel, R. Thomas, M. U. M. Patel, M. Tromp, H. A. Gasteiger, and Y. Gorlin, "The Importance of Chemical Reactions in the Charging Process of Lithium-Sulfur Batteries," *J. Electrochem. Soc.*, vol. 165, no. 7, pp. A1288–A1296, 2018.
- [57] "Synchrotron Instruments." [Online]. Available: https://warwick.ac.uk/fac/cross_fac/xmas/impact/meetings/multiferroics/main/synchrotron/. [Accessed: 23-Aug-2018].
- [58] Y. Ye, A. Kawase, M. K. Song, B. Feng, Y. S. Liu, M. A. Marcus, J. Feng, E. J. Cairns, J. Guo, and J. Zhu, "X-ray Absorption Spectroscopy Characterization of a Li/S Cell," *Nanomaterials*, vol. 6, no. 1, p. 14, 2016.
- [59] K. H. Wujcik, D. R. Wang, T. A. Pascal, D. Prendergast, and N. P. Balsara, "In Situ X-ray Absorption Spectroscopy Studies of Discharge Reactions in a Thick Cathode of a Lithium Sulfur Battery," *J. Electrochem. Soc.*, vol. 164, no. 2, pp. A18–A27, 2017.
- [60] K. H. Wujcik, J. Velasco-Velez, C. H. Wu, T. Pascal, A. A. Teran, M. A. Marcus, J. Cabana, J. Guo, D. Prendergast, M. Salmeron and N. P. Balsara, Fingerprinting Lithium-Sulfur Battery Reaction Products by X-ray Absorption Spectroscopy, *J. Electrochem. Soc.*, vol. 161, pp. A1100–A1106, 2014.
- [61] M. Cuisinier, P. E. Cabelguen, S. Evers, G. He, M. Kolbeck, A. Garsuch, T. Bolin, M. Balasubramanian, and L. F. Nazar, "Sulfur Speciation in Li – S Batteries Determined by Operando X - ray Absorption Spectroscopy," *J. Phys. Chemistry Lett.*, vol. 4, pp. 3227–3232, 2013.
- [62] G. Almkvist, K. Boye, and I. Persson, "K-edge XANES analysis of sulfur compounds: An investigation of the relative intensities using internal calibration," *J. Synchrotron Radiat.*, vol. 17, no. 5, pp. 683–688, 2010.

- [63] B. Baubet, V. Moizan, and C. Pichon, "Comptes Rendus Chimie Co-K and Mo K edges Quick-XAS study of the sulphidation properties of Mo / Al₂O₃ and CoMo / Al₂O₃ catalysts," pp. 1–15, 2016.
- [64] M. Greger, M. Kollar, and D. Vollhardt, "Isosbestic Points: Theory and Applications," vol. 87, no. 19, p. 191540, 2012.
- [65] U. Boesenberg, M. A. Marcus, A. K. Shukla, T. Yi, E. McDermott, P. F. The, M. Srinivasan, A. Moewes, and J. Cabana, "Asymmetric pathways in the electrochemical conversion reaction of NiO as battery electrode with high storage capacity," *Sci. Rep.*, vol. 4, no. 7133, pp. 1–9, 2014.
- [66] C. Zu, N. Azimi, Z. Zhang, and A. Manthiram, "Insight into lithium-metal anodes in lithium-sulfur batteries with a fluorinated ether electrolyte," *J. Mater. Chem. A*, vol. 3, no. 28, pp. 14864–14870, 2015.
- [67] M. E. Fleet, "XANES spectroscopy of sulfur in Earth materials," *Can. Mineral.*, vol. 43, pp. 1811–1838, 2005.
- [68] H. Lin, J. Shi, B. Wu, J. Yang, Y. Chen, Y. Zhao, and T. Hu, "Speciation and biochemical transformations of sulfur and copper in rice rhizosphere and bulk soil-XANES evidence of sulfur and copper associations," *J. Soils Sediments*, vol. 10, no. 5, pp. 907–914, 2010.
- [69] M. L. Greenfield, M. Byrne, S. M. Kirtley, E. M. Kercher, T. B. Bolin, T. Wu, P. R. Craddock, K. D. Bake, and A. R. Pomerantz, "XANES measurements of sulfur chemistry during asphalt oxidation," *Fuel*, vol. 162, pp. 179–185, 2015.
- [70] B. Ravel and M. Newville, "ATHENA, ARTEMIS, HEPHAESTUS: Data analysis for X-ray absorption spectroscopy using IFEFFIT," *J. Synchrotron Radiat.*, vol. 12, no. 4, pp. 537–541, 2005.

Chapter 3

Effects of Electrolytes

3.1 Introduction

The performance of Li-S cells can be strongly influenced by the choice of the electrolyte compositions. The important role of the electrolyte is to dissolve the polysulphides formed during the cell operation and to bring the reaction forward. With increasing concentration of the polysulphide dissolved into the electrolyte, the viscosity of the electrolyte is increased hence lowering the ionic conductivity of the cell. [1]

Generally, ether-based solvents are used in Li-S batteries as oppose to carbonate-based solvents commonly used in other Li-ion batteries. This is because carbonate-based solvents, such as ethylene carbonate (EC) and diethyl carbonate (DEC) are known to react irreversibly with polysulphides. One possible explanation for this is the nucleophilic reaction involving a radical attacking the carbonate species in the electrolyte. However, the nature of the nucleophile (radical species) has not yet been clearly determined. [2] Currently, the most-common electrolyte used for Li-S battery is 1 M LiTFSI dissolved in 1:1 volume ratio of DOL:DME binary solvent with an addition of LiNO_3 . It is generally accepted that DOL and DME are appropriate solvents to encourage the reduction of soluble polysulphides during cycling. However, the low boiling points and high vapour pressures arising from two small ether molecules pose problems for practical use of a long-term cycling due to its self-evaporation issue. [3] Also, the volatility of DOL:DME solvent raises the flammability, thus leading to a safety concern. [4]

Despite the fact that it is widely accepted that the Li-S cell reaction heavily depends on the electrolyte compositions, less attention has been paid for the improvement of electrolytes for the superior performance of Li-S battery. The reason for this may be due to a number of requirements that should be fulfilled in the development of new

formulations. A successful electrolyte solvent should meet the criterion of; (i) high ionic conductivity, (ii) good polysulphide solubility, but low polysulphide permeability through the separator (iii) low viscosity, (iv) electrochemical stability, (v) chemical stability towards lithium, and (vi) high safety (low volatility, low flammability, as well as low toxicity). [5]–[7]

Unlike traditional Li-ion batteries, the electrochemical tests of Li-S batteries involve a full-cell configuration, hence it is difficult to optimise each component individually. Therefore, it is indispensable to have a good understanding of Li-S reaction mechanisms to see the influence of each component on its electrochemical properties. [8] The configuration of Li-S varies significantly between each study, including the cathode fabrication methods and electrolyte compositions, which makes direct comparisons between different studies difficult. [9]

The fact that the Li-S cell performance is heavily influenced by the electrolyte, the motivation of this work is to explore the optimal electrolyte composition to achieve successful Li-S battery performance. Within this chapter, an overview of different electrolyte compositions is presented using electrochemical measurement as well as *operando* XANES (X-ray absorption near-edge structure) techniques to understand the reaction mechanisms of sulphur during battery cycling associated with the different electrolyte systems. The recent trend of the analytical technique for Li-S cell has been focused on *operando/in situ* measurements. [10] It is widely accepted that the spectral feature of the S K-edge XANES in Li-S batteries provides information about the types of sulphur species that exists in the cells, such as, Li_2S , elemental octasulphur (S_8), and Li_2S_x ($2 \leq x \leq 8$). The energy position of the absorption edge, in which XAS is dependent on the sulphur species, provides information about the oxidation state of the probed atom. [5][11] Additionally, the XAS can give us information of the estimated overall chain lengths of polysulphide species present in the probed area. [12] Therefore, it is a precise method to obtain the picture of polysulphide intermediate formation processes and their behaviour within composite electrodes. [2][3][5][6][13]–[17]

The electrolyte components analysed in this study were chosen based on their availability, properties, and more importantly, spectroscopic suitability. The properties of the solvent and salts used in this study are described below.

Solvents:

The solvents used as electrolytes in this work are listed in **Table 3-1**. Here, the properties of each electrolyte solvent are explained based on the dielectric constant, viscosity, and donor number (DN). Dielectric constant expressed in 'ε_r' is a rough measure of the polarity of solvents. [18] Generally, a high dielectric constant means that the solvent has high polarity, hence, greater ability to dissolve and dissociate the conducting lithium salt. [19] A high viscosity means that the migration of ions in the solvent is slow. [20] DN is a measure of the Lewis base behaviour of the solvent, and a good metric for explaining the solvating power of lithium polysulphides in organic electrolytes. [21] A high DN indicates that it will dissolve solutes more readily. [20] Considering all these parameters, high dielectric constant with low viscosity, and high DN are, therefore, the preferred solvent for Li-S batteries.

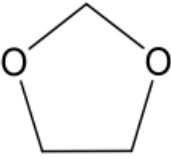
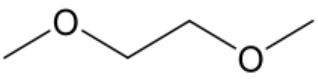
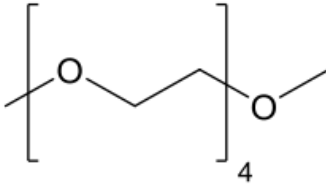
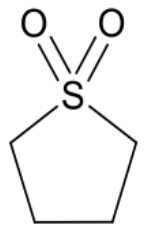
DOL (1,3-dioxolane) is a common solvent choice for the Li-S cell electrolyte known to generate an insoluble and flexible surface electrolyte interface (SEI) layer of dioxolane oligomer $-(\text{OCH}_2\text{CH}_2\text{OCH}_2)_n-$, which prevents dendrite formation. A SEI layer offers to accommodate Li morphology/volume changes upon cycling, while enabling highly facile Li-ion transport. [22][23] Despite these attractive advantages, DOL provides low polysulphide solubility and slow polysulphide reaction kinetics due to slightly low dielectric constant. [24]

DME (1,2-Dimethoxyethane) is a polar solvent with relatively higher dielectric constant than DOL and low viscosity, which makes it a suitable solvent for Li-S cells because it offers good polysulphide solubility and faster polysulphide reaction kinetics so the complete redox reaction can be expected. [21][24]

TEGDME (Tetraethylene glycol dimethyl ether) has a glyme structure with dielectric constant similar to DOL and DME solvents with relatively high DN. Additionally, it contains more solvating oxygen atoms in its structure than DME, which greatly dissolve and dissociate the lithium salt as well as sulphur active materials. [19] Additional advantages of TEGDME are the high boiling point, low vapour pressure, and lower flammability of glyme-based solvents in comparison to the small-molecular ethers DOL and DME. [3][4]

TMS (Tetramethylene sulphone) has a considerably high dielectric constant, hence considered as a solvent with high polarity. It is an excellent solvent with regards to safety concerns, as it shows low volatile toxic properties. [20] However, the limitation may arise from its high viscosity with relatively low DN. [21]

Table 3-1. Basic properties of organic solvents tested for this study [5][25]

| Solvents | | Dielectric constant (ϵ_r) | Donor number (DN) | Viscosity (cP) |
|----------|--|--------------------------------------|-------------------|----------------|
| DOL |  1,3-Dioxolane | 7.0 | 24 | 0.6 |
| DME |  1,2-Dimethoxyethane | 7.4 | 17 | 0.455 |
| TEGDME |  Tetraethylene glycol dimethyl ether | 7.3 | 20 | 4.05 |
| TMS |  Tetramethylene sulphone | 43.4 | 14.8 | 10.34 |

Lithium salts:

Lithium salt is used as the source of Li^+ -ions in the electrolyte, which is required to provide an ion carrier hence required to easily dissolve in the non-polar solvents. [26]

Two different salts (**Figure 3-1**), LiTFSI and LiTDI were tested in this study. Among these two, LiTFSI is more commonly used in Li-S batteries compared to LiTDI. [26] Both LiTFSI and LiTDI salts are composed of weakly coordinating anions (WCA), enabling them to dissolve in non-aqueous organic solvents. [27] The WCA nature of those salts is also a key parameter to dissolve lithium polysulphides in the electrolyte to achieve successful cell operation. [21]

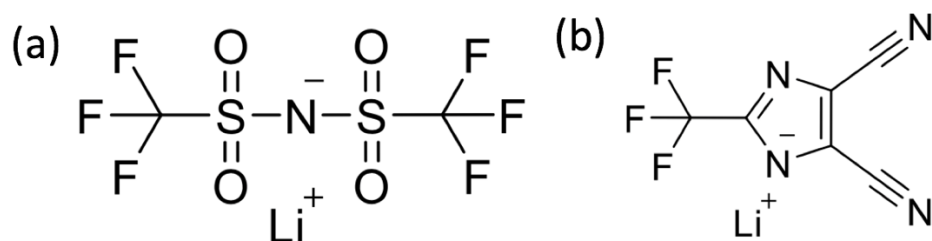


Figure 3-1. Structures of lithium salts used in this study, (a) LiTFSI and (b) LiTDI.

LiTFSI is internally flexible, it can adopt different conformations by rotating the two groups attached to the central N atom, [13] whereas LiTDI is rigid (**Figure 3-1**). [14]

The popularity of LiTFSI is based on its high thermal stability, stable and high tolerant to water, good compatibility with the ether-based solvents, and a high dissociation ability. [15] The highly delocalised negative charge distribution of TFSI⁻ effectively reduce the interaction between Li⁺-ion and TFSI⁻-anion hence dissociate easily with increasing the solubility of LiTFSI in ether-based solvents, resulting in enhanced ionic conductivity at room temperature. [23]

On the other hand, LiTDI is a relatively new salt, which is also thermally and electrochemically stable, [16] as well as fully stable against water. [17][28] In the work of Han *et al.*, LiTDI is reported to give intermediate anodic stability and found to be a successful salt, which effectively reduced the permeability of polysulphides thereby minimising the shuttle effect. [29] Later on, the Han group demonstrated that this improvement is due to the slow mobility of TDI⁻-anion and weak interactions with polysulphides. [30]

Though the LiTFSI is the most commonly used salt in Li-S batteries, it is not the best choice of salt when the cell is analysed using an element specific XAS technique,

because the sulphone group of LiTFSI contributes to a dominant peak at 2480 eV in the S K-edge XAS, which potentially masks the peaks originating from electrochemically active sulphur species. Therefore, LiTDI was chosen as an example of a sulphur-free Li salt for the XAS measurements.

LiNO₃ is currently considered as a standard component in Li-S electrolytes due to its effectiveness to control the polysulphide shuttle reaction since the first proposal by Mikhaylik. [31][32] LiNO₃ is oxidised to form Li_xNO_y which functions as a protective layer to the Li metal, preventing the parasitic reaction between polysulphide species and the Li anode. Additionally, the introduction of LiNO₃ was found to give a synergetic effect to improve the sulphur utilisation in the cathode. [33][34] These promising results have made LiNO₃ the major additive for electrolytes and almost appear in every reports of Li-S cell. Nevertheless, the relevance of Li_xNO_y layer towards redox shuttle mitigation is still a matter of debate. [35] Ding *et al.* claimed that the Li_xNO_y layer is ineffective towards polysulphide suppression. Instead, LiNO₃ function through the NO₃⁻ anions which strongly binds with polysulphides, facilitating the fast conversion reaction from lithium polysulphides to sulphur, which mitigates the diffusion of polysulphide to the anode side during charging process. [36]

Despite its excellent merits in suppressing the shuttle reaction, the use of the LiNO₃ salt in the electrolyte introduces few drawbacks to the Li-S cells. Unfortunately, it is consumed over time and progressively reduced on the Li anode, elevating the internal resistance of the cell, lowering the output voltages of the discharge plateaus. [37] Also, the strong oxidising nature of LiNO₃ raises safety concerns, as it can be explosive in nature under high concentration and high temperature. [38] For these reasons, the LiNO₃ salt should not be relied too heavily upon in the future, and searching for a replacement or the new design of electrolyte available to work without the LiNO₃ salt becomes necessary for practical applications. [39]

3.2 Material preparations

3.2.1 Electrode preparations

To study the effect of the different electrolyte systems on Li-S cells, conventional sulphur cathode electrodes were prepared and characterised, and these electrodes were assembled in CR2016 cells and electrochemically tested using VMP-3

potentiostat in-house. Fabrication of the sulphur composite was done by impregnation of sulphur in active carbon and mix with PVP in a ratio of 60:25:15, then stirred in NMP to become a homogeneous slurry. The slurry was then cast on an Al-sheet, dried in a vacuum oven, and cut into 12.7 mm cathodes and kept in an argon-filled glovebox until cell assembly. *In operando* electrodes were prepared using Al-sheets with pre-cut holes with a diameter of 2 mm. Again, the slurry was coated on the Al-sheet, dried and cut into 12.7 mm and stored under argon atmosphere. These electrodes were assembled in X-ray transparent coin cells (see **Section 2.4.2**) to be characterised at the BM28 beamline at the ESRF. Details of the composite cathode fabrication and slurry coating methods can be found in **Section 2.4**.

In this chapter, all sulphur electrodes are prepared using polyvinylpyrrolidone (PVP) binder, which is one of a common binder used in Li-S batteries. Recently, PVP was reported to utilise sulphur more sufficient than PVDF, which is also used as a common binder in Li-S cells. [40] PVP is advantageous due to its amphiphilic nature. The oxygenated groups offer strong bonding with the polarised lithium polysulphides and hydrophobic groups bind with the non-polarised carbon surface. [41][42] Using the same electrode composition in all cells allowed a direct comparison of the electrolyte systems.

3.2.2 Electrolyte preparations

Electrolytes were prepared as described in **Section 2.1.2**. The compositions of electrolytes tested are represented in **Table 3-2** with their acronyms. In order to observe the effect of LiNO₃ salt towards the Li anode and the sulphur cathode, each electrolyte was prepared with and without LiNO₃ and electrochemically tested. The concentration of LiTFSI and LiTDI were kept constant at 1 M and 0.25 M LiNO₃ was used for LiNO₃-containing electrolytes, unless otherwise stated. In this chapter, the amount of electrolyte was standardised to 80 $\mu\text{L mg}^{-1}$ of sulphur.

Table 3-2. List of electrolyte compositions examined in this study. (a) 1 M LiTFSI used as the lithium salt and (b) 1 M LiTDI used as the lithium salt. All combinations have been studied both with and without LiNO₃.

| (a) 1 M LiTFSI | | |
|----------------|--------------|-------------------------------------|
| Solvent | Volume ratio | Acronym |
| DOL:DME | 1:1 | LiTFSI/DOL:DME |
| | | LiTFSI/DOL:DME/LiNO ₃ |
| TEGDME:DOL | 1:1 | LiTFSI/TEGDME:DOL |
| | | LiTFSI/TEGDME:DOL/LiNO ₃ |
| TEGDME | | LiTFSI/TEGDME |
| | | LiTFSI/TEGDME/LiNO ₃ |
| TMS | | LiTFSI/TMS |
| | | LiTFSI/TMS/LiNO ₃ |

| (b) 1 M LiTDI | | |
|---------------|--------------|------------------------------------|
| Solvent | Volume ratio | Acronym |
| DOL:DME | 1:1 | LiTDI/DOL:DME |
| | | LiTDI/DOL:DME/LiNO ₃ |
| TEGDME:DOL | 1:1 | LiTDI/TEGDME:DOL |
| | | LiTDI/TEGDME:DOL/LiNO ₃ |
| TEGDME | | LiTDI/TEGDME |
| | | LiTDI/TEGDME/LiNO ₃ |
| TMS | | LiTDI/TMS |
| | | LiTDI/TMS/LiNO ₃ |

Additionally to those electrolytes listed above, ultrahigh concentration electrolyte (7 M LiTFSI in DOL:DME) is also investigated.

3.3 Material characterisations

XRD measurements

The phase purity of sulphur cathode composite was confirmed by X-ray Diffraction (XRD). As-prepared cathode composite powder (mixture of S and acetylene black (AB)), heated at 155 °C, pure sulphur, and pure AB were measured on the zero-background sample holders and displayed in **Figure 3-2**.

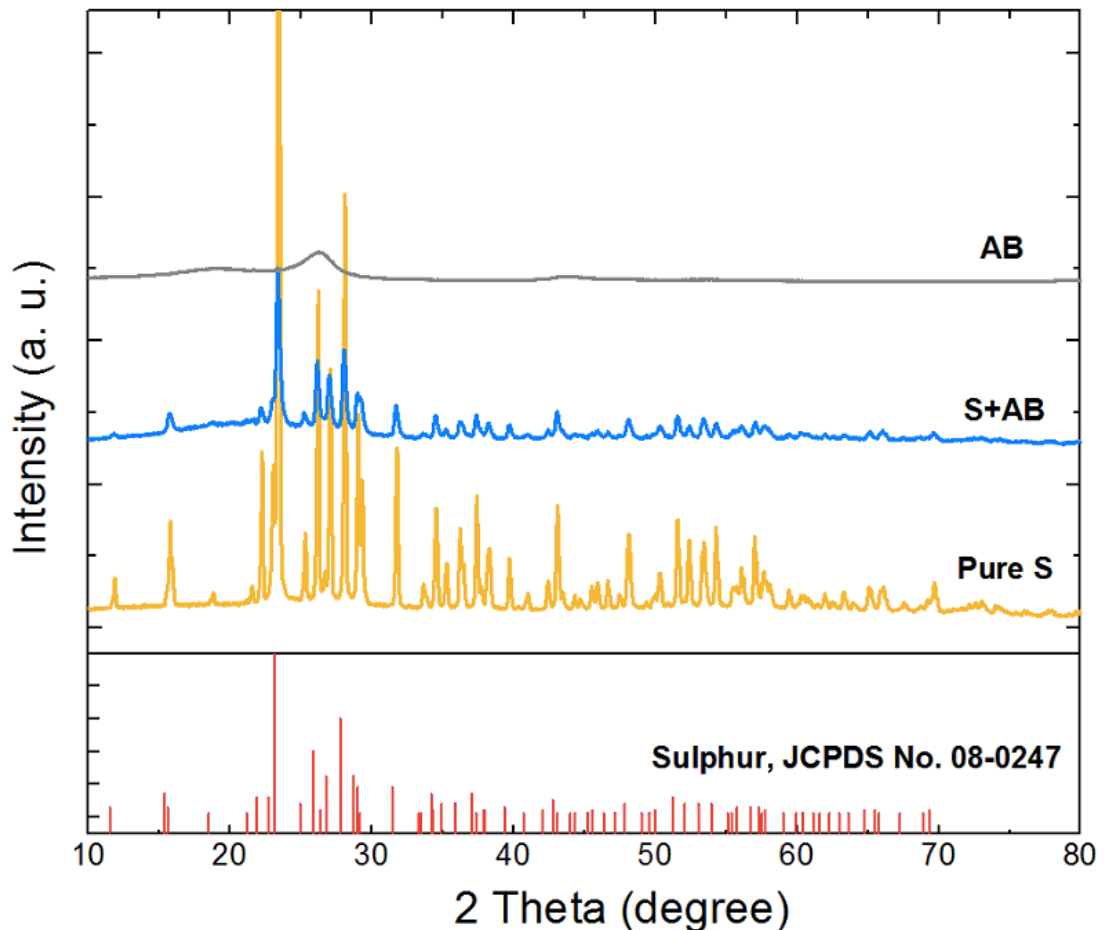


Figure 3-2. XRD patterns of pure AB, S+AB powder after heating, and pure sulphur.

The XRD patterns of pure AB show a broad peak around 26°, indicating an amorphous structure, in agreement with the literature. [43] All the diffraction peaks of the synthesised sulphur cathode are in good agreement with the XRD standard patterns of the orthorhombic phase of sulphur (JCPDS #08-0247), except a broad peak around 26°, arising from the addition of AB. [44] It should be noticed that diffraction peaks of the synthesised cathode are distinctly lower than that of the pure sulphur, which is

ascribed to the decreased crystallinity of sulphur or the even dispersion of S within the composites through the melt-diffusion process. Additionally, none of the new peaks was found in the synthesised sulphur composite, indicating that no additional phase was formed during the fabrication of the sulphur composite cathode material.

3.4 Electrochemical measurements

In this section, the electrochemistry characterisations of the as-prepared electrodes using variety of electrolyte systems were performed in-house using a VMP-3 potentiostat. All cells were assembled using conventional CR2016 coin cells with a help of a coin cell crimper. The detailed cell configuration can be found in **Section 2.1.4**.

Reference electrolyte - LiTFSI/DOLDME/LiNO₃

The first system to investigate electrochemically is the S+AB+PVP cathode in the LiTFSI/DOL:DME/LiNO₃ electrolyte, as this battery is used as a reference in our study to confirm that reported results are in agreement with previous publications. [45][46] **Figure 3-3a-c** represents the cyclic voltammetric (CV) curves of the reference cell recorded at a scanning rate of 0.10 mV s⁻¹ between 1.3 – 2.8 V. The first cycle shows the first cathodic peak at 2.10 V corresponding to the formation of long-chain polysulphides (Li₂S₈) from elemental sulphur (S₈). A dominant broad cathodic peak is exhibited at 1.47 V accompanied by a shoulder at 1.7V, corresponding to the irreversible reduction of LiNO₃. This is a typical behaviour of the LiNO₃ contained cell when the cathodic peak is scanned at a lower current of 1.3 V. [24][47] This peak is not observed in the absence of LiNO₃ as shown in **Figure 3-5a** (LiTFSI/DOL:DME). The size of this peak greatly diminished in the second cycle as indicated by curve 2 in **Figure 3-3a**, suggesting that the major reduction of LiNO₃ occurs mostly in the first cycle. This observation is an indication that the SEI-layer formation associated with LiNO₃ is particularly important in the 1st cycle, suggesting that any SEI-layer formed is stable and protecting the anode in the following cycles. One anodic peak located at 2.48 V in **Figure 3-3b** represents the re-oxidation of polysulphides to elemental sulphur.

In the following cycling, there are two cathodic peaks observed at 2.33 V and 2.05 V (**Figure 3-3c**), corresponding to the reduction of S₈ to long/medium-chain polysulphide and long/medium-chain polysulphide to short-chain polysulphide, respectively. From

the 3rd cycle onwards, these two cathodic peaks become clearer with the increasing numbers of cycles. This could be attributed to the distribution of polysulphides within the cell, which could explain the increasing discharge capacity between cycles 3 to 10 in the discharge capacity plotted in **Figure 3-4b**.

Additionally, CV curves of another reference cell are obtained with higher cut-off voltage (1.8 – 2.8 V) to avoid the LiNO_3 reduction peak (**Figure 3-3d**). Positions of the two cathodic peaks and one anodic peak resemble those observed in **Figure 3-3**, indicating that cut-off voltage alteration does not influence the redox potential, which was expected.

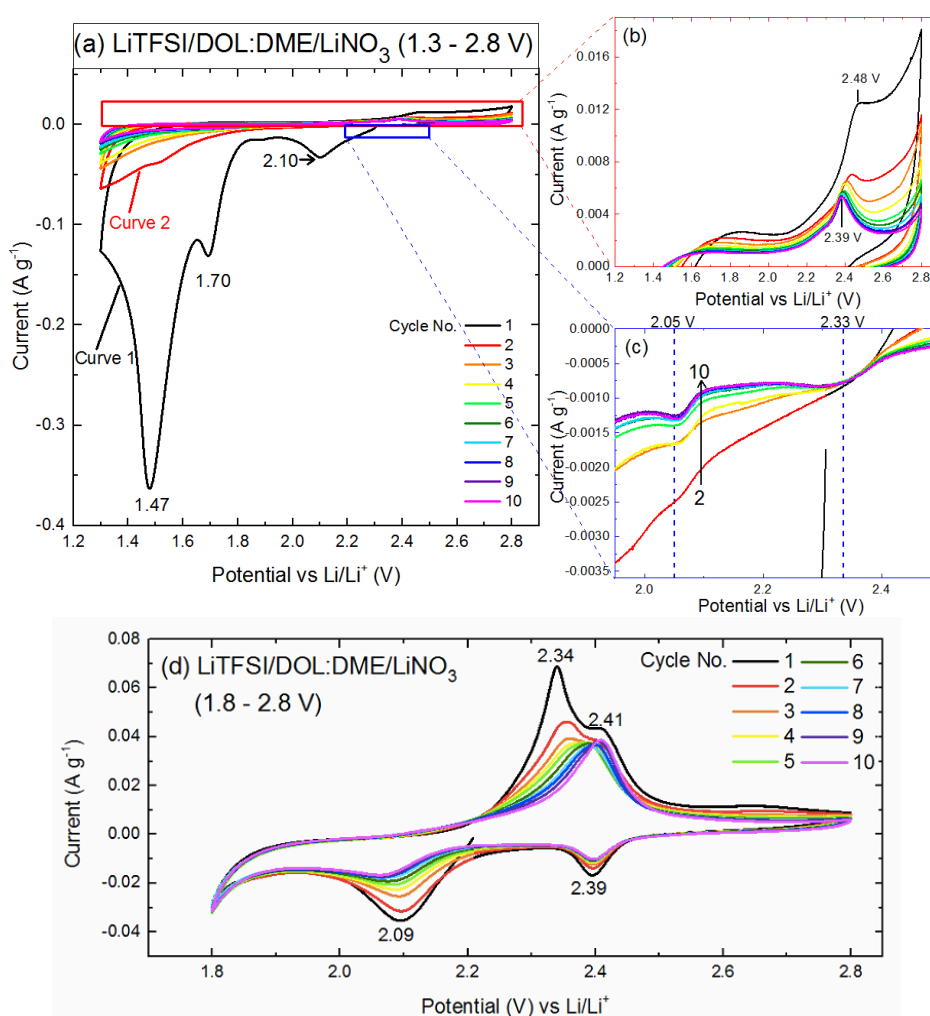


Figure 3-3. (a) CV profiles of the S+AB+PVP cathode cycled in $\text{LiTFSI/DOL:DME/LiNO}_3$ electrolyte, recorded by scanning rate of 0.1 mV s^{-1} between 1.3 – 2.8 V, (b) an expanded view of the cathodic peaks in the potential range between 1.95 V and 2.50 V, (c) an expanded view of the anodic peaks, and (d) CV profiles of another cell recorded at the same scanning rate between potential window of 1.8 – 2.8 V.

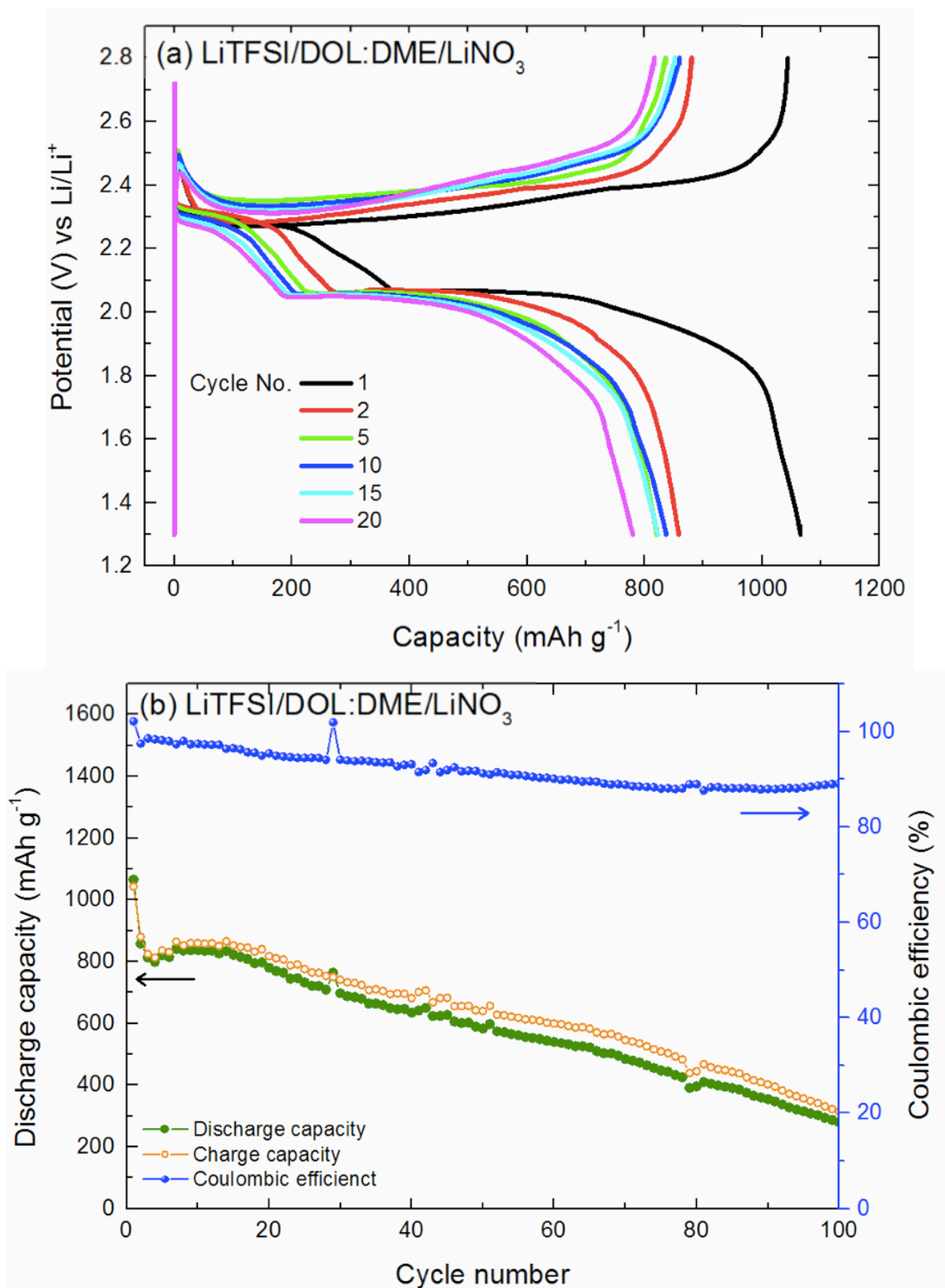


Figure 3-4. Electrochemical analysis of S+AB+PVP cathode in LiTFSI/DOL:DME/LiNO₃ electrolyte cycled at a rate of 0.1 C. (a) Galvanostatic discharge and charge curves, and (b) Cycling performance and Coulombic efficiency.

The reference electrolyte cell demonstrated an initial discharge capacity of 1065 mAh g⁻¹ with two expected voltage plateaus at 2.30 V and 2.04 V (**Figure 3-4a**). This observation is consistent with the CV results reported earlier. In LiTFSI/DOL:DME/LiNO₃ electrolyte, it was observed that the discharge capacity increases slightly with the increasing number of cycles up to 15 cycle where it reaches a maximum, and decreases gradually afterwards (**Figure 3-4b**). This behaviour is not observed in any other electrolytes (**Figure 3-6e, f**). This might be closely related to the distribution behaviour of polysulphide in the cell, which agrees with the CV results where two peaks at 2.33 V and 2.05 V are becoming more obvious after few scans (**Figure 3-3c**). [48] We postulated that this behaviour is observed because at the beginning of the cell operation, only small amount of active sulphur is involved in the reaction and utilisation of sulphur increases with increasing cycling number when more polysulphide species are dissolved into the electrolyte. Therefore, the full capacity is not achieved at the beginning of the battery operation until 15 cycles. After 30 cycles, a reversible capacity of 700 mAh g⁻¹ is achieved (65% capacity retention). This cell had an excellent CE value of average 92 % (inset of **Figure 3-4b**) over 100 cycles. This cell was further investigated using *in operando* XAS characterisation techniques in **Section 3.6.3.1**.

3.4.1 Electrochemical performances of S+AB+PVP electrode in various electrolyte systems

A number of studies have shown that the choice of electrolyte composition may change the reaction mechanism of the Li-S batteries and, thus, change the potentials of a plateau values by 10 - 100 mV. [49] As part of the study, as-prepared sulphur electrodes were assembled in cells using different electrolyte systems to evaluate the electrochemical properties.

First, the reduction/oxidation of the sulphur electrodes in different electrolyte compositions were investigated using CV measurement at a scan rate of 0.1 mV s⁻¹ and results are shown in **Figure 3-5**.

3.4.1.1 CV curves

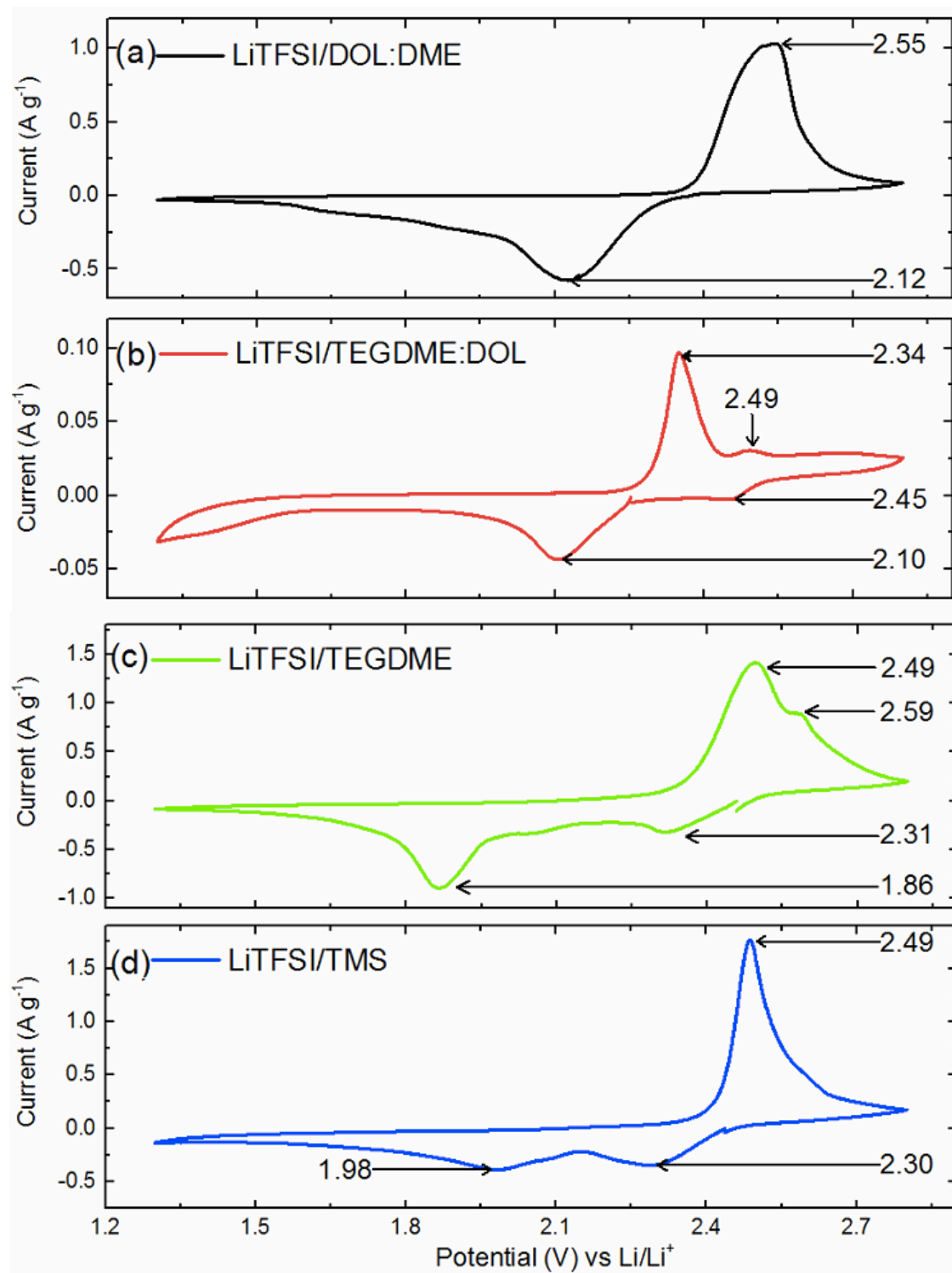


Figure 3-5. CV curves of sulphur electrode of 1 M LiTFSI in different solvents recorded at a scan rate of 0.1 mV s^{-1} ; (a) DOL:DME, (b) TEGDME:DOL, (c) TEGDME, and (d) TMS.

The cathodic scan of the LiTFSI/DOL:DME cell is dominated by a broad peak centred at 2.12 V with a broad shoulder at around 1.9 V (**Figure 3-5a**), indicating that two reductive peaks of S₈ to long-chain polysulphides and subsequent formation of short chain polysulphides overlap with each other. Following the anodic curve shows a broad peak at 2.55 V, assigned to a reversible conversion of polysulphide to S₈. The overlapped single broad cathodic and anodic peaks are most likely caused by the high polarisation between long-chain, short-chain, and insoluble polysulphides. [50]

For the LiTFSI/TEGDME:DOL cell (**Figure 3-5b**), the absolute magnitude of the current is much lower than that of the other electrolytes by a factor of 10, suggesting that this electrolyte cannot contribute to the capacity due to low utilisation of active sulphur. This agrees with the discharge/charge data, as the LiTFSI/TEGDME:DOL cell could only reach ~ 400 mAh g⁻¹ in the initial discharge (**Figure 3-6a**).

Similar peak trends were observed in the LiTFSI/TEGDME cell (**Figure 3-5c**) but with higher currents of the first cathodic peak centred at 2.31 V, followed by the second peak at 1.86 V. It is noticeable that those peaks were shifted to lower potential than the TEGDME:DOL cell, indicating a higher polarisation. Also, a shift in the anodic peaks is recognised. The cathodic peaks of the LiTFSI/TMS cell (**Figure 3-5d**) is similar to what was observed in the LiTFSI/TEGDME:DOL cell. Both exhibited a sharp anodic peak around 2.4 V attributing to stable charging reaction.

Overall, the CV scans of S+AB+PVP electrode in four different electrolyte solvents displayed different positions of the potentials and intensities of currents, indicating that that the solvents influence the reduction/oxidation behaviour of the sulphur cathode.

3.4.1.2 Discharge/charge curves

All electrolyte compositions listed in **Table 3-2** were then tested by the galvanostatic discharge/charge cycling (**Figure 3-6**).

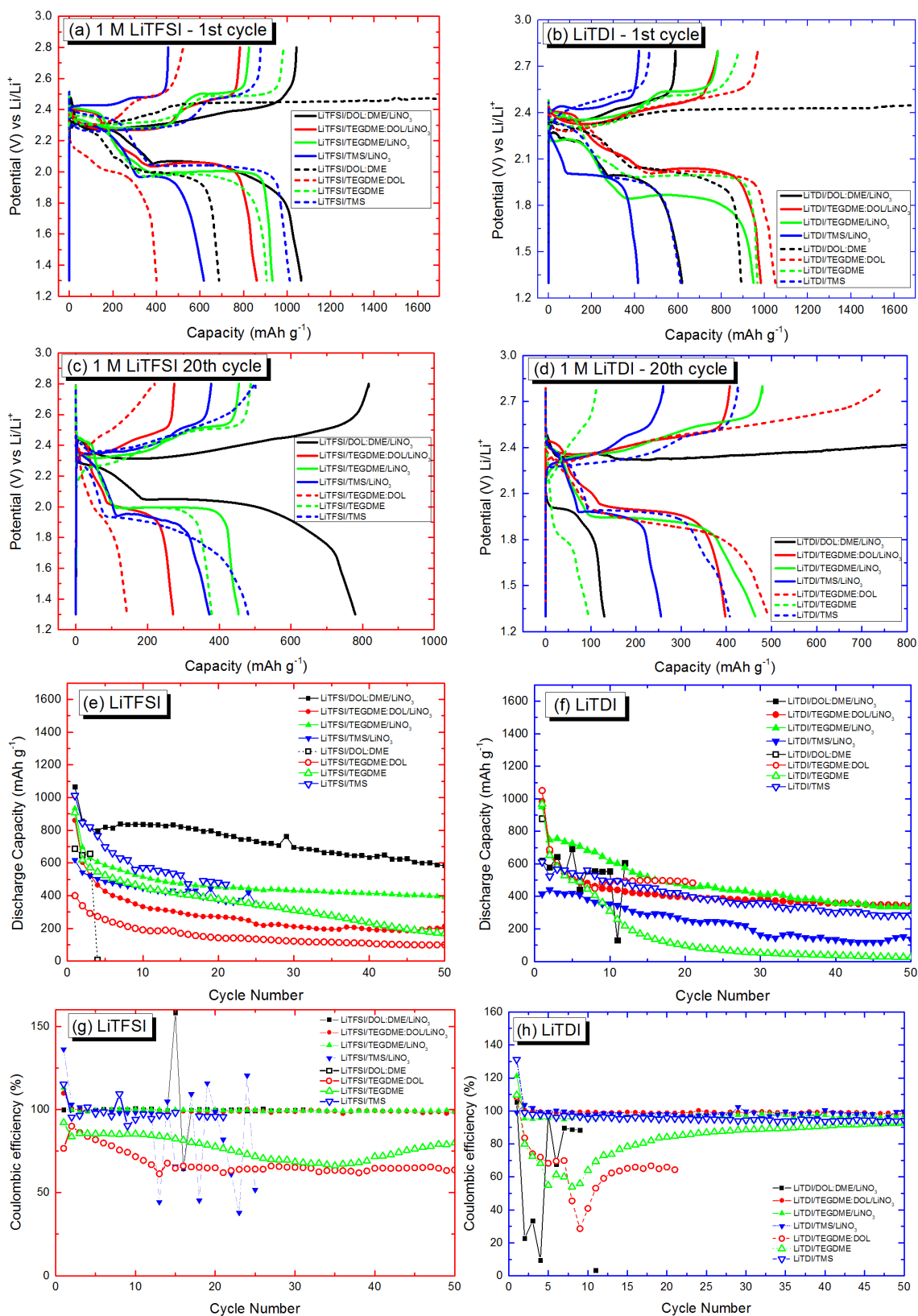


Figure 3-6. Electrochemical performances of S+AB+PVP electrode in various electrolyte systems with LiTFSI and LiTDI salt, and with/without LiNO₃. (a) (b) The first discharge/charge curves, (c) (d) the 20th cycle, (e) (f) Cycling performances, and (g) (h) show the coulombic efficiencies.

Overall, the discharge curves of the most of cell have two voltage plateaus, indicating that the reaction mechanisms of sulphur in these electrolytes follow the traditional two-step conversion process.

TEGDME:DOL

The LiTFSI/TEGDME:DOL electrolyte (dashed red line in **Figure 3-6a**) was an exception, the high voltage plateau is almost diminished in the initial discharge, resulting in very low discharge capacity of 400 mAh g^{-1} , which is less than a quarter of the theoretical capacity. This agrees with the CV plots represented in **Figure 3-5b**, which exhibited extremely low current. There are two possible explanation to this behaviour described as follows. Firstly, the disappearance in the high voltage plateau may be explained by the high rate of self-discharge phenomenon. Secondly, this behaviour may be caused by the extremely low sulphur utilisation, which is more possible, because the high voltage plateau is still very small in the 20th cycle (**Figure 3-6c**), suggesting that the amount of active sulphur engaged in the reaction is little. The introduction of the LiNO_3 salt to this electrolyte, (LiTFSI/TEGDME:DOL/ LiNO_3 , solid red line in **Figure 3-6a**) showed an improvement in the extension of the high voltage plateau, but experienced very quick capacity decay (**Figure 3-6e**, red filled circle). Among all LiTFSI salt containing electrolytes, the binary solvent mixture of TEGDME and DOL was the worst behaving solvent showing the lowest capacity contribution independently of the presence of the LiNO_3 salt (**Figure 3-6e**, filled and open red circles).

Instead, with the LiTDI salt, the TEGDME:DOL solvent maintained the voltage output and achieved high initial discharge capacity of 1050 and 980 mAh g^{-1} using LiTDI/TEGDME:DOL and LiTDI/TEGDME:DOL/ LiNO_3 electrolytes, respectively (red lines in **Figure 3-6b**, respectively). Particularly, the LiTDI/TEGDME:DOL/ LiNO_3 cell showed very good cycling stability, with a decay rate of 1.1 % per cycle between the 5th and 50th cycles while retaining the high CE values nearing 100 % (**Figure 3-6f, h**, filled red circles).

TMS

On the contrary, TMS electrolyte exhibited short voltage plateaus in the initial discharge in the presence of the LiNO_3 , when combined with the LiTDI salt. LiTDI/TMS (dashed blue line in **Figure 3-6b**) and LiTDI/TMS/ LiNO_3 (solid blue line in **Figure 3-6b**) both exhibited initial discharge capacities of 611 and 414 mAh g^{-1} , respectively, which are relatively lower compared to other LiTDI-based electrolytes. Whereas the LiTFSI salt in TMS solvent, (LiTFSI/TMS, dashed blue line in **Figure 3-6a**), exhibited a high initial capacity of 1012 mAh g^{-1} , which is almost similar to that of the reference electrolyte (solid black line in **Figure 3-6a**). For LiTFSI/TMS/ LiNO_3 cell, a relatively high discharge capacity is delivered up to 20 cycles (**Figure 3-6e**, filled blue triangles), but the charging capacity fluctuated between each cycle after cycle number 10, leading to low CE values and eventually the cell was terminated by the endless polysulphide shuttle.

TEGDME

LiTFSI/TEGDME/ LiNO_3 (solid green line in **Figure 3-6a**) observed very clear plateaus in the initial discharge and achieved an excellent capacity retention with a decay rate of 1.0 % per cycle between the 5th and 50th cycles while retaining an excellent CE values nearing 100 % (green filled triangle in **Figure 3-6g**), indicating that the shuttle reaction is largely minimised in this systems. Moreover, after 20 cycles, both the LiTFSI/TEGDME/ LiNO_3 (solid green line in **Figure 3-6c**) and the LiTFSI/TEGDME (dashed green line) cells maintained their voltage output at the same level with their first discharge, suggesting that the polarisation is very little in this system.

In contrast, large voltage polarisation was observed in LiTDI/TEGDME/ LiNO_3 electrolyte in the initial discharge (solid green line in **Figure 3-6b**), indicating the low ionic conductivity and elevated internal resistance of this cell. However, this was only seen in the initial cycle, and voltage plateaus were elevated to about 2.4 V and 2.0 V at the 20 th cycle (**Figure 3-6d**). The cycling performance of this cell is the best among all LiTDI salt-based electrolytes, (**Figure 3-6f**) showing a small capacity decay rate of 1.7 % per cycle between the 5th and 50th cycles. However, this electrolyte is impractical without the support of LiNO_3 salt, experiencing very fast capacity decay falling to less

than 100 mAh g⁻¹ capacity within 20 cycles for LiTDI/TEGDME electrolyte (dashed green line in **Figure 3-6d**).

DOL:DME

The binary solvent mixture of DOL and DME used with LiTFSI salt showed very poor cycling performance in the absence of the LiNO₃ salt. The initial discharge capacity of the LiTFSI/DOL:DME cell is 690 mAh g⁻¹ (dashed black line, **Figure 3-6a**) which is only 41 % of the theoretical capacity value (1673 mAh g⁻¹). In the following charging process, charge ending is drastically delayed and an extremely low CE of 21.5 % is found (**Figure 3-7a**). The strong overcharge can be explained by the reaction of dissolved polysulphide at the negative electrode, encouraging the shuttle mechanism. The fluctuating charging process eventually lead to a premature failure of the cycling process at the cut-off voltage (**Figure 3-7a**). This is associated with lithium dendrite growth inducing internal short circuiting, owing to the inability of this electrolyte to function without the LiNO₃ salt protecting the Li anode. The DOL:DME solvent is not usable with LiTDI salt, exhibiting a similar observation to the LiTFSI/DOL:DME cell (**Figure 3-7b,c**). These observations suggest that the binary solvent of DOL:DME is not as variable as other solvents and only able to work with the LiTFSI salt in the presence of LiNO₃ salt.

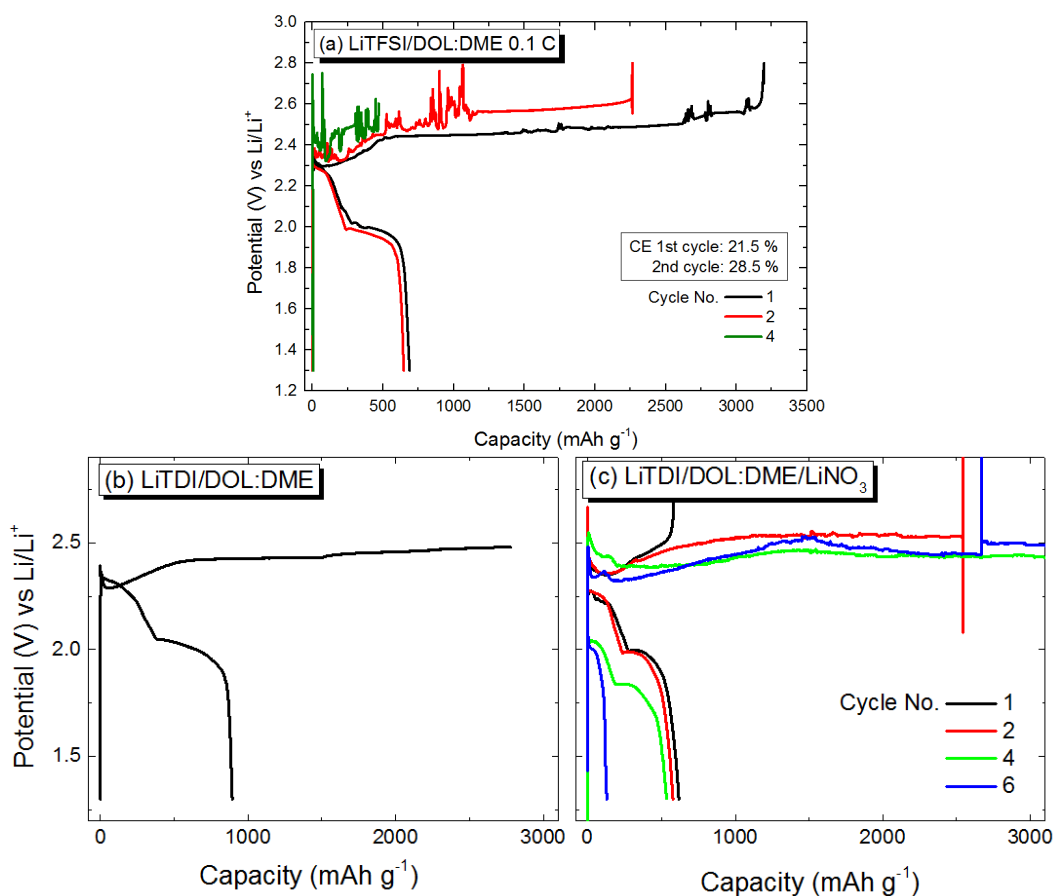


Figure 3-7. Discharge/charge curves for S+AB+PVP electrode cycled at a C-rate of 0.1 C in (a) LiTFSI/DOL:DME, (b) LiTDI/DOL:DME, and (c) LiTDI/DOL:DME/LiNO₃ electrolytes.

Concentrated electrolyte; 7M LiTFSI/DOL:DME

Additionally, a concentrated electrolyte, 7M LiTFSI in DOL:DME (1:1 volume ratio), close to the saturation limit is tested using the same sulphur electrode material. **Figure 3-8** shows the galvanostatic discharge/charge curves for the first 8 cycles of this cell cycled at a rate of 0.1 C with the inset showing the CV curves scanned at a rate of 0.1 mV s⁻¹.

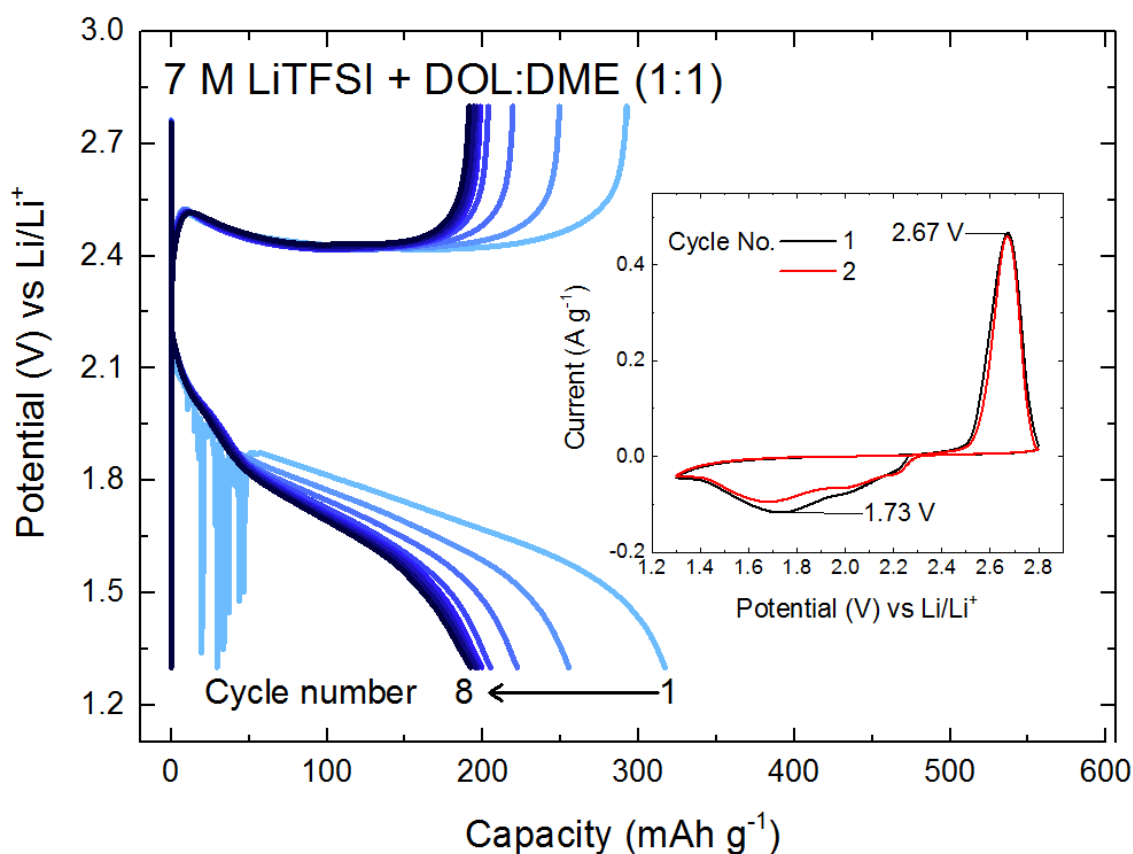


Figure 3-8. Discharge/charge curves from 1st to 6th cycle of S+AB+PVP electrode using 7M LiTFSI/DOL:DME electrolyte cycled at a rate of 0.1 C between 1.3 – 2.8 V. Inset shows the CV response of this cell scanned at a rate of 0.1 mV s⁻¹.

This cell showed an unusual voltage profile. No apparent plateau was observed in the discharge curves. Instead, they consist of a slope-shaped curve and very low initial discharge of 320 mAh g⁻¹ was found (**Figure 3-8**). This may be indicating that the reaction mechanism in this electrolyte does not follow the two-step conversion process and is highly related to the decreased ionic conductivity due to increased concentration of salt. [51] The CV curve of this cell exhibits a very broad cathodic peak with the lowest current at 1.73 V, indicating a high polarisation of the cell (inset of **Figure 3-8**). This may suggest that the thermodynamic stabilisation of the soluble polysulphide is altered in the high concentration of lithium salt in the electrolyte. [52] Overcharge phenomenon is not observed in this cell, suggesting that the polysulphide shuttle reaction is inhibited. In this ultra-high concentration of salt, long-chain polysulphide intermediates (Li₂S_x) are poorly soluble due to the saturation of lithium

salt in the electrolyte. Therefore, polysulphide species are not diffused out of the cathode, strongly preventing the redox shuttle. However, because the polysulphides are not dissolved in the electrolyte, sulphur utilisation was very low, resulting in poor discharge capacity. Similar results were observed in other reports. [51][53]

3.4.2 Summary of electrochemical observations

1. Effects of the solvents

Overall, for the LiTFSI salt, the reference LiTFSI/DOL:DME/LiNO₃ electrolyte demonstrated the best cell performance as shown in **Figure 3-6e,f**, representing the highest capacity retention over the 50 cycles. However, this solvent system (DOL:DME, 1:1 by volume) can only access the standard electrochemical performance when used with 1 M LiTFSI salt in the presence of 0.25 M LiNO₃ salt. Modification of the salts introduces severe shuttle effect as highlighted in **Figure 3-7**. Therefore, DOL:DME is not as flexible as other solvents and we cannot expect for further improvement of this solvent system. On the contrary, the single solvent of TEGDME was capable to work with both LiTFSI and LiTDI salts in the presence of LiNO₃, which shows the flexibility of this solvent system.

2. Effects of the LiNO₃ salt

Most of the systems exhibited better capacity retention and higher CE values in the presence of the LiNO₃ salt, except for the TMS solvent, which showed a better cell performance in the absence of LiNO₃, independently on the choice of LiTDI or LiTFSI. This result highlighted the capability of the TMS solvent in the absence of LiNO₃ salt.

3. Effects of the LiTFSI and LiTDI salts

Over the prolonged cycling, LiTFSI-based system pronounced heavier voltage depression (**Figure 3-6c**) compared to those with the LiTDI salt (**Figure 3-6d**). This indicates that the internal resistance is mitigated when using the LiTDI salt. This capacity decay mechanism, due to voltage depression, should be distinguished from other cases, where the capacity loss occurs simply from shortening of voltage plateaus, while the plateau potentials are still maintained. [54]

Overall, the reference electrolyte system exhibited the best cell performance among all the electrolyte components tested here. However, there is no room for further modification and improvements can be expected for this system. In contrast, the single solvent system, such as, TEGDME and TMS, proved the potential capability to work with variety of Li salt choices. These electrolytes are, therefore, worth investigating further to gain a clear understanding of their effects towards the sulphur reaction mechanisms.

3.5 Visual examinations of the transparent cells

The electrolyte composition influences the solubility and mobility of polysulphide, which subsequently affects the Li-S cell performance. [29][30] A direct visual observations allow us to identify the different chains of polysulphides exist in the electrolyte, which are known to promote different colour. Herein, we assess the polysulphide dissolution behaviour of two cells using optically transparent glass cells, which gave a good identification of the polysulphide dissolution behaviour. First, we started by comparing the electrolyte colour change upon contact with the sulphur electrode. **Figure 3-9** shows the two different electrolytes systems (LiTFSI/DOL:DME/LiNO₃ and LiTFSI/TEGDME:DOL/LiNO₃) immediately after the cell assembly.

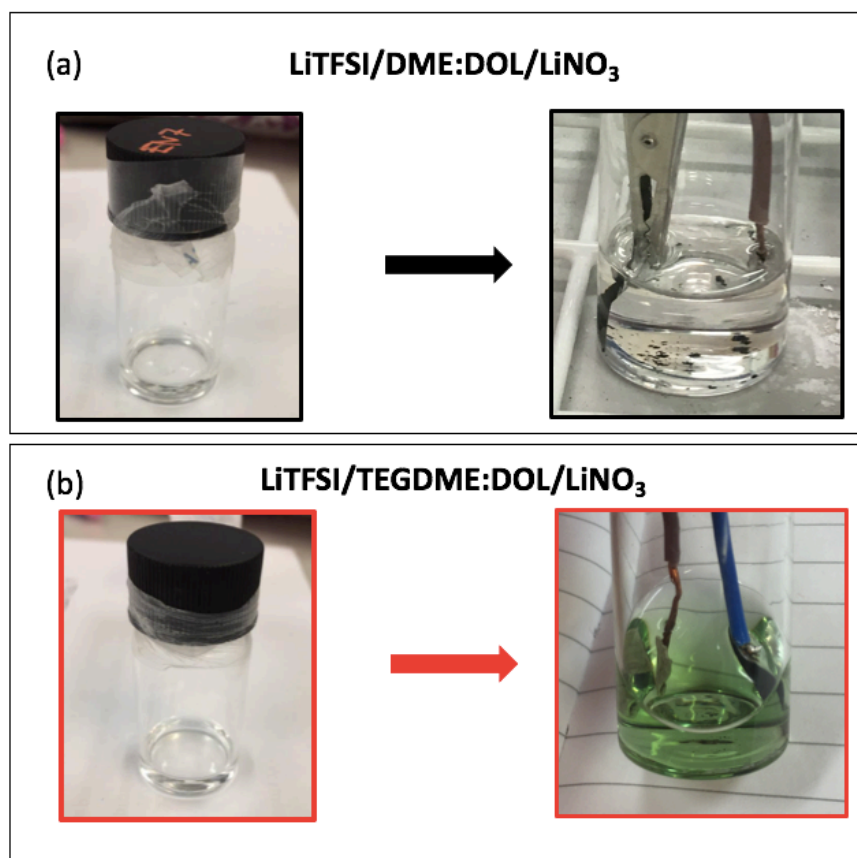


Figure 3-9. The appearance of transparent cells immediately after the cell assembly. (a) LiTFSI/DOL:DME/LiNO₃ and (b) LiTFSI/TEGDME:DOL/LiNO₃

LiTFSI/DOL:DME/LiNO₃ does not exhibit any colour change at the point of the cell assembly (**Figure 3-9a**). On the contrary, the LiTFSI/TEGDME:DOL/LiNO₃ electrolyte in **Figure 3-9b** exhibited an immediate colour change to green upon contact with the electrode.

The Nazar group reported that the different donor number of the solvents give rise to different colouration in contact with polysulphide species. [2] Ultraviolet-visible (UV-VIS) spectroscopy study of Barchasz *et al.* demonstrated that the coexistence of free radicals and dianions in equilibrium in TEGDME solution introduces green colouration of the solvent. [2][55][56] Therefore, immediate colourisation observed in the LiTFSI/TEGDME:DOL/LiNO₃ suggests that the active sulphur is dissolved into the electrolyte, leading to self-discharge phenomenon soon after the cell assembly. Also, this may be a sign of possible presence of radical species. This could explain why

LiTFSI/TEGDME:DOL and LiTFSI/TEGDME:DOL/LiNO₃ exhibited very poor cycle performance in **Figure 3-6e** (red circles). We further investigated the colour change of these electrolytes at different depths of discharge.

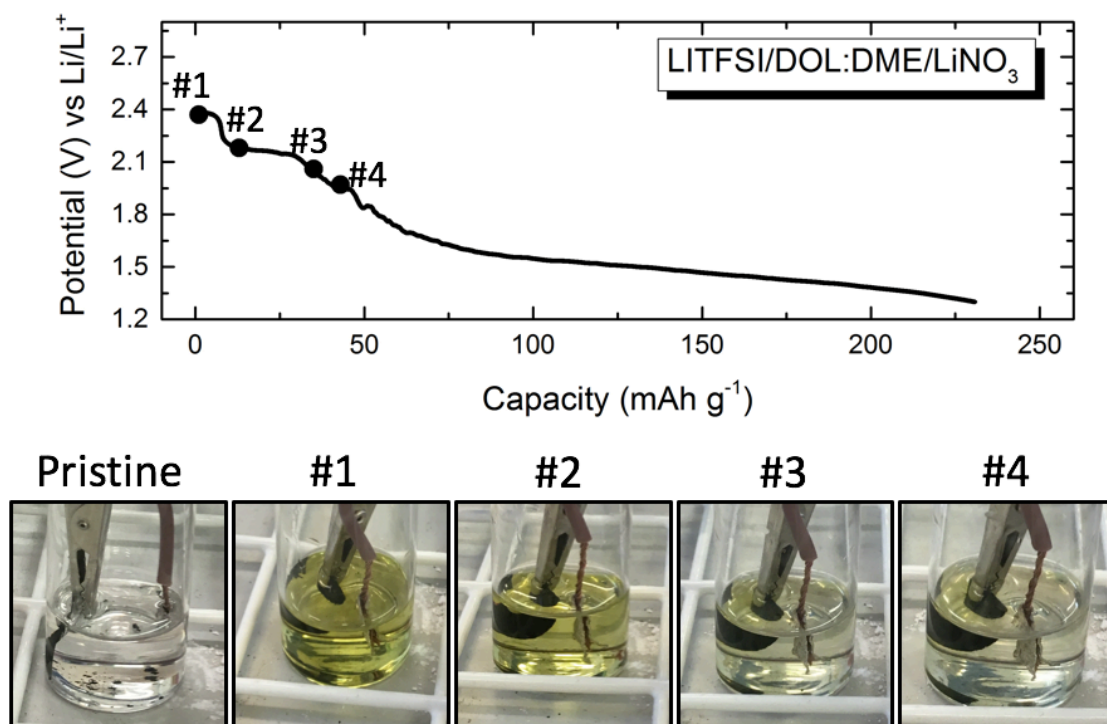


Figure 3-10. Visual examination of the LiTFSI/DOL:DME/LiNO₃ cell.

LiTFSI/DOL:DME/LiNO₃ changes from colourless to yellow in the beginning of the discharge. It is widely accepted that dissolution of polysulphides in the electrolyte result in yellow to brown colour, therefore, this indicates the polysulphide formation and dissolution in the electrolyte (#1 in **Figure 3-10**). At the end of the low voltage plateau, (#3 in **Figure 3-10**) yellow colour is slightly diminished and the solution is returning to colourless, suggesting that the concentration of polysulphide is decreased and converted into insoluble Li₂S. Li₂S deposition can only happen on the carbon surface. Due to the insulating nature of Li₂S and lithium polysulphide, these intermediates require conductive support for reduction. Therefore, if any Li₂S is formed during the discharge process, it would be on the surface of the carbon material, rather than seen as crystals in the solution. This reflects the disappearance of the yellow colour in the #3 and #4 in **Figure 3-10**.

The colour change of the LiTFSI/TEGDME:DOL/LiNO₃ electrolyte upon discharge reaction is represented in **Figure 3-11**.

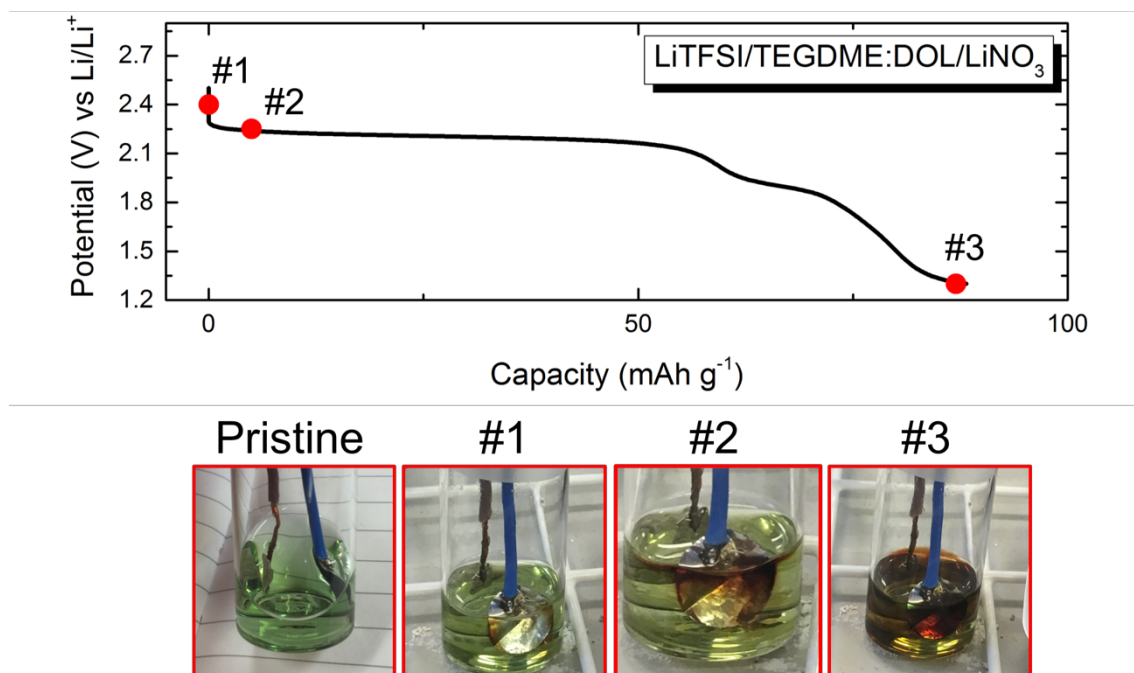


Figure 3-11. Visual examination of the LiTFSI/TEGDME:DOL/LiNO₃ cell.

The LiTFSI/TEGDME:DOL/LiNO₃ electrolyte turned dark reddish-brown colour with increasing depth of discharge. Again, this is considered as the dissolution of polysulphides in the electrolyte. [57] The electrolyte colour is observed much darker than that in the LiTFSI/DOL:DME/LiNO₃ cell, suggesting that the dissolution of polysulphide is more severe in this electrolyte. Also, the colour does not disappear at the end of discharge (#3 in **Figure 3-11**), indicating that the soluble polysulphides still exist in considerably high concentration. Additionally, this colourisation of the electrolyte can also be considered as the reduction of LiNO₃ to LiNO₂, where NO₂ is known to exist in reddish-brown colour, [58] which could be causing the oxidation of active sulphur material.

Summary of visual examinations

An *in situ* visual electrochemical study of different electrolytes demonstrated that dissolution rate of the S₈ in the electrolyte upon cell assembly is influenced by the electrolyte solvent. The LiTFSI/DOL:DME/LiNO₃ electrolyte is effective in inhibiting and recapturing polysulphide diffusion during the discharge process. When DME is replaced with TEGDME (LiTFSI/TEGDME:DOL/LiNO₃), the cell shows an immediate dissolution of sulphur into the electrolyte and diffusion of polysulphides into the electrolyte was more severe.

TEGDME has stronger solubility power of polysulphides in the electrolyte solvent. This may be explained by the difference in DN, of which TEGDME is 20 whereas that of DME is 17 (**Table 3-1**). Also, this result suggested potential reduction of LiNO₃ in the cell when TEGDME:DOL solvent is used.

3.6 *Operando* sulphur K-edge XAS analysis

To better understand the influence of the electrolyte on the sulphur reaction mechanism, *operando* XANES measurements were performed at the sulphur K-edge during galvanostatic cycling for the selected electrolytes. The LiTFSI/DOL:DME/LiNO₃ cell was used as a reference system to compare with other systems, as this electrolyte is most widely used for Li-S batteries. [23] LiTFSI/DOL:DME and LiTDI/DOL:DME electrolytes were investigated to examine the failure mechanisms. Additionally, single-solvent electrolytes, TEGDME and TMS were examined with LiTDI salt in the absence of LiNO₃.

3.6.1 *Operando* cell

For XAS experiments, cathodes were prepared to transmit the X-ray with 2 mm hole in the Al current collector. The detailed configuration of the X-ray transparent cell can be found in **Figure 2-14** in **section 2.4.2**. All cells were assembled using a coin-cell crimper (MTI, USA) to ensure the perfect sealing, which prevents the evaporation of the electrolyte while maintaining enough pressure.

Operando XANES data collection

All XAS measurement represented in this chapter were collected at the beamline BM28 at the ESRF (Grenoble, France) using a double crystal Si (1,1,1) monochromator and a Keytek fluorescence detector. Measurements for reference compounds were carried out under vacuum, whereas all *operando* cells were measured under He atmosphere. XANES spectra were recorded over the energy range between 2450 and 2520eV, with a step size of 1.5 eV before the pre-edge (2450 – 2465 eV), 0.16 eV in the pre-edge, main-edge, and electrolyte region (2465 - 2495 eV), and 1 eV in the EXAFS region between 2495 – 2520 eV, with a counting time of 3 s per point, resulting in a total acquisition time of 14-15 minutes per spectrum.

The electrolytes analysed in this study are summarised in **Table 3-3**.

Table 3-3. List of electrolyte compositions measured by *operando* XAS.

| Li salt | Solvent | Acronym | XANES | |
|--------------------------------------|---------|----------------------------------|-----------|-----------|
| | | | 1st cycle | 2nd cycle |
| 1 M LiTFSI, 0.25 M LiNO ₃ | DOL:DME | LiTFSI/DOL:DME/LiNO ₃ | ✓ | ✓ |
| 1 M LiTFSI | DOL:DME | LiTFSI/DOL:DME | ✓ | ✓ |
| 1 M LiTDI | DOL:DME | LiTDI/DOL:DME | ✓ | ✗ |
| 1 M LiTDI | TEGDME | LiTDI/TEGDME | ✓ | Discharge |
| 1 M LiTDI | TMS | LiTDI/TMS | ✓ | ✓ |

3.6.2 Validation of sulphur cathode and electrolytes.

To ensure that the impurities or oxidised form of sulphur species do not exist in the cathode composite (S+AB+PVP), the S K-edge XANES spectrum of the sulphur electrode was collected and compared to that of the S₈ reference compound (**Figure 3-12**). Because XAS is an element specific technique, it probes all sulphur species exist in the sample, therefore, extreme care is required that the spectra are only arising from the cathode composite.

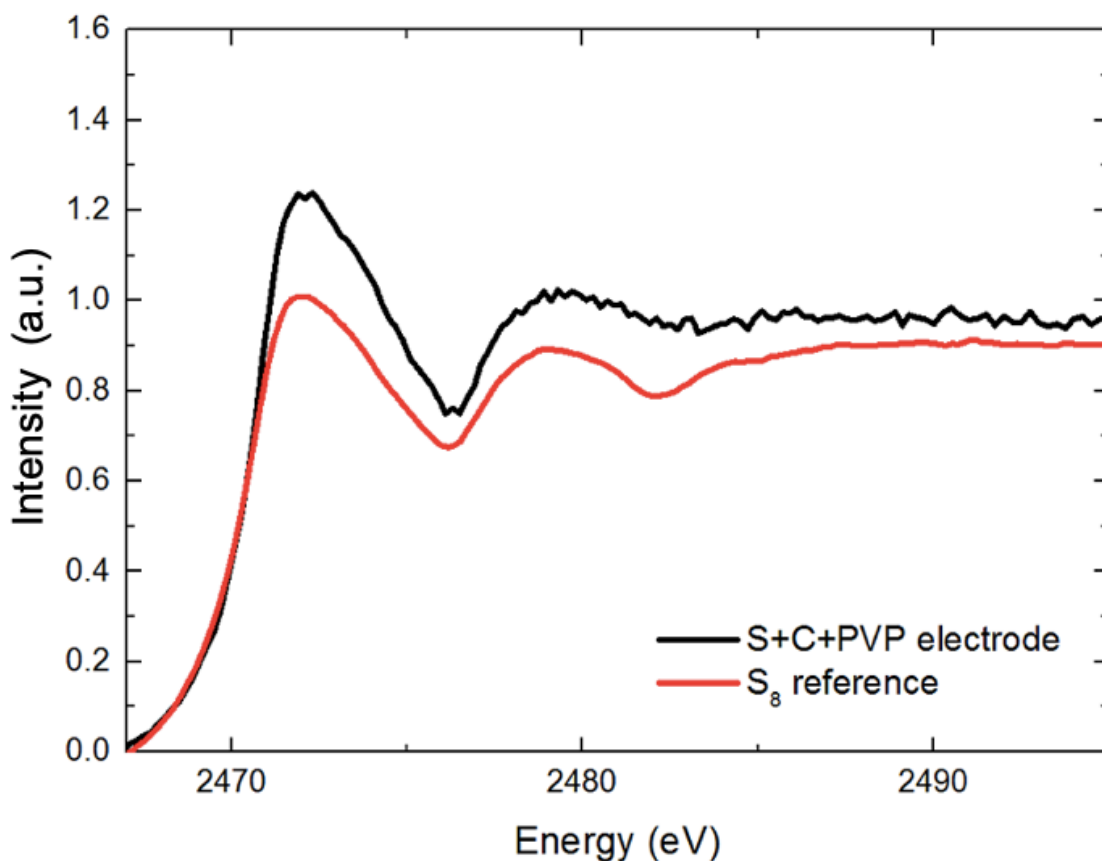


Figure 3-12. S K-edge XANES spectra of the sulphur electrode (S+AB+PVP) and S_8 reference compound.

The sulphur electrode was directly measured on the sample holder, without any window in front of it. In the sulphur electrode spectrum, only the signature of S_8 was seen, demonstrating that the sulphur particles in the electrode do not experience the change in their atomic environment.

3.6.2.1 Sulphur-containing electrolytes

Sulphur containing electrolytes, such as, LiTFSI and tetra methylene sulphone (TMS) can also contribute to the S K-edge XANES spectrum. It is important to distinguish between the electrochemically active sulphur species and other sulphur species originating from the electrolyte components. To determine the electrolyte sulphur peaks, we measured the pure electrolytes under exactly the same conditions as were measured using *operando* cells (using X-ray transparent cells with Mylar window) and those were compared with the cells at the pristine states collected immediately before

starting the discharge process. Here, it is worth remembering that no sulphur peak was detected in the Mylar film (**Figure 2-17** in **Section 2.5.2**).

1. LiTFSI/DOL:DME/LiNO₃ electrolyte

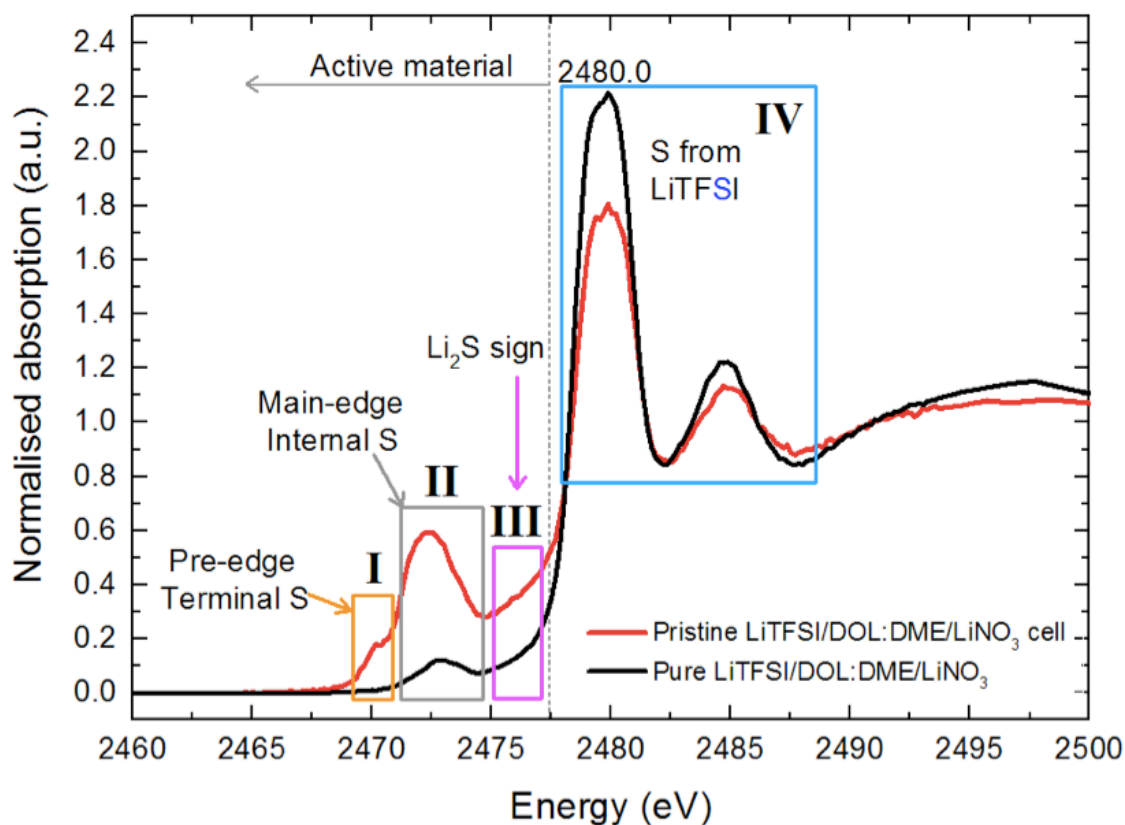


Figure 3-13. Normalised S K-edge XANES spectra of the LiTFSI/DOL:DME/LiNO₃ electrolyte and the LiTFSI/DOL:DME/LiNO₃ cell at the pristine state.

Hereby, we divide the S K-edge XANES spectra into the four regions, pre-edge, main-edge, Li₂S signal, and the electrolyte region marked as I, II, III, and IV, respectively in **Figure 3-13**. Pure LiTFSI/DOL:DME/LiNO₃ electrolyte exhibits a small peak in the sulphur main-edge and a dominant peak at 2480.0 eV arising from the sulphonyl functional group in Li salt (LiTFSI). In the pristine cell, the electrochemically active sulphur peak (main-edge) is observed at 2472 eV together with the small pre-edge resonance. These peaks are accompanied by the dominant electrolyte peak at 2480.0 eV.

2. LiTDI/TMS electrolyte

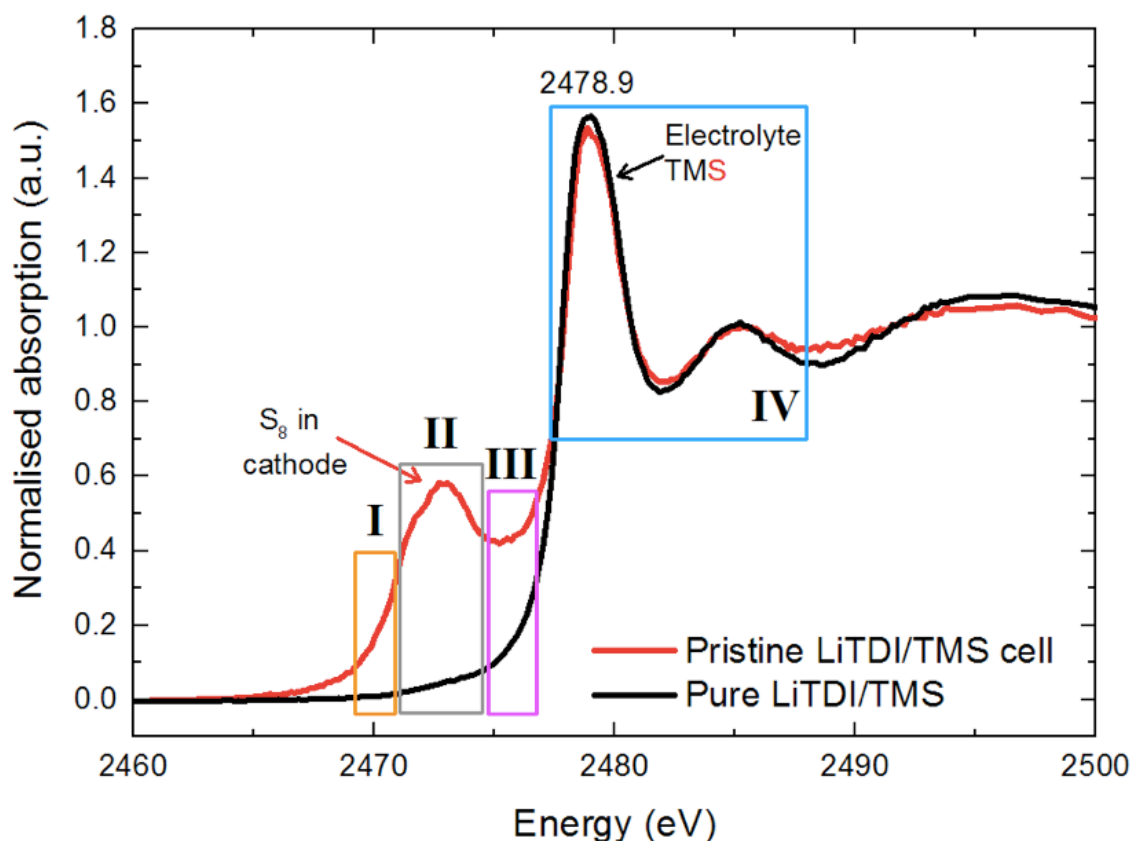


Figure 3-14. Normalised S K-edge XANES spectra of the pure LiTDI/TMS electrolyte and the LiTDI/TMS cell at the pristine state.

In the pure LiTDI/TMS electrolyte, again a dominant peak is observed at 2478.9 eV, attributed to the sulphone group in TMS solvent (**Figure 3-14**). The pristine state of the LiTDI/TMS cell exhibited the main-edge at 2472 eV arising from the electrochemically active sulphur in the electrode, and again, the dominant peak at 2478.9 assigned to the TMS solvent.

Although these two electrolytes exhibit the dominant peaks in the region IV of the S K-edge XANES spectra, they do not hinder the evaluation of polysulphide formation during electrochemical reaction because the pre- and the main-edges arising from the active sulphur species are well below the electrolyte peaks and easily distinguishable.

3.6.2.2 Sulphur-free electrolytes

We then measured the electrolytes free from sulphur species. For the pristine spectra of each sulphur-free electrolyte cell, we expected to see no oxidised sulphur peaks in the region IV.

1. LiTDI/DOL:DME electrolyte

Figure 3-15 shows the S K-edge XANES spectra of the pristine LiTDI/DOL:DME cell compared with Li_2S_4 reference compound to show that no oxidation of the sulphur was reported after assembly of the cell.

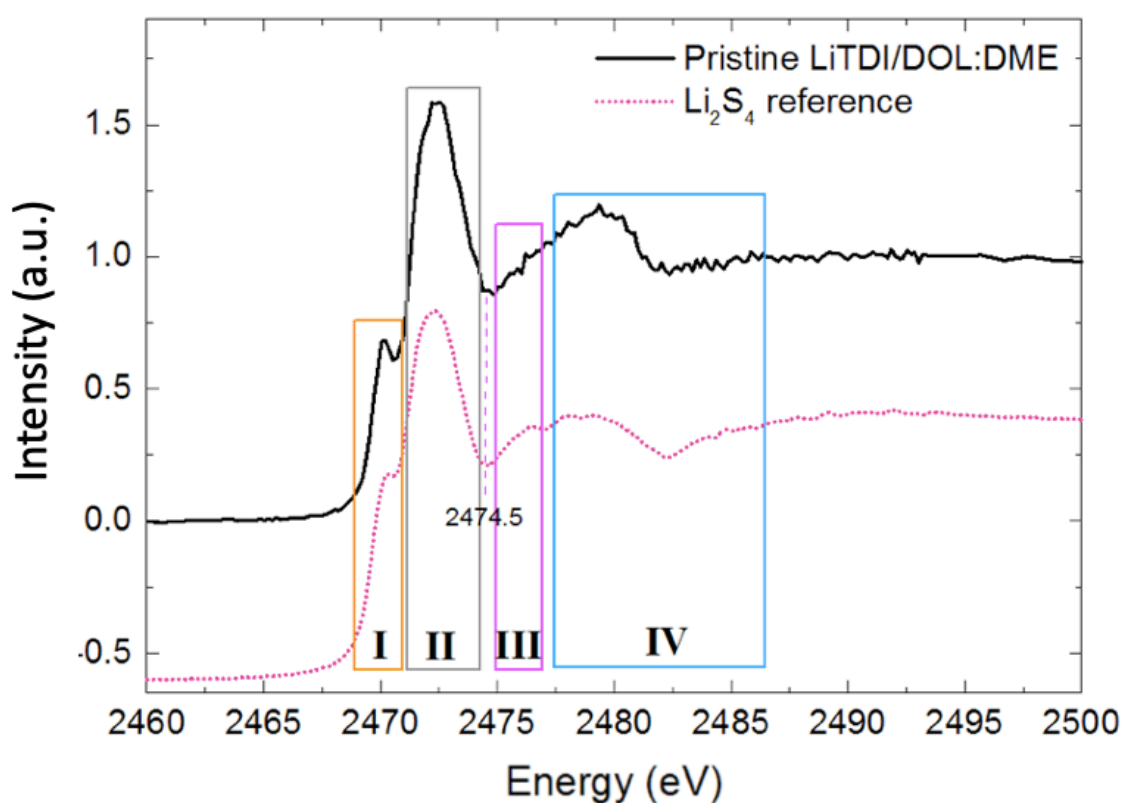


Figure 3-15. S K-edge XANES spectra of the LiTDI/DOL:DME cell at the pristine state compared to Li_2S_4 reference compound. The spectra are shown offset for clarity.

The XANES spectra collected at the pristine state of the LiTDI/DOL:DME cell is dominated by the polysulphides and the spectral features were very similar to those observed in the Li_2S_4 reference compound represented by the pink dotted line in **Figure 3-15**. Both spectra observed the distinct pre-edge feature at 2470.3 eV (region I), accompanied by the main-edge feature at 2472.3 eV (region II). After the main-

edge, a concave shape is recognised at 2474.5 eV followed by a single broad peak in region IV and no oxidised peaks is exhibited. This observation indicates that this cell is drastically influence by self-discharge phenomenon during the cell storage and sulphur species are already in the form of linear-chain polysulphides.

2. LiTDI/TEGDME electrolyte

The XANES spectrum of the LiTDI/TEGDME cell at the pristine state (**Figure 3-16**) exhibits a weak sign of the pre-edge and a dominant main-edge arising from the sulphur electrode at 2470.3 and 2472 eV, respectively. Additionally, two absorption peaks are exhibited at the higher energy region (IV) at 2478.0 and 2480.0 eV, hereby denoted as peak A and B, respectively, as shown in **Figure 3-16**. The LiTDI/TEGDME electrolyte does not contain any sulphur species. It is, therefore, unexpected to find these oxidised sulphur peaks. There are four possibilities to describe these oxidised sulphur peaks; (i) impurities introduced by the electrolyte, (ii) air-exposure damage of the cell, (iii) beam-induced damage, and (iv) chemical reaction between the Li, S, and O within the cell upon contact of the electrolyte and the electrode. These possibilities are investigated and presented in the below discussions.

(i) These peaks were first thought to be originated from the impurities in the electrolyte. To investigate this, the XANES spectrum was collected for pure LiTDI/TEGDME/LiNO₃ electrolyte and compared with the pristine spectrum of the LiTDI/TEGDME cell as displayed in **Figure 3-16**. The raw spectra were chosen in order to directly probe the relative amount of the sulphur species present in the two samples, rather than the normalised spectra which show the relative ratio of components. In the raw spectrum, the edge step at 2500 eV presents the 'total population of sulphur' (a value beyond the edge where all sulphur species are excited) that is contained in the sample. [59][60][61] As can be seen in **Figure 3-16**, pure LiTDI/TEGDME/LiNO₃ electrolyte does not contribute to the S K-edge XANES spectrum. This eliminates the possibility of the contamination of the cell.

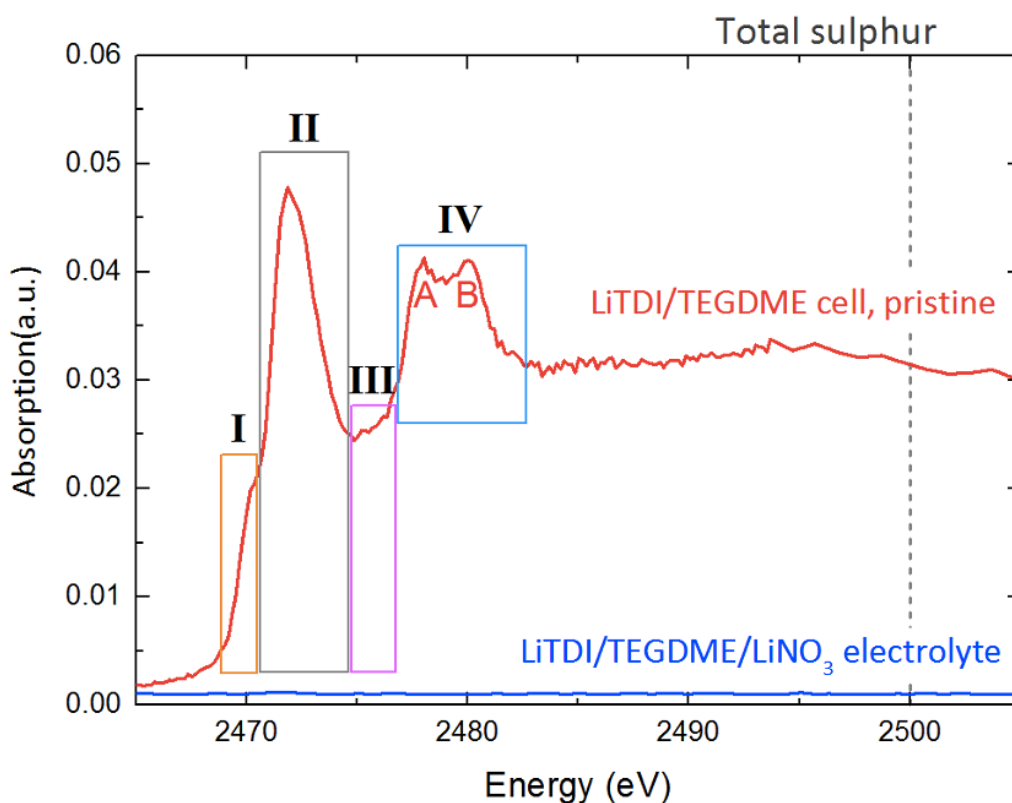


Figure 3-16. Raw XANES spectra of pure LiTDI/TEGDME/LiNO₃ electrolyte compared with the LiTDI/TEGDME cell at the pristine state, validating that the LiTDI/TEGDME/LiNO₃ electrolyte does not contain any sulphur species.

(ii) Other possibility is the oxidation of the electrode due to air exposure. The Mylar window used in this experiment is 3.4 μm thick, and damage can be caused anytime between the cell assembly and the *operando* measurement, leading to the oxidation of the cell, resulting in oxidation of the sulphur species. To evaluate this, the Mylar film on one of the fresh back-up cells with the same cell components was poked to expose the electrode to air to mimic the Mylar window damage situation and measured at the S K-edge. **Figure 3-17** compares the S K-edge spectra of the air-exposed cell, thiosulphate reference compound, and the LiTDI/TEGDME cell at the pristine state. As can be seen, the spectral feature of the air-exposed sample is very similar to that of the thiosulphate reference compound and peak at 2480.0 eV is much more pronounced than that at 2478.2 eV, exhibiting different spectral feature to the LiTDI/TEGDME pristine spectrum. This confirms that two peaks at higher energy region in LiTDI/TEGDME pristine cell is not arising from air-exposure of the cell.

(iii) It was also thought that these two peaks are caused by the beam-induced damage of sulphur. However, *operando* measurement confirmed that these peak features and intensities are relatively stable throughout the discharge and the charge processes (Figure 3-28a). If those peaks were due to beam-damage oxidation of sulphur, then the intensity would progressively increase.

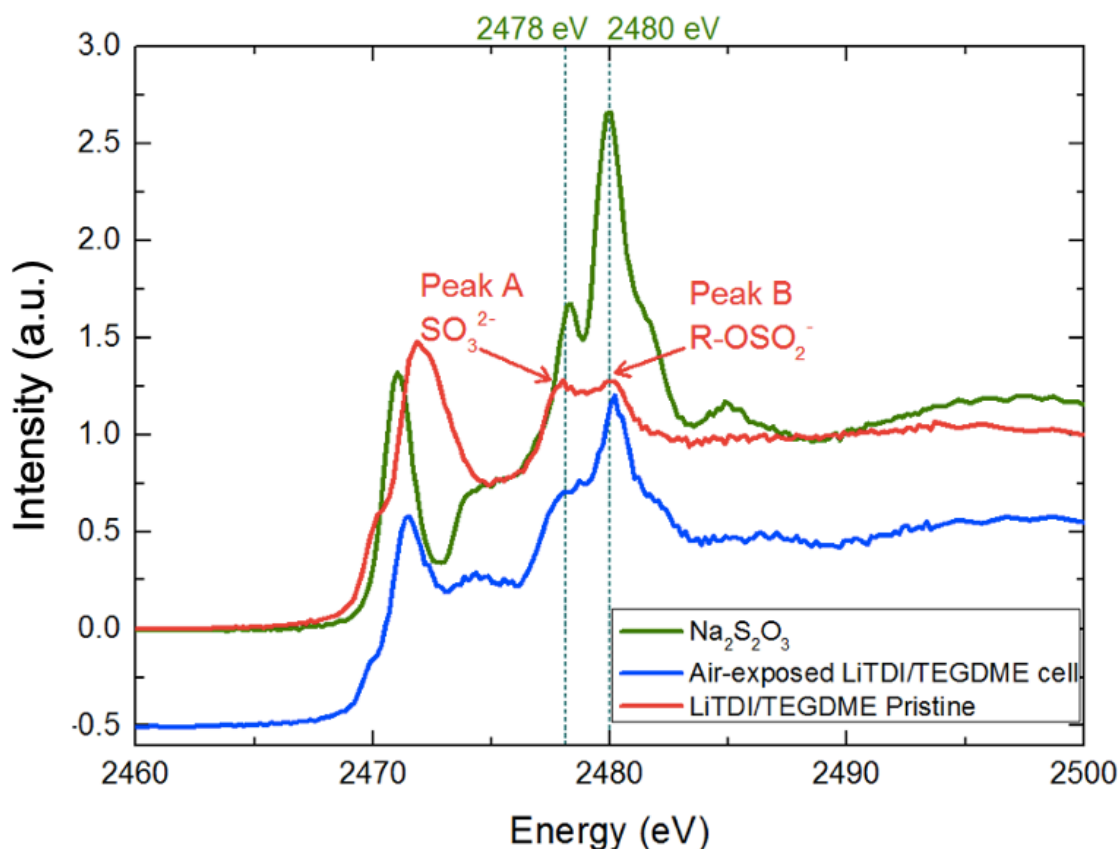


Figure 3-17. Sulphur K-edge XANES spectra of the LiTDI/TEG cell at the pristine state (red line) compared with $\text{Na}_2\text{S}_2\text{O}_3$ reference (green line) and the air-exposed cell (blue line). The spectra are shown offset for clarity.

(iv) Elimination of these three possibilities leaves the last postulation, that the oxidised sulphur peaks are arising from the chemical reaction within the cell. According to the previous publications, peak at 2478.0 eV is assigned to S^{2-} σ^* and/or SO_3^{2-} σ^* , and peak at 2480.0 eV is attributed to R-OSO_2^- (where R represents alkyl group) σ^* . [62][63] These insulating species are possibly caused by the reactions between Li, S, and oxygen containing functional groups present in the electrolyte. [64][65] This is therefore ascribed to partial oxidation of active sulphur within the cell.

To conclude, these features were not found in the other electrolytes, and the visual colour analysis in **Section 3.5**, as well as the absence of oxidised sulphur impurities in pure LiTDI/TEGDME electrolyte suggests that it is reasonable to believe that the postulation (iv) is the most probable.

Very similar peaks of oxidised sulphur were seen in the previous publications upon cycling of sulphur-graphene nanocomposite [63] and CTAB-modified sulphur-graphene oxide composite (CTAB: cetyltrimethylammonium bromide) [65] both in PYR₁₄TFSI/DOL:DME (PYR₁₄TFSI: N-methyl-N-butyl-pyrrolidinium bis(trifluoromethanesulphonyl)imide) electrolyte in the presence of LiNO₃ salt. Both studies used total electron yield (TEY) and total fluorescence yield (TFY) XANES techniques probing at the cathode surface.

3.6.3 *Operando* measurement

3.6.3.1 Reference electrolyte system - LiTFSI/DOL:DME/LiNO₃

Operando XANES measurements were performed on the sulphur electrode assembled in the reference electrolyte system, LiTFSI/DOL:DME/LiNO₃. **Figure 3-18a** presents the *operando* XANES spectra set recorded during the cell cycling and **Figure 3-18b** shows the corresponding electrochemical data. The cell is discharged at the 0.05 C rate and charged at the 0.1 C rate. Before starting of the cell cycling, the pristine spectrum was recorded (black line in **Figure 3-18a**).

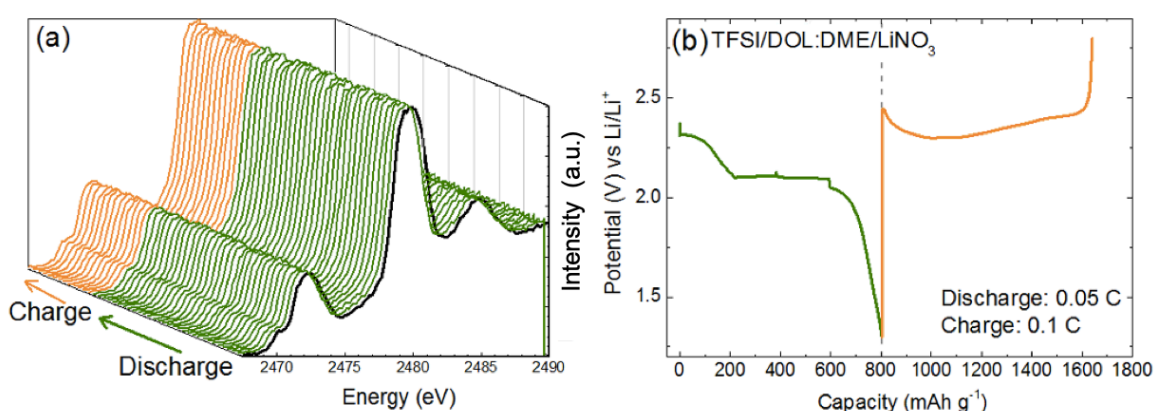


Figure 3-18. (a) *Operando* XANES spectra of the LiTFSI/DOL:DME/LiNO₃ cell and (b) corresponding experimental voltage profile during the initial discharge (green line) and following charge (orange line).

The pre-edge feature was detected at the pristine state (**Figure 3-18a**, black line) and the spectrum was dominated by the polysulphide species, indicating the dissolution of active S_8 and reaction with Li-ions present in the electrolyte during cell storage. This is due to the non-negligible solubility of sulphur in DOL:DME binary solvent, especially DOL has considerably higher DN. During the first discharge and sequential charge, spectral feature remains unchanged including the absorption energy positions and peak intensities, suggesting that the sulphur species in the detected area do not engage in the reaction. The lack of evidence for change in sulphur chemistry in the spectral features of the S K-edge is not consistent with the electrochemical curve represented in **Figure 3-18b**. The discharge capacity of $\sim 800 \text{ mAh g}^{-1}$ is obtained with two clear voltage plateaus with subsequent $\sim 1000 \text{ mAh g}^{-1}$ charge capacity, which clearly indicates that the active sulphur undergoes conversion reaction. It is important to note here that the reaction products may be different in different positions of the electrode, therefore, it is possible that the sulphur undergoes structural change within the cell but not appeared in the detected area.

We postulate that this is because the polysulphide species formed during storage are not dispersed into the electrolyte and masking the probing of the active sulphur that is involved in the electrochemical reaction. This explains the unique cycling performance of the LiTFSI/DOL:DME/LiNO₃ cell exhibited in **Figure 3-4b**, where the discharge capacity increased slightly with increasing cycle number in the beginning of battery operation up to 15 cycles. The increasing discharge capacity is due to low utilisation of active sulphur in the first few cycles, which is related to the distribution of the polysulphides in the cell. Polysulphides formed during the cell storage did not dissolve into the electrolyte and stayed on the surface of carbon, which hindered the access of Li-ions to the remaining active sulphur underneath the layer of polysulphides. Due to the insulating nature of sulphur and intermediate species, reduction of these species can only take place on the surface of conductive carbon. Dissolution of polysulphide into the electrolyte disconnects the polysulphide from the carbon so that the remaining sulphur is exposed to the conductive carbon and reduction can progressively move forward.

3.6.3.2 LiTFSI/DOL:DME

Although this cell failed to cycle successfully in the conventional coin cells (**Figure 3-7a**), *operando* XANES measurement was performed to evaluate the failure mechanism of this system. LiTDI/DOL:DME cell was characterised under the same conditions as the cell measured above, but maintaining the constant C-rate at 0.1 C throughout discharge and charge processes. **Figure 3-19** shows the summary of this measurement.

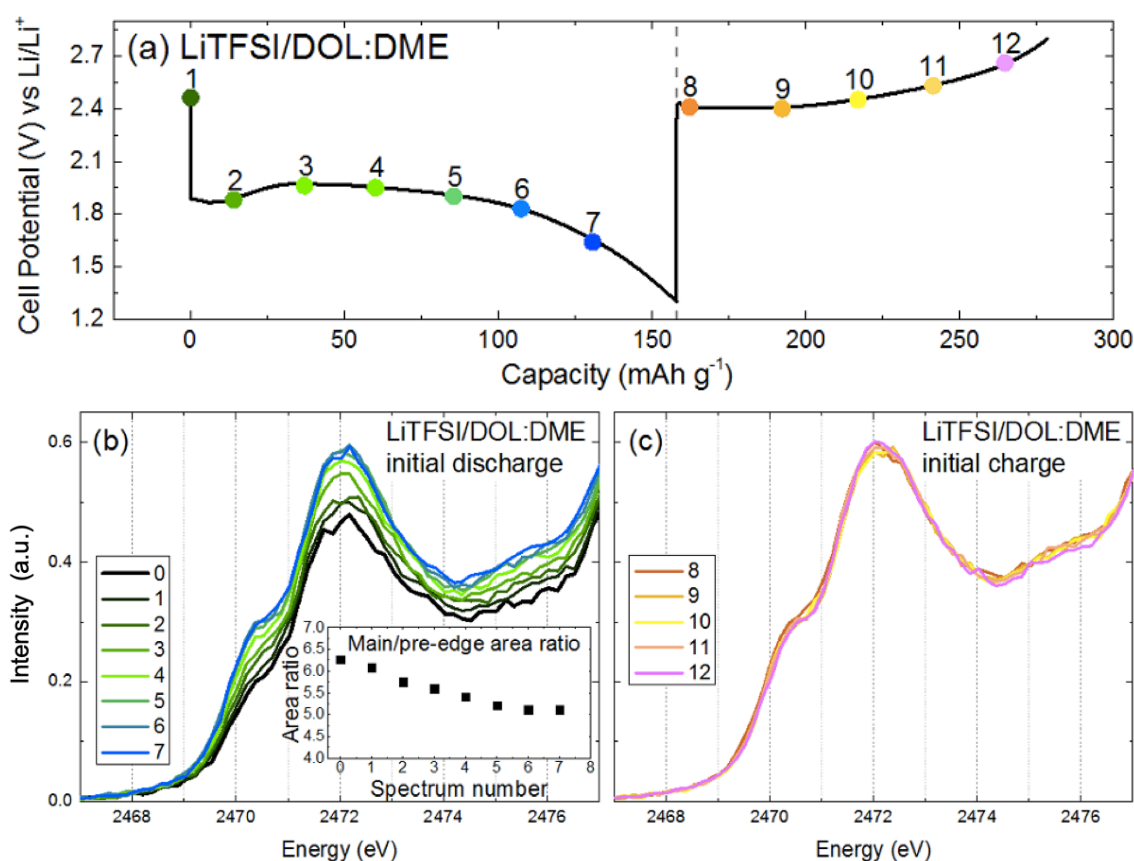


Figure 3-19. *Operando* measurement of the LiTFSI/DOL:DME cell. (a) Discharge and charge profile of the measured cell at a 0.1 C rate. The symbols on the voltage curve indicate the point where the XANES spectra were collected. (b) S K-edge XANES spectra collected during the initial discharge. Spectrum number 0 corresponds to the pristine spectrum collected before applying the current to the cell. The inset represents the area ratio of the main-edge to the pre-edge which guides the chain length of polysulphide species exist in the sample, and (c) S K-edge XANES spectra collected during the charging process.

Again, the pre-edge is found at 2470.3 eV in the pristine state and the spectrum is dominated by polysulphide (**Figure 3-19b**, black line), indicating the self-discharge reaction. As the extent of discharge process, the pre-edge feature and its accompanying main-edge feature at 2472 eV become more dominant, indicating the overall proportion of polysulphide is increasing, as a result of the polysulphide diffusion into the electrolyte. [66] The area ratio of the main/pre-edge for each spectrum is calculated to estimate the average chain-lengths of polysulphides formed during the reaction (inset of **Figure 3-19b**). The values decrease slightly from 6.3 to 5.1 throughout the discharge process, corresponding to the reduction of polysulphide chain-length but only slightly. No spectroscopic evidence for insoluble $\text{Li}_2\text{S}_2/\text{Li}_2\text{S}$ formation was found during this reaction, as the energy position of the main-edge remained unchanged.

During the charging process, spectral change is not observed in the S K-edge XANES. This result indicates that the sulphur did not experience any phase change at the detected area. Polysulphides formed during discharge remained unchanged and did not undergo oxidation reaction to form S_8 , which explains the extremely low charge capacity of this cell ($\sim 120 \text{ mAh g}^{-1}$).

Difference in the higher energy region between with and without LiNO_3

We have noticed some difference in the electrolyte region between these two cells.

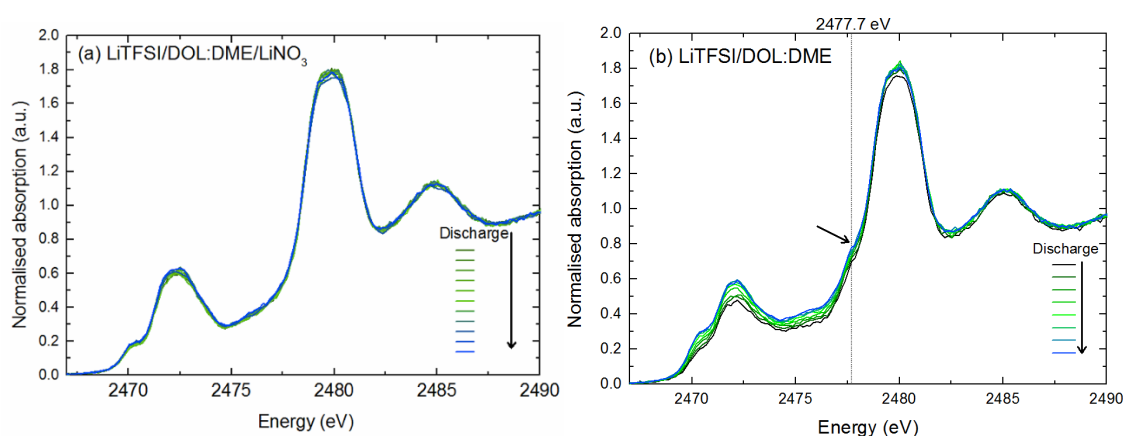


Figure 3-20. Normalised S K-edge XANES spectra set of (a) LiTFSI/DOL:DME/LiNO₃ cell and (b) LiTFSI/DOL:DME cell.

Figure 3-20 shows the collective results of LiTFSI/DOL:DME/LiNO₃ and LiTFSI/DOL:DME cells highlighting the spectral change in the electrolyte region. During the cell reactions, the electrolyte region remained unchanged in both cells. However, we have noticed a weak shoulder at 2477.7 eV in the LiTFSI/DOL:DME cell, suggesting the presence of oxidised sulphur. Zhang *et al.* found a similar feature in the presence of LiNO₃ salt, where the XANES spectra were recorded on the separator from the cathode side. It was demonstrated the formation of Li₂SO₃ and Li₂SO₄ via reduction of LiNO₃ and identified as a SEI layer. [67] However, this cell does not contain LiNO₃ salt, and the shoulder peak is already present at the pristine state. Therefore, in this cell, the sulphur is already oxidised by the reaction of S, Li, and oxygen present in the electrolyte, which adversely influenced the active sulphur loss. Although it is not possible to identify whether this peak is originating from the oxidation of active sulphur species or side reactions of sulphur species in the electrolyte (LiTFSI), the formation of oxidised sulphur may be the reason why the cell without LiNO₃ is incompatible in DOL:DME solvent.

3.6.3.3 LiTDI/DOL:DME

To compare the salt effect of between LiTFSI and LiTDI in DOL:DME solvent (1:1 by volume), LiTDI/DOL:DME electrolyte was examined in a similar fashion. **Figure 3-21** summarises the *operando* dataset.

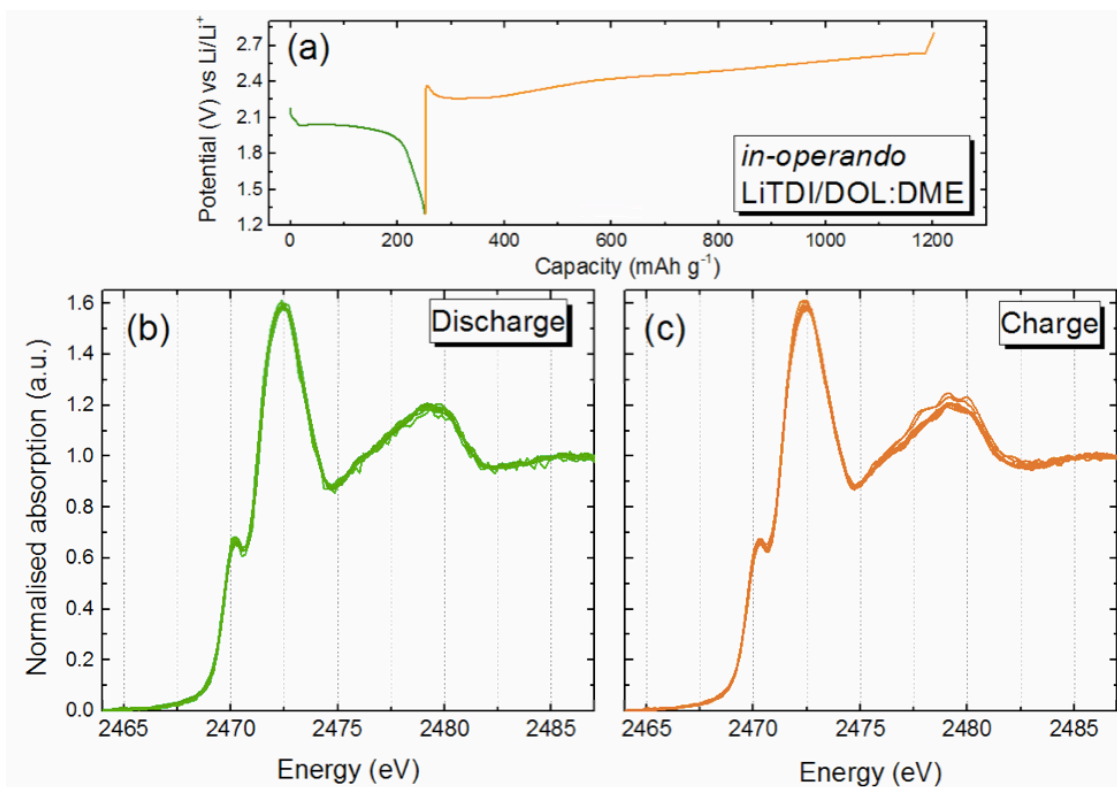


Figure 3-21. *Operando* measurement of the LiTDI/DOL:DME cell. (a) Discharge/charge curve of the cell cycled at the 0.1 C rate, and the normalised S K-edge XANES spectra set during the initial (b) discharge and (c) charge processes.

Polysulphides are clearly detected in a significant amount in the pristine spectrum, indicated by the presence of the pre-edge at 2470.3 eV, suggesting a high rate of self-discharge reaction of this cell (**Figure 3-21b**). During the initial discharge and charge process, it is seen that the XANES feature remains unchanged. The pre- and the main-edge features are stable at the absorption energy of 2470.3 and 2472.4 eV, respectively, including their intensities. This indicates that the sulphur species do not undergo any change in the structure where the cell is probed by the X-rays. This means, polysulphides formed during self-discharge are blocking the access of Li-ions from other sulphur active materials, resulting in extremely low discharge capacity (250 mAh g⁻¹). The recent work of Chen *et al.*, demonstrated that LiTDI salt in DOL:DME solvent decreases the solubility of Li₂S₈ by 83 % compared to LiTFSI in DOL:DME. [29] This agrees to the reduced capacity found in LiTDI, limiting the utilisation and conversion

reaction of active sulphur, hence reducing the access of Li-ions to electrochemically active sulphur particles.

Although this cell has not shown a successful polysulphide conversion reaction, the XANES spectra set can be used as an indication of whether the active sulphur species are oxidised by the beam or not. Beam-induced damage is one of a major obstacles for *operando* analysis of Li-S batteries using XAS techniques because it can change the composition of the electrolyte species and oxidises the sulphur, significantly influencing the XANES spectra. The beam-induced damage of sulphur was found in the work of Gorlin *et al*, in which the increasing concentration of sulphate is found with the increasing irradiation time. Typically, sulphur is oxidised to sulphate (SO_4^{2-}), giving rise to two features at incident energies of 2482 eV and 2498 eV growing with increasing incident time. This may alter the electrochemical and spectroscopic response, therefore, an extreme care is needed to avoid this effect. [68]

Figure 3-22 displays the S K-edge of higher energy region of this cell, where beam-damaged sulphate peaks can be expected at 2482 and 2498 eV. [69]

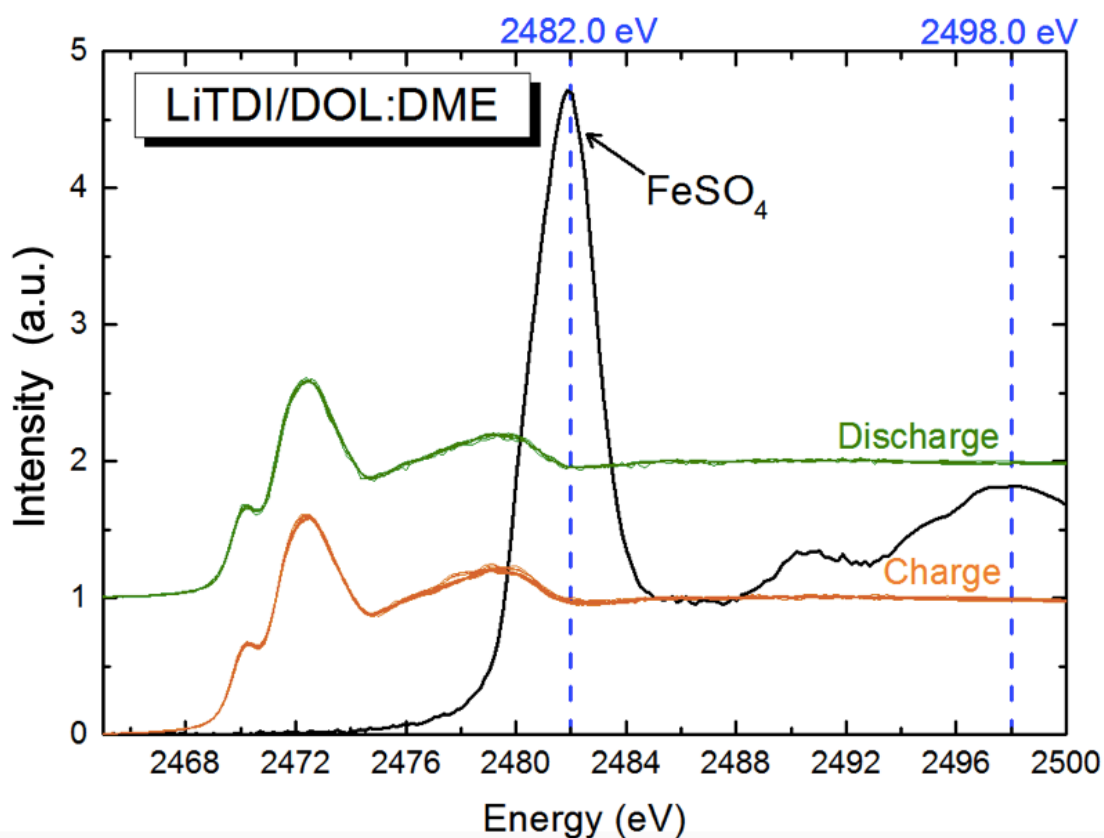


Figure 3-22. A series of *operando* XANES spectra of the LiTDI/DOL:DME cell demonstrating spectral changes during the (a) discharge and (b) charge. Time between each measurement was about 15 min, the spectra are shown offset for clarity. Reference spectra of FeSO₄ (black line) is shown for comparison. Indication of stable features at the higher energy region confirms that beam-damaged sulphur is absent.

As clearly seen in **Figure 3-22**, there was no change in the peak intensities at 2482 and 2498 eV during the period of data collection of over 7 hours of multiple scans, which confirms no spectroscopic evidence for beam damage with increasing acquisition time. In addition, other oxidised sulphur peaks, such as, SO₃²⁻ and S₂O₃²⁻ were not found. Therefore, it is confirmed that our measurements were performed without beam-induced material damage, hence the change of XANES feature during *operando* measurements is caused by the electrochemical reaction of the electrode. Also, none of the other cells show any sign of such beam damage.

3.6.3.4 LiTDI/TMS

LiTDI/TMS electrolyte gained considerable interest as its discharge/charge voltage plateaus were very stable throughout the number of cycling as observed in **Figure 3-6d**. **Figure 3-23** shows a summary of the S K-edge XANES spectra set during the initial cycle of the LiTDI/TMS cell.

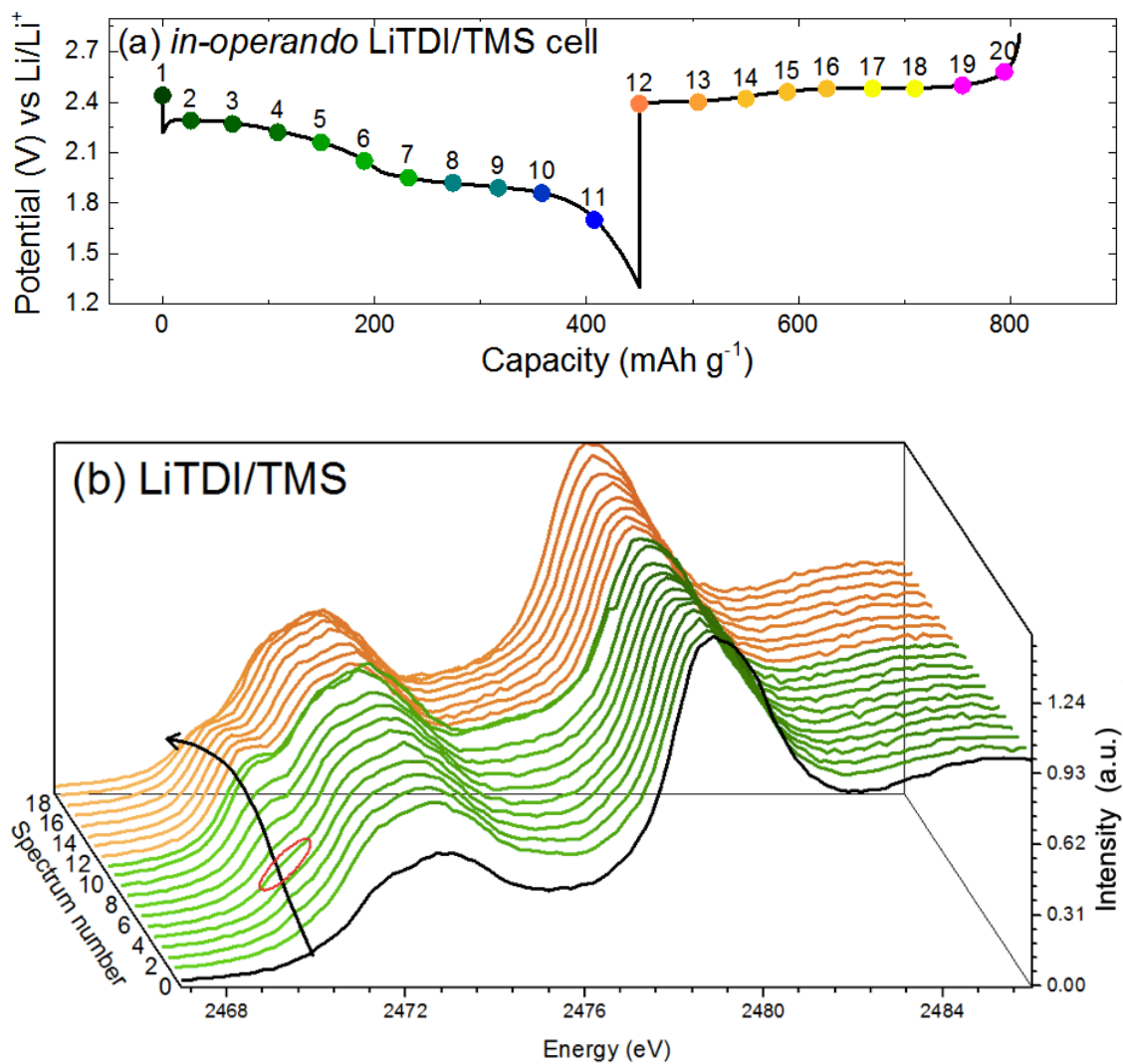


Figure 3-23. Operando measurement for the LiTDI/TMS cell. (a) Discharge/charge curve of the cell cycled at the 0.1 C rate. (b) Waterfall plot of the S K-edge XANES spectra.

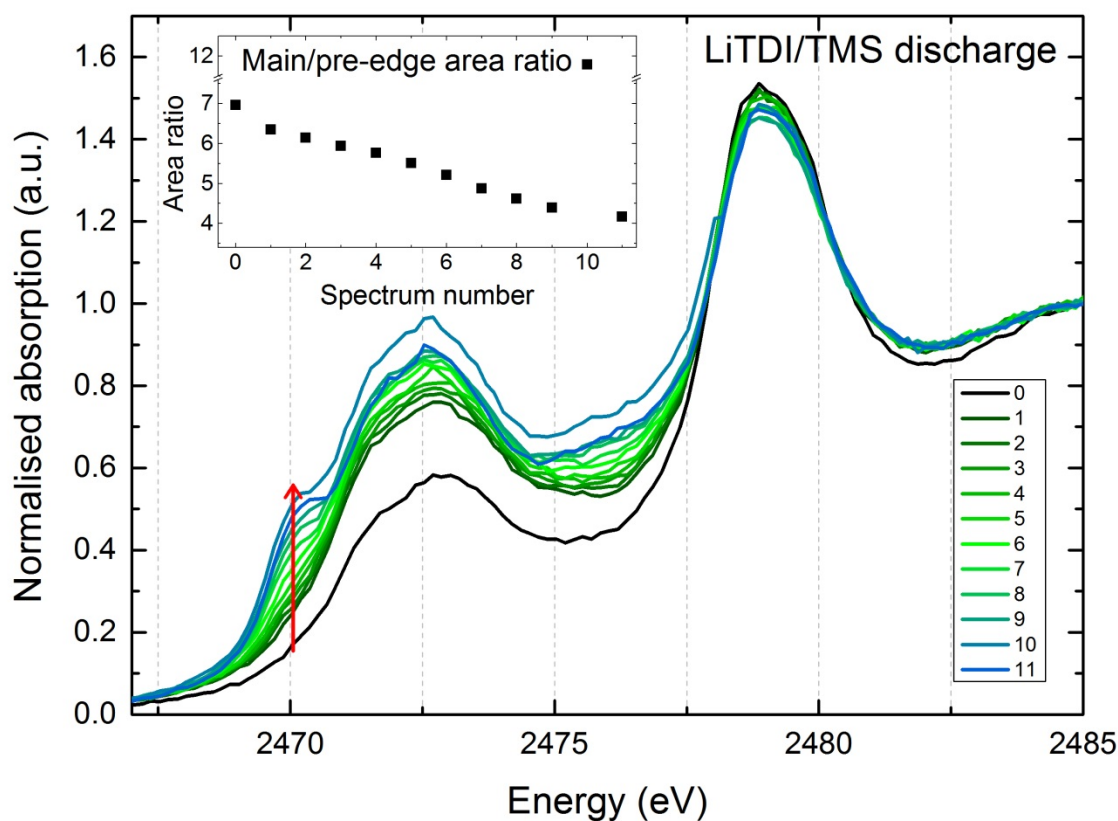


Figure 3-24. Normalised S K-edge XANES spectra set of the LiTDI/TMS cell during the first discharge. The inset shows the calculated area ratio of the main/pre-edge peak.

The pristine spectrum is presented in **Figure 3-23b**, black line. The main-edge is exhibited at 2472.5 eV, accompanying with a convex shape nearing 2475 eV. The pre-edge signature was not detected at the lower energy, indicating the minimised self-discharge reaction, and the structure of sulphur is identified as S_8 . The mitigation of self-discharge reaction is highly related to the DN of the TMS solvent. As previously shown in **Table 3-1**, TMS has the lowest DN among four solvents used in this study. The weaker solvating power prevented the dissolution of active sulphur species in the electrolyte, resulting in the low rate of self-discharge reaction.

As soon as the current is applied, a distinct increase in the main-edge intensity is observed (**Figure 3-24**). This is assigned to the dissolution of sulphur species in the electrolyte, hence concentration of the sulphur at the detected area is lowered, which decreased the self-absorption (SA) effect, and resulted in the higher intensity of the resonances. It is worth nothing that in **Figure 3-23b**, the sign of polysulphide is not yet

seen in the beginning of the discharge, which means, at this point, majority of sulphur species are still in the form of S_8 . This suggests that in LiTDI/TMS electrolyte, not only the polysulphide is formed during storage but also the dissolution of the S_8 is significantly inhibited. Again, this can be related to the low DN of the TMS solvent. With increasing depth of discharge, the concave feature around 2475.5 eV flattens out and the pre-edge peak growth is recognised after the end of high voltage plateau, corresponding to 150 mAh g^{-1} , as indicated by the red circle in **Figure 3-23b**, confirming the polysulphide formation. With increasing depth of discharge, the pre-edge feature became more pronounced, suggesting the shortening of the overall chain-lengths of polysulphide species. This spectra set did not involve any isosbestic points in the energy region ascribed to the active sulphur (region I, II, and III). This means that conversion reaction happened sequentially, rather than two reaction happening simultaneously. Therefore, the reaction mechanisms are suggested as follows; $S_8 \rightarrow Li_2S_8 \rightarrow Li_2S_6 \rightarrow Li_2S_4$. These changes are visualised in the inset of **Figure 3-24** by plotting the area ratio of the peak intensities of the main-edge to pre-edge, which shows a steady decrease, indicating that the polysulphide chain lengths are sequentially reduced.

Although, the absorption energy edge position of the main-peak remains unchanged, suggesting that the formation of insoluble Li_2S_2/Li_2S was not achieved. This may be explaining why this cell exhibits the shortest discharge capacity in the initial cycle with significantly short voltage plateaus compared to other systems (**Figure 3-4b**, solid blue line), but capable to maintain the voltage plateau output because the volume expansion and contraction of the cathode is suppressed by limited formation of Li_2S particles.

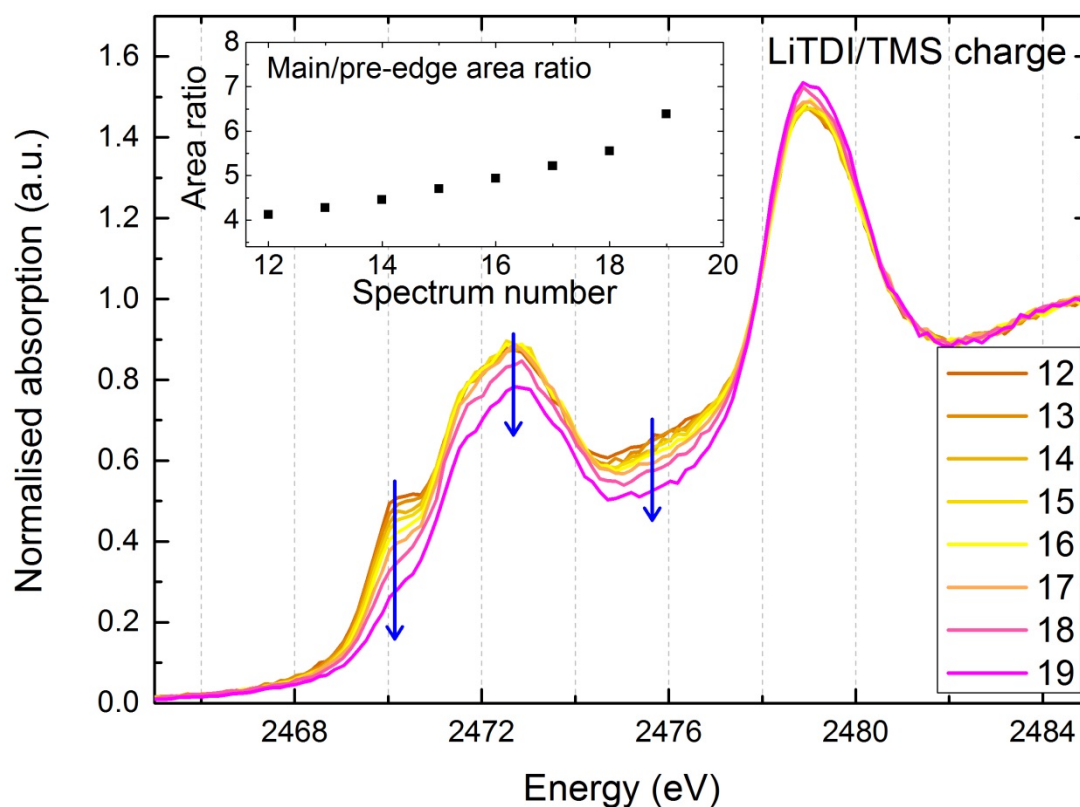


Figure 3-25. Normalised S K-edge XANES spectra dataset during the first charge of the LiTDI/TMS cell. The inset shows the evolution of the main/pre-edge area ratio.

During the charging process, similar spectral feature as observed during discharge process but in reverse sequence is indicated by the blue arrows. The pre-edge at 2470.3 eV diminishes with increasing depth of charge, suggesting the conversion reaction of short chain polysulphides to long-chain polysulphides. Again, this reaction proceeds without involving isosbestic points in energy region ascribed to the active sulphur, indicating the sequential re-oxidation process.

Figure 3-26 compares the normalised spectrum collected at the pristine state and the last spectrum of the charging state, which directly reflects the reversibility of the sulphur structure at the cathode as a result of cycling. The weak pre-edge at 2470.3 eV is still observed near the end of charging process, indicating that polysulphide species still exist in a small amount. The inset of **Figure 3-26** represents the raw S K-edge spectra, which shows the direct concentration of sulphur species present in the sample at the edge step of 2500 eV. The edge-step exhibited at the end of the charging

process is significantly lower than that of the pristine state, suggesting the loss of active material during battery cycling process.

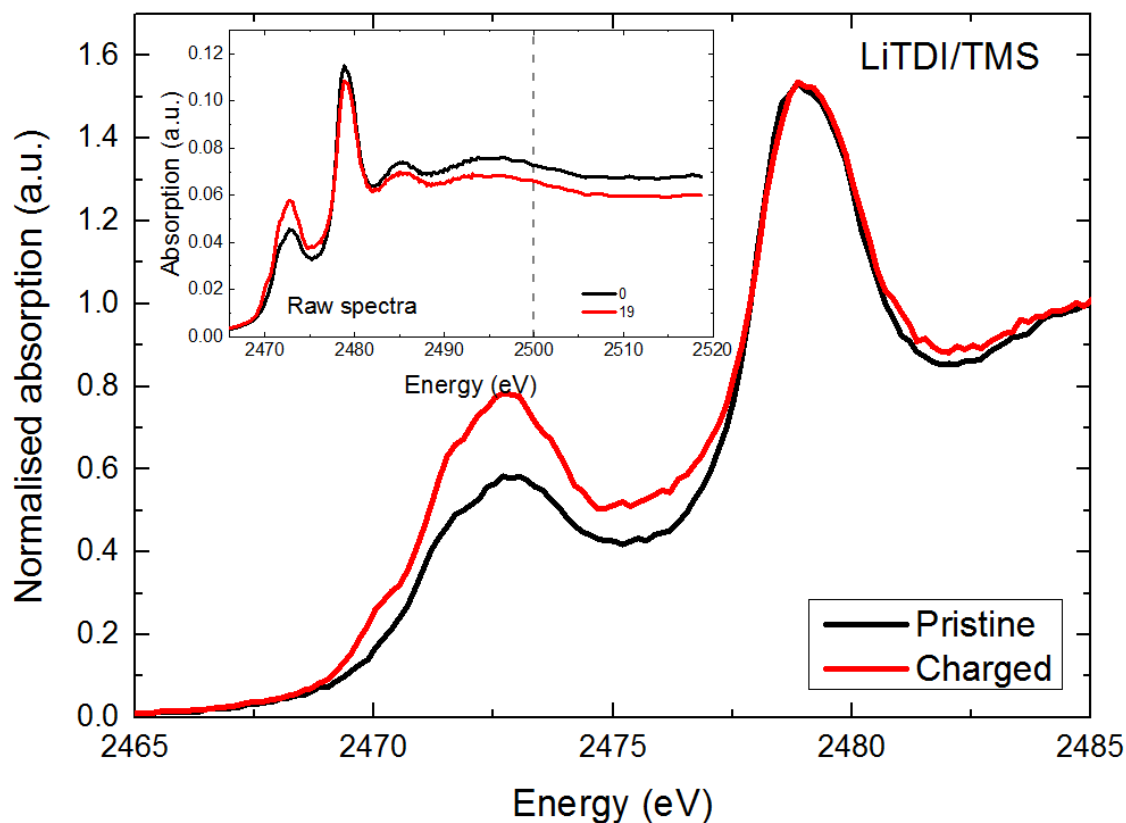


Figure 3-26. Normalised S K-edge spectra of LiTDI/TMS cell at the pristine state and end of the charging process, with the inset showing the raw spectra to show the direct concentration of sulphur species present in the sample.

From these results, it can be speculated that the mitigation of the voltage polarisation in this electrolyte system is due to the sequential conversion reaction of long-chain polysulphides to medium/short-chain polysulphides, and limited formation of Li_2S species. Polarisation happens during nucleation of Li_2S . The delay or elimination of Li_2S nucleation prevents the elevation of internal resistance of the cell, contributing to maintain the output voltage of the discharge plateaus. In fact, there are no signs of Li_2S formation observed in the XANES spectra and the discharge capacity of the low voltage plateau is considerably shorter than other electrolyte systems in the first cycle, further supporting that Li_2S is not formed in this electrolyte system.

3.6.3.5 LiTDI/TEGDME

The LiTDI/TEGDME cell is investigated by *operando* XAS under the same conditions as other cells, but with the cycling rate of the 0.1 C rate during the first discharge, followed by the charging at the 0.05 C rate. **Figure 3-27** shows the summary of the *operando* dataset.

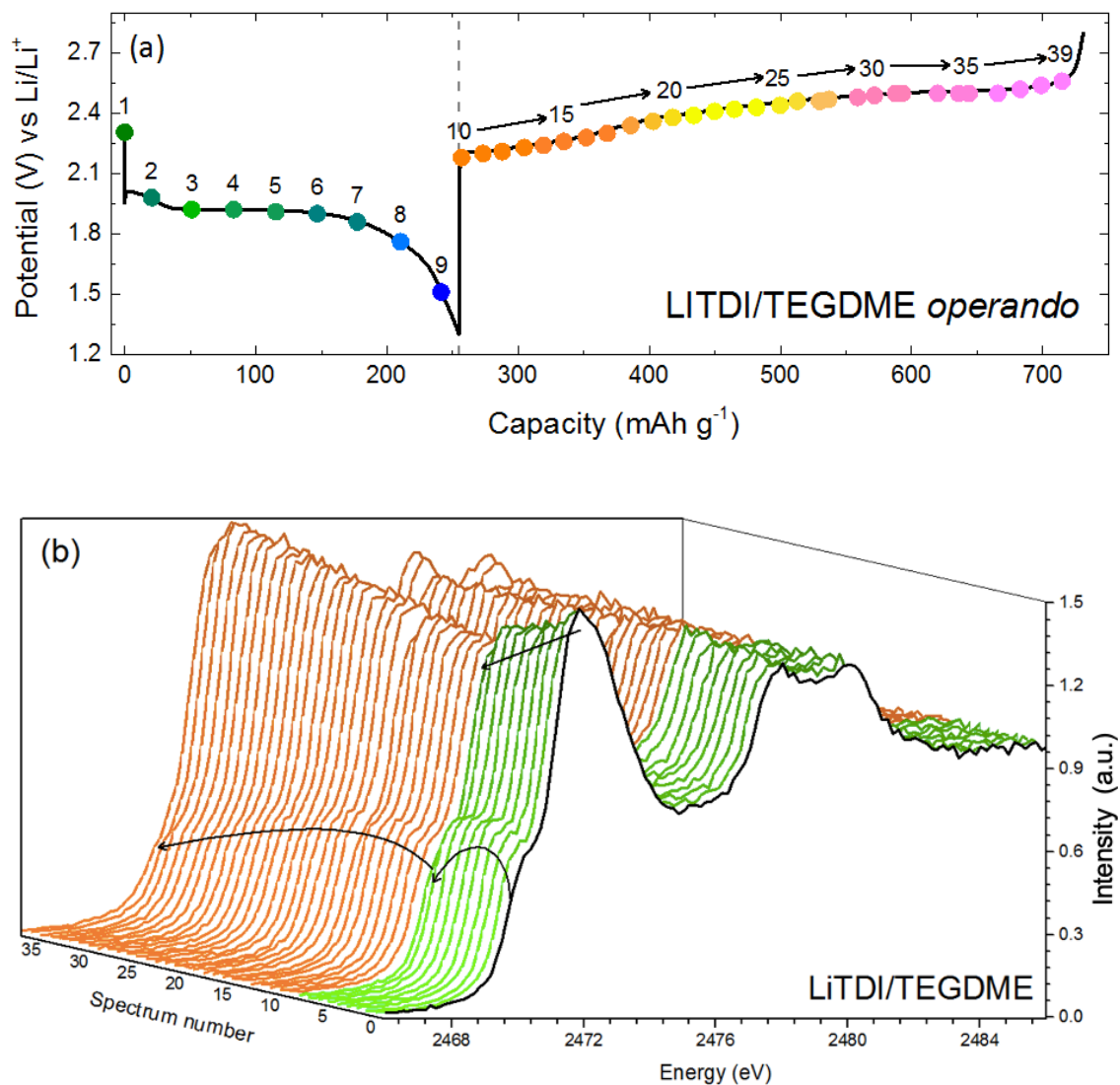


Figure 3-27. *Operando* measurement for the LiTDI/TEGDME cell. (a) Galvanostatic curve for the first discharge at the 0.1 C rate, followed by the charge at the 0.05 C. (b) waterfall plot of the S K-edge XANES spectra.

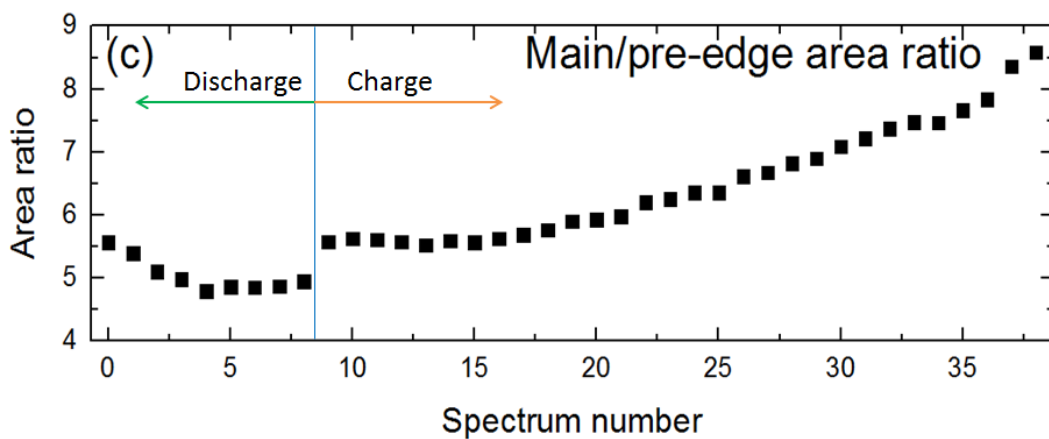


Figure 3-27. Continued. (c) Plot of the calculated area ratio of the main/pre-edge peak.

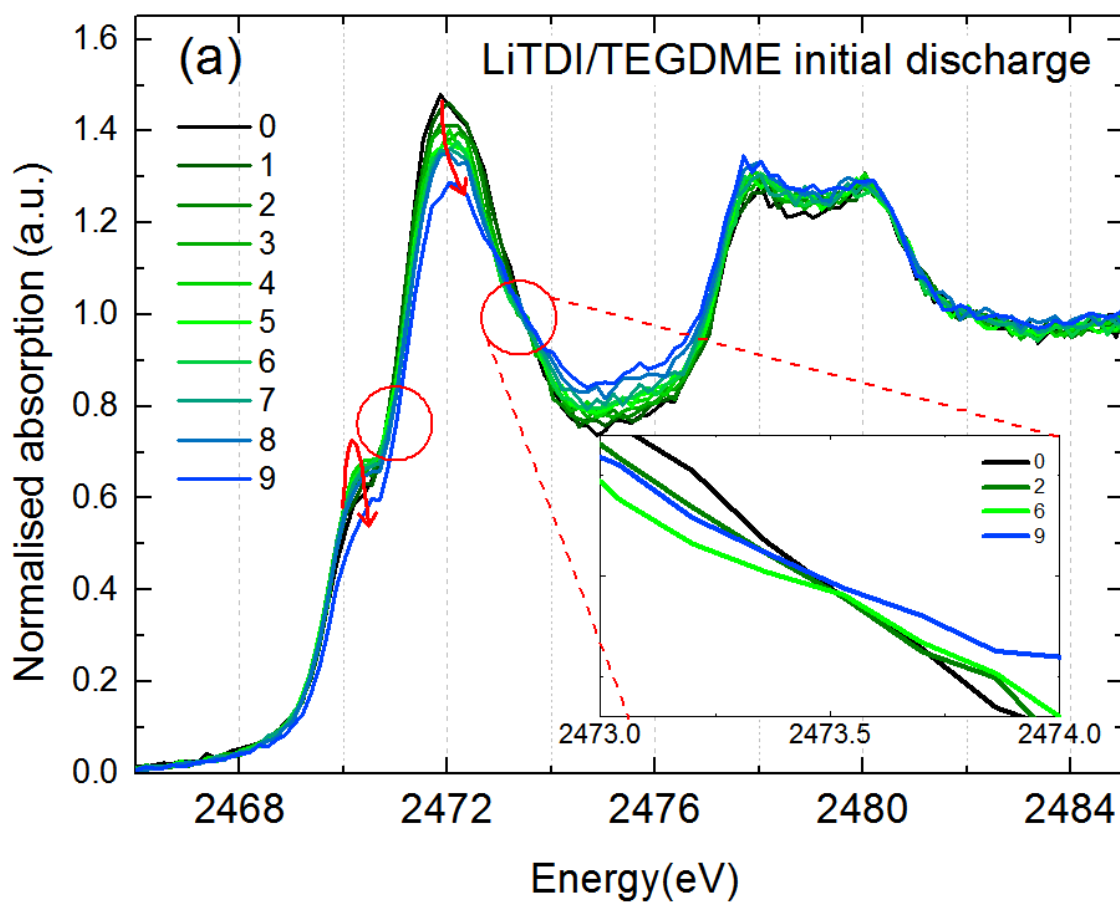


Figure 3-28. Normalised S K-edge spectra collected during *operando* measurement of the (a) initial discharge of the LiTDI/TEGDME cell.

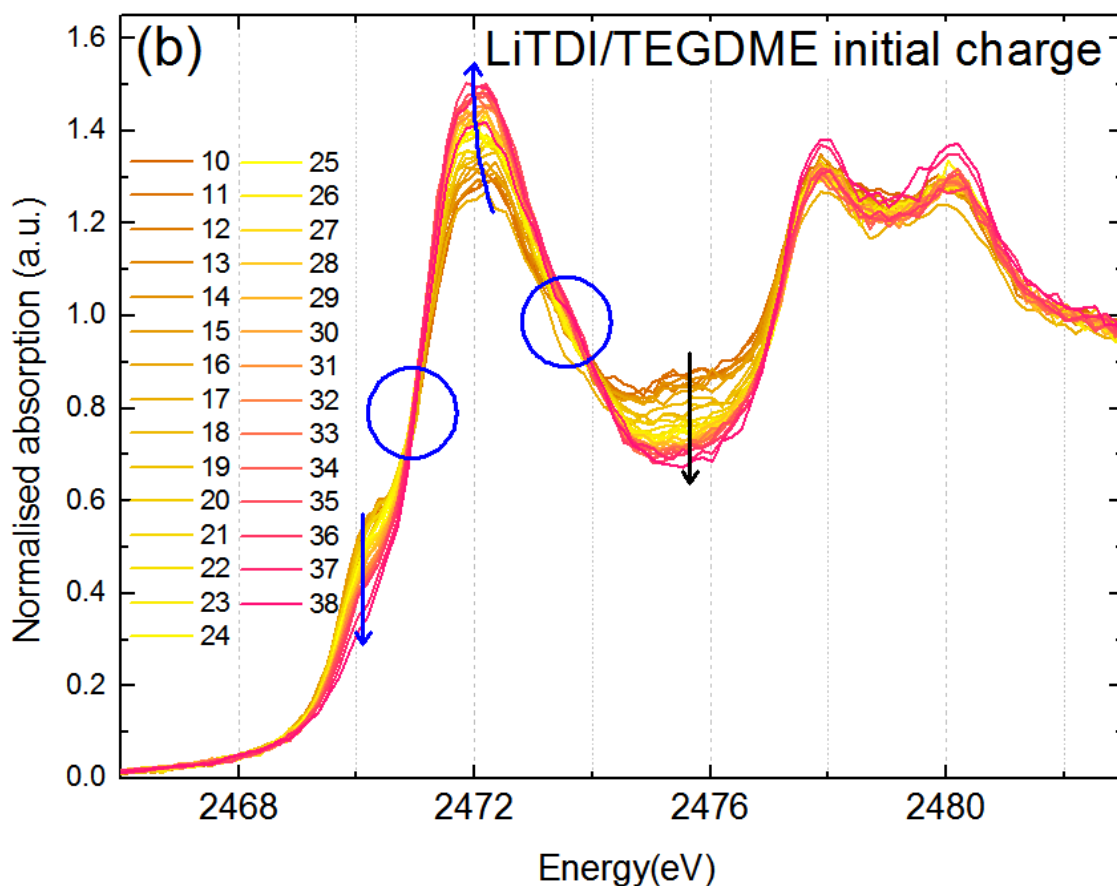


Figure 3-28. Continued. (b) XANES spectra collected during the following charge.

There was a unique spectral feature trend compared to the previous electrolyte systems studied. In the pristine state, the pre-edge is evident at 2470.3 eV (**Figure 3-27b**, solid black line), indicating the influence of the self-discharge phenomenon during cell storage. TEGDME has a relatively high DN of 20 (**Table 3-1**), and it is, therefore, dissolving polysulphides in the electrolyte easily. However, the rate of the self-discharge is lower than that in the LiTDI/DOL:DME electrolyte. This can be confirmed by the less pronounced pre-edge feature in the pristine state of LiTDI/TEGDME cell compared to that in the LiTDI/DOL:DME cell (**Figure 3-21b**). Very similar results have been reported in the literature by the group of Abruna, using an *in situ* XAS analysis. [70] The self-discharge reaction resulted in the elimination of the high voltage plateau corresponding to the reduction series of S_8 to Li_2S_8 in the initial discharge (**Figure 3-27a**). Instead, the conversion reaction started from Li_2S_8 to Li_2S_6 , which resulted in the low discharge capacity due to the limited utilisation of active sulphur species. During

the discharge, the main-edge intensity progressively becomes weaker while the pre-edge becomes more pronounced. This means that the concentration of terminal sulphur grows while the population of the internal sulphur decreases, confirming the formation of shorter chain polysulphides ($\text{Li}_2\text{S}_{4-6}$). This can be recognised by the area ratio values of the main/pre-edge plotted in **Figure 3-27b**, which decreases slightly in the beginning of the discharge process. Detection of isosbestic points (indicated by the red circles in **Figure 3-28a** and the inset figure) suggests that there is a two-step conversion reaction. The last scan of the discharge (corresponding to 1.51 V) experience an abrupt disappearance of the pre-edge while the main-edge absorption energy shifts to higher energy by 0.3 eV, as indicated by the red arrow in **Figure 3-28a**, which is an indication of the further reduction of polysulphide chain lengths to even shorter ones, possibly forming insoluble $\text{Li}_2\text{S}_2/\text{Li}_2\text{S}$. This result indicates that the sulphur reaction mechanism in the LiTDI/TEGDME electrolyte is different from other electrolyte systems and the shortening of long-chain polysulphide to medium-chain polysulphide happens simultaneously with the conversion of medium to short-chain polysulphides.

In the following charging process, again, the pre-edge grows in the beginning before it starts decreasing (**Figure 3-27b**). Simultaneously, the main-edge shifts to the lower energy values with increasing depth of charge (**Figure 3-28b**), which was an inverse effect to what was observed during the discharge process, hence indicating the reversibility of the energy position. In the beginning of the charge, a flat feature is seen at 2475.7 eV, which evolves to a concave shape throughout the charging process, as indicated by the black arrow in **Figure 3-28b**, further confirming the re-oxidation of polysulphides to S_8 . This reaction also involve isosbestic points (indicated by the blue circles in **Figure 3-28b**) at the same energy positions detected during the discharge process, confirming that the oxidation process also involves two-step reaction.

Throughout the first discharge/charge process, the oxidised sulphur peaks at 2478 and 2480 eV do not experience in significant spectral change. Therefore, these peaks are not considered as one of the influencing factors to the sulphur reaction mechanisms, but oxidation of sulphur might have caused the inactivation of the active sulphur leading to the fast capacity decay.

To compare the structural difference and relative concentration of sulphur species at the pristine and charged state, the normalised (a) and raw (b) spectra are shown in **Figure 3-29**.

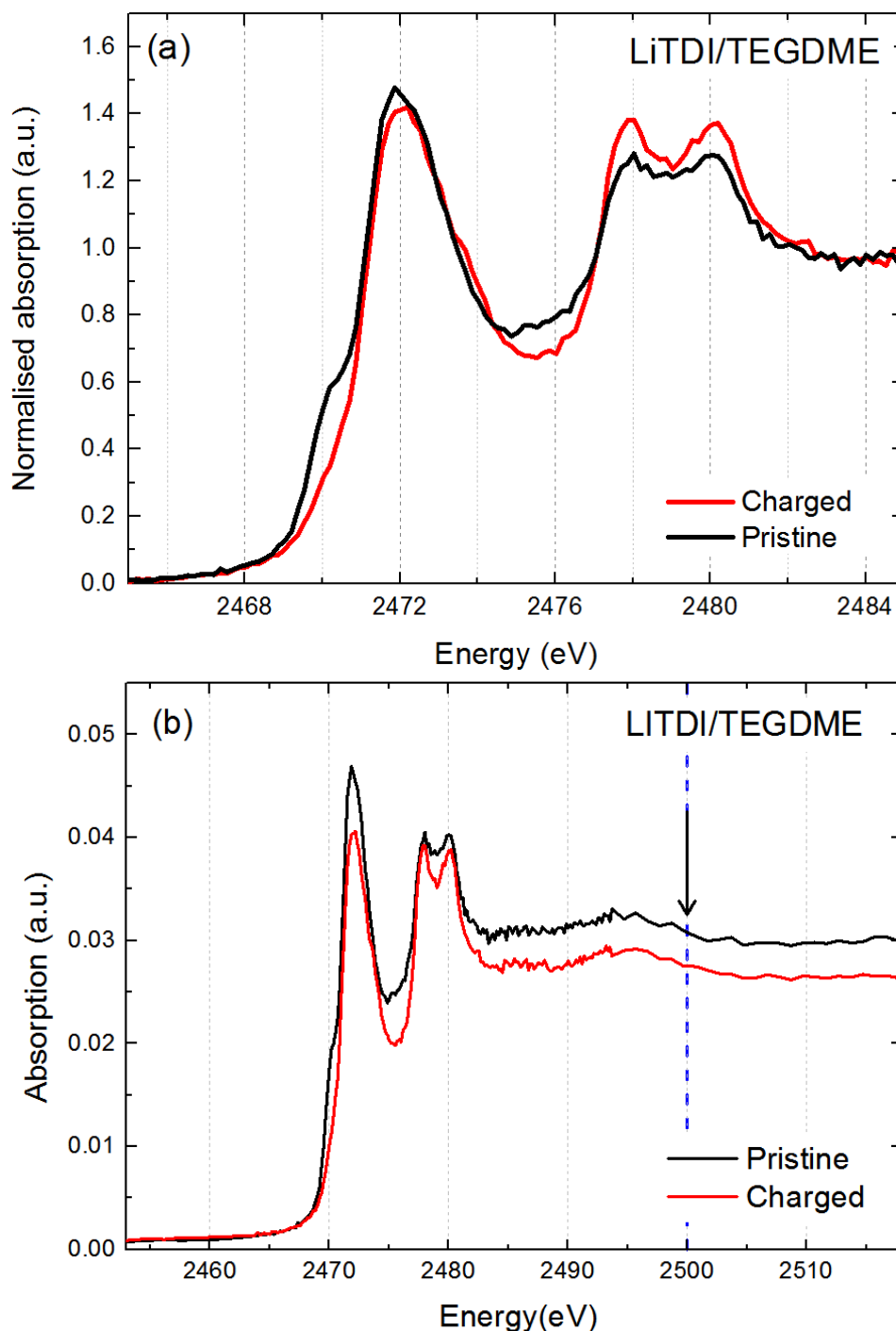


Figure 3-29. (a) Normalised and (b) raw S K-edge XANES spectra of LiTDI/TEGDME at the pristine state and charged state.

At the end of the charging process, the concave shape after the main-edge became deeper than that of the pristine and the minimum intensity is located at higher energy

position, as seen in **Figure 3-29a**. Also, the pre-edge is vanished in the charged state, indicating that the polysulphide species are not present. This result indicates that the complete conversion of polysulphide to S_8 is achieved. Although the loss of active sulphur after the cycling was inevitable as recognised by the difference in the edge-step at 2500 eV in **Figure 3-29b**.

It can be concluded that the LiTDI/TEGDME electrolyte is effective in enhancing the conversion reaction from long-chain polysulphides to short-chain polysulphides, and possible formation of Li_2S is also suggested. Although the successful redox kinetic of polysulphide is achieved using LiTDI/TEGDME electrolyte, very poor cycling performance is observed (**Figure 3-6f**, open green triangles), which decays the discharge capacity to less than 300 mAh g^{-1} in the initial 10 cycles and almost no capacity is obtained after 30 cycles. This is possibly caused by an inverse effect of the active sulphur oxidation by the presence of the electrolyte, detected as two peaks in the S K-edge XANES at higher energy region of 2478 and 2480 eV. The cycling performance and CE values of this cell are greatly improved by the addition of $LiNO_3$ salt, therefore, the severe capacity decay of this cell is also caused by the polysulphide shuttle reaction. One valuable objective for future work would be to conduct *in-operando* XAS measurements on the anode side and the separator of the LiTDI/TEGDME/ $LiNO_3$ cell and LiTDI/TEGDME cell. These data would then allow investigation of a SEI layer formation and contribution of the $LiNO_3$ salt towards the cell reactions.

3.6.4 Radical polysulphides

Additionally, we investigated the presence of polysulphide radicals. Currently, the presence of radicals during the cell reaction is a subject to some debate. [27] [56][68][71] In the S K-edge XAS studies, polysulphide radicals are reported and can be identified in an XAS signal as a shoulder peak at lower energy nearing 2468-2469 eV. [69] Based on the XAS studies, it has been reported that radicals species are present when a sulphur electrode is cycled in the high dielectric DMAC electrolyte, [71] while in the low dielectric DOL:DME electrolyte, radical species is not recognised.

Alloin *et al.* demonstrated the presence of radical species in TEGDME electrolyte using the UV-VIS technique. [55] Wujcik *et al.* also agreed to the presence of such species in

ether-based solvents, TEGDME and PEO based on UV-VIS and electron paramagnetic resonance (EPR) spectroscopy. [56] To verify the existence of radical species, we have done a close inspection of the XANES spectra in the lower energy region. **Figure 3-30** shows the S K-edge XANES dataset of DOL:DME, TEGDME, and TMS electrolyte cells at the low energy region where shoulder peaks of radical species are expected.

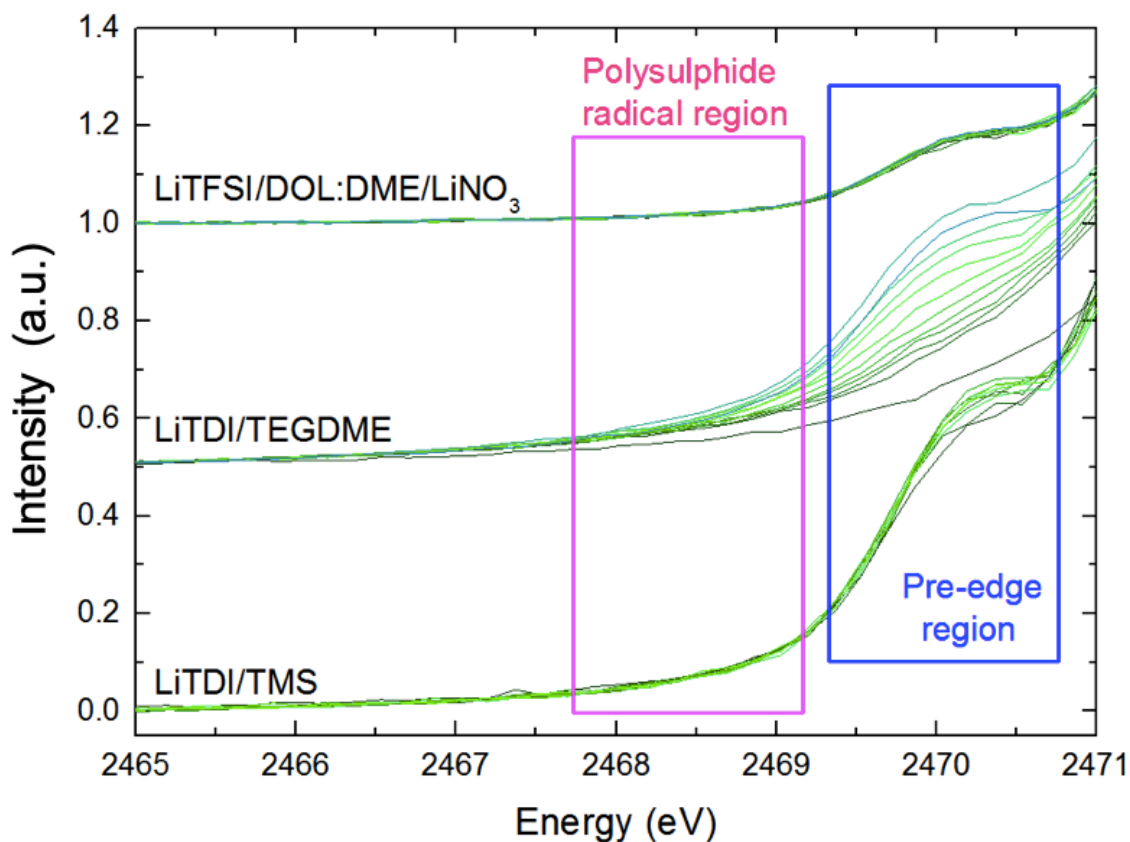


Figure 3-30. Sulphur K-edge spectra; the region before the pre-edge shows no peaks of radical species.

As can be seen in **Figure 3-30**, signature of polysulphide radicals were not detected in any of our electrolyte compositions reported in this work. [47][48][50][51][53][70] Nevertheless, it is worth noting that the polysulphide radicals would need to be long-lived and present in relative high concentrations in order to be detectable in the S K-edge XAS. [12] To obtain more accurate results, combination of UV-VIS spectroscopy and EPR spectroscopy study is ideal, where UV-VIS can detect the difference in colour arising from different chain lengths of polysulphides, and EPR can provide information about the interaction of unpaired electrons with the surrounding nuclei. [8][71]

3.7 Conclusions

In this study, a large variety of the electrolyte systems were investigated to search for the most optimal system for the Li-S batteries. Our collective results indicated that the best performing electrolyte for LiTFSI salt was found to be the binary solvent of DOL:DME with the presence of 0.25 M LiNO₃, which is the standard electrolyte mostly used in the Li-S cells. However, this electrolyte system is also found non-flexible, as the DOL:DME could only work in those salt combinations. A single solvent of TEGDME was found to be a compatible choice for both LiTFSI and LiTDI salts, in the presence of LiNO₃.

Operando XANES measurements of some of the systems were carried out, which have provided important fundamental insights in the reaction kinetics and polysulphide evolution during battery operations by real time observations. This revealed that the self-discharge rate and sulphur conversion reaction of intermediate species differs by the electrolytes used in the cell. It is demonstrated that LiTDI/TMS electrolyte has an excellent merit in preventing the self-discharge phenomenon during cell storage, i.e. the dissolution of S₈ was strongly limited. It was also revealed that the sulphur conversion reaction takes places sequentially rather than simultaneously in LiTDI/TMS electrolyte. On the contrary, LiTDI/TEGDME electrolyte is advantageous in faster reaction kinetics of the reduction reaction favouring the conversion of long-chain polysulphides to short-chain polysulphides.

Additionally, this work demonstrated that no radical species is recognised in any of our S K-edge XANES spectra, which decreases the possibility of formation of radical anions during cell cycling in ether based and sulphone based electrolytes. To support this finding, EPR analysis is necessary for a clear detection of radical anions. For a further analysis, we will be conducting more detailed optical studies using open-cell investigations, combined with UV-vis measurements to investigate dispersion behaviour of polysulphides. Based on these results, we conducted more *operando* XANES measurements using sulphur electrodes modified by inorganic additives and represented in **Chapter 4**.

3.8 References

- [1] Y. J. Choi, B.S. Jung, D.J. Lee, J.H. Jeong, K.W. Kim, H.J. Ahn, K.K. Cho, and H.B. Gu, "Electrochemical properties of sulfur electrode containing nano Al₂O₃ for lithium/sulfur cell," *Phys. Scr.*, vol. T129, pp. 62–65, 2007.
- [2] M. Cuisinier, C. Hart, M. Balasubramanian, A. Garsuch, and L. F. Nazar, "Radical or Not Radical: Revisiting Lithium-Sulfur Electrochemistry in Nonaqueous Electrolytes," *Adv. Energy Mater.*, vol. 5, no. 16, p. 1401801, 2015.
- [3] X. Yu and A. Manthiram, "A class of polysulfide catholytes for lithium–sulfur batteries: energy density, cyclability, and voltage enhancement," *Phys. Chem. Chem. Phys.*, vol. 17, no. 3, pp. 2127–2136, 2015.
- [4] A. Benítez, D. Di Lecce, Á. Caballero, J. Morales, E. Rodríguez-Castellón, and J. Hassoun, "Lithium sulfur battery exploiting material design and electrolyte chemistry: 3D graphene framework and diglyme solution," *J. Power Sources*, vol. 397, no. April, pp. 102–112, 2018.
- [5] S. M. Ahn, J. Suk, D. Y. Kim, Y. Kang, H. K. Kim, and D. W. Kim, "High-Performance Lithium-Oxygen Battery Electrolyte Derived from Optimum Combination of Solvent and Lithium Salt," *Adv. Sci.*, vol. 4, no. 10, p. 1700235, 2017.
- [6] H. J. Yang and Y. Jung, "Effects of polysulfide nonsolvents on the electrochemical performance of Li-S batteries," *Int. J. Electrochem. Sci.*, vol. 10, no. 11, pp. 9049–9055, 2015.
- [7] D. Chang, S. Lee, S. Kim, and H. Kim, "Binary electrolyte based on tetra (ethylene glycol) dimethyl ether and 1 , 3-dioxolane for lithium – sulfur battery," *J. Power Sources*, vol. 112, pp. 452–460, 2002.
- [8] R. Dominko, M. U. M. Patel, V. Lapornik, A. Vizintin, M. Koželj, N. N. Tušar, I. Arcon, L. Stievano, and G. Aquilanti, "Analytical Detection of Polysulfides in the Presence of Adsorption Additives by Operando X-ray Absorption Spectroscopy," *J. Phys. Chem. C*, vol. 119, no. 33, pp. 19001–19010, 2015.

- [9] M. J. Lacey, F. Jeschull, K. Edström, and D. Brandell, "Porosity Blocking in Highly Porous Carbon Black by PVdF Binder and Its Implications for the Li-S System," *J. Phys. Chem. C*, vol. 118, no. 45, pp. 25890–25898, 2014.
- [10] K. H. Wujcik, D. R. Wang, T. A. Pascal, D. Prendergast, and N. P. Balsara, "In Situ X-ray Absorption Spectroscopy Studies of Discharge Reactions in a Thick Cathode of a Lithium Sulfur Battery," *J. Electrochem. Soc.*, vol. 164, no. 2, pp. A18–A27, 2017.
- [11] A. Deb, U. Bergmann, S. P. Cramer, and E. J. Cairns, "In situ x-ray absorption spectroscopic study of the Li[Ni_{1/3}Co_{1/3}Mn_{1/3}]O₂ cathode material," *J. Appl. Phys.*, vol. 97, no. 11, p. 113523, 2005.
- [12] T. A. Pascal, K.H.Wujcik, J. Velasco-Velez, C. Wu,A.A.Teran, M. Kapilashrami, J.Cabana, J. Guo, M. Salmeron,N.Balsara and D. Prendergast, "The X-ray Absorption Spectra of Dissolved Polysulfides in Lithium–Sulfur Batteries from First Principles," *J. Phys. Chem. Lett.*, vol. 5, pp. 1547–1551, 2014.
- [13] Y. Umebayashi, "Potential Energy Landscape of Bis (fluorosulfonyl) amide," *J. Phys. Chem. Part B*, vol. 112, pp. 9449–9455, 2008.
- [14] P. Jankowski, M. Dranka, W. Wieczorek, and P. Johansson, "TFSI and TDI Anions: Probes for Solvate Ionic Liquid and Disproportionation-Based Lithium Battery Electrolytes," *J. Phys. Chem. Lett.*, vol. 8, no. 15, pp. 3678–3682, 2017.
- [15] K. Matsumoto, K. Inoue, K. Nakahara, R. Yuge, T. Noguchi, and K. Utsugi, "Suppression of aluminum corrosion by using high concentration LiTFSI electrolyte," *J. Power Sources*, vol. 231, pp. 234–238, 2013.
- [16] L. Niedzicki, E. Karpierz, A. Bitner, M. Kasprzyk, G.Z. Zukowska, M. Marcinek, and W. Wieczorek, "Optimization of the lithium-ion cell electrolyte composition through the use of the LiTDI salt," *Electrochim. Acta*, vol. 117, pp. 224–229, 2014.
- [17] C. Xu, S. Renault, M.Ebadi, Z. Wang, E. Björklund, D. Guyomard, D. Brandell, K. Edström, and T. Gustafsson, "LiTDI : A Highly Efficient Additive for Electrolyte Stabilization in Lithium-Ion Batteries LiTDI : A Highly Efficient Additive for

- Electrolyte Stabilization in Lithium-Ion Batteries,” *Chem. Mater.*, vol. 29, no. 5, pp. 2254–2263, 2017.
- [18] R. Younesi, G. M. Veith, P. Johansson, K. Edström, and T. Vegge, “Lithium salts for advanced lithium batteries: Li-metal, Li-O₂, and Li-S,” *Energy Environ. Sci.*, vol. 8, no. 7, pp. 1905–1922, 2015.
- [19] F. Alloin, “Revisiting TEGDME / DIOX Binary Electrolytes for Lithium / Sulfur Batteries : Importance of Solvation Ability and Additives,” *J. Electrochem. Soc.*, vol. 160, no. 3, pp. 430–436, 2013.
- [20] S. Yoon, Y. H. Lee, K. H. Shin, S. B. Cho, and W. J. Chung, “Binary sulfone/ether-based electrolytes for rechargeable lithium-sulfur batteries,” *Electrochim. Acta*, vol. 145, pp. 170–176, 2014.
- [21] S. Zhang, K. Ueno, K. Dokko, and M. Watanabe, “Recent Advances in Electrolytes for Lithium-Sulfur Batteries,” *Adv. Energy Mater.*, vol. 5, no. 16, p. 1500117, 2015.
- [22] D. Aurbach, E. Pollak, R. Elazari, G. Salitra, C. S. Kelley, and J. Affinito, “On the Surface Chemical Aspects of Very High Energy Density, Rechargeable Li–Sulfur Batteries,” *J. Electrochem. Soc.*, vol. 156, no. 8, pp. A694–A702, 2009.
- [23] X. Judez, H. Zhang, C. Li, G. G. Eshetu, J. A. Gonzalez-Marcos, M. Armand, and L. M. Rodriguez-Martinez, “Review—Solid Electrolytes for Safe and High Energy Density Lithium-Sulfur Batteries: Promises and Challenges,” *J. Electrochem. Soc.*, vol. 165, no. 1, pp. A6008–A6016, 2018.
- [24] S. S. Zhang, “Liquid electrolyte lithium / sulfur battery : Fundamental chemistry , problems , and solutions,” *J. Power Sources*, vol. 231, pp. 153–162, 2013.
- [25] C. Barchasz, J. Leprêtre, S. Patoux, and F. Alloin, “Electrochimica Acta Electrochemical properties of ether-based electrolytes for lithium / sulfur rechargeable batteries,” *Electrochim. Acta*, vol. 89, pp. 737–743, 2013.
- [26] J. Scheers, S. Fantini, and P. Johansson, “A review of electrolytes for lithium e sulphur batteries,” *J. Power Sources*, vol. 255, pp. 204–218, 2014.

- [27] A. Shyamsunder, W. Beichel, P. Klose, Q. Pang, H. Scherer, A. Hoffmann, G. K. Murphy, I. Krossing, and Linda F. Nazar, "Inhibiting Polysulfide Shuttle in Lithium–Sulfur Batteries through Low-Ion-Pairing Salts and a Triflamide Solvent," *Angew. Chemie - Int. Ed.*, vol. 56, no. 22, pp. 6192–6197, 2017.
- [28] S. Paillet, G. Schmidt, S. Ladouceur, J. Frechette, F. Barray, D. Clement, P. Hovington, A. Guerfia, A. Vijh, I. Cayrefourcq, and K. Zaghib, "Determination of the electrochemical performance and stability of the lithium-salt, lithium 4,5-dicyano-2-(trifluoromethyl) imidazolide, with various anodes in Li-ion cells," *J. Power Sources*, vol. 299, pp. 309–314, 2015.
- [29] J. Chen, K. S. Han, W. A. Henderson, K. C. Lau, M. Vijayakumar, T. Dzwiniel, H. Pan, L. A. Curtiss, J. Xiao, K. T. Mueller, Y. Shao, and J. Liu, "Restricting the Solubility of Polysulfides in Li-S Batteries Via Electrolyte Salt Selection," *Adv. Energy Mater.*, vol. 6, no. 11, p. 1600160, 2016.
- [30] K. S. Han, J. Chen, R. Cao, N. N. Rajput, V. Murugesan, L. Shi, H. Pan, J. G. Zhang, J. Liu, K. A. Persson, and K. T. Mueller "Effects of Anion Mobility on Electrochemical Behaviors of Lithium-Sulfur Batteries," *Chem. Mater.*, vol. 29, no. 21, pp. 9023–9029, 2017.
- [31] K. Hancock, J. Becherer, M. Hagen, M. Joos, M. Abert, D. Muller, P. Fanz, S. Straach, and J. Tubke, "Electrolyte Decomposition and Electrode Thickness Changes in Li-S Cells with Lithium Metal Anodes, Prelithiated Silicon Anodes and Hard Carbon Anodes," *J. Electrochem. Soc.*, vol. 165, no. 1, pp. A6091–A6106, 2018.
- [32] Y. Mikhaylik, "United States Patent 7354680 B2," 2008.
- [33] S. S. Zhang, "A new finding on the role of LiNO₃ in lithium-sulfur battery," *J. Power Sources*, vol. 322, pp. 99–105, 2016.
- [34] D. Aurbach, E. Pollak, R. Elazari, G. Salitra, C. S. Kelley, and J. Affinito, "On the Surface Chemical Aspects of Very High Energy Density, Rechargeable Li–Sulfur Batteries," *J. Electrochem. Soc.*, vol. 156, no. 8, pp. A694–A702, 2009.

- [35] R. Xu, J. C. M. Li, J. Lu, K. Amine, and I. Belharouak, "Demonstration of highly efficient lithium-sulfur batteries," *J. Mater. Chem. A*, vol. 3, no. 8, pp. 4170–4179, 2015.
- [36] N. Ding, L. Zhou, C. Zhou, D. Geng, J. Yang, S. W. Chien, Z. Liu, M.-F. Ng, A. Yu, T. S. A. Hor, M. B. Sullivan, and Y. Zong, "Building better lithium-sulfur batteries: from LiNO₃ to solid oxide catalyst," *Sci. Rep.*, vol. 6, no. 1, p. 33154, 2016.
- [37] S. S. Zhang, "Role of LiNO₃ in rechargeable lithium/sulfur battery," *Electrochim. Acta*, vol. 70, pp. 344–348, 2012.
- [38] Z. W. Seh, Y. Sun, Q. Zhang, and Y. Cui, "Designing high-energy lithium–sulfur batteries," *Chem. Soc. Rev.*, vol. 45, no. 20, pp. 5605–5634, 2016.
- [39] C. Qu, Y. Chen, X. Yang, H. Zhang, X. Li, and H. Zhang, "LiNO₃-free electrolyte for Li-S battery: A solvent of choice with low K_{sp} of polysulfide and low dendrite of lithium," *Nano Energy*, vol. 39, no. June, pp. 262–272, 2017.
- [40] E. Peled, I. Shekhtman, T. Mukra, M. Goor, I. Belenkaya, and D. Golodnitsky, "Improving the Durability and Minimizing the Polysulfide Shuttle in the Li/S Battery," *J. Electrochem. Soc.*, vol. 165, no. 1, pp. A6051–A6057, 2018.
- [41] G. Zheng, Q. Zhang, J. J. Cha, Y. Yang, W. Li, Z. W. Seh and Y. Cui "Amphiphilic Surface Modification of Hollow Carbon Nano fibers for Improved Cycle Life of Lithium Sulfur Batteries," *Nano Lett.*, vol. 13, no. 3, pp. 1265–1270, 2013.
- [42] J. Liang, Z. Sun, F. Li, and H. Cheng, "Carbon materials for Li – S batteries : Functional evolution and performance improvement," *Energy Storage Mater.*, vol. 2, pp. 76–106, 2016.
- [43] B. Zhang, C. Lai, Z. Zhou, and X. P. Gao, "Preparation and electrochemical properties of sulfur-acetylene black composites as cathode materials," *Electrochim. Acta*, vol. 54, no. 14, pp. 3708–3713, 2009.
- [44] S. Wang, K. Dong, H. Zhang, and J. Wu, "Preparation and electrochemical performance of sulfur-alumina cathode material for lithium-sulfur batteries," *Mater. Res. Bull.*, vol. 48, no. 6, pp. 2079–2083, 2013.

- [45] W. Weng, V. G. Pol, and K. Amine, "Ultrasound assisted design of sulfur/carbon cathodes with partially fluorinated ether electrolytes for highly efficient Li/S batteries," *Adv. Mater.*, vol. 25, no. 11, pp. 1608–1615, 2013.
- [46] Q. Li, J. Chen, L. Fan, X. Kong, and Y. Lu, "Progress in electrolytes for rechargeable Li-based batteries and beyond," *Green Energy Environ.*, vol. 1, pp. 18–42, 2016.
- [47] S. S. Zhang, "Effect of Discharge Cutoff Voltage on Reversibility of Lithium/Sulfur Batteries with LiNO₃-Contained Electrolyte," *J. Electrochem. Soc.*, vol. 159, no. 7, pp. A920–A923, 2012.
- [48] S. Kim, Y. Jung, and S. J. Park, "Effect of imidazolium cation on cycle life characteristics of secondary lithium-sulfur cells using liquid electrolytes," *Electrochim. Acta*, vol. 52, no. 5, pp. 2116–2122, 2007.
- [49] Y. Lu, Q. He, and H. a Gasteiger, "Probing the Lithium – Sulfur Redox Reactions: A Rotating-Ring Disk Electrode Study," *J. Phys. Chem. C*, vol. 118, no. 1, pp. 5733–5741, 2014.
- [50] J. Yan, X. Liu, M. Yao, X. Wang, T. K. Wafle, and B. Li, "Long-Life, High-Efficiency Lithium-Sulfur Battery from a Nanoassembled Cathode," *Chem. Mater.*, vol. 27, no. 14, pp. 5080–5087, 2015.
- [51] L. Suo, Y. S. Hu, H. Li, M. Armand, and L. Chen, "A new class of Solvent-in-Salt electrolyte for high-energy rechargeable metallic lithium batteries," *Nat. Commun.*, vol. 4, p. 1481, 2013.
- [52] Y. Z. Zhang, S. Liu, G. C. Li, G. R. Li, and X. P. Gao, "Sulfur/polyacrylonitrile/carbon multi-composites as cathode materials for lithium/sulfur battery in the concentrated electrolyte," *J. Mater. Chem. A*, vol. 2, no. 13, pp. 4652–4659, 2014.
- [53] R. Cao, J. Chen, K. S. Han, W. Xu, D. Mei, P. Bhattacharya, M. H. Engelhard, K. T. Mueller, J. Liu, and J.-G. Zhang, "Effect of the Anion Activity on the Stability of Li Metal Anodes in Lithium-Sulfur Batteries," *Adv. Funct. Mater.*, vol. 26, no. 18, pp. 3059–3066, 2016.

- [54] K. Sun, Q. Wu, X. Tong, and H. Gan, "Electrolyte with Low Polysulfide Solubility for Li-S Batteries," *ACS Appl. Energy Mater.*, vol. 1, no. 6, pp. 2608–2618, 2018.
- [55] C. Barchasz, F. Molton, C. Duboc, J. C. Leprêtre, S. Patoux, and F. Alloin, "Lithium/Sulfur Cell Discharge Mechanism: An Original Approach for Intermediate Species Identification," *Anal. Chem.*, vol. 84, no. 9, pp. 3973–3980, 2012.
- [56] K. H. Wujci, D. R. Wang, A. Raghunathan, M. Drake, T. A. Pascal, D. Prendergast, and N. P. Balsara, "Lithium Polysulfide Radical Anions in Ether-Based Solvents," *J. Phys. Chem. C*, vol. 120, no. 33, pp. 18403–18410, 2016.
- [57] C. Qu, Y. Chen, X. Yang, H. Zhang, X. Li, and H. Zhang, "LiNO₃-free electrolyte for Li-S battery: A solvent of choice with low K_{sp} of polysulfide and low dendrite of lithium," *Nano Energy*, vol. 39, no. October 2016, pp. 262–272, 2017.
- [58] M. Thiemann, E. Scheibler, and K. W. Wiegand, *Nitric Acid, Nitrous Acid, and Nitrogen Oxides*, vol. 24. 2000.
- [59] Y. Gorlin, M.U.M. Patel, A. Freiberg, Q. He, M. Piana, M. Tromp, and H.A. Gasteiger, "Understanding the Charging Mechanism of Lithium-Sulfur Batteries Using Spatially Resolved Operando X-Ray Absorption Spectroscopy," *J. Electrochem. Soc.*, vol. 163, no. 6, pp. A930–A939, 2016.
- [60] A. Berger, A. T. S. Freiberg, A. Siebel, R. Thomas, M. U. M. Patel, M. Tromp, H. A. Gasteiger, and Y. Gorlin, "The Importance of Chemical Reactions in the Charging Process of Lithium-Sulfur Batteries," *J. Electrochem. Soc.*, vol. 165, no. 7, pp. A1288–A1296, 2018.
- [61] E. C. Miller, R. M. Kasse, K. N. Heath, B. R. Perdue, and M. F. Toney, "Operando Spectromicroscopy of Sulfur Species in Lithium-Sulfur Batteries," *J. Electrochem. Soc.*, vol. 165, no. 1, pp. A6043–A6050, 2018.
- [62] Z. Lin, C. Nan, Y. Ye, J. Guo, J. Zhu, and E. J. Cairns, "High-performance lithium/sulfur cells with a bi-functionally immobilized sulfur cathode," *Nano Energy*, vol. 9, pp. 408–416, 2014.

- [63] X. Feng, M.-K. Song, W. C. Stolte, D. Gardenghi, D. Zhang, X. Sun, J. Zhu, E. J. Cairns, and J. Guo, "Understanding the degradation mechanism of rechargeable lithium/sulfur cells: A comprehensive study of the sulfur-graphene oxide cathode after discharge-charge cycling," *Phys. Chem. Chem. Phys.*, vol. 16, no. 32, pp. 16931–16940, 2014.
- [64] A. T. S. Freiberg, A. Siebel, A. Berger, S. M. Webb, Y. Gorlin, M. Tromp, and H. A. Gasteiger, "Insights into the Interconnection of the Electrodes and Electrolyte Species in Lithium-Sulfur Batteries Obtained Using Spatially Resolved *Operando* X-ray Absorption Spectroscopy and X-ray Fluorescence Mapping," *J. Phys. Chem. C*, vol. 122, pp. 5303–5316, 2018.
- [65] Y. Ye, A. Kawase, M.K. Song, B. Feng, Y. S. Liu, M. Marcus, J. Feng, E. Cairns, J. Guo and J. Zhu, "X-ray Absorption Spectroscopy Characterization of a Li/S Cell," *Nanomaterials*, vol. 6, no. 1, p. 14, 2016.
- [66] X. Yu, H. Pan , Y. Zhou , P. Northrup , J. Xiao , S. Bak , M. Liu , K. W. Nam , D. Qu, J. Liu , T. Wu, and X. Q. Yang, "Direct Observation of the Redistribution of Sulfur and Polysulfides in Li-S Batteries during the First Cycle by in Situ X-Ray Fluorescence Microscopy," *Adv. Energy Mater.*, vol. 5, no. 16, p. 10500072, 2015.
- [67] L. Zhang, M. Ling, J. Feng, L. Mai, G. Liu, and J. Guo, "The synergetic interaction between LiNO_3 and lithium polysulfides for suppressing shuttle effect of lithium-sulfur batteries," *Energy Storage Mater.*, vol. 11, no. July 2017, pp. 24–29, 2018.
- [68] M. A. Lowe, J. Gao, and H. D. Abruña, "Mechanistic insights into operational lithium–sulfur batteries by in situ X-ray diffraction and absorption spectroscopy," *RSC Adv.*, vol. 4, no. 35, pp. 18347–18353, 2014.
- [69] Y. Gorlin, A. Siebel, M. Piana, T. Huthwelker, H. Jha, G. Monsch, F. Kraus, H. A. Gasteiger, and M. Tromp, "Operando Characterization of Intermediates Produced in a Lithium-Sulfur Battery," *J. Electrochem. Soc.*, vol. 162, no. 7, pp. A1146–A1155, 2015.

- [70] J. Gao, M. a Lowe, Y. Kiya, and D. Abru, "Effects of Liquid Electrolytes on the Charge-Discharge Performance of Rechargeable Lithium / Sulfur Batteries : Electrochemical and in-Situ X-ray Absorption Spectroscopic Studies," *J. Phys. Chem. C*, vol. 115, pp. 25132–25137, 2011.
- [71] T. A. Pascal, C. D. Pemmaraju, and D. Prendergast, "X-ray spectroscopy as a probe for lithium polysulfide radicals," *Phys. Chem. Chem. Phys.*, vol. 17, no. 12, pp. 7743–7753, 2015.
- [72] K. Sun, Q. Wu, X. Tong, and H. Gan, "Electrolyte with Low Polysulfide Solubility for Li-S Batteries," *ACS Appl. Energy Mater.*, vol. 1, no. 6, pp. 2608–2618, 2018.

Chapter 4

Sulphur Cathodes with Inorganic Additives

4.1 Introduction

Diffusional loss of sulphur active material during Li-S cell cycling is a serious issue, strongly affecting the cycle life and rate performance of the system. The optimisation of the electrode structure is one of the most appropriate and promising approaches to this problem. In this chapter, attention will be given to the effect of using metal oxides and sulphides (hereby denoted as 'MX') as additives in the sulphur cathode. MXs are expected to control the polysulphide shuttle mechanism by trapping lithium polysulphides via electrostatic attraction between the lithium polysulphide and MX particles preventing a diffusional loss of polysulphides [1] It has also been proposed that some MX additives behave as catalysts favouring the conversion of polysulphides. [2]

Recently, there has been a trend for the utilisation of materials that adsorb polysulphides, such as, metal oxides, [3] metal sulphides, [2] metal carbides, [4] metal-organic frameworks (MOFs) [5] into the cathode to entrap polysulphides within the sulphur cathode stabilising the battery cycling performance. [6][7] Metal oxides tend to be insoluble in most organic solvents due to their strong ionic and covalent bonding between the oxygen and metal. [2] Such materials, including MgO [8], TiO₂ [9], Al₂O₃ [10][11] are inherently polar that can strongly bind with polar polysulphide molecules preventing the detachment of lithium polysulphides into the electrolyte as well as providing the enhanced utilisation of sulphur active material. [2][12][13] It is also known that the bonding energies between some metal oxides and polysulphide species are higher than those with classic carbon materials and polymers. [14] Thus, the inorganic non-carbon materials and bonding mechanism have been attracting great attention. Additionally, these materials offer the possibility of accelerating the

reaction kinetics of soluble lithium polysulphides to insoluble $\text{Li}_2\text{S}_2/\text{Li}_2\text{S}$, or the inverse process, [2] explaining why MX additives sometimes are referred to as catalysts. [12]

However, most of these inorganic non-carbon materials cannot achieve the high rate performance on its own due to their poor-conductive nature. Therefore, they are often fabricated with a combination of carbon supporters, such as, graphene/carbon nanotubes, mesoporous carbon, and hollow carbon nanofiber [14], forming composite cathodes. These carbon supporters also serve as additives and boost the conductivity of the overall electrode and improving the performance of the batteries. [15] Therefore, it is difficult to solely measure the effect of the inorganic materials. For this reason, despite these attractive attributes of MXs, the direct effect of these materials is less investigated at the moment and the exact mechanisms of interactions between metal oxides and polysulphides are still unclear. [2][16] The polysulphide shuttle effect has been extensively studied in the presence of MX particles, but manipulating the redox reactivity of polysulphides and how this influences the polysulphide formation are rarely investigated.

In this study, to gain insights into the effect of these materials towards the sulphur reaction mechanisms, *operando* XANES analysis was conducted as well as electrochemical analysis. There is a wide range of selections of such inorganic materials. To help choosing the materials to investigate for this study, we followed the guidelines discussed below.

The Nazar group proposed their 'goldilocks' principle to search for the best metal oxides. [3] It was demonstrated that entrapment of polysulphides relies on the chemical catenation of lithium polysulphides by the thiosulphate or/and polythionate conversion. The anchor mechanism differs by the redox potential of metal oxides, which are divided into three groups in terms of their redox potentials versus Li/Li^+ summarised schematically in **Figure 4-1**. It was reported that the metal oxides with redox potential in a target window of 2.4 to 3.05 V effectively adsorb the polysulphide and engage in surface redox chemistry which oxidise lithium polysulphide to form thiosulphate or/and polythionate groups to chemically bind with reduced metal oxide surface. On the other hand, materials with the redox potential below 1.5 V do not contribute to the redox reaction with polysulphide, although strong surface

interactions still exist to hinder the polysulphide dissolution, while materials with excessive redox potential (> 3.05 V) oxidise polysulphide to inactive sulphate groups. [17][18][19][20]

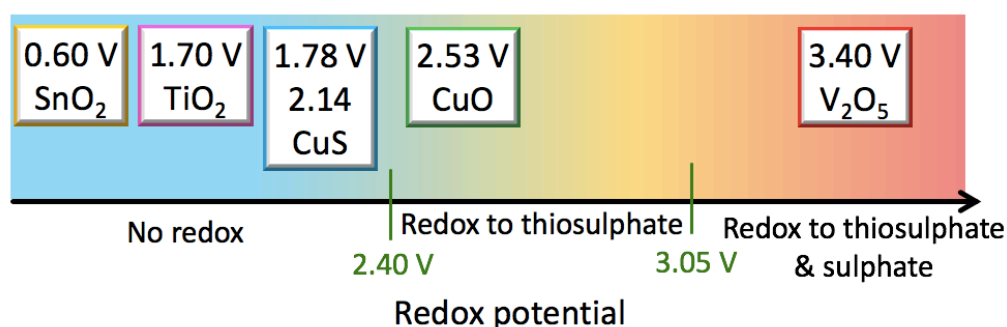


Figure 4-1. Reactivity of different MXs with lithium polysulphides as a function of redox potentials vs Li/Li⁺. Graph reproduced from [17].

Nazar and co-workers also proposed the use of the Magneli-phase of Ti₄O₇, it was demonstrated that Ti₄O₇ strongly binds polysulphide and Li₂S, enhancing surface-mediated redox reaction. [21] The Cui group [22] recently reported a standard procedure to quantitatively compare the polysulphide adsorption capability of several metal oxides, sulphides, and nitrides using Ultraviolet-visible spectroscopy (UV-VIS), X-ray Photoelectron Spectroscopy (XPS), and inductively coupled plasma atomic emission spectroscopy (ICP-AES). UV-VIS determines the polysulphide adsorption capability, while XPS detects the species adsorbed, and ICP-AES is used to measure the total concentration of lithium and sulphur atoms in the sample. It was reported that MnO₂ and V₂O₅ are significantly strong polysulphide adsorbing additives.

In this work, the impact of the MX additives on polysulphide shuttle phenomenon in Li-S cell is examined with the aim of understanding the function of MXs redox reactions and polysulphide formation during the electrochemical cycling. Based on interest and availability, four metal oxides and one metal sulphide, TiO₂, CuO, SnO₂, V₂O₅, and CuS are tested. When referring to MX in this chapter, M = metal and X = oxides or sulphides. Advantageous properties of those selected MXs are explained below.

V₂O₅ is a good solid-state lithium ion conductor and commonly used as a cathode material for Li-ion batteries. [23] In the work of Kim *et al*, [24] it was found that

excessive formation of Li_2S degrades the capacity retention due to large volume expansion, which disturbs the network between active sulphur species and carbon. V_2O_5 -carbon nanocomposite was fabricated as an additive to sulphur electrode and demonstrated to suppress the excessive formation of Li_2S and contribute to minimise the shuttle reaction by capturing polysulphides. [24] Another approach is the use of V_2O_5 -decorated carbon nanofibers as an interlayer between the cathode and the separator, which effectively restrained the shuttle effect and remarkably mitigated the self-discharge phenomenon in Li-S batteries. [25] Nevertheless, slow Li^+ -ion diffusion coefficient ($10^{-12} \text{ cm}^2 \text{ s}^{-1}$) and low electrical conductivity ($10^{-4} \sim 10^{-5} \text{ S cm}^{-1}$) of V_2O_5 hinders its practical application.

TiO₂ has proven effective in promoting the chemical attractions with polar polysulphides due to its high chemical adsorption ability. [26] TiO_2 is known as a nontoxic and economical material. [27] The hydrophilic properties of Ti-O groups and surface hydroxyl groups favors the binding with polysulphide anions, which can mitigate the dissolution of polysulphides. [9][28] Application of TiO_2 in the Li-S battery systems became attractive after it was first report by Cui *et al*, [29] proposing the use of yolk-shell structured TiO_2 which provide sufficient voids to comfortably accommodate the volume expansion of sulphur associated with the lithiation process. The yolk-shell design contributes to maintain the structural integrity of the shell to effectively control the polysulphide dissolution. [30] Moreover, these metal oxide materials also render the possibility of catalytic effect to favour the conversion of lithium polysulphides to $\text{Li}_2\text{S}_2/\text{Li}_2\text{S}$ or the inverse process, directing the relatively less diffusion of polysulphides in the electrolyte. [31]

CuO is a well-known semiconductor material with a redox potential of 2.53 V, which is in the lower end of the 'goldilocks' principle target range and expected to promote polythionate formation to improve the cycling performance of Li-S cell. [17] Additionally, CuO can be an efficient material in restricting sulphur and polysulphide in the cathode of Li-S batteries [32] With these merits, the sulphur cathode fabricated using CuO additive is expected to show significant improvements in both cycling stability and efficiency.

CuS is a good electric conductor (870 S cm^{-1}) and a promising material researched as cathode material in Li-ion batteries. Among the variety of different transition metal sulphides, CuS exhibits a high theoretical capacity (560 mAh g^{-1}) with a flat discharge plateau and ability to retain good capacity over repeated cycles. CuS gives the opportunity for additional capacity when used as an additive for Li-S cathode, because its redox potential ($2.14 \text{ V vs Li/Li}^+$) is in the vicinity of the working voltage of Li-S cell. [33]

SnO₂ is typically studied as an anode material for Li-ion batteries, [34] but also reported as an effective adsorbent for polysulphides although it has low electrical conductivity. Jing *et al.* [15] demonstrated the use of SnO₂ as an interlayer between the cathode and the separator to efficiently trap lithium polysulphides.

To investigate the influences of these MX additives listed above, cathodes were prepared with sulphur content of 48 wt% and 12 wt % of MX additives using a cost-effective method. Electrochemical characterisation along with comprehensive chemical analysis using *operando* XAS measurement was performed to understand the impact of the MX additives on polysulphide shuttle phenomenon in Li-S cell. Also, a unique XAS measurement technique of simultaneously probing at the K-edges of two elements is demonstrated in this study.

4.2 Material preparations

4.2.1 Electrode preparations

Cathodes were composed of sulphur, MX additives, acetylene black (AB) and PVP binder with a mass ratio of 48:12:25:15. MX@S composites were synthesised via hydrothermal process as described in Chapter 2. Sulphur was melt diffused in MXs by heat treatment at $155 \text{ }^\circ\text{C}$ for 12 hours prior to mixing with carbon and PVP in NMP solution to make a slurry. For CuS@S electrode, composite mixing step is carried out in an argon glove box due to the sensitivity CuS towards moisture and oxygen. The sulphur impregnated MXs were denoted as “MX@S” where MX = CuO, CuS, SnO₂, TiO₂ or V₂O₅. Slurry coating and coin cell fabrication are described in **Section 2.1.1**. Simple and standardised electrode fabrication method was chosen to elucidate only the effect of the MXs on the electrochemical performance, avoiding the possible contribution from advanced carbon materials.

4.3 Material characterisations

XRD measurements

To characterise the composite cathodes, the structural features of the as-prepared electrodes were analysed using powder XRD and displayed in **Figure 4-2a-e**. No new peaks were found, indicating phase purity of these materials.

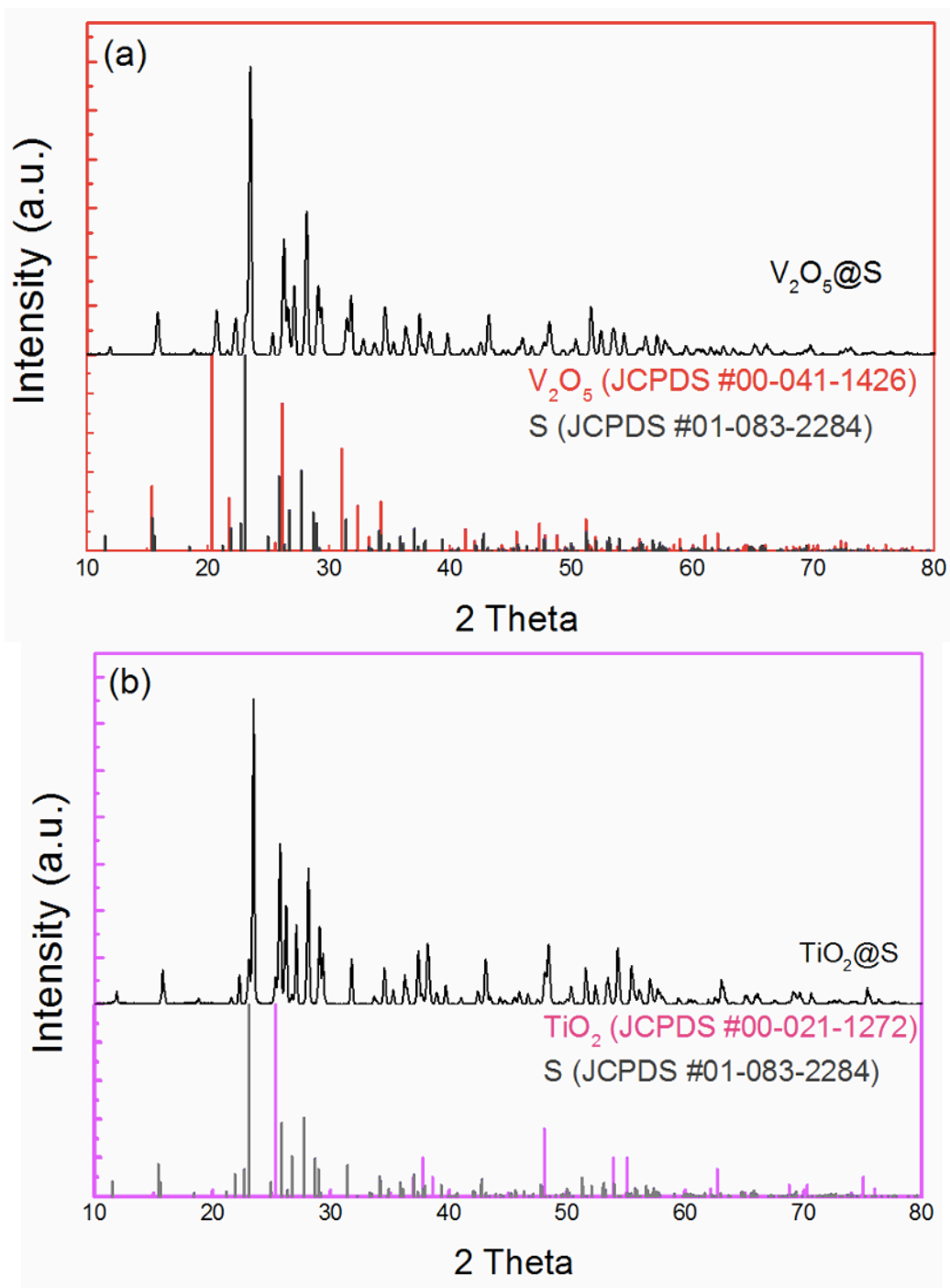


Figure 4-2. XRD patterns of prepared composites. (a) V₂O₅@S and (b) TiO₂@S.

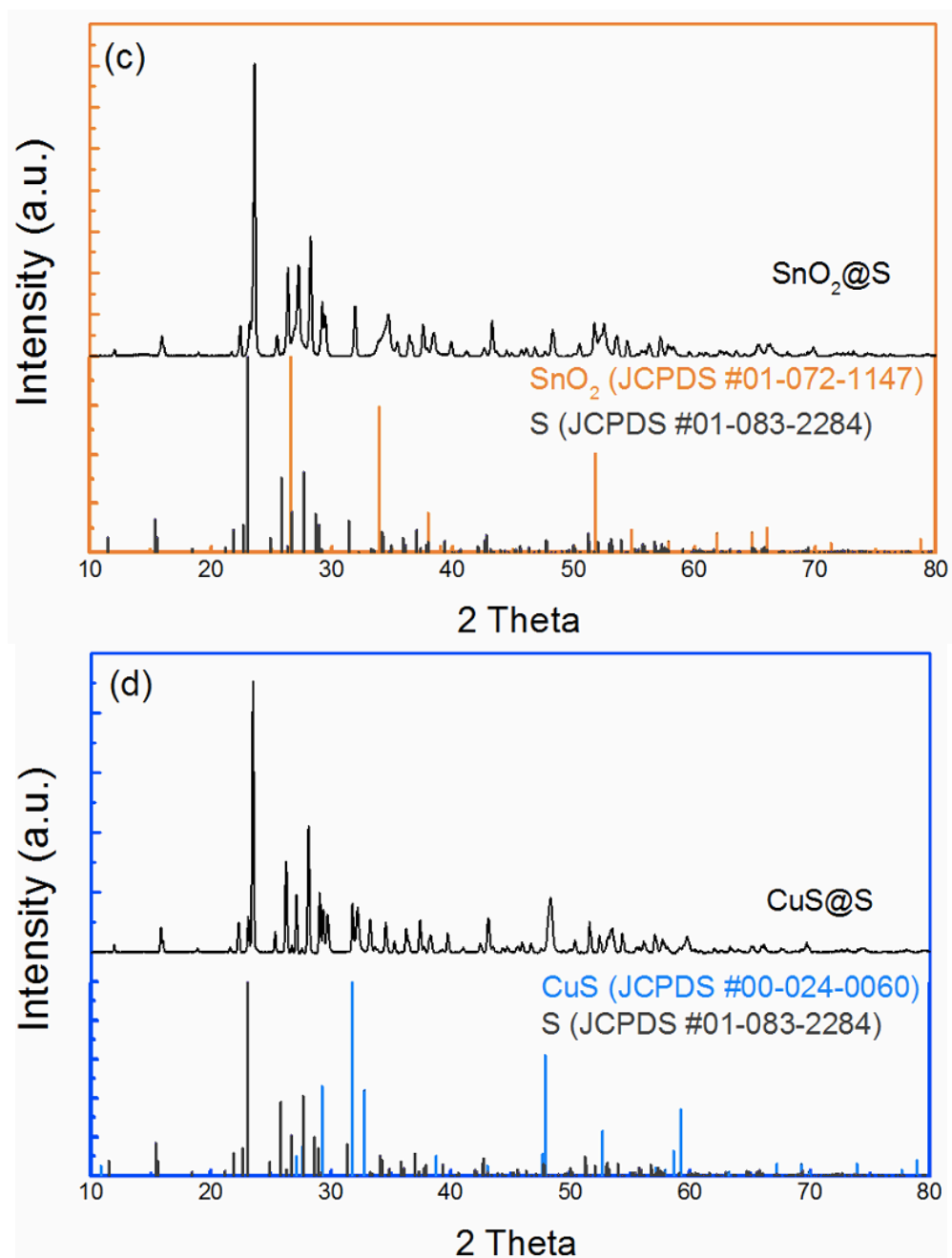


Figure 4-2. Continued. (c) XRD patterns of SnO₂@S and (d) CuS@S.

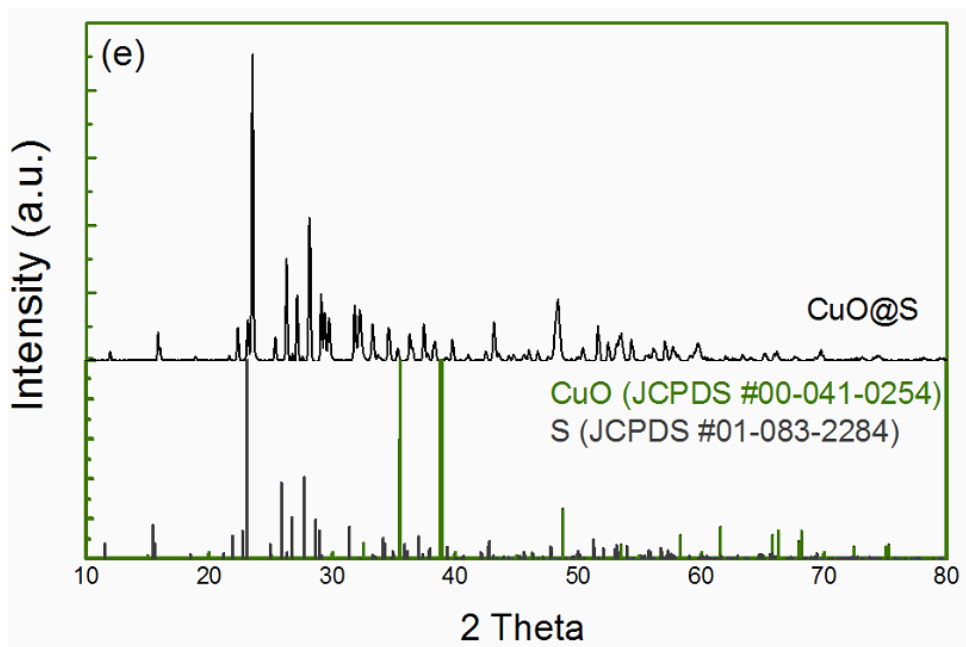


Figure 4-2. Continued. (e) CuO@S.

4.4 Electrochemical measurements

Galvanostatic discharge/charge were performed on each electrode to evaluate their electrochemical performances. These measurements were undertaken using conventional CR2016 coin cells. All cells were cycled using TEGDME solvent with 1 M LiTDI salt as the electrolyte. Electrolytes were prepared both with and without LiNO₃ as an additive and denoted by the acronyms “LiTDI/TEGDME” for the LiNO₃-free electrolyte and “LiTDI/TEGDME/LiNO₃” for the 0.25 M LiNO₃-containing electrolyte.

The summary of discharge/charge curves, cycle performance, and colombic efficiency of sulphur electrode with different MX additives are represented in **Figure 4-3** (without LiNO₃) and **Figure 4-4** (with LiNO₃), compared with pure sulphur electrode. **Table 4-1** summarises the redox potential of each MX additives and 1st discharge capacities of each cell. In this study, pure S electrodes (S+AB+PVP) were used as a reference electrode to compare the electrochemical behaviour without MX additives.

Table 4-1. Redox potentials of the MX additives studied in this work and the initial discharge capacities of each MX@S cycled using LiTDI/TEGDME and LiTDI/TEGDME/LiNO₃ electrolytes. (* indicates the higher capacity compared between an electrolyte with and without LiNO₃)

| Supporting additive | Redox potential (V) vs Li/Li ⁺ | 1st discharge capacity LiTDI/TEGDME | 1st discharge capacity LiTDI/TEGDME/LiNO ₃ |
|-------------------------------|---|-------------------------------------|---|
| Pure S | 2.4, 2.0 | * 970 mAh g ⁻¹ | 950 mAh g ⁻¹ |
| SnO ₂ | 0.6 [35] | 1345 mAh g ⁻¹ | *1545 mAh g ⁻¹ |
| TiO ₂ | 1.70 [36] | 1285 mAh g ⁻¹ | *1290 mAh g ⁻¹ |
| CuS | 2.14, 1.78 [37] | 1335 mAh g ⁻¹ | *1560 mAh g ⁻¹ |
| CuO | 2.53 [32] | *1390 mAh g ⁻¹ | 1175 mAh g ⁻¹ |
| V ₂ O ₅ | 3.40 [17] | *1270 mAh g ⁻¹ | 1040 mAh g ⁻¹ |

Firstly, the electrochemical performance of each electrode cycled in LiTDI/TEGDME electrolyte is discussed followed by the discussion of LiTDI/TEGDME/LiNO₃ electrolyte.

4.4.1 LiTDI/TEGDME

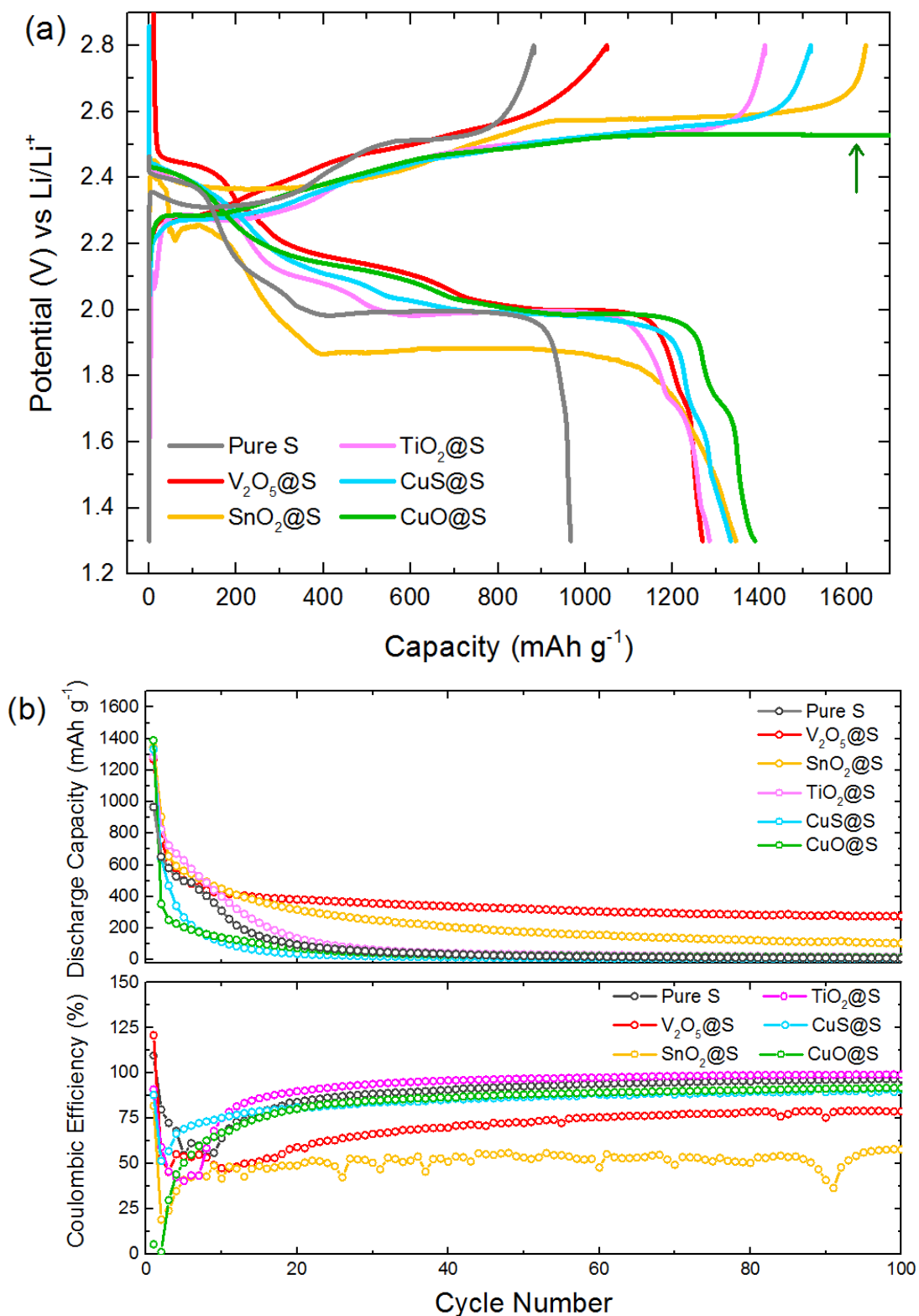


Figure 4-3. Electrochemical performances of sulphur composite electrodes with different MX additives assembled in LiTDI/TEGDME electrolyte cycled at the 0.1 C rate. (a) Discharge/charge curves and (b) Cycling performances and coulombic efficiencies.

Overall, the initial discharge profiles of most of the electrodes with MX additives exhibit a two-step lithiation process as in the reference cell (**Figure 4-3a**). The two voltage plateaus obtained during the discharging curves located around 2.4 V and 2.0 V are generally regarded as the reduction of S₈ to long/medium-chain polysulphides for the high voltage plateau and long/medium chain to short chain polysulphides for the low voltage plateau, respectively.

An important observation in **Figure 4-3a** is that all cells with MX additives achieved higher initial discharge capacity than that of the pure sulphur (also reported in **Table 4-1**). This is probably because MX additives provide additional surface area where polysulphide can adhere increasing the utilisation of sulphur. [24] Based on the initial discharge and charge profile, it is clear that the variation of MXs selected have positive effect on the Li-S cell capacities independently of the presence of the LiNO₃ salt. However, only V₂O₅ and SnO₂ additives seem to give comparable results with the pure S electrode in the reference cell in prolonged cycles.

The electrochemical performances of each MX@S electrode cycled in LiTDI/TEGDME electrolyte will be discussed individually starting with the SnO₂ additive as it appears to have a positive effect to on the cell stability (**Figure 4-3b**).

In the initial discharge, SnO₂@S suffers from large voltage polarisation, with the high voltage plateau decreased from 2.4 to 2.25 V and low voltage plateau decreased from 2.0 to 1.8 V (**Figure 4-3a**, yellow line), which is a result of the low efficiency of sulphur reduction kinetics due to elevated internal resistance. [21] Despite this negative effect, the SnO₂ additive improved the initial discharge capacity from 970 mAh g⁻¹ (pure sulphure electrode) to 1345 mAh g⁻¹ and maintained a larger capacity than pure S electrode after 100 cycles (**Figure 4-3b**).

CuO@S cell presented the highest initial discharge capacity of 1390 mAh g⁻¹ among all the cells studied in **Figure 4-3a**, but exhibits endless charging associated with a polysulphide shuttle as marked by the green arrow in **Figure 4-3a**. Despite its high initial discharge capacity, this cell exhibits very fast capacity decay, indicating a significant impact of the shuttle effect of polysulphides (**Figure 4-3b**). The redox potential of CuO (2.53 V) lies between the targeted range of the 'goldilocks' principle (**Table 4-1**), 2.4 V < E < 3.05 V vs Li/Li⁺, proposed to effectively promote the

polythionate formation and suppress the shuttle reaction. From this guideline, we expected the CuO@S electrode to show the best cycling performance among other MX additives studied here. However, in fact, the CuO@S electrode exhibited the worst cell performance as oppose to our speculation. This suggests that the simple sulphur impregnation synthetic route is not good enough to prepare a CuO stabilised sulphur cathode. More sophisticated preparation method is required to employ CuO as a successful additive in sulphur cathode composite. CuS@S cell exhibited a similar electrochemical performance as the CuO@S cell (**Figure 4-3**); very high initial discharge capacity but significantly fast capacity decay phenomenon.

The TiO₂@S electrode shows a slightly better capacity stability than the pure S electrode (**Figure 4-3b**), but still suffers from fast capacity decay that falls below 400 mAh g⁻¹ within 10 cycles.

While most of the cells (pure S, CuO@S, CuS@S, and TiO₂@S) shown in **Figure 4-3b** failed to reach 100 mAh g⁻¹ after 25 cycles (average < 10% capacity retention), V₂O₅@S and SnO₂@S cells showed stable cycling performance retaining 445 mAh g⁻¹ and 175 mAh g⁻¹ after 50 cycles, respectively. For the V₂O₅@S cell, although a considerable irreversible charging capacity found in the initial cycle (**Figure 4-3a**) and the CE values are inferior to that of other cells (**Figure 4-3b**), this electrode showed the slowest capacity fading rate after 10 cycles.

From these results, we can conclude that the sulphur electrodes with MX additives are difficult to achieve a desired cell performance in the absence of LiNO₃. This is probably because the severe shuttle reaction, as can be suggested from low CE values observed in each cell. However, the V₂O₅ and SnO₂ seem to be promising additives effectively improving the cell cycle life with low capacity fading rate after few cycles. We can safely assume that the additional capacities are not arising from these two additives, as V₂O₅ and SnO₂ redox potentials versus Li/Li⁺ of 3.40 V and 0.6 V, respectively, which are far from the voltage window tested here (1.3 – 2.8 V). This improvement agrees to the previous publications, where V₂O₅/carbon nanocomposite to the cathode of a Li-S battery was demonstrated to capture long-chain polysulphides and limiting the excess formation of Li₂S, hence mitigating the volume expansion of the sulphur particles. This was in the case of the electrolyte containing 3 M LiTFSI dissolved in DOL:DME [24].

4.4.2 LiTDI/TEGDME/LiNO₃

The MX@S electrodes were also tested in the electrolyte systems containing 0.25 M LiNO₃ under the same conditions. **Figure 4-4a** shows the initial discharge/charge curves of the MX@S electrodes and pure S electrode cycled in LiTDI/TEGDME/LiNO₃ electrolyte and **Figure 4-4b** represents the cycling performance of each cell. A summary of the repeated discharge/charge curves are displayed in **Figure 4-5**.

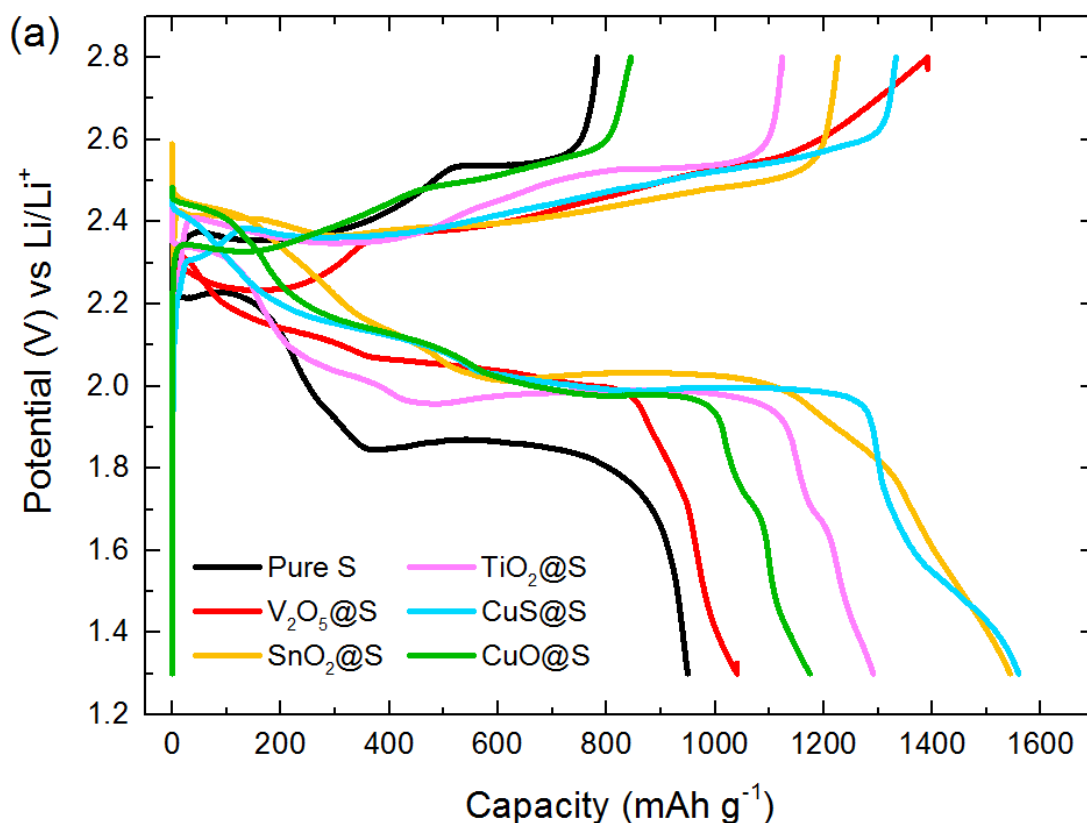


Figure 4-4. Electrochemical performances of sulphur composite electrodes with different MX additives assembled in LiTDI/TEGDME/LiNO₃ electrolyte cycled at a current rate of 0.1 C. (a) The first discharge/charge curves.

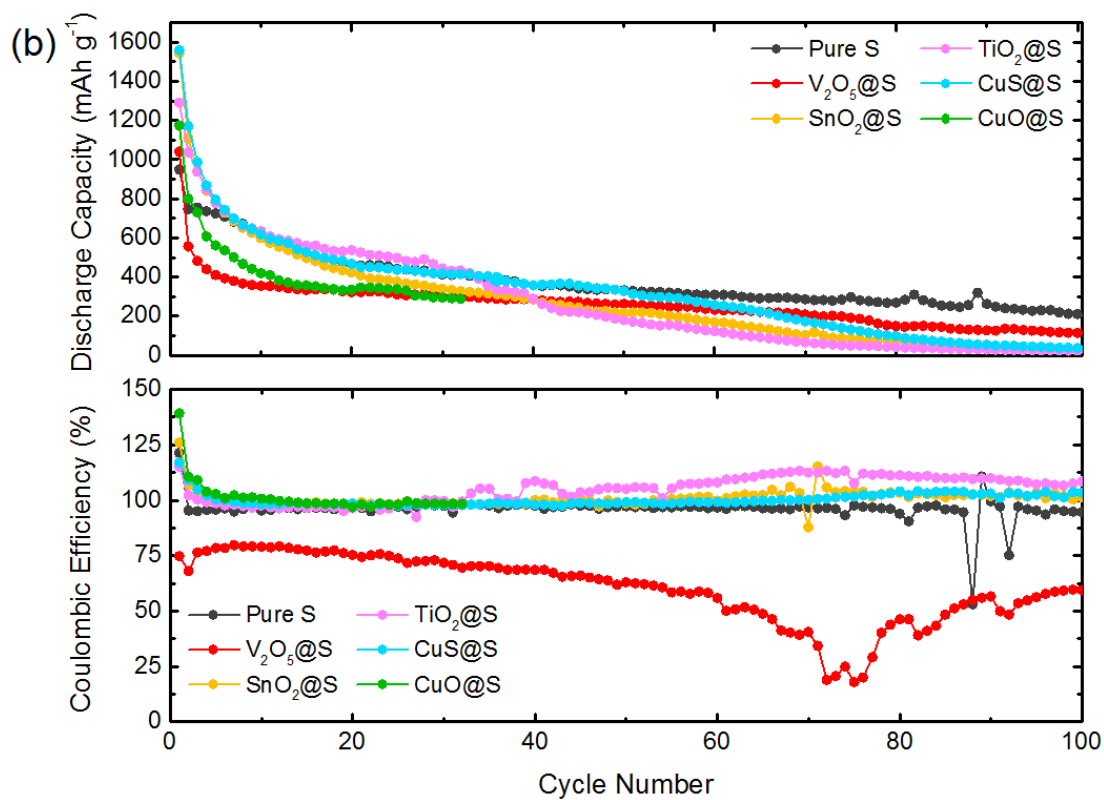


Figure 4-4. Continued. (b) Cycling performances and coulombic efficiencies.

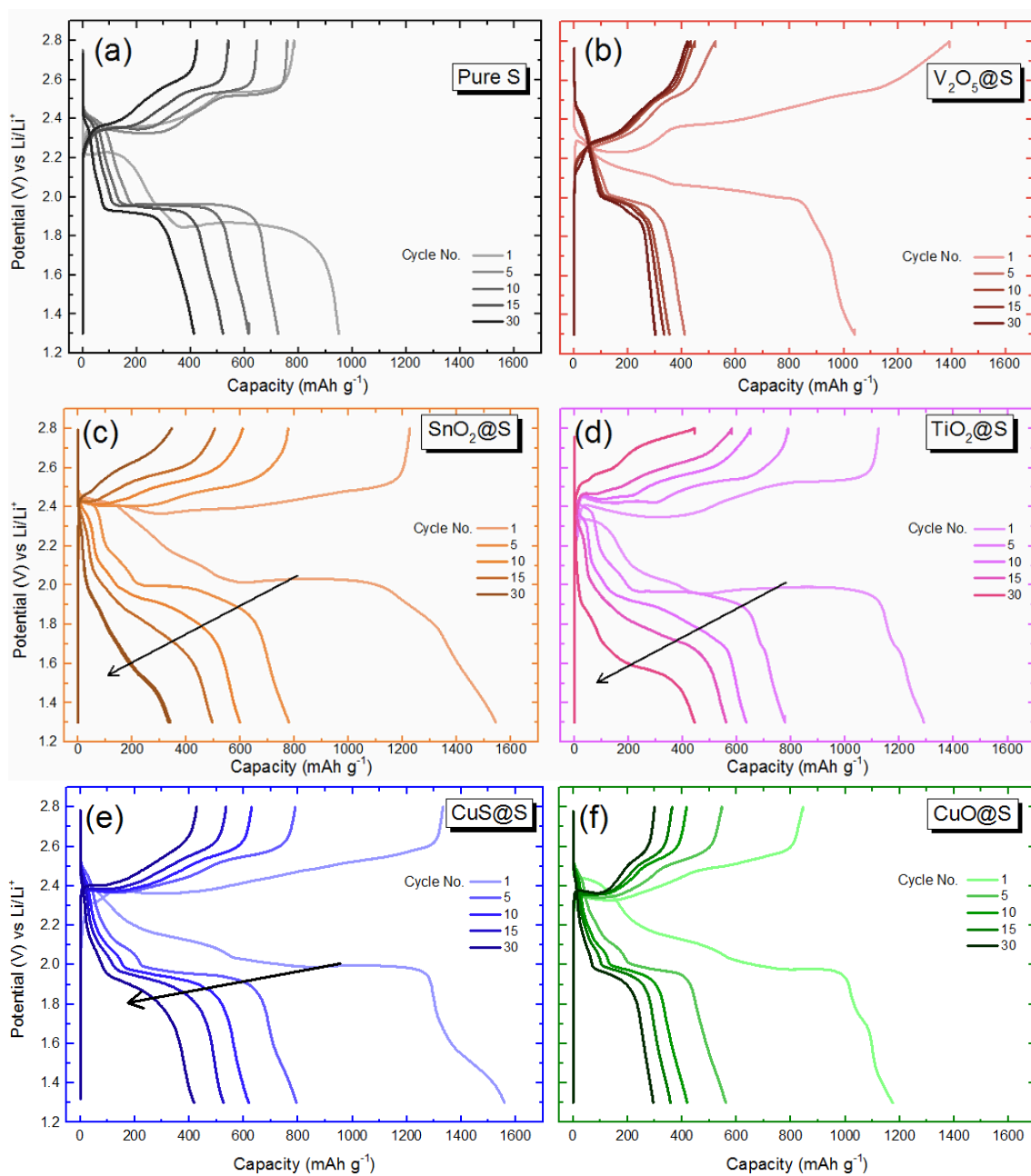


Figure 4-5. Galvanostatic discharge/charge curves of pure S electrode and MX@S electrodes cycled in LiTDI/TEGDME/LiNO₃ electrolyte at a constant current rate of 0.1 C. (a) Pure sulphur electrode, (b) V₂O₅@S cathode, (c) SnO₂@S cathode, (d) TiO₂@S cathode, (e) CuS@S cathode, and (f) CuO@S cathode.

The remarkable advantages of the MXs as additives to the sulphur electrode are evident in the initial discharge capacity, again, all MX-stabilised S cathodes yielding significantly higher capacity values than that of the pure S cathode (**Table 4-1**).

The initial discharge capacities of $V_2O_5@S$, $SnO_2@S$, $TiO_2@S$, $CuS@S$, $CuO@S$, and pure S electrodes at the 0.1 C rate are measured to be 1040, 1545, 1290, 1560, 1175, and 950 mAh g^{-1} , respectively. These capacities are all higher than those without $LiNO_3$, except for the $CuO@S$ and $V_2O_5@S$ cells, both demonstrating about 200 mAh g^{-1} less capacities in the presence of the $LiNO_3$ salt. The electrochemical performances of each $MX@S$ electrode are discussed individually starting with the $SnO_2@S$ cell.

The discharge voltage plateaus of $SnO_2@S$ are successfully elevated to the expected values of about 2.4 V and 2.0 V (**Figure 4-4b**), in the presence of $LiNO_3$ and the CE values are effectively improved, as opposed to the cell system in the absence of the $LiNO_3$ salt (**Figure 4-3a**).

Over the first 30 cycles, the cells based on $TiO_2@S$, $CuS@S$, and pure S electrodes exhibit similar capacity stabilities (**Figure 4-4b**), retaining 445, 420, and 410 mAh g^{-1} , respectively. After this point, the behaviour of the $TiO_2@S$ cell diverges, showing more pronounced capacity decay on continued cycling with the CE values exceeding 100%, indicating that some side reaction may happen at the anode between the Li metal and polysulphides during the discharge process. These degradation products can not be reversibly oxidised in the following charging process. This cell reaches the lowest discharge capacity after 50 cycles among all the cells.

After 50 cycles, the $CuS@S$ cell shows degrading electrochemical performance (**Figure 4-4b**), which again accelerated the capacity fading rate after this point. The capacity fading behaviour of these two cells ($CuS@S$ and $TiO_2@S$) are highly related to the voltage polarisation effect, indicated by the arrows in **Figure 4-5d** and **e**, which seem to be more severe in $TiO_2@S$ at earlier stages of the prolonged cycling.

In contrast, the $CuO@S$ and $V_2O_5@S$ cathodes exhibit drastic capacity fade in the first 10 cycles, but the capacity fading rate is kept very low afterwards. In the repeated cycling curves shown in **Figure 4-5b** and **f**, it is notable that these two electrodes achieved to retain the discharge voltage plateaus flat and stable with small polarisations. In these cells, the capacity fading is simply caused by the shortening of the plateau capacities. While in the other cells the output voltages of discharge plateaus being reduced. This type of capacity fading mechanism should be separated from the one above, where the large voltage polarisation causes the degradation of

the cell. The suppressed polarisation effect may be related to the limited nucleation of the insoluble $\text{Li}_2\text{S}_2/\text{Li}_2\text{S}$, as the cell polarisation happens due to the elevated internal resistance of the cell during formation of insoluble $\text{Li}_2\text{S}_2/\text{Li}_2\text{S}$. [38] This means, cells are mostly operating via conversion between long and short-chain polysulphide, so the capacity delivered for each cycle are relatively small, but the voltage degradation is kept to the minimum and excellent cell stabilities are achieved for the CuO@S and $\text{V}_2\text{O}_5\text{@S}$ cells. Particularly, the $\text{V}_2\text{O}_5\text{@S}$ cell delivers low capacity fading rate of only 1.3 % per cycle between 10 th and 100 th cycles.

Summary of electrochemical performances

It was found that the MXs additives largely improve the initial discharge capacity and this effect was independent of the presence of LiNO_3 . It should be emphasised that the SnO_2 and V_2O_5 additives contribute to an excellent cell stability even after 50 cycles in the absence of LiNO_3 salt. Specifically, the $\text{V}_2\text{O}_5\text{@S}$ electrode highlighted its capability to suppress the capacity fading rate independently of the presence of LiNO_3 . The electrochemical results suggest that degradation mechanisms are different in different MXs, implying that the polysulphide conversion reactions are altered by MXs. These cells are further investigated using *operando* XAS technique.

4.5 XAS analysis

To track the redox chemistry of S in working electrodes and reveal the detailed capacity decay mechanism, *operando* XANES analysis were performed on the as-prepared five different MX@S cathodes. All the measured cells were cycled at the 0.1 C rate and XAS spectra were recorded throughout the first discharge and charge electrochemical cycle, unless otherwise stated. Before applying a current to start the *operando* measurements, the pristine spectra were collected at the OCV (indicated as the pristine state, “spectrum number 0” in each XANES set).

Spectra were recorded in the energy range of 2450 to 2520eV, with a step size of 1.5 eV before the pre-edge (2450 – 2465 eV), 0.16 eV in the pre-edge, main-edge, and electrolyte region (2465 - 2495 eV), and 1 eV between 2495 – 2520 eV, with a counting time of 5 seconds per point, resulting in a total acquisition time of 25 - 27 minutes, corresponding to approximately 50 ~ 60 mAh g^{-1} per spectrum, unless otherwise stated.

In this chapter, XAS measurements were performed at two different synchrotrons facilities: (i) ESRF; beamline BM28 and (ii) DLS; beamline B18. **Table 4-2** summarise the samples analysed in each beamline. Details of the XAS experiment set-up is described in **Section 2.3**. All *operando* measurements were performed using a Ketek detector and modified coin cells described in **Section 2.4.2**.

From the previous section, it was revealed that better cycling performance can be achieved using LiNO₃-contained electrolyte, therefore, we focus our attention particularly on the LiNO₃-contained electrolyte, where all cells were standardised with sulphur-free LiTDI/TEGDME/LiNO₃ electrolyte to avoid the strong signals arising from the sulphur present in the electrolyte masking the electrochemically active sulphur peaks in the XAS measurements.

Table 4-2. List of additives tested using XAS measurements

| Synchrotron | Edge | Additive | Type of measurement | Data collection |
|-------------|-----------------------|-------------------------------|--------------------------------------|-----------------|
| ESRF | S K-edge | SnO ₂ | <i>Operando</i> XANES | ✓ |
| | S K-edge | V ₂ O ₅ | <i>Operando</i> XANES | ✓ |
| | S K-edge | CuO | <i>Operando</i> XANES | ✓ |
| | S K-edge | CuS | <i>Operando</i> XANES | ✓ |
| | S K-edge | TiO ₂ | <i>Operando</i> XANES | ✓ |
| | S K-edge Ti K-edge | TiO ₂ | <i>Operando</i> double-edge XANES | ✓ |
| DLS | Ti K-edge | TiO ₂ | <i>Ex situ</i> EXAFS | ✓ |

| | |
|--|-----------------------------------|
| | XAS obtained for a complete cycle |
| | Part XAS data missing |

4.5.1 S K-edge XANES – Pristine spectrum of each cell

Slight difference was already observed in the pristine state when comparing the S K-edge spectra of each MX@S electrode, which is highly related to the rate of self-discharge effect. As previously explained in **Chapter 3**, the self-discharge phenomenon

occurred during cell storage and can be recognised by the presence of the pre-edge feature in XANAES spectrum at the pristine state, where the pre-edge feature represents the presence of long-chain polysulphides. **Table 4-3** summarises the observation of the pre-edge feature in the pristine spectrum of each cell and **Figure 4-6** represents the pristine spectra of each cell.

Table 4-3. A summary of the pre-edge detection in different MX@S electrodes at OCV after storage

| Detection of the pre-edge in the pristine state | |
|--|--------------------------|
| No/little pre-edge | Pre-edge detected |
| V ₂ O ₅ | SnO ₂ |
| CuO | TiO ₂ |
| | CuS |

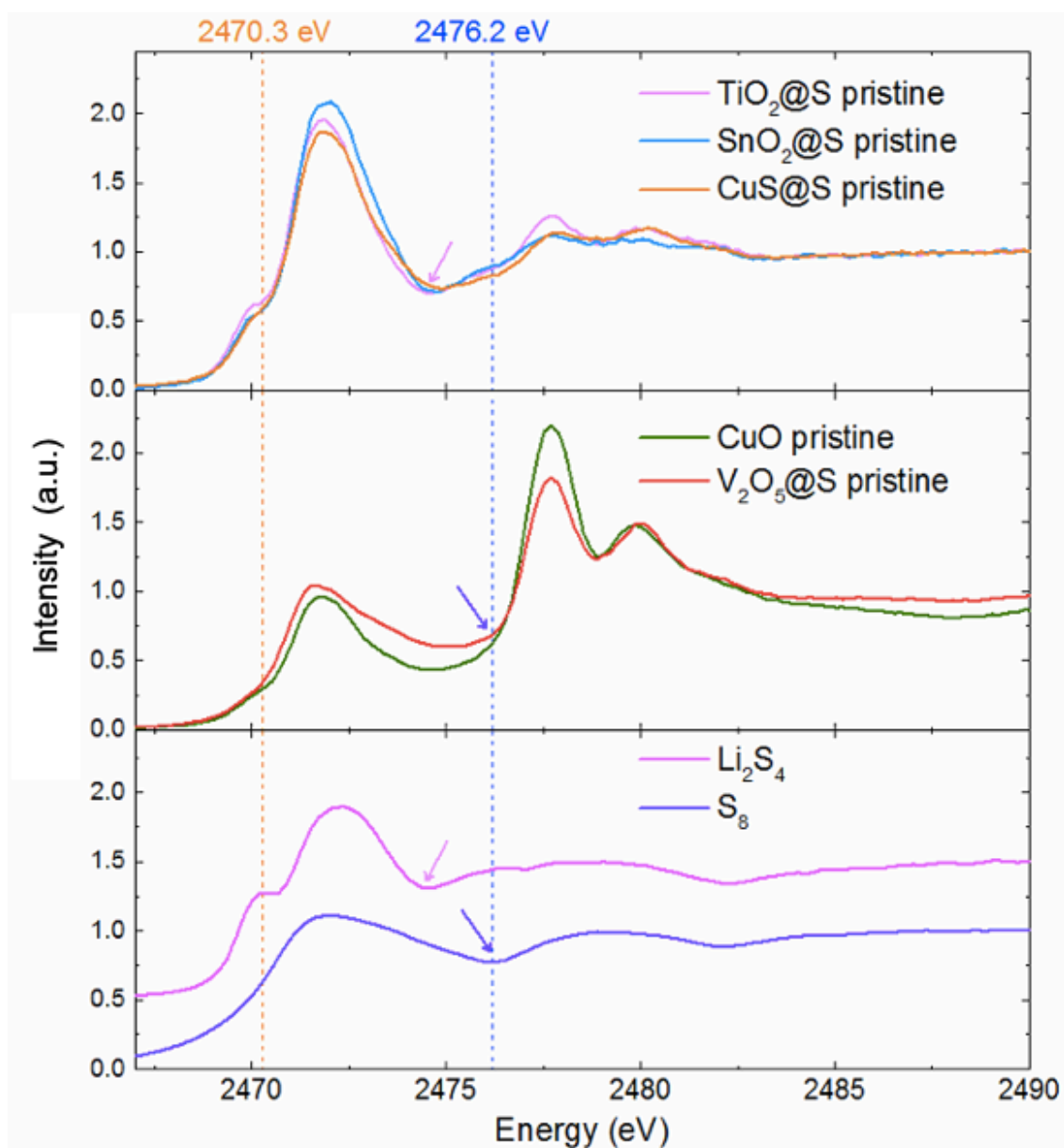


Figure 4-6. S K-edge XANES spectra of (a) $\text{TiO}_2@S$, $\text{SnO}_2@S$, and CuS@S cells, (b) CuO@S and $\text{V}_2\text{O}_5@S$ cells, all at the pristine state, and (c) S_8 and Li_2S_4 reference compounds (offset for clarity).

The S K-edge XANES spectra of the pristine state of each MXs@S cell are compared with the reference compounds of S_8 and Li_2S_4 in **Figure 4-6**. The pristine spectra of $\text{TiO}_2@S$, $\text{SnO}_2@S$ and CuS@S cells exhibited the pre-edge feature at 2470.3 eV accompanying with the main-edge at about 2472 eV, and the concave feature at 2474.5 eV (**Figure 4-6a**), indicating that the long-chain polysulphides being present in the cells. At OCV, polysulphides can only be formed from chemical reaction between

dissolved S_8 and Li-ions that exist in the electrolyte, therefore, the pre-edge detected at the OCV is a strong evidence of self-discharge reaction.

On the contrary, the $V_2O_5@S$ electrode did not observe the pre-edge signature, indicating the absence of terminal sulphur atoms (**Figure 4-6b**). This observation strengthens by the fact that the concave feature coincides with that of S_8 reference compounds, as highlighted by the arrow in **Figure 4-6b**. These findings confirm that polysulphide species are not formed during cell storage. In other words, V_2O_5 additive successfully limiting the self-discharge phenomenon.

The pristine spectrum of the $CuO@S$ cell also exhibited spectral feature similar to that of S_8 reference compound in the active sulphur region, but the weak pre-edge detected at 2470.3 eV and broad concave centered at around 2475.0 eV is noticed (**Figure 4-6b**). This suggests that the CuO additive also contributes to inhibiting self-discharge, but not as effective as the V_2O_5 additive.

We have also noticed some difference in the peak intensities at higher absorption energy region of 2478 and 2480 eV. (**Figure 4-6a,b**) In the previous chapter, these two peaks are also detected in the LiTDI/TEGDME cells and attributed to SO_3^{2-} and $R-OSO_2^-$ species (**Section 3.6.2.2, Figure 3-17**). In the pristine states, these peaks are less pronounced in the sulphur electrode fabricated with MXs with the redox potential below 2.4 V vs Li/Li^+ (**Figure 4-1**), such as, $SnO_2@S$, $TiO_2@S$, and $CuS@S$ cells (**Figure 4-6a**). Whereas the sulphur electrode fabricated with additives with higher redox potentials show prominent peaks ($CuO@S$ and $V_2O_5@S$, **Figure 4-6b**). Also, the evolution of these peaks behaved differently in different additives, which is discussed later in **Section 4.5.3**.

4.5.2 *Operando* XAS analysis

Operando XAS measurements were used to detect the evolution of polysulphides in all five different electrodes. Some differences in the polysulphide reduction process is observed. Overall, spectral trends of the pre-edge, main-edge, and Li_2S signature can be divided into three classes.

1. Reversible pre-edge intensity and reversible main-edge absorption energy shift during discharge and charge processes. ($TiO_2@S$)

2. Reversible pre-edge intensity during discharge and charge, but irreversible main-edge energy shift. (V_2O_5)
3. Irreversible pre-edge intensity and no energy shift of the main-edge (CuO , CuS , SnO_2)

4.5.2.1 $TiO_2@S$

For the $TiO_2@S$ electrode, two different batteries were measured where one battery focused only at the S K-edge with the aim to examine the change in the sulphur chemistry as a comparison with other $MX@S$ electrodes, while the second battery was analysed for the K-edges of both S and Ti element to investigate the changes in the oxidation number of Ti while recording the S K-edge simultaneously. Both cells were cycled at the 0.1 C rate between the voltage range of 1.3 - 2.8 V. First, we discuss the cell focused only on the S K-edge spectra. This cell showed spectral trends remarkably different compared to other $MX@S$ cells.

4.5.2.1.a) *Operando* S K-edge analysis

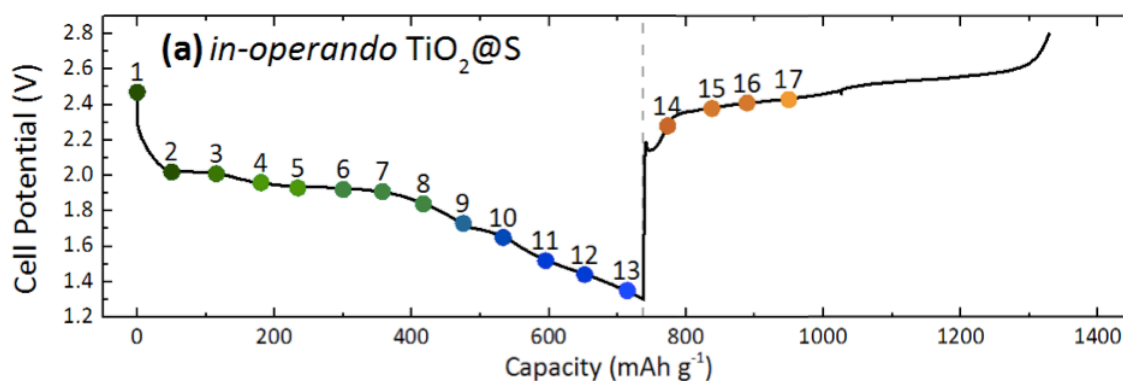
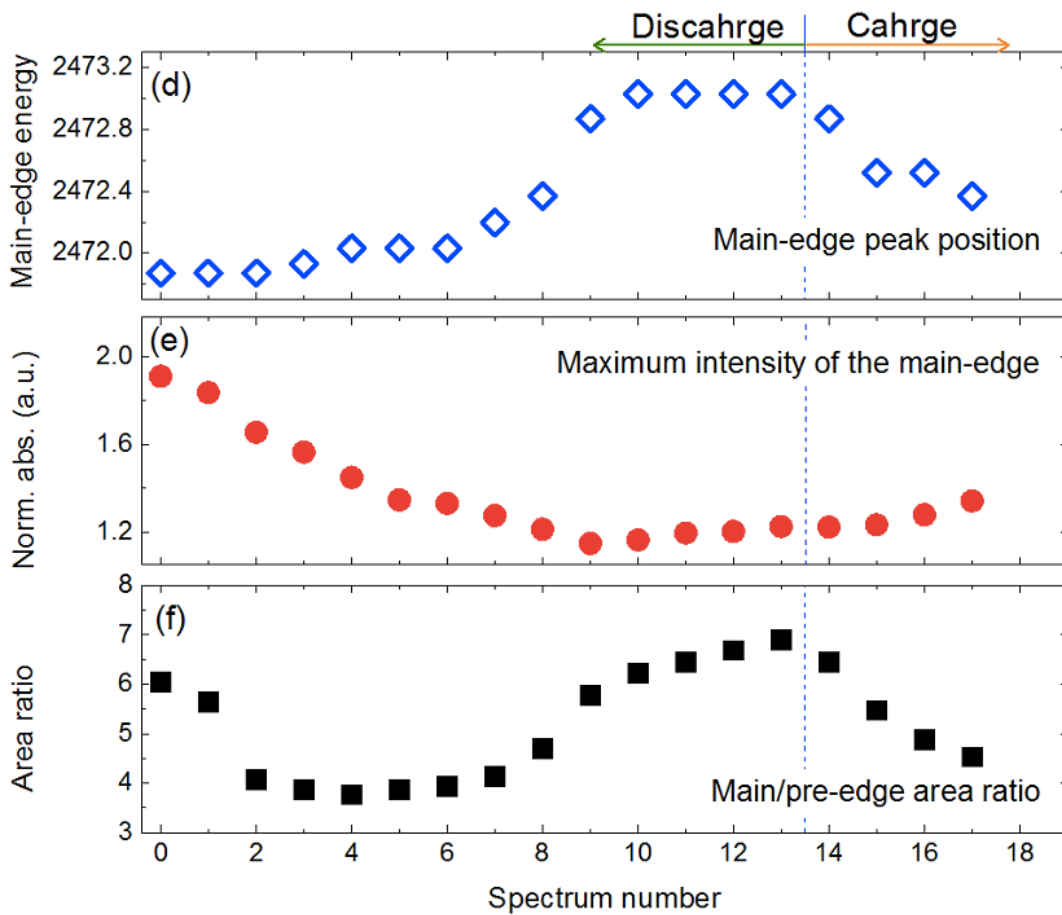
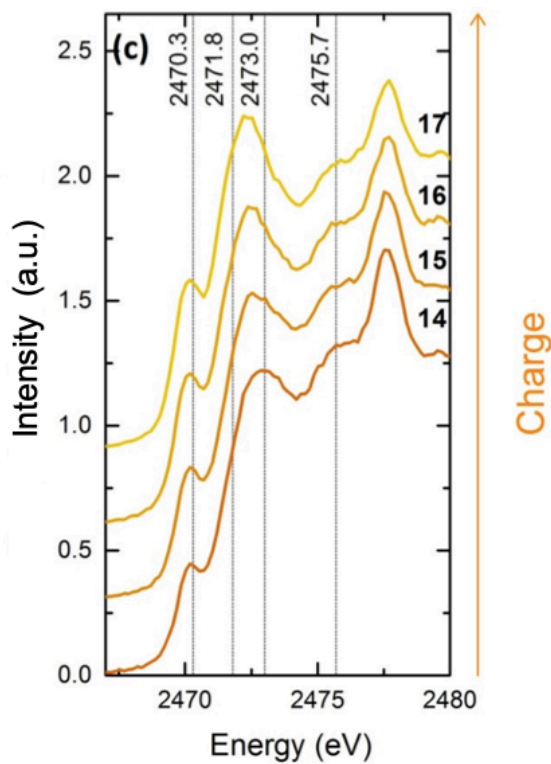
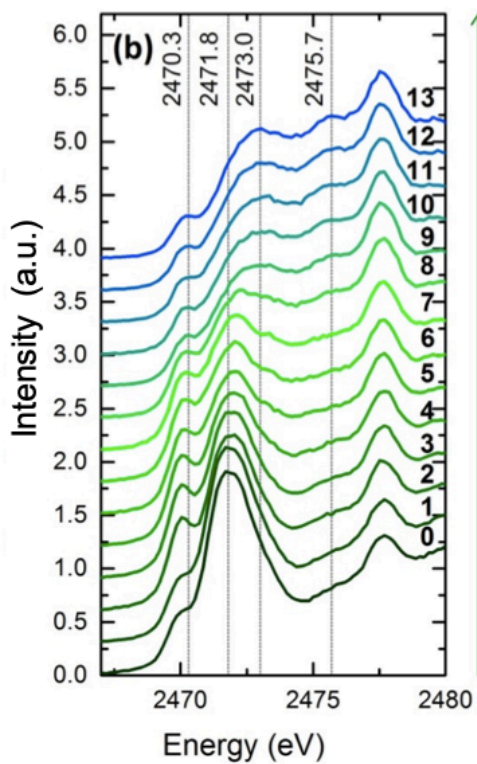


Figure 4-7. *Operando* XANES dataset for the $TiO_2@S$ cell. (a) Voltage profile for the first cycle with dots indicating the points where XAS spectra were collected and labelled from 1 – 17. This cell is cycled at a constant rate of 0.1 C.



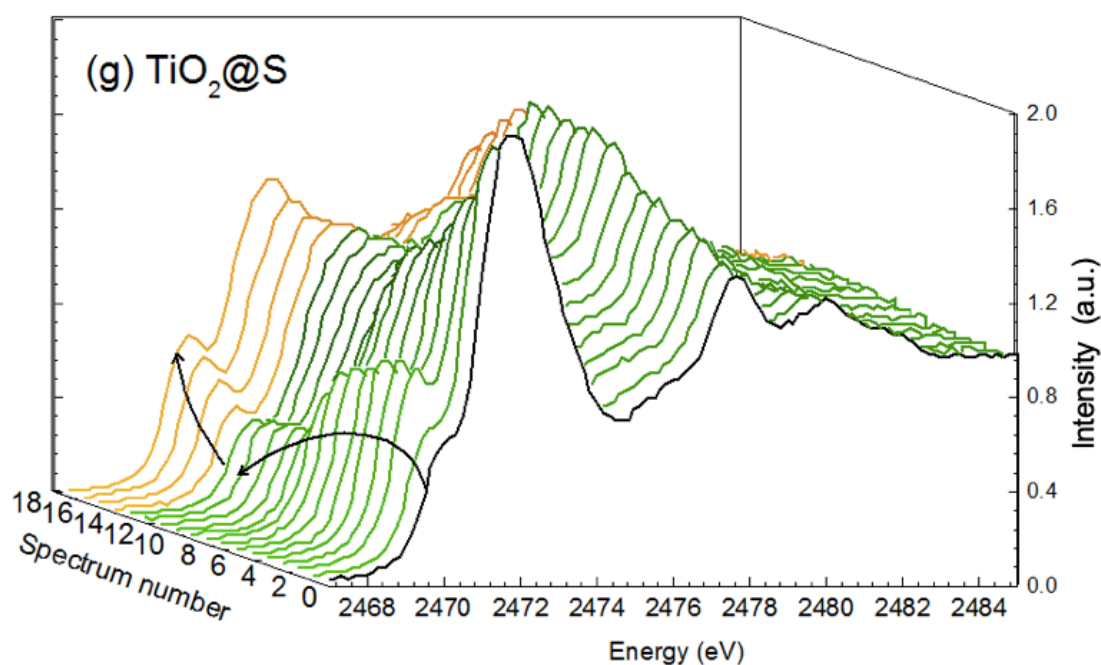


Figure 4-7. Continued. (b, c) XANES spectra of the S K-edge during the first discharge and charge processes, respectively, corresponding to the labels in the voltage profile, and spectrum number 0 indicating the pristine spectrum (offset for clarity). (d) Data points correspond to the energy position of the main-edge of each spectrum, (e) plot of the maximum intensity of the main-edge (normalised), (f) area ratio of the main/pre-edge, and (g) waterfall graph of S K-edge XANES spectra to show a clear image of the pre-edge evolution.

The changes in the spectral feature are similar to what was observed in the LiTDI/TEGDME cell, presented previously in **Section 3.6.3.5**; reversible energy shift in the main-edge and the presence of isobestic points along with the main-edge (represented in **Figure 4-8a**). The pre-edge feature is observed in the pristine spectrum, indicating the inevitable self-discharge phenomenon (**Figure 4-7b** spectrum number 0). This shows that the active sulphur reacted with the electrolyte and formed long-chain polysulphide during cell storage. As can be seen in **Figure 4-7e**, the main-edge intensity is at its maximum in the pristine state. This is because a significant amount of polysulphides are already formed and diffused out to the electrolyte to high self-discharge rate, suggesting that the reduction of sulphur starts from Li_2S_8 to $\text{Li}_2\text{S}_{6-4}$ conversion, instead of S_8 to Li_2S_8 conversion. This can be recognised in the

electrochemical discharge curve, by the elimination of the high voltage plateau (**Figure 4-7a**).

In the beginning of the first discharge (spectrum number 1 and 2 in **Figure 4-7b**), the pre-edge grows significantly while its accompanying main-edge at 2472 eV is decreasing. This indicates shortening of the polysulphide chain length, due to the growth of terminal sulphur concentration with decreasing the population of the internal sulphur atoms, hence, confirming the Li_2S_8 to $\text{Li}_2\text{S}_{6-4}$ reaction reduction process. This is also evident by the significant decrease in the area ratio of the main/pre-edge from 6.0 to 4.0 during this process (**Figure 4-7f**).

During the low voltage plateau corresponding to spectrum number 3 to 8 in **Figure 4-7b**, the polysulphide signature of the pre-edge and its accompanying main-edge decrease in their intensities and these features are becoming closer to that of Li_2S reference compound. Simultaneously, the main-edge energy shifts to a slightly higher value by around 0.5 eV and splitting of the pre and main-edge peaks becomes larger. This is a characteristic of the increased charge density, i.e. shortening of the linear polysulphide chain lengths. Concurrently, the concave shape after the main-edge slowly becomes flat and the additional Li_2S feature at 2475.7 eV is recognised.

For the indication of an isosbestic point, the spectra series is displayed without offset in **Figure 4-8**. The XANES spectra involves several isosbestic points along the main-edge, where curves do not share a single point as represented by the inset in **Figure 4-8a**. This gives convincing evidence of a two-phase transition behaviour of the conversion reactions with existing side reaction. [39] The imperfect isosbestic point indicates that the additional disproportionation steps are involved in the formation of Li_2S . [40] Therefore, it is considered that shortening of linear polysulphide chain lengths happened simultaneously with the formation of Li_2S , rather than a sequential series of reactions. Those findings suggest that the Li_2S co-exists with linear-chain polysulphides during the cell reaction. [41][42] It must be noted that, at spectrum 8 in **Figure 4-7b** (end of the low voltage plateau), not only the signature of Li_2S is confirmed, but also the pre-edge is detected which is a characteristics of linear polysulphide chains. This observation supports the possibility of the co-existence of polysulphide species and

Li₂S. This was previously suggested by other XANES studies. [41][42] This behaviour is not true for all other MX@S electrodes, which will be discussed later.

On the other hand, the value of the area ratio exhibits an increasing trend after spectrum number 8. As explained previously in **Chapter 2**, the polysulphide chain length estimation using the area ratio of the main/pre-edge can only be applied when the detected species are in the form of linear polysulphide chain, because the pre-edge feature is only present in such species. Therefore, the value of the area ratio does not correlate to the polysulphide chain lengths when Li₂S is the dominant species, hence, the data represented in **Figure 4-7f** is not meaningful after spectrum number 8 because Li₂S is clearly detected at this point.

Upon further lithiation (spectrum number 8 - 11 in **Figure 4-7b**), the Li₂S signs become more pronounced due to a further increase in the main-edge energy position, which is detected at 2473.0 eV. Simultaneously, the second peak of the Li₂S feature at 2475.7 eV becomes more dominant than the first peak at 2473 eV and continues to grow until the end of discharge. Additionally, the pre-edge intensity decreases gradually. These findings indicate that Li₂S species becomes the dominant species present in the cathode side at the end of discharge.

In the previous chapter, the LiTDI/TEGDME electrolyte cell also exhibited a shift in the main-edge towards higher energy during discharge, but did not reach to the energy position of 2473 eV. Whereas in this cell (TiO₂@S cycled in the LiTDI/TEGDME/LiNO₃ electrolyte), the XANES spectral feature clearly characterises the conversion of polysulphides to Li₂S, suggesting more successful disproportionation reaction to form Li₂S and deposition of Li₂S on the cathode side. This result clearly demonstrated the polysulphide adsorbing effect of TiO₂. This could be owing to the potential interaction of Ti-S, which is facilitated by formation of oxygen vacancies and utilising the interaction between TiO₂ and polysulphides. This is also previously suggested by the Cui group. [43]

To clearly show the evolution of the Li₂S peaks, **Figure 4-9** compares the XANES spectra at the discharged state and Li₂S reference compound, which gives a direct evidence of Li₂S formation by the new peaks formed at 2473.0 eV and 2475.7 eV as they both match the XANES spectra of the Li₂S reference.

In the last spectrum collected during the discharge, the pre-edge feature was still detected. This is associated with residual polysulphide being present, suggesting that some polysulphide species were left unreacted during discharge and did not fully convert into Li_2S (Figure 4-8a spectrum number 13).

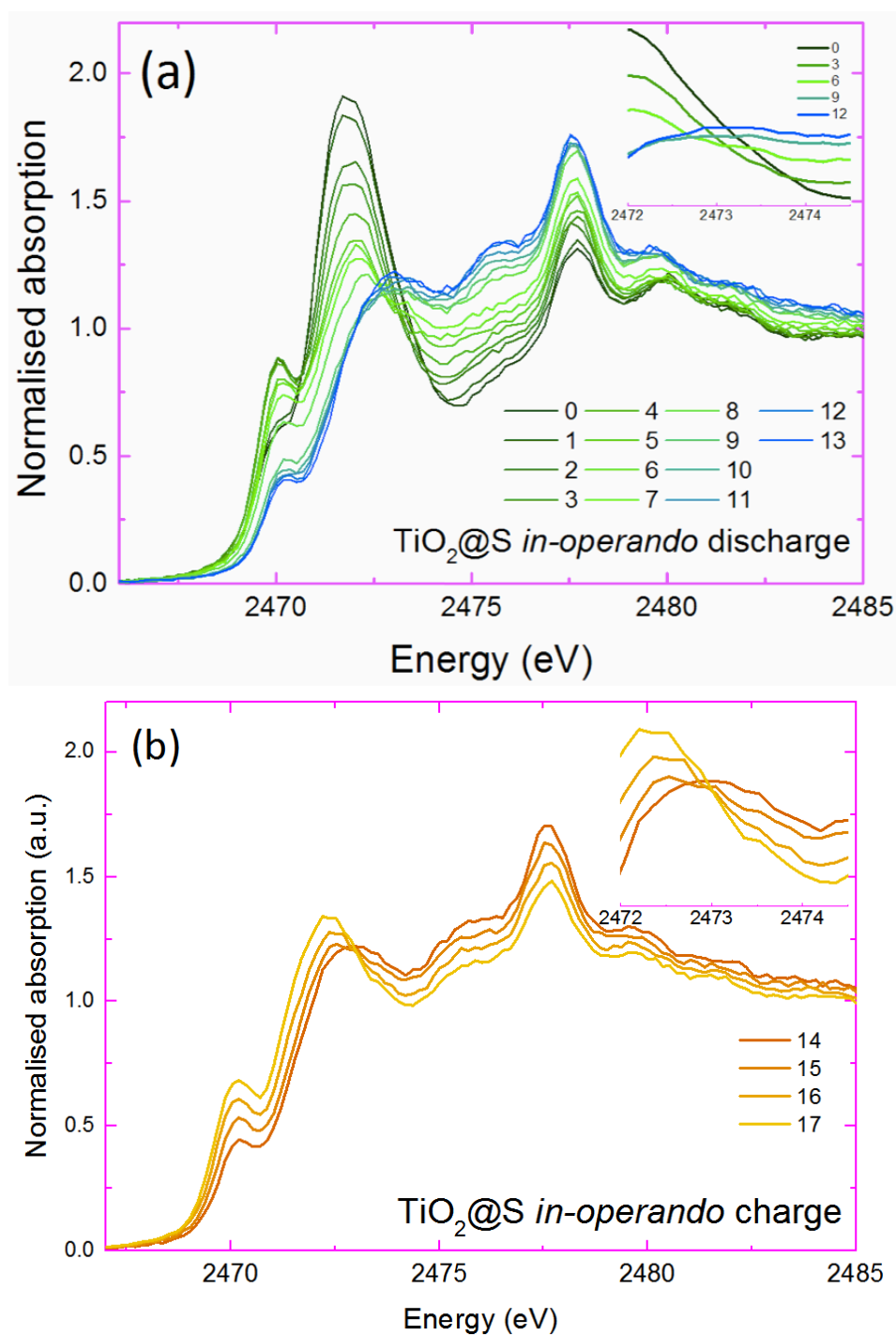


Figure 4-8. Normalised S K-edge XANES spectra set without offset. (a) During the initial discharge and (b) during the initial charge. The inset show an expanded view of the isosbestic points.

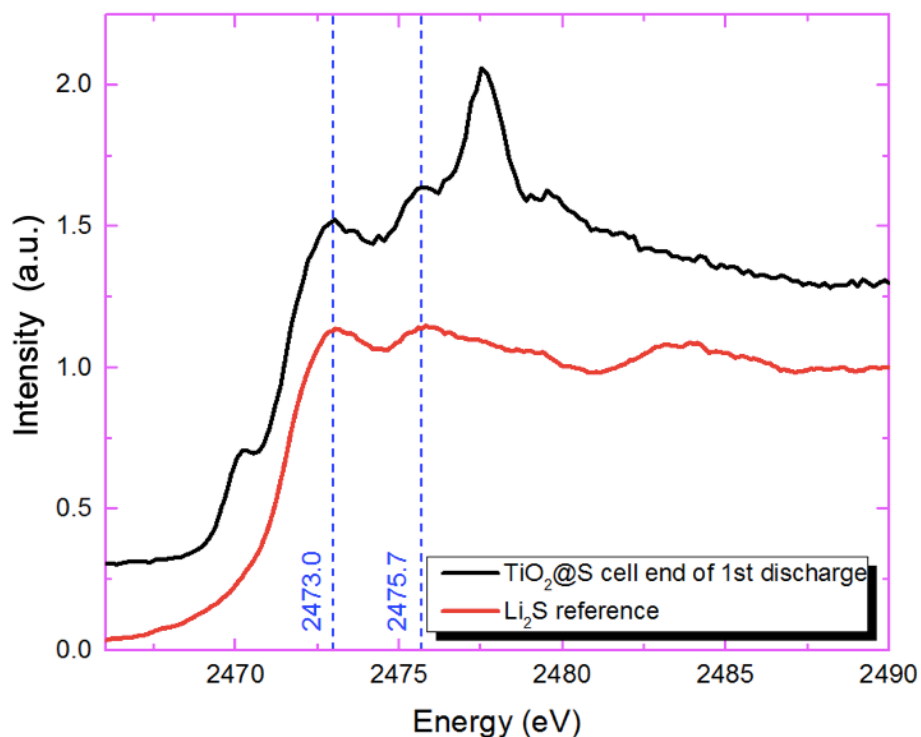


Figure 4-9. Sulphur K-edge XANES spectra of Li_2S reference compound and end of the initial discharge of the $\text{TiO}_2@\text{S}$ cell cycled at 0.1 C rate (offset for clarity).

Charge $\text{TiO}_2@\text{S}$

Only four spectra were collected during the charging process of the $\text{TiO}_2@\text{S}$ cell due to the beam loss. However, those spectra still provide the strong evidence of the oxidation reaction of Li_2S to linear-chain polysulphide at an early stage of the charging process. During this process, the XANES spectra shows a similar feature to the discharge process but in reverse sequence, indicating that the same sulphur species are involved in the Li extraction process (**Figure 4-8b**). With increasing depth of charge, the spectra become more dominant by the polysulphide, characterised by the energy shift of the main-edge towards lower value (**Figure 4-7d**), and the pre-edge peak at 2470.3 eV becomes more pronounced.

High-energy region

With increasing depth of discharge, an obvious growth is recognised at the higher absorption energy of 2478 eV and 2480 eV. In **Section 3.6.2.2**, these two peaks were assigned as the reaction between Li, S and oxygen in the electrolyte. The growth of these peaks originate to the detriment of active sulphur species, but considered as non-effective towards the redox mechanism of polysulphides. [44][45] In contrast to the pure sulphur electrode cycled in the LiTDI/TEGDME electrolyte, these two peaks, especially the 2478 eV peak, show a systematic increase and decrease in the intensity during discharge and charge processes, respectively. There is also an additional shoulder at 2482 eV identified, which follows the trend of two peaks at 2478 and 2480 eV. The differences between those two cells are (i) the presence of LiNO₃ in the electrolyte and (ii) TiO₂ support on the sulphur cathode. The discussions of these oxidised sulphur peaks will be explained in **Section 4.5.3**.

4.5.2.1.b) Operando double edge (S K-edge and Ti K-edge) analysis

To gain additional insights of the redox reactions that takes place between Li and TiO₂, *operando* XANES measurement was performed on a fresh TiO₂@S cell probing both the S and the Ti K-edges simultaneously and to correlate these results with the electrochemical behaviour.

It should be noted that the *operando* S K-edge spectra were collected with low counts, hence a larger signal to noise ratio was unavoidable. The S K-edge spectra are therefore used only to ensure that sulphur species are active as expected. Our main focus here is to elucidate the electrochemical redox activity and reversibility of the TiO₂ additive in the electrode.

Ti K-edge references

Firstly, two reference Ti K-edge XANES spectra, Ti₂O₃ and anatase TiO₂ are shown in **Figure 4-10** corresponding to the Ti(III) (Ti₂O₃) and Ti(IV) (anatase-TiO₂) oxidation states, respectively.

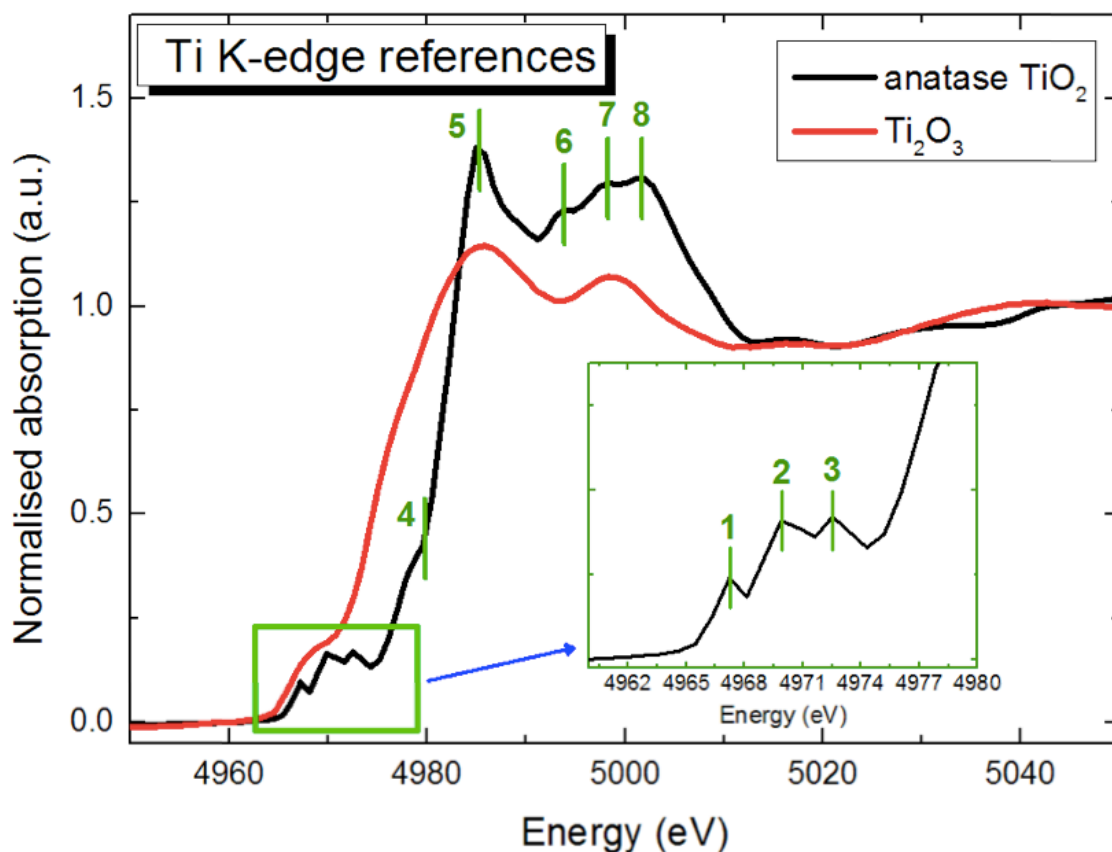


Figure 4-10. Normalised Ti K-edge XANES spectra of two references: Ti_2O_3 , Ti(III) and anatase- TiO_2 , Ti(IV). The inset shows an expanded view of the pre-edge area.

The main difference between these two spectra is related to the energy position of the absorption edge that is located at lower energy with lower oxidation state of Ti, indicating the lower valence. The energy position of the absorption edge values for Ti_2O_3 and TiO_2 are reported at 4975 and 4980 eV, respectively. [46] The pre-edge peaks also exhibit a notable difference. One broad shoulder peak is identified in the Ti_2O_3 reference, whereas three distinct peaks were detected in the anatase- TiO_2 reference compound. For the anatase- TiO_2 reference, three peaks labelled 1, 2, and 3, in the pre-edge region are separated by approximately 2.6 eV (inset of **Figure 4-10**). This multiplet is a feature of six-coordinated titanium compounds arising from hybridisation of p and d orbitals of the Ti and neighbouring atoms. [47][48] Although the exact assignments of these peaks are still not clear, it is generally accepted that peak 1,2,3 arise from a 1s to 3d dipole electronic transitions and those peak intensities are affected by the local geometry and the medium range structure of the sample around

the central Ti atom. [47][49] The sharp peak at 4985 eV (peak 5) arises from the dipole allowed $1S$ to $3p_{xy}$ electron transition, indicating the presence of Ti(IV). [50] Sharpness of the peaks 6 and 7 identifies the crystallinity of TiO_2 . These peaks become broader with reduced crystallinity. The crystallinity of TiO_2 can also be identified by the intensity of the pre-edge. The local geometry and the particular medium range structure of atoms around the central Ti atom affect the pre-edge peak intensity. [49] For less crystalline TiO_2 , the Ti environment is expected to be distorted or defective, increasing the pre-edge resonance. These facts will be used in the following to analyse the different phases that may appear in our electrodes cycled at different stages.

Operando S K-edge & Ti-K-edge XANES spectra

Operando XAS measurement was performed on the $TiO_2@S$ electrode probing both at the Ti K-edge and the S K-edge, cycled at 0.1 C rate between 1.3 – 2.8 V for two complete set of discharge and charge cycles of a single test cell. In this way, we were able to measure the K-edges of two elements subsequently without having the uncontrolled difference between cells.

Firstly, the S K-edge XANES was collected, followed by moving the monochromator to the Ti K-edge collecting the XANES region, then the monochromator was moved back to the S K-edge to collect new sequence of XANES spectra. This was carried out consecutively during the discharge and charge process. Such difficult measurements were achieved thanks to the motorised XYZ sample mount, which allows precise and reproducible movements of the X, Y and Z translation. [51]

Because our main focus was on the Ti K-edge, the counts and the acquisition time of the S K-edge is decreased to obtain as many spectra as possible during the discharge and charge state. The S K-edge XANES spectra were recorded over the energy range between 2430 and 2530 eV with a step size of 2.0 eV before the pre-edge (2430 – 2460 eV), 0.2 eV in the pre-edge, main-edge, and electrolyte region (2460 - 2490 eV), 0.25 eV between 2490 – 2510 eV, 0.125 eV between 2510 – 2520, and 0.5 eV between 2520 – 2540 eV, with a counting time of 2 seconds per point, resulting in a total acquisition time of 18 minutes per spectrum. Subsequently, the Ti K-edge XANES spectra were recorded between 4940 and 5100 eV with a step size of 2 eV before the pre-edge (4940 - 4960 eV), 0.25 eV in the pre-edge and white line region, (4960 - 4995 eV), 1.88

eV after the white line (4995 – 5040 eV), and 3 eV between 5040 – 5100 eV, with a counting time of 2 seconds per point, resulting in a total acquisition time of 14 minutes per spectrum.

The summary of the *operando* measurement of the initial cycle is presented in **Figure 4-11**.

S K-edge

The pre- and the main-edge trends of the S K-edge XANES spectra were similar to the previous finding where all focus was on the S K-edge XANES region. The observation of the shift in the main-edge energy towards higher absorption energy value as well as presence of isosbestic points confirm the two-step conversion reaction in the electrode. Again, the dominant peaks of oxidised sulphur are detected at 2478.0 and 2480 eV, which may have masked signals arising from Li_2S at 2457.7 eV because the signal/noise ratio is a lot higher than those studied solely on the S K-edge. For the charging process, the same XANES spectral features are observed in the reverse sequence to the discharge process. This result ensures the reproducibility of the *operando* S K-edge spectra.

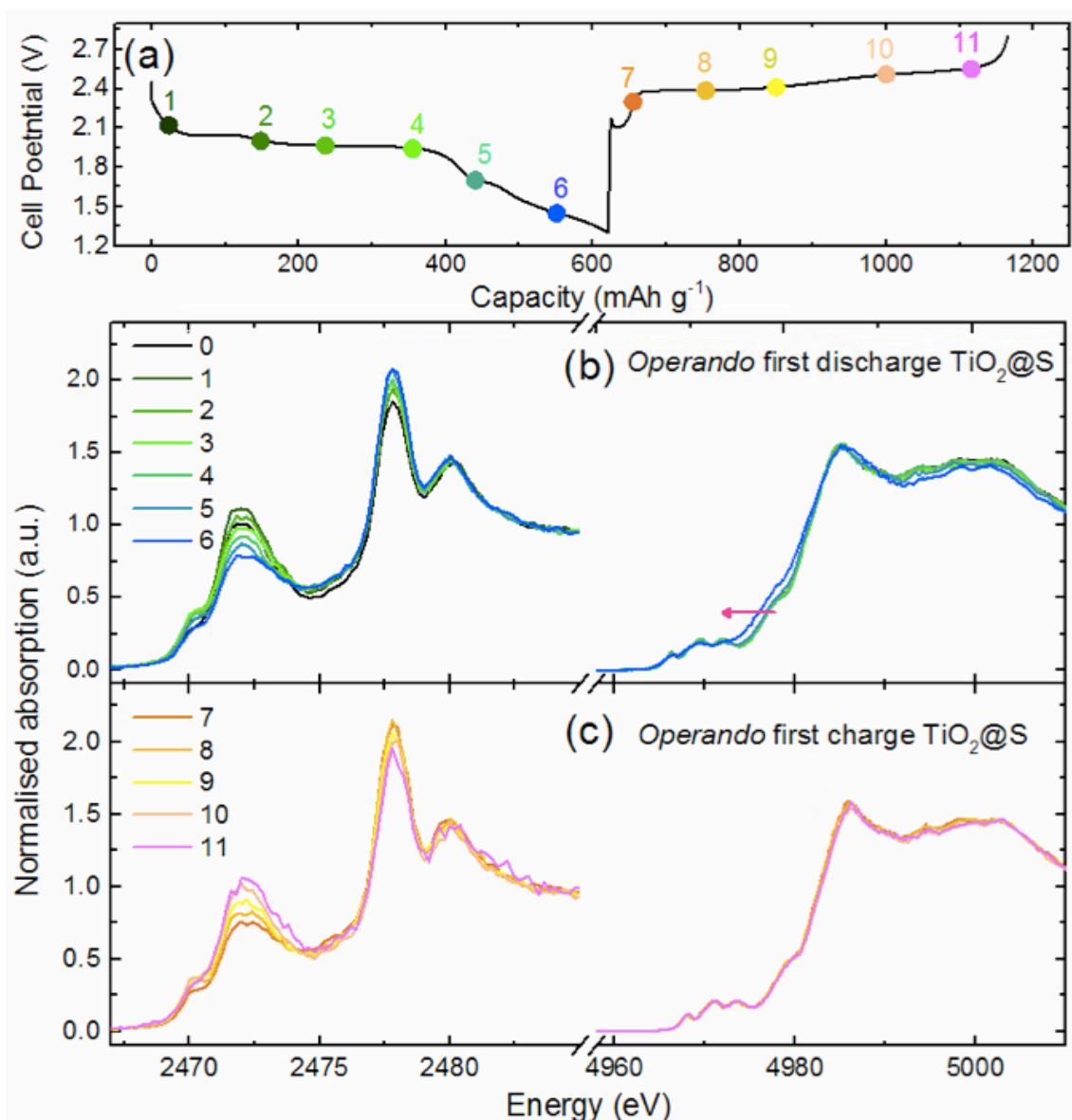


Figure 4-11. Operando XANES of the TiO₂@S cell measured at 0.1 C rate. (a) Voltage profile for the first discharge and charge. The points at which measurements were collected are marked with dots of corresponding colour on each point and labeled 1 to 11. The corresponding normalised XANES spectra for; (b, c) the initial discharge and (c) charge. The S K-edge spectra are shown in the left panels, and the right panels represents the Ti K-edge spectra.

Ti K-edge

The Ti K-edge energy edge at the pristine state is same as the TiO₂ reference compound, suggesting that the oxidation state of Ti in the as-prepared material is

Ti(IV). Throughout the initial discharge, no measurable difference is observed in the spectral feature until the last scan of the discharge process collected at 1.40 V (**Figure 4-11b** right panel, spectrum number 6).

To clearly see the pre-edge features, the Ti K-edge spectrum at the end of 1st discharge is displayed with TiO₂ and Ti₂O₃ references in **Figure 4-12**.

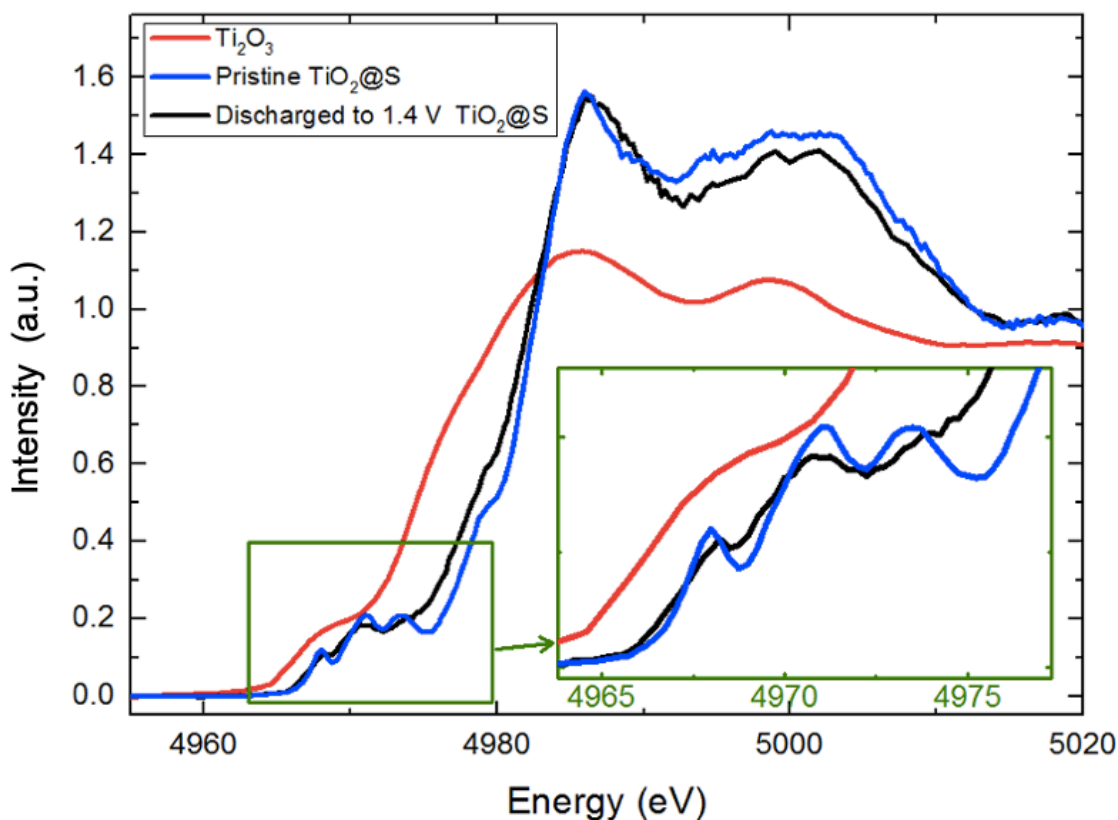


Figure 4-12. Ti K-edge XANES spectra of Ti₂O₃ (Ti³⁺) reference, TiO₂@S cell at the pristine, and discharged to 1.4 V state. The inset shows the expanded view of the pre-edge region.

After the discharge voltage reaches to 1.4 V, where the cell voltage is lower than the redox potential of TiO₂ (1.7 V vs Li/Li⁺), the pre-edge peaks lose their sharpness and flattens out while the main-edge shifts to slightly lower energy, in line with the reduction of Ti(IV) to Ti(III) (**Figure 4-12**). The loss of the pre-edge features observed in **Figure 4-11b** and **Figure 4-12** is highly related to the distortion of TiO₆ octahedral coordination. [52] This peak stretching is also observed in other studies during lithiation of TiO₂ in other Li-ion battery material. [53] The observed shift of the Ti K-

edge is understood as a result of the Li insertion into TiO₂, and the shift does not appear gradually. Instead, the shift is observed abruptly below the redox potential of TiO₂. This means that TiO₂ does not change in its chemical structure until lithiated. Despite this fact, the sign of Li₂S is already observed before the voltage reaches to 1.7 V (**Figure 4-7b**). This means that the TiO₂ additive still has some effect of accelerating the reduction reaction of polysulphides to Li₂S without changing its chemical structure, suggesting that TiO₂ functions as a catalyst.

Following charging process revealed that this is a reversible observation. The Ti K-edge energy position returns to higher absorption energy at 4980 eV (Ti(IV)), and the triplet pre-edge feature reappeared at their original locations and sharpness. It is worth nothing that the first spectrum of the charging process, as shown in **Figure 4-11c** right panel, the Ti has already returned to its original energy, suggesting that there was some relaxation between the last scan of the discharge (1.40 V) and the beginning of the charging process (at 2.38 V, 55 mAh g⁻¹ charged).

In the second cycle of the same cell, we observed very similar XANES behaviour in both the S K-edge and Ti K-edge, indicating a good reproducibility of the compounds formed during the following cycle (See **Appendix A-2**).

Additionally, *ex situ* XAS measurement of TiO₂@S electrode is conducted at B18 at the DLS, the results obtained from this is presented in **Appendix A-3**, which highlights the importance of the *operando* measurements.

Conclusions of TiO₂@S

Operando XANES spectra of TiO₂@S cell revealed that TiO₂ has strong interactions with lithium polysulphides and we can conclude that the TiO₂ additive favours the polysulphide redox reactions and supports the progressive deposition of insoluble Li₂S₂/Li₂S species on the cathode side, confirmed by a large energy shift of the S K-edge XANES main-edge towards higher energy value and clear detection of Li₂S peak at the end of the discharge process. This confirms that the diffusion of long-chain polysulphide to the anode side is inhibited and disproportionation and deposition of Li₂S is achieved on the cathode side. Despite this advantage, the long-term capacity fading seen in **Figure 4-4b**, which is likely related to the excessive formation of Li₂S,

which eventually leading to the increase in the internal resistance of the cell and elevate the polarisation. [54] The growth of Li_2S leads to the large volumetric change during cell cycling in expense of achieving the high capacity. Also, the precipitation of insoluble discharge product Li_2S on the cathode hinders the Li^+ -ion transportation. Li_2S also behave as an insulator disconnecting the pathways for electrons migrating from the carbon matrix to long chain polysulphides. [55] This result shows that it is important to control the optimal balance between the redox kinetics and insoluble polysulphide formation which is the origin of the volume expansion and contraction, during the redox conversion.

Also, Ti K-edge *operando* XAS results verify that the partial conversion of Ti between Ti(IV)/Ti(III) and Ti(III)/Ti(IV) redox couples during discharge and charge process, respectively. This proves that the TiO_2 additive can also behaves as an additional capacity contributor.

4.5.2.2 (2) $\text{V}_2\text{O}_5@\text{S}$: reversible pre-edge

Figure 4-13 summarises the *operando* S K-edge XANES spectra series of the $\text{V}_2\text{O}_5@\text{S}$ cell during the initial discharge/charge measurement.

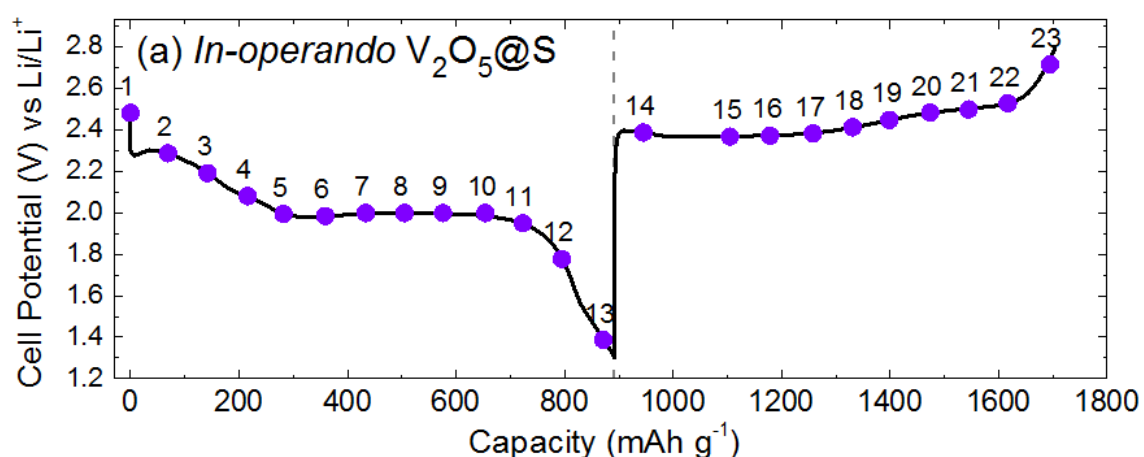


Figure 4-13. *Operando* XANES dataset for the $\text{V}_2\text{O}_5@\text{S}$ cell. (a) Voltage profile for the first cycle with dots indicating the points where XAS spectra were collected and labelled from 1 – 23.

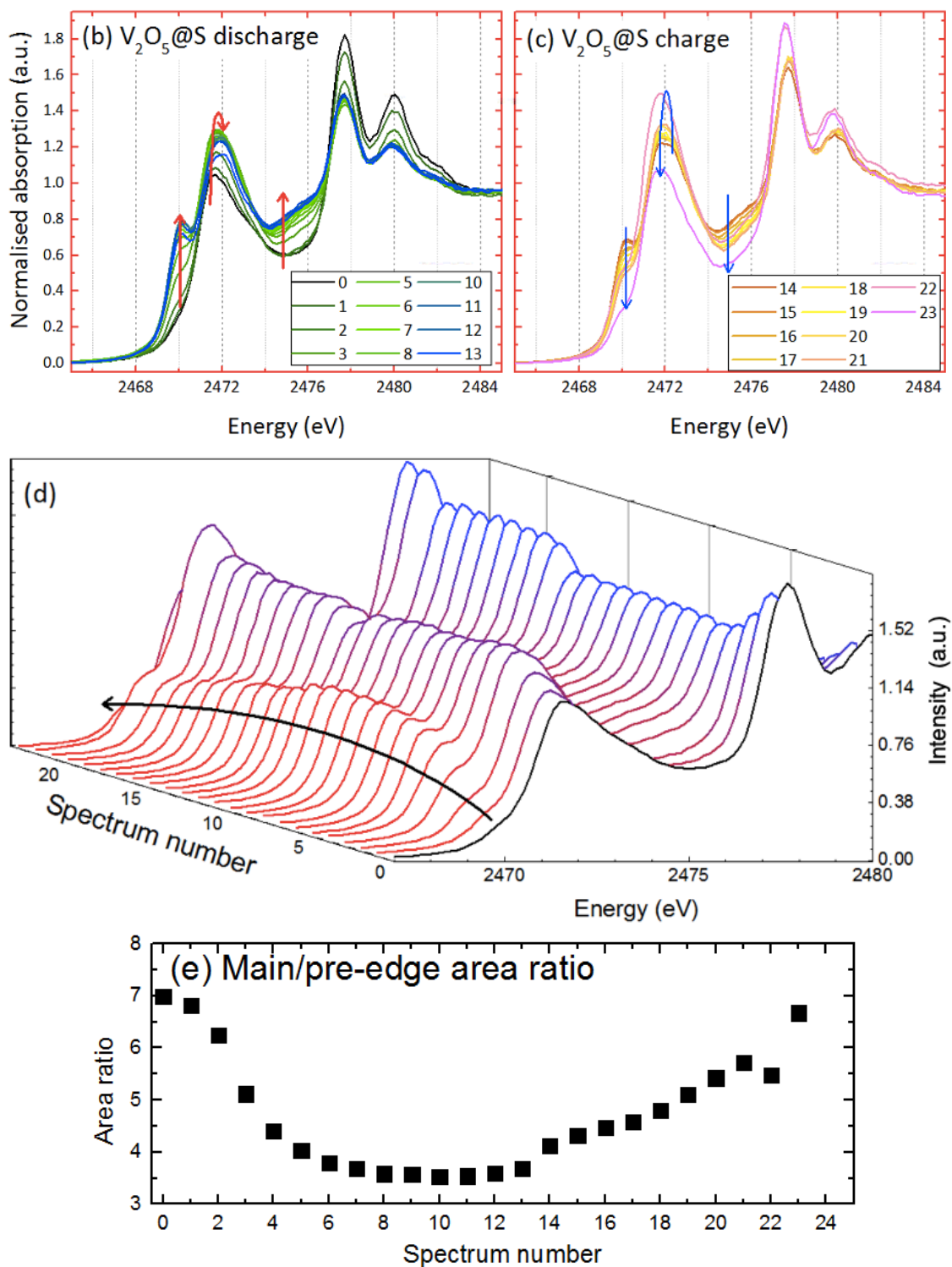


Figure 4-13. Continued. (b) Normalised S K-edge XANES spectra during the first discharge and (c) charge, corresponding to the labels in the voltage profile, and the spectrum number 0 indicating the pristine state of the cell. (d) Waterfall graph of XANES to show a clear image of the evolution of the pre-edge. (e) Plot of the calculated area ratio of the main/pre-edge.

Discharge $V_2O_5@S$

As explained earlier, the S K-edge XANES indicates that the starting material is S_8 , as the pre-edge is not detected in the pristine spectrum of the $V_2O_5@S$ cell. This indicates the excellent self-discharge mitigation achieved by the V_2O_5 additive (**Figure 4-13d**, black line). Upon lithiation, the formation of polysulphide is confirmed by the progressive growth of the pre-edge feature at 2470.3 eV (**Figure 4-13d**). Simultaneously, the main-edge is gradually increased and the concave shape at 2476 eV is lost, accounting for the formation of lithium polysulphides (**Figure 4-13b**). The polysulphide species formed are gradually dissolved in the electrolyte, which reduced the self-absorption (SA) effect of the XANES spectra observed as an increase in the main-edge intensity between spectrum number 0 to 3, as can be seen in the waterfall spectra set in **Figure 4-13d**. The polysulphide species formed during high voltage plateau are identified to be long-chain polysulphides, as the ratio of the main/pre-edge area is relatively high at the beginning of the discharge **Figure 4-13e**. A gradual decrease in the values of ratio suggests that the polysulphide chain length is decreasing with increasing depth of discharge. This can also be recognised by the increase in the main-edge absorption energy to slightly higher value, which is also an indication of the reduction of polysulphide chain-lengths (**Figure 4-13b**).

Yet, the formation of Li_2S was not recognised as there were no peaks detected at 2473 and 2476 eV. The energy position of the main-edge is still far from 2473 eV at the end of discharge. Isosbestic points were only seen near the end of discharge, which is almost accumulated to one point. The delay in the isosbestic point suggests that the conversion reaction of polysulphides occurs sequentially from long-chain to medium-chain polysulphides, followed by the conversion of medium-chain to short-chain polysulphides in the most of the reaction steps.

Charge $V_2O_5@S$

The spectral features observed during the discharge process appeared irreversibly during the charging process as indicated by the blue arrows in **Figure 4-13c**. At the last spectrum of the charging process, the intensity of the pre-edge and the main-edge declined abruptly, and the spectral feature becomes very close to S_8 . The abrupt decline in the peak can be attributed to the concentrated sulphur species at the

cathode, which induced the SA effect and decreased the peak intensity. To compare the total concentration of sulphur species, **Figure 4-14** shows the raw spectra at the pristine state and charged to 2.71 V.

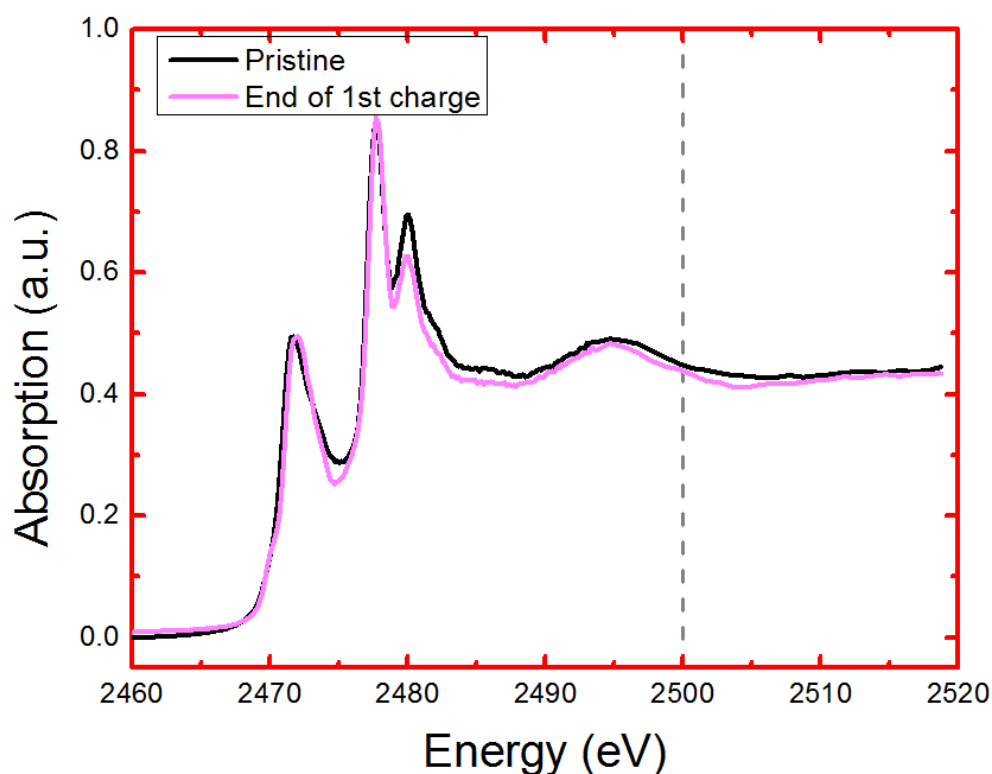


Figure 4-14. Raw spectra (not normalised) of the pristine state and the charged state of $V_2O_5@S$ electrode.

It is clear that those two spectra are very similar, indicating that the species present at the end of the initial charge is similar to those present at the pristine state. Additionally, the edge steps at 2500 eV of two spectra are very close, suggesting that the relative concentration of sulphur species in these two are close to each other. In other words, the active sulphur is not lost during the first cycling and the charging process is fully reversible. This is a remarkable improvement compared to the previous cells measured in **Chapter 3**. As the sulphur electrode cycled in LiTDI/TMS and LiTDI/TEGDME electrolytes experienced loss in the active sulphur at the end of the first cycle.

4.5.2.3 (3) CuO, CuS, and SnO₂ additive – irreversible pre-edge feature

In the CuO@S, CuS@S, and SnO₂@S cells, the S K-edge spectra set observed the pre-edge growth during the discharge process but this peak was irreversible during the charge process. Especially, CuS@S and SnO₂@S cells exhibited relatively similar spectral behaviour of XANES spectra during their first discharge and charge processes. The spectral feature changes of these cells are described individually, starting with the CuO@S cell.

CuO@S

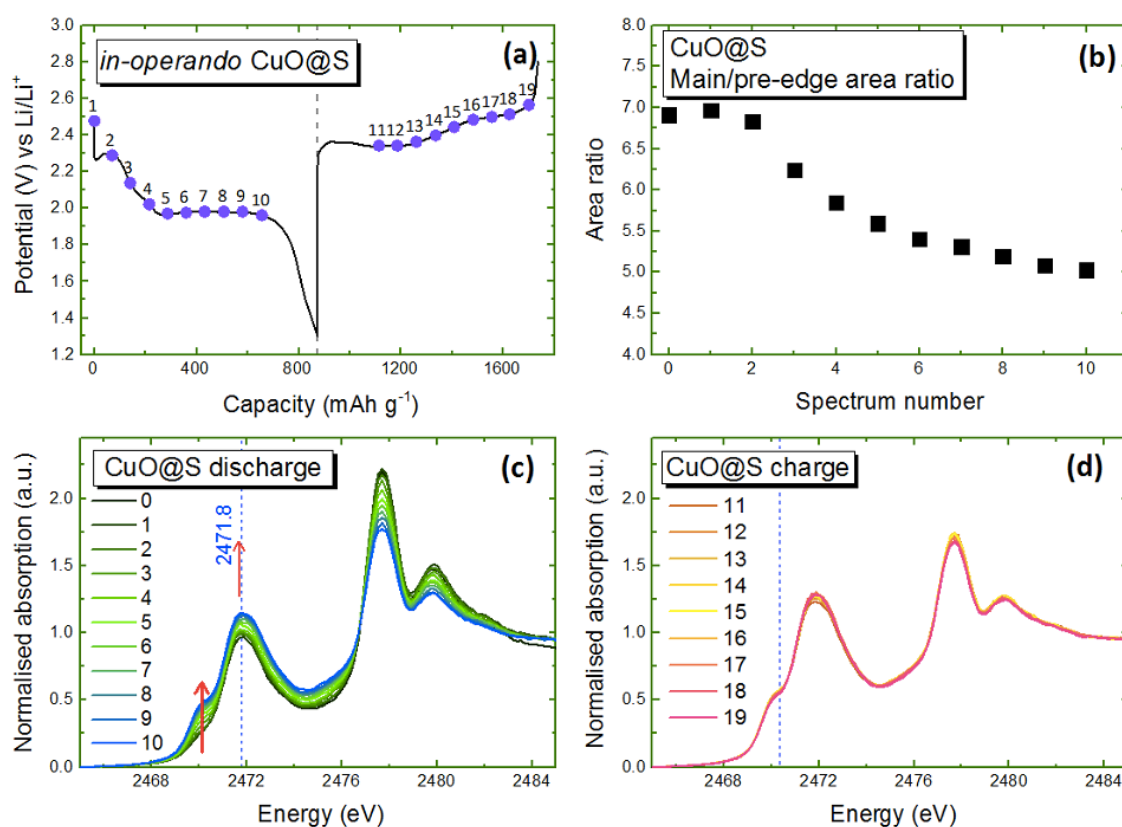


Figure 4-15. Operando XANES dataset for the CuO@S cell. (a) Voltage profile for the first cycle with dots indicating the points where XAS spectra were collected and labelled from 1 – 19. This cell is cycled at a constant rate of 0.1 C. (b) Plot of the calculated area ratio of the main/pre-edge. (c) Normalised S K-edge XANES spectra collected during first discharge and (d) charge, corresponding to the labels in the voltage profile. The pristine spectrum is labelled as spectrum number 0.

Only a weak resonance of the pre-edge is exhibited in the pristine state of this cell (**Figure 4-15b** spectrum number 0), suggesting a successful mitigation of self-discharge achieved by the CuO additive. Therefore, most of the starting material are in the form of S_8 rather than polysulphides and the reduction process starts from S_8 to long-chain polysulphide conversion. During the discharging process (**Figure 4-15c**), the pre-edge peak growth is confirmed, ascribed to the formation of long-chain lithium polysulphide. The intensities of the main-edge and pre-edge increase progressively, attributed to the dissolution of polysulphides into the electrolyte and decreased SA effect. **Figure 4-15b** shows the calculated area ratio of the main/pre-edge during the discharge process, which starts decreasing after the high voltage plateau (spectrum number 3) from the value of 6.8 to 5.0 towards the end of the discharge process. This suggests the conversion of the long-chain polysulphides to medium-chain polysulphides. However, there is essentially no difference in the main-edge energy position, indicating that short-chain polysulphides are not formed during this reaction. The XANES spectra do not involve any isosbestic points in the active sulphur energy region, indicating that the reduction process is sequential reaction (**Figure 4-15b**).

During the subsequent charging process, no obvious change in the XANES feature is observed, including the pre- and main-edge energy position and intensities of those peaks, identifying that the type of sulphur species remained unchanged during the delithiation reaction, hence some of the active sulphur became inactive. As opposed to the unchanged XANES features during the charging process, the electrochemical measurement still delivers the initial charge capacity of more than 860 mAh g^{-1} involving a sloping plateau. Hence, it is reasonable to assume that the re-oxidation process is taking place in the entire cell, but the sulphur species at the probed area do not engage in this reaction. This suggests that some of the polysulphide species are unable to be re-oxidised, hence became inactive in the following cycles and deposited on the cathode, which blocks the Li^+ -ion transport, behaving as an insulating product. This tells us that the active sulphur is not only lost on the anode side, but also become inactive in the cathode side. This explains the significant capacity fade phenomenon in prolonged cycling (**Figure 4-4b**).

Additionally, the XANES spectra exhibit a trend similar to that of the $\text{V}_2\text{O}_5@\text{S}$ cell in the higher energy region (2478 – 2483 eV). This is explained in detail in later section.

SnO₂@S

The SnO₂@S cell was then investigated under the same condition and the results are summarised in **Figure 4-16**.

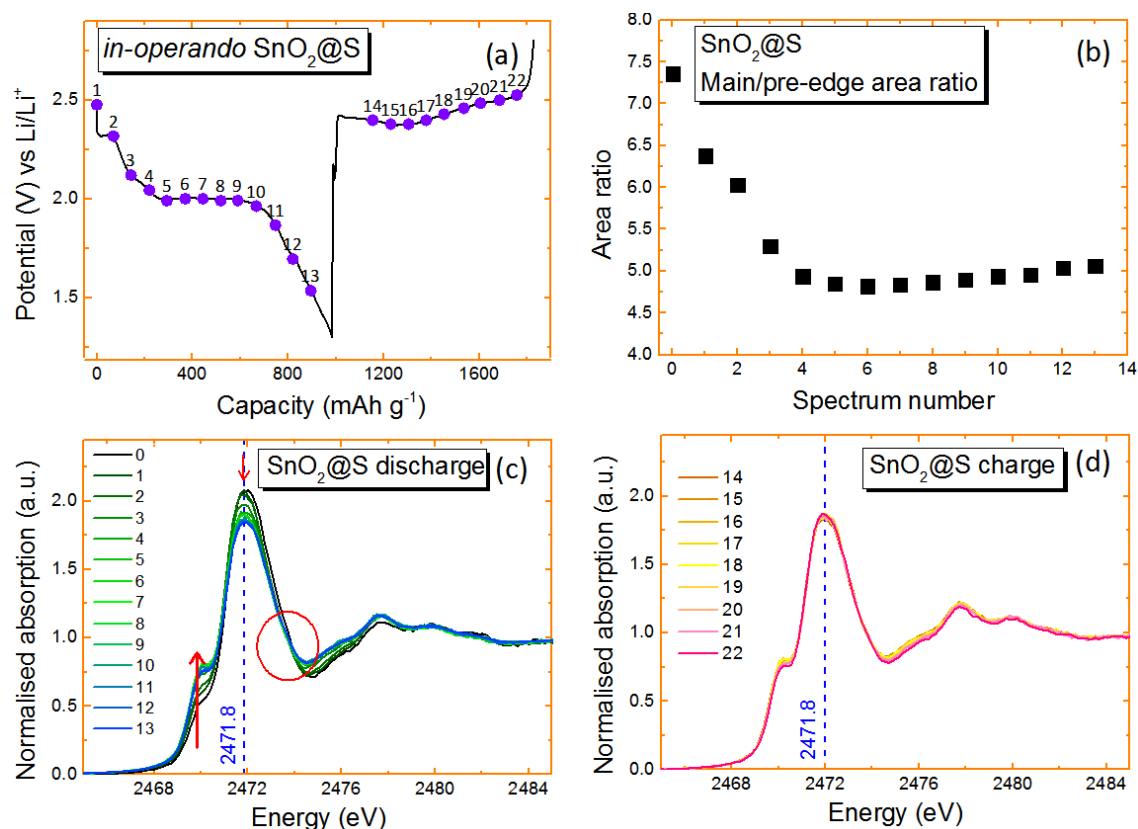


Figure 4-16. Operando XANES dataset for the SnO₂@S cell. (a) Voltage profile for the first cycle with dots indicating the points where XAS spectra were collected and labelled from 1 – 22. This cell is cycled at a constant rate of 0.1 C. (b) Plot of the calculated area ratio of the main/pre-edge. (c, d) Normalised XANES spectra for S K-edge during first discharge and charge, respectively, corresponding to the labels in the voltage profile, and spectrum number 0 indicating the pristine spectrum.

As reported previously in **Section 4.5.1**, the XANES spectrum at the pristine state is dominated by the polysulphide, characterised by the pre-edge at 2740.3 eV with the main-edge at 2472 eV, indicating the self-discharge phenomenon (**Figure 4-16c**, spectrum number 0). During the discharge process, the main-edge and the pre-edge showed an inverse evolution. The pre-edge becomes more pronounced with increasing depth of discharge, while the intensity of the main-edge is decreased as indicated by

the red arrows in **Figure 4-16c**, suggesting that the overall polysulphide chain length is shortened. This is confirmed by the main/pre-edge area ratio which decreases steeply as the extent of the discharge process until the beginning of the low voltage plateau, where it reaches to its minimum at spectrum number 5 (**Figure 4-16b**). Isosbestic point is detected along the main-edge, which is almost gathered at one point as indicated by the red circle in **Figure 4-16c**. This suggests that the conversion of sulphur comprise of a two-phase reaction that is distinctly different from the CuO@S cell. This can be interpreted as a simultaneous reduction of the linear-chain polysulphides.

During the following charging process, the S K-edge XANES spectra series hardly undergoes any change and remains dominated by polysulphides throughout. This was similar to what was observed in the charging process of the CuO@S electrode and considered as a limited re-oxidation process of lithium polysulphide formed during the discharge, which inactivated some of the active sulphur species.

CuS@S

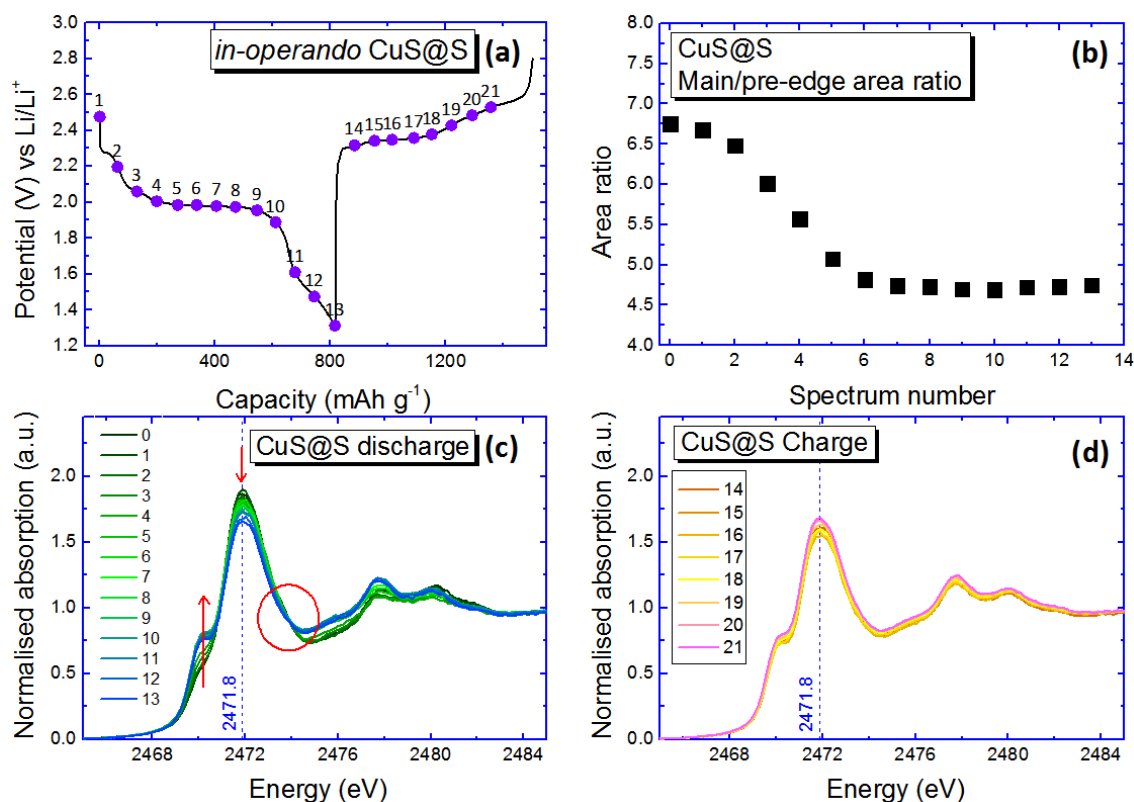


Figure 4-17. Operando XANES dataset for the CuS@S cell. (a) Voltage profile for the first cycle with dots indicating the points where XAS spectra were collected and labelled from 1 - 21, (b) Plot of the calculated area ratio of the main/pre-edge. (c, d) Normalised XANES spectra for S K-edge during first discharge and charge, respectively, corresponding to the labels in the voltage profile, and spectrum number 0 indicating the pristine spectrum.

The normalised S K-edge XANES spectra of the CuS@S cell exhibited very similar trends as seen in the SnO₂@S cell; no energy shift in the main-edge, an opposite trend in the evolution of the pre- and the main-edge, a step decrease of the ratio of the main/pre-edge in the beginning of the discharge process, and almost perfect isosbestic point. Again, no measurable difference in the XANES spectra is detected during the charging process showing an irreversible polysulphides species remained at the reduced state. These findings indicate that the sulphur behaves similar in the CuS@S cell and the SnO₂@S cell.

The *operando* XAS results suggests that it is harder to achieve the re-oxidation of polysulphides during the charging process in the presence of CuO, CuS, and SnO₂ additives.

4.5.3 High-energy region

Operando S K-edge spectra detected the additional oxidised sulphur peaks at the higher energy region in the TiO₂@S, CuO@S, and V₂O₅@S cells, as displayed in **Figure 4-18a-f**.

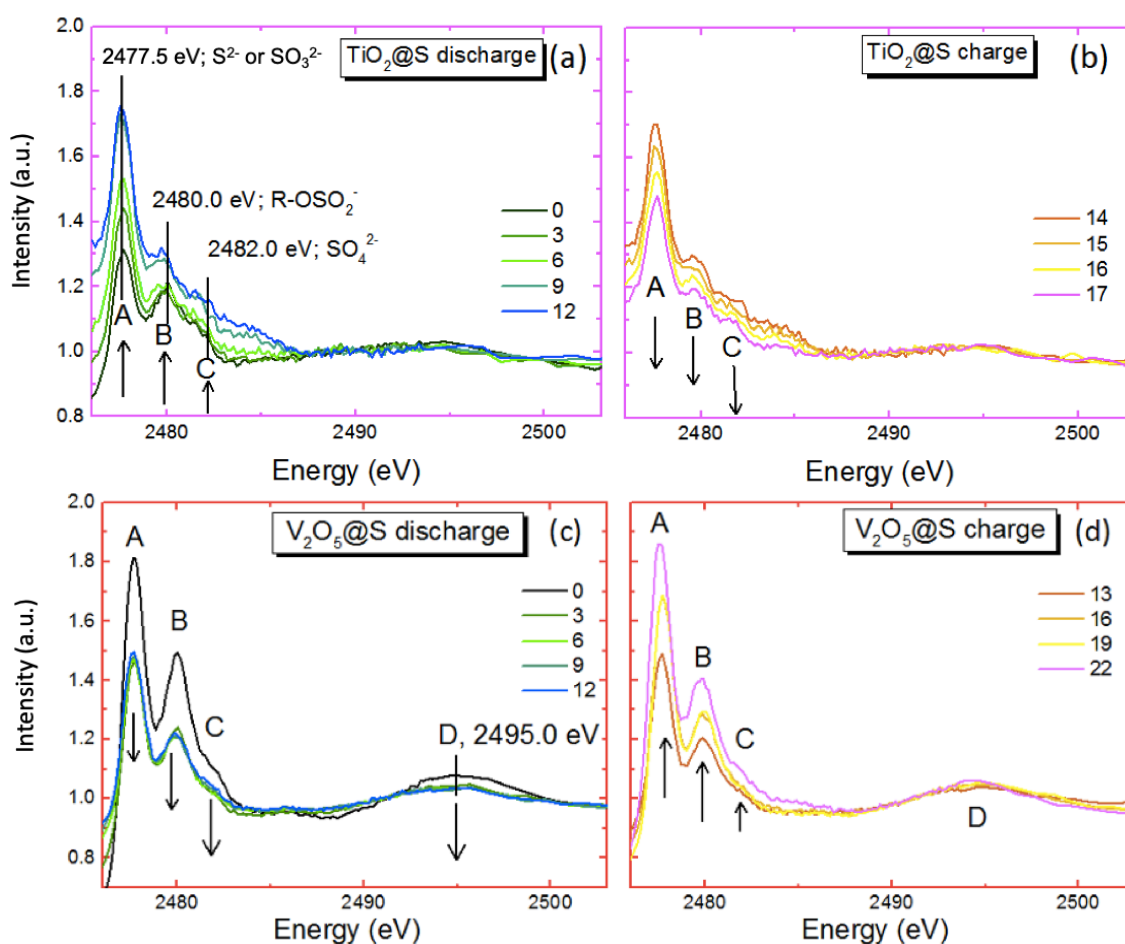


Figure 4-18. Expanded view of the higher energy region of normalised S K-edge XANES spectra. (a, b) TiO₂@S and (c, d) V₂O₅@S, during the first discharge and charge, respectively.

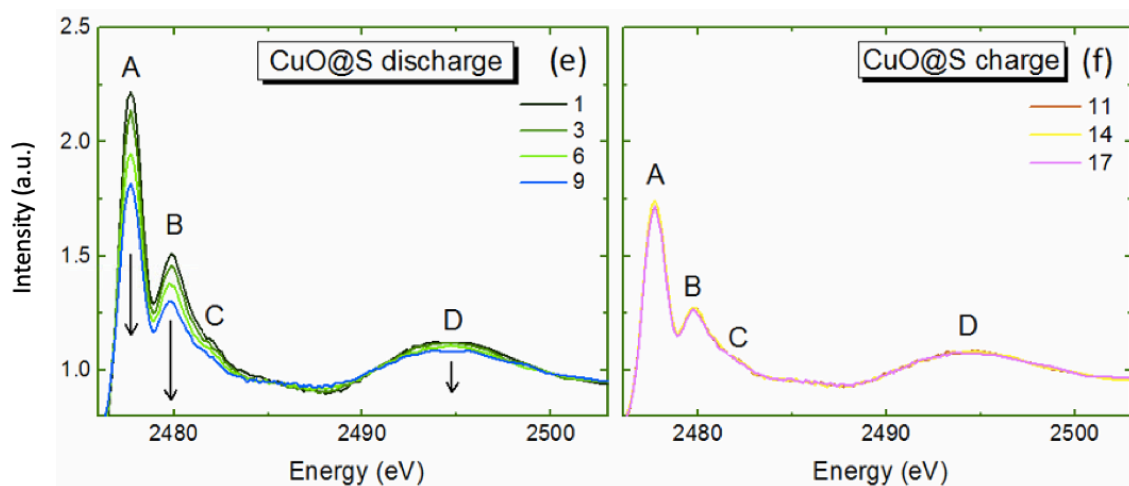


Figure 4-18. Continued. (e, f) CuO@S.

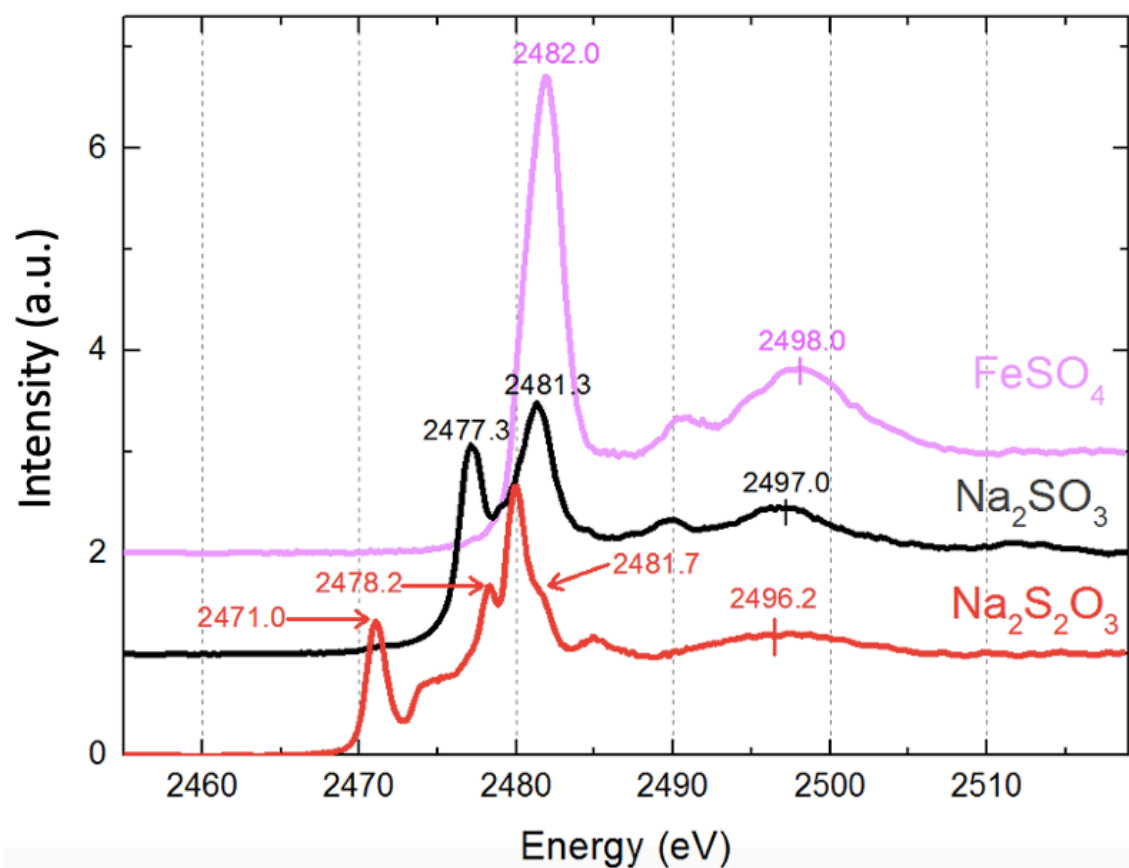


Figure 4-19. S K-edge XANES spectra of reference compounds – $\text{Na}_2\text{S}_2\text{O}_3$, Na_2SO_3 , and FeSO_4 (offset for clarity).

There are three plausible explanations of the origin of oxidised sulphur peaks; (i) beam-induced oxidation of sulphur species, (ii) oxidation of sulphur by the presence of MX additives, and (iii) oxidation of sulphur by the presence of the LiNO_3 salt.

(i) These peaks were firstly considered as the beam-induced oxidation. However, the irrelevance of beam-induced damage to this experimental conditions already proven in Chapter 3 (**Section 3.6.3.3**). In the previous chapter, two oxidised sulphur peaks at 2478.0 and 2480.0 eV were relatively stable throughout the discharge and the charge processes and it was considered that the reaction of active sulphur is not influenced by these oxidised species. However, in this study, these peaks exhibited a reversible tendency during the discharge and charge processes. Such behaviour is not observed in the pure sulphur electrode cycled in the LiNO_3 -free electrolyte. Hence, it is reasonable to deduce that these peaks are due to the oxidation of the active sulphur within the cell. Also, the reversible tendency of these peaks suggest that these peaks are related to the cell reaction, which supports the postulations (ii) and (iii).

(ii) Comparison of **Figure 4-18** demonstrates that these oxidised peaks in the $\text{TiO}_2@\text{S}$ cell evolve differently from those in the $\text{V}_2\text{O}_5@\text{S}$ and $\text{CuO}@\text{S}$ cells. The oxidised sulphur peaks are located at 2477.5, 2480.0, and a weak shoulder at 2482.0 eV, hereby denoted as peak A, B, and C, respectively. Additionally, a broad feature is observed at 2495.0 eV in the $\text{V}_2\text{O}_5@\text{S}$ and the $\text{CuO}@\text{S}$ cells, denoted as peak D. Despite the overall shape being different, those spectra share peak positions at the similar to those in the sulphite, thiosulphate, and sulphate reference compounds (**Figure 4-19**). The peak A can be assigned either as SO_3^{2-} (sulphite) and/or $\text{S}_2\text{O}_3^{2-}$ (thiosulphate). Peak B is a signature of R-OSO_2^- originating from thiosulphate. Thiosulphate reference compound also exhibits a weak shoulder peak at 2481.7 eV, which resembles to the weak shoulder peak C at 2482.0 eV in **Figure 4-18**. This can also be a sign of SO_4^{2-} which gives a peak at 2482.0 eV (**Figure 4-19**). Peak D in the $\text{V}_2\text{O}_5@\text{S}$ cell and the $\text{CuO}@\text{S}$ cell can be assigned to the broad feature in thiosulphate. For the $\text{TiO}_2@\text{S}$ cell, these peaks increase progressively during the discharge process and decrease during the charging process, while the opposite trend is exhibited for the $\text{CuO}@\text{S}$ and $\text{V}_2\text{O}_5@\text{S}$ cells, as indicated by the arrows in **Figure 4-18**.

In the CuO@S and V₂O₅@S cells, oxidised sulphur peaks are at their maximum in the pristine state. The common property of CuO and V₂O₅ is that both have relatively high redox potentials vs Li/Li⁺ (2.53 and 3.40 V, respectively) This could be causing the oxidation of active sulphur after cell assembly and preventing the reduction of sulphur by Li-ions, hence, mitigating the self-discharge reaction. In the V₂O₅@S cell, the pre-edge is not found in the pristine state indicating no formation of polysulphides during cell storage, where as in the CuO@S cell, only a weak sign of the pre-edge is recognised (**Figure 5-6b**). This suggests that the redox potentials of MXs are related to the ability of self-discharge mitigation. During the discharge process, these oxidised sulphur are reduced and becomes active to form polysulphides to proceed the cell reaction, and re-oxidised during the charging process.

In contrast, the redox potential of the TiO₂ additive is low, hence did not oxidise the sulphur species until the start of the cell reaction nor contribute to the mitigation of the self-discharge. Instead, TiO₂ is reduced by Li-ions during the discharge process causing the oxidation of sulphur by the excess oxygen released from TiO₂, therefore, oxidised sulphur peaks become more pronounced. During the charging process, TiO₂ is re-oxidised, resulted in the reversible tendency of the oxidised sulphur peaks.

In the SnO₂@S (**Figure 4-16**) and the CuS@S (**Figure 4-17**) cells, such interaction was not activated and the oxidised sulphur peaks were moderate and unchanged during the cell cycling.

(iii) Another postulation is the oxidation of sulphur by the presence of LiNO₃. It is previously published that the LiNO₃ salt oxidises shuttled polysulphides, which gives Li₂SO₃ and Li₂SO₄ and simultaneously reduces LiNO₃ to LiNO₂. These oxidised polysulphide can also contribute to those peaks observed in the higher energy region of the S K-edge XANES spectra. [56]

Further investigation is required to be able to accurately understand the origin of the oxidation of sulphur.

4.6 Conclusions

Sulphur cathode were prepared utilising five different MX additives and the effect of these MXs towards sulphur reaction mechanisms is directly compared using XAS techniques as well as the electrochemical analysis.

In the electrolyte system employed here (1 M LiTDI in TEGDME), LiNO₃ did not improve the electrochemical performance after 50 cycles, the electrode without the MX additives retained the best capacity in the LiTDI/TEGDME/LiNO₃ electrolyte for prolonged cycling. Nonetheless, the V₂O₅ and SnO₂ additives showed improved capacity retentions compared to the pure S electrode in the absence of the LiNO₃ salt.

These electrodes were investigated under real operating conditions using an *operando* XAS technique. Since the absorption of X-rays is sensitive to the element of interest, good contrast of sulphur change is obtained without being interfered with MX additives. This study confirmed that the influences towards sulphur conversion reaction are different between each MX additive.

We endow that the TiO₂ additive strongly adsorbs polysulphides and is capable of retaining the polysulphide species within the cathode side, as well as tuning the sulphur redox reaction, behaving as a catalyst. The Li₂S disproportionation and deposition is clearly seen when TiO₂ is used as an additive, while in the other MX@S electrodes, we did not detect the clear peaks of Li₂S in the XANES spectra. Further work will need to focus on linear combination fitting (LCF) of the Ti K-edge measurements, which would be useful to quantitatively identify the evolution of TiO₂ to Ti₂O₃. Also, the double-edge experiment of V₂O₅@S will enable us to directly compare the redox activity and influence of the metal oxides towards sulphur chemistry.

The CuO and V₂O₅ additives exhibited very low rate of self-discharge phenomenon during cell storage. This is evident by the absence of the pre-edge feature in **Figure 4-6**. Both CuO and V₂O₅ additives have relatively high redox potential and mutually observed distinct two peaks of oxidised sulphur in the S K-edge XANES at the pristine state. This could be arising from the oxidation of active sulphur during cell storage, which mitigated the reduction to form polysulphides. This suggests that the formation

and dissolution of polysulphides during cell storage can be effectively suppressed by the presence of MXs with high redox potential. However, further investigation is needed to clearly define this behaviour.

4.7 References

- [1] L. Qie and A. Manthiram, "High-Energy-Density Lithium–Sulfur Batteries Based on Blade-Cast Pure Sulfur Electrodes," *ACS Energy Lett.*, vol. 1, no. 1, pp. 46–51, 2016.
- [2] X. Liu, J.-Q. Huang, Q. Zhang, and L. Mai, "Nanostructured Metal Oxides and Sulfides for Lithium-Sulfur Batteries," *Adv. Mater.*, vol. 29, no. 20, p. 1601759, 2017.
- [3] X. Liang, C. Y. Kwok, F. Lodi-Marzano, Q. Pang, M. Cuisinier, H. Huang, C. J. Hart, D. Houtarde, K. Kaup, H. Sommer, T. Brezesinski, J. Janek, and L. F. Nazar "Tuning Transition Metal Oxide-Sulfur Interactions for Long Life Lithium Sulfur Batteries: The 'goldilocks' Principle," *Adv. Energy Mater.*, vol. 6, no. 6, pp. 1501636, 2016.
- [4] H. Al Salem, V. R. Chitturi, G. Babu, J. A. Santana, D. Gopalakrishnan, and L. M. Reddy Arava, "Stabilizing polysulfide-shuttle in a Li-S battery using transition metal carbide nanostructures," *RSC Adv.*, vol. 6, no. 111, pp. 110301–110306, 2016.
- [5] Z. Zhao, S. Wang, R. Liang, Z. Li, Z. Shi, and G. Chen, "Graphene-wrapped chromium-MOF(MIL-101)/sulfur composite for performance improvement of high-rate rechargeable Li-S batteries," *J. Mater. Chem. A*, vol. 2, no. 33, pp. 13509–13512, 2014.
- [6] X. Wang, G. Li, J. Li, Y. Zhang, A. Wook, A. Yu and Z.Chen "Structural and chemical synergistic encapsulation of polysulfides enables ultralong-life lithium-sulfur batteries," *Energy Environ. Sci.*, vol. 9, no. 8, pp. 2533–2538, 2016.
- [7] R. V. Bugga, S. C. Jones, J. Pasalic, C. S. Seu, J.-P. Jones, and L. Torres, "Metal Sulfide-Blended Sulfur Cathodes in High Energy Lithium-Sulfur Cells," *J. Electrochem. Soc.*, vol. 164, no. 2, pp. A265–A276, 2017.
- [8] R. Ponraj, A. G. Kannan, J. H. Ahn, and D. W. Kim, "Improvement of Cycling Performance of Lithium-Sulfur Batteries by Using Magnesium Oxide as a Functional Additive for Trapping Lithium Polysulfide," *ACS Appl. Mater. Interfaces*, vol. 8, no. 6, pp. 4000–4006, 2016.
- [9] X. Z. Ma, B. Jin, H. Y. Wang, J. Z. Hou, X. Bin Zhong, H. H. Wang, and P. M. Xin, "S – TiO₂ composite cathode materials for lithium / sulfur batteries," *J. Electroanal. Chem.*, vol. 736, pp. 127–131, 2015.
- [10] K. Dong, S. Wang, H. Zhang, and J. Wu, "Preparation and electrochemical performance of sulfur-alumina cathode material for lithium-sulfur batteries," *Mater. Res. Bull.*, vol. 48, no. 6, pp. 2079–2083, 2013.
- [11] Y. J. Choi, B.S. Jung, D.J. Lee, J.H. Jeong, K.W. Kim, H.J. Ahn, K.K. Cho, and H.B. Gu, "Electrochemical properties of sulfur electrode containing nano Al₂O₃ for lithium/sulfur cell," *Phys. Scr. T*, vol. T129, pp. 62–65, 2007.

- [12] Z. Yuan, H. J. Peng, T. Z. Hou, J. Q. Huang, C. M. Chen, D. W. Wang, X. B. Cheng, F. Wei, and Q. Zhang, "Powering Lithium-Sulfur Battery Performance by Propelling Polysulfide Redox at Sulfiphilic Hosts," *Nano Lett.*, vol. 16, no. 1, pp. 519–527, 2016.
- [13] Q. Pang, X. Liang, C. Y. Kwok, and L. F. Nazar, "Review—The Importance of Chemical Interactions between Sulfur Host Materials and Lithium Polysulfides for Advanced Lithium-Sulfur Batteries," *J. Electrochem. Soc.*, vol. 162, no. 14, pp. A2567–A2576, 2015.
- [14] Z. Zhang, Q. Li, S. Jiang, K. Zhang, Y. Lai, and J. Li, "Sulfur encapsulated in a TiO₂-anchored hollow carbon nanofiber hybrid nanostructure for lithium-sulfur batteries," *Chem. Eur. J.*, vol. 21, no. 3, pp. 1343–1349, 2015.
- [15] J. Liu, L. Yuan, K. Yuan, Z. Li, Z. Hao, J. Xiang, and Y. Huang, "SnO₂ as a high-efficiency polysulfide trap in lithium-sulfur batteries," *Nanoscale*, vol. 8, no. 28, pp. 13638–13645, 2016.
- [16] Y. Yang, G. Zheng, and Y. Cui, "Nanostructured sulfur cathodes," *Chem. Soc. Rev.*, vol. 42, no. 7, pp. 3018–3132, 2013.
- [17] X. Liang, C. Y. Kwok, F. Lodi-Marzano, Q. Pang, M. Cuisinier, H. Huang, C. J. Hart, D. Houtarde, K. Kaup, H. Sommer, T. Brezesinski, J. Janek, and L. F. Nazar, "Tuning Transition Metal Oxide-Sulfur Interactions for Long Life Lithium Sulfur Batteries: The 'goldilocks' Principle," *Adv. Energy Mater.*, vol. 6, no. 6, p. 1501636, 2016.
- [18] Q. Pang, X. Liang, C. Y. Kwok, and L. F. Nazar, "Advances in lithium-sulfur batteries based on multifunctional cathodes and electrolytes," *Nat. Energy*, vol. 1, no. 9, p. 16132, 2016.
- [19] Q. Pang, D. Kundu, M. Cuisinier, and L. F. Nazar, "Surface-enhanced redox chemistry of polysulphides on a metallic and polar host for lithium-sulphur batteries," *Nat. Commun.*, vol. 5, no. May, p. 4759, 2014.
- [20] X. Liang, C. Hart, Q. Pang, A. Garsuch, T. Weiss, and L. F. Nazar, "A highly efficient polysulfide mediator for lithium-sulfur batteries," *Nat. Commun.*, vol. 6, pp. 1–8, 2015.
- [21] N. Ding, L. Zhou, C. Zhou, D. Geng, J. Yang, S. W. Chien, Z. Liu, M.-F. Ng, A. Yu, T. S. A. Hor, M. B. Sullivan, and Y. Zong, "Building better lithium-sulfur batteries: from LiNO₃ to solid oxide catalyst," *Sci. Rep.*, vol. 6, no. 1, p. 33154, 2016.
- [22] D. S. Wu, F. Shia, G. Zhoua, C. Zua, C. Liua, K. Liua, Y. Liua, J. Wanga, Y. Penga, and Y. Cui, "Quantitative investigation of polysulfide adsorption capability of candidate materials for Li-S batteries," *Energy Storage Mater.*, vol. 13, no. January, pp. 241–246, 2018.
- [23] W. Li, J. Hicks-Garner, J. Wang, J. Liu, A. F. Gross, E. Sherman, J. Graetz, J. J. Vajo, and P. Liu, "V₂O₅ Polysulfide Anion Barrier for Long-Lived Li-S Batteries," *Chem. Mater.*, vol. 26, no. 1, pp. 3403–3410, 2014.

- [24] M. S. Kim, E. S. Shin, J. S. Kim, W. Il Cho, and S. H. Oh, "The effect of V_2O_5/C additive on the suppression of polysulfide dissolution in Li-sulfur batteries," *J. Electroceramics*, vol. 33, no. 3–4, pp. 142–148, 2014.
- [25] M. Liu, Q. Li, X. Y. Qin, G. M. Liang, W. J. Han, D. Zhou, Y. B. He, B. H. Li and F. Y. Kang, "Suppressing Self-Discharge and Shuttle Effect of Lithium–Sulfur Batteries with V_2O_5 -Decorated Carbon Nanofiber Interlayer," *Adv. Sci.*, vol. 13, no. 12, pp. 1602539-1602545, 2017.
- [26] S. Evers, T. Yim, and L. F. Nazar, "Understanding the Nature of Adsorption/Adsorption in Nanoporous Polysulfide Sorbents for the Li–S Battery," *J. Phys. Chem. C*, no. 116, pp. 19653–19658, 2012.
- [27] D. Mardare, A. Yildiz, P. Rambu, D. Florea, N. G. Gheorghe, D. Macovei, C. M. Teodorescu, and D. Luca, "The Meyer-Neldel rule in amorphous TiO_2 films with different Fe content," *J. Mater. Res.*, vol. 27, no. 17, pp. 2271–2277, 2012.
- [28] Q. Sun, C. Lau, D. Geng, and X. Meng, "Atomic and Molecular Layer Deposition for Superior Lithium-Sulfur Batteries : Strategies , Performance , and Mechanisms," *Batter. Supercaps*, vol. 1, no. 2, pp. 41–68, 2018.
- [29] Z. W. Seh, S. Z. Wei, W. Li, J. J. Cha, G. Zheng, Y. Yang, M. T. Mcdowell, P. C. Hsu, and Y. Cui, "Sulphur- TiO_2 yolk-shell nanoarchitecture with internal void space for long-cycle lithium-sulphur batteries," *Nat. Commun.*, vol. 4, 2013.
- [30] W. Zhou, Y. Yu, H. Chen, and F. J. Disalvo, "Yolk – Shell Structure of Polyaniline-Coated Sulfur for Lithium – Sulfur Batteries," *J. Am. Chem. Soc.*, vol. 135, pp. 16736–16743, 2013.
- [31] Y. Zhao, J. Lin, Z. X. Shen, "Metal organic frameworks for energy storage and conversion," *Energy Storage Mater.*, vol. 2, pp. 35–62, 2016.
- [32] Y. Yang, Z. Wang, G. Li, T. Jiang, Y. Tong, X. Yue, J. Zhang, Z. Mao, W. Sun, and K. Sun, "Inspired by the 'tip effect': a novel structural design strategy for the cathode in advanced lithium–sulfur batteries," *J. Mater. Chem. A*, vol. 5, no. 7, pp. 3140–3144, 2017.
- [33] K. Sun, D. Su, Q. Zhang, D. C. Bock, A. C. Marschilok, K. J. Takeuchi, E. S. Takeuchi, and H. Gan, "Interaction of CuS and Sulfur in Li-S Battery System," *J. Electrochem. Soc.*, vol. 162, no. 14, pp. A2834–A2839, 2015.
- [34] C. J. Pelliccione, E. V. Timofeeva, and C. U. Segre, "Potential-Resolved in Situ X-ray Absorption Spectroscopy Study of Sn and SnO_2 Nanomaterial Anodes for Lithium-Ion Batteries," *J. Phys. Chem. C*, vol. 120, no. 10, pp. 5331–5339, 2016.
- [35] J. S. Chen, "for lithium-ion batteries Recent developments in nanotechnology and materials science offer potential," *Mater. Today Energy*, vol. 15, no. 6, pp. 246–254, 2012.
- [36] E. Ventosa, E. Madej, G. Zampardi, B. Mei, P. Weide, H. Antoni, F. L Mantia, M. Muhler, and W. Schuhmann, "Solid Electrolyte Interphase (SEI) at TiO_2 Electrodes in Li-Ion Batteries: Defining Apparent and Effective SEI Based on

- Evidence from X-ray Photoemission Spectroscopy and Scanning Electrochemical Microscopy," *ACS Appl. Mater. Interfaces*, vol. 9, no. 3, pp. 3123–3130, 2017.
- [37] B. Jache, B. Mogwitz, F. Klein, and P. Adelhelm, "Copper sulfides for rechargeable lithium batteries : Linking cycling stability to electrolyte composition," *J. Power Sources*, vol. 247, pp. 703–711, 2014.
- [38] F. Y. Fan and Y.-M. Chiang, "Electrodeposition Kinetics in Li-S Batteries: Effects of Low Electrolyte/Sulfur Ratios and Deposition Surface Composition," *J. Electrochem. Soc.*, vol. 164, no. 4, pp. A917–A922, 2017.
- [39] F. Wang, S. W. Kim, D. H. Seo, K. Kang, Li. Wang, D. Su, J. J. Vajo, J. Wang and J. Graetz, "Ternary metal fluorides as high-energy cathodes with low cycling hysteresis," *Nat. Commun.*, vol. 6, p. 6668, 2015.
- [40] M. A. Lowe, J. Gao, and H. D. Abruña, "Mechanistic insights into operational lithium–sulfur batteries by in situ X-ray diffraction and absorption spectroscopy," *RSC Adv.*, vol. 4, no. 35, pp. 18347–18353, 2014.
- [41] Y. Gorlin, A. Siebel, M. Piana, T. Huthwelker, H. Jha, G. Monsch, F. Kraus, H. A. Gasteiger, and M. Tromp, "Operando Characterization of Intermediates Produced in a Lithium-Sulfur Battery," *J. Electrochem. Soc.*, vol. 162, no. 7, pp. A1146–A1155, 2015.
- [42] S. Waluś, C. Barchasz, J. F. Colin, J. F. Martin, E. Elkaim, J.-C. Lepretre, and F. Alloin, "New insight into the working mechanism of lithium-sulfur batteries: In situ and operando X-ray diffraction characterization," *Chem. Commun.*, vol. 49, no. 72, pp. 7899–7901, 2013.
- [43] Z. Liang, G. Zheng, W. Li, Z. W. Seh, H. Yao, K. Yan, D. Kong, and Y. Cui, "Sulfur Cathodes with Hydrogen Reduced Titanium Dioxide Inverse Opal Structure," *ACS Nano*, vol. 8, no. 5, pp. 5249–5256, 2014.
- [44] X. Feng, M.-K. Song, W. C. Stolte, D. Gardenghi, D. Zhang, X. Sun, J. Zhu, E. J. Cairns, and J. Guo, "Understanding the degradation mechanism of rechargeable lithium/sulfur cells: A comprehensive study of the sulfur-graphene oxide cathode after discharge-charge cycling," *Phys. Chem. Chem. Phys.*, vol. 16, no. 32, pp. 16931–16940, 2014.
- [45] Y. Ye, A. Kawase, M.K. Song, B. Feng, Y. S. Liu, M. Marcus, J. Feng, E. Cairns, J. Guo and J. Zhu, "X-ray Absorption Spectroscopy Characterization of a Li/S Cell," *Nanomaterials*, vol. 6, no. 1, p. 14, 2016.
- [46] L. C. Wen, H.Y. Hsieh, S.C. Chang, M.Y. Lin, Y.H. Lee, W.P. Su, H.-C.I. Kao, H.S. Sheu, L.Y. Jang, M.C. Lee and Y.S. Lee, "Compact Li-doped Gd₂Ti₂O₇ prepared with LiO_{0.5} self-flux," *Mater. Res. Bull.*, vol. 50, pp. 297–302, 2014.
- [47] M. H. Rittmann-Frank, C. J. Milne, J. Rittmann, M. Reinhard, T. J. Penfold, and M. Chergui, "Mapping of the Photoinduced Electron Traps in TiO₂ by Picosecond X-ray Absorption Spectroscopy," *Angew. Chemie Int. Ed.*, vol. 53, no. 23, pp. 5858–5862, 2014.

- [48] D. Wang, L. Liu, X. Sun, and T.-K. Sham, "Observation of lithiation-induced structural variations in TiO₂ nanotube arrays by X-ray absorption fine structure," *J. Mater. Chem. A*, vol. 3, no. 1, pp. 412–419, 2015.
- [49] C. E. Rodríguez-Torres, A. F. Cabrera, L. A. Errico, C. Adan, F. G. Requejo, M. Weissmann, and S. J. Stewart, "Local structure and magnetic behaviour of Fe-doped TiO₂ anatase nanoparticles: Experiments and calculations," *J. Phys. Condens. Matter*, vol. 20, no. 13, 2008.
- [50] K. S. Lin, Y. J. Mai, S. W. Chiu, J. H. Yang, and S. L. I. Chan, "Synthesis and characterization of metal hydride/carbon aerogel composites for hydrogen storage," *J. Nanomater.*, vol. 2012, 2012.
- [51] S. D. Brown, L. Bouchenoire, D. Bowyer, J. Kervin, D. Laundry, M. J. Longfield, D. Mannix, D.F. Paul, A. Stunault, P. Thompson, M.J. Cooper, C. A. Lucas, and W. G. Stirling, "The XMaS beamline at ESRF: Instrumental developments and high resolution diffraction studies," *J. Synchrotron Radiat.*, vol. 8, no. 6, pp. 1172–1181, 2001.
- [52] M. Fehse, L. Monconduit, F. Fischer, C. Tessier, and L. Stievano, "Study of the insertion mechanism of lithium into anatase by operando X-ray diffraction and absorption spectroscopy," *Solid State Ionics*, vol. 268, no. PB, pp. 252–255, 2014.
- [53] M. Fehse, S. Cavaliere, P.E. Lippens, I. Savych, A. Iadecola, L. Monconduit, D.J. Jones, J. Rozière, F. Fischer, C. Tessier, L. Stievano, "Nb-Doped TiO₂ Nanofibers for Lithium Ion Batteries To cite this version : HAL Id : hal-00845155 Nb-doped TiO₂ Nanofibers for Lithium Ion Batteries," *J. Phys. Chem. C*, vol. 117, no. 27, pp. 13827–13835, 2013.
- [54] E. S. Shin, K. Kim, S. H. Oh, and W. Il Cho, "Polysulfide dissolution control: the common ion effect," *Chem. Commun.*, vol. 49, no. 20, pp. 2004–2006, 2013.
- [55] Z. Liu, S. Bertolini, P. B. Balbuena, and P. P. Mukherjee, "Li₂S Film Formation on Lithium Anode Surface of Li-S batteries," *ACS Appl. Mater. Interfaces*, vol. 8, no. 7, pp. 4700–4708, 2016.
- [56] L. Zhang, M. Ling, J. Feng, L. Mai, G. Liu, and J. Guo, "The synergetic interaction between LiNO₃ and lithium polysulfides for suppressing shuttle effect of lithium-sulfur batteries," *Energy Storage Mater.*, vol. 11, no. July 2017, pp. 24–29, 2018.

Chapter 5

Electrically Conducting Polymer Additives

5.1 Introduction

The binder plays an important role in improving the mechanical integrity of the sulphur cathode as well as adhesion and bonding for the composite on the current collector in Li-S batteries. Currently, PVDF is the mostly used binder for the Li-S batteries, which is far from being the perfect choice and reported as having an adverse effect towards Li-S cell cycling. [1][2] This chapter explored interesting approaches to the design of the sulphur cathode. One is the binder-free approach, which is beneficial for increasing the practical energy densities of Li-S batteries by elimination of the electrochemically inactive materials from the cell components. [2][3] Another approach is the replacement of insulating binder with conductive polymers, as a multifunctional binder for the Li-S cathode, and introduction of an environmentally friendly synthesis method. The discussion below introduces a variable use of such conductive polymer materials for an advanced design of sulphur electrodes.

With the issue of diffusional loss of the active sulphur materials to the liquid electrolyte, the introduction of conductive polymers to the cathode composite is one of the promising options to improve the Li-S battery systems. [4] The chain-like structure and rich functional groups of polymers achieve the polysulphide trapping while maintaining good physical confinement in a similar manner to carbon. [5] Hence, offering the improvement of interfacial polarisation of the cell. [6] Recently, it was found that the polysulphide dissolution can be suppressed via lithium bonds formed between lithium in the lithium polysulphide and the electron donating groups of the polymers. [7] For example, the Cui group recently reported that polyvinylpyrrolidone (PVP) shell coating of hollow sulphur nanosphere for cathode shows an excellent long-term cycling of 1000 cycles with a specific capacity of 535 mAh g⁻¹ at the C/2 rate demonstrating 54 % capacity retention and the average Coulombic efficiency (CE)

value of $\sim 98.5\%$. [8] More recently, Cui's group demonstrated the use of aqueous inorganic polymer, ammonium polyphosphate as a multifunction binder successfully inhibiting the polysulphide shuttle effect by blocking the diffusion of polysulphide anions. [9]

Generally, an ideal binder materials should meet the following criterion: (i) It should be both rigid and stable but still feasible to avoid cracking during the volume expansion of sulphur upon cycling, [10] (ii) capable to create a good ionic and electronic conductive network between sulphur and conductive carbon, and (iii) good adhesion to the electrode materials. [11] Following these guidelines, we chose two conductive polymer materials and analysed the behaviour of those as additives for the sulphur cathode composite. We investigated electrically conducting polymers (ECP), [12] polyaniline (PANI) and Poly(3,4-ethylenedioxythiophene)-poly(styrenesulphonate) (PEDOT:PSS) due to their advantages described below.

PANI

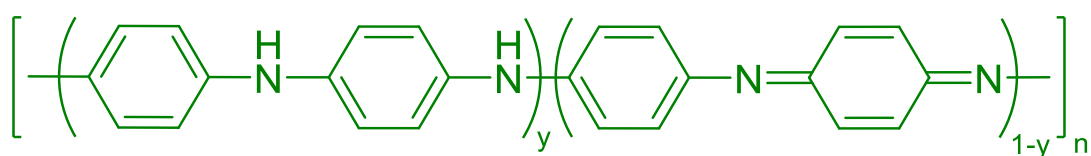


Figure 5-1. Chemical structure of PANI. [13]

Polyaniline (PANI), shown in **Figure 5-1** is one of the most frequently studied conductive polymers due to its electrochemical, electrical, and optical properties, as well as its high affordability owing to its simple components (C, H, and N). [13][14][15] PANI consists of monomer units built from reduced (y in **Figure 5-1**) and oxidised ($1-y$ in **Figure 5-1**) blocks, where $0 \leq y \leq 1$. PANI can exist in three different oxidation states; (i) fully reduced leucoemeraldine ($y = 1$), (ii) half oxidised emeraldine base ($y = 0.5$), and (iii) fully oxidised pernigraniline ($y = 0$). [13] Among these different forms of PANI, emeraldine base is the most suitable type to use in the electrochemistry due to its highest stability and conductivity. Leucoemeraldine slowly oxidises in air and not electrically conducting. Pernigraniline readily decomposes in air because it is

composed of alternating aminobenzene and quinonediimine fragments, which is unstable in the presence of nucleophiles. [16] The morphologies of PANI can be accurately controlled via chemical polymerisation of aniline. PANI can be synthesised into various shapes such as, nanofibers, nanotubes, and nanospheres. [17]

PANI is widely applied in energy storage and conversion devices, such as, supercapacitors, batteries and fuel cells. [13] A recent trend in PANI-related energy research has been focused on Li-S systems to use as a coating material due to its low solubility in the organic electrolyte and high flexibility for encapsulation of sulphur. For example, the Abruna group has adopted Cui and co-workers' TiO₂ yolk-shell structure sulphur encapsulation and designed a polyaniline-sulphur yolk-shell nanocomposite. This composite exhibits a stable capacity of 765 mAh g⁻¹ at 0.2 C rate after 200 cycles. [18] The yolk-shell structure was able to accommodate the volumetric expansion of sulphur within the internal void space, which successfully leads to an excellent performance due to reduced polysulphide dissolution into the electrolyte. Another example is a three-dimensional, cross-linked, structurally stable sulphur-PANI nanotube composite synthesised via *in situ* vulcanisation process. [19] This electrode retains a discharge capacity of 837 mAh g⁻¹ after 100 cycles at the 0.1 C rate. Even at a higher C-rate (1 C), very stable cycling is observed up to 500 cycles. The successful performance is achieved due to the vulcanisation that encapsulates sulphur compounds in molecular-level. Also, a flexible framework of the matrix reduced the stress and structural degradation that can be caused during lithiation and de-lithiation. Moreover, the electropositive amine and imine groups on sulphur-PANI nanotube composite were found to attract polysulphides via electrostatic forces, hence, reduce the detachment of sulphur during prolonged cycling. [19]

PEDOT:PSS

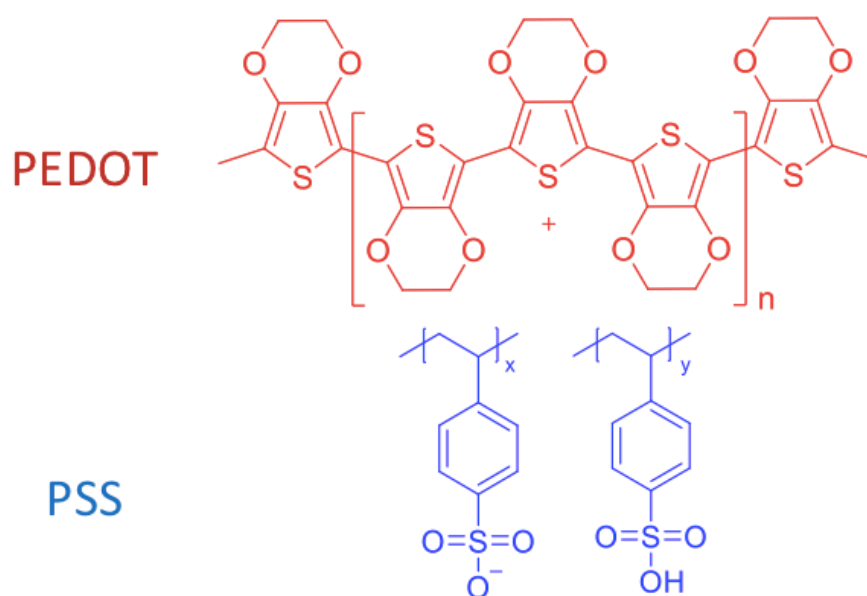


Figure 5-2. Chemical structure of PEDOT:PSS. [20]

PEDOT:PSS, shown in **Figure 5-2**, is another promising material widely studied to enhance the battery performance due to its high electronic conductivity and excellent robustness. [21][22] PEDOT:PSS is described by PEDOT groups that belong to the polythiophene family forming a high electric conducting poly-electrolyte complex when combined with PSS. [23] The SO₃⁻ group in PSS offers good ionic conductivity and attract positive lithium ions. PEDOT:PSS has also been used in Li-S batteries. For example, Cui *et al.* developed the PEDOT:PSS coating on the surface of mesoporous carbon/sulphur particles which effectively minimised the dissolution of polysulphides and loss of active material in sulphur cathodes by strong trapping capability of polysulphides. The initial discharge capacity of 1140 mAh g⁻¹ is achieved with remaining 600 mAh g⁻¹ after 150 cycles at a rate of 0.2 C, and slow capacity decay of 15 % per 100 cycles is observed. [7] PEDOT:PSS coating of sulphur-activated porous graphene cathode composite has been designed by the Wang group. [24] This composite achieved a remarkable rate capability and cycling stability of the initial discharge capacity of 1198 mAh g⁻¹ at a rate of 0.1 C retaining 845 mAh g⁻¹ after 200 cycles. The conductive PEDOT:PSS layer effectively facilitate the charge transportation and minimised the polysulphide diffusion. Zhang *et al.* also concluded that PEDOT:PSS

can serve as an assisted 'current collector' to enhance the electronic conductivity of sulphur cathode and controls the polarisation of the battery. [25]

Generally, for Li-S battery cathodes, Polyvinylidene fluoride (PVDF) and polyethylene glycol (PEO) are commonly used as binders. [26] For Li-S battery synthesis these binders are typically dissolved in NMP, which brings few disadvantages. NMP could dissolve sulphur out of pre-constructed nanostructures, and the evaporation of NMP raises environmental related concerns. [18] The drying of NMP solvents requires high temperature and long time in a vacuum oven, which could cause sublimation of sulphur from the cathode. Recently, it has been found that these binders have some adverse effects on cell performance due to [27]; (i) their linear polymer chains structure and weaker interchain interaction cannot accommodate the large volume change of sulphur particles during lithium insertion and extraction, and undermines the structural integrity of the cathode leading to the loss of electrical contact with conductive additives; (ii) they have weak affinity towards polysulphides and cannot contribute to prevent the shuttle effect of polysulphides; (iii) low swellability of PVDF in DOL:DME based electrolyte restricting the surface area and pore volume of carbon available to the electrolyte during cell operation, [26] (iv) their electrically insulating nature do not effectively transfer electrons, hence, elevate the internal resistance of the cell. Moreover, at high temperature, PVDF decompose into toxic compounds, such as, hydrofluoric acid and fluorocarbons. [2] Alternative binders with high binding strength as well as high electrical conductivity should, therefore, be considered for Li-S cells. [28]

In this chapter we present a simple and low-cost approach to synthesise the binder-free sulphur cathodes (AB@S) composite as well as fabrication of the sulphur electrode using PANI and PEDOT:PSS as the alternative to PVDF binders (PANI-AB@S and PEDOT:PSS-AB@S, respectively). These conductive polymers binders were investigated as conductive additives to AB@S composite or more importantly, utilised in similar fashion to the PVDF binder. In this study, colloidal nanometric sulphur powders were chosen as active materials to aim for more finely distributed sulphur particles within these conductive polymers. In order to understand the influence of the conductive polymer binders, we will focus on the investigation of cathodes varying

PANI and PEDOT:PSS as additives while keeping all other materials and fabrication processes constant. The binder-free electrode sample without PANI or PEDOT:PSS additives was also fabricated in the same method as PANI-AB@S and PEDOT:PSS-AB@S.

In the previous chapters, PVP was used as a binder, which required the use of environmentally hazardous organic solvents, NMP to transform PVP binder from crystalline to amorphous, which is the most widely used method for slurry making during electrode fabrication step. NMP solvent is highly volatile and combustible as well as highly toxic. This introduces the contamination risks particularly upon drying of the electrode. [1] The operational safety is the prime importance as well as desirable parameters, such as, high energy efficiency, long cycle life, low cost, and sustainability. [29] Whereas the slurry fabrication in this chapter employed the aqueous dispersion of composite materials in methanol and no such toxic solvent are used, which provides an additional advantage of being highly safety as well as environmentally friendly.

The objectives in this study is to investigate the influence of the conductive polymer binders on sulphur at an atomic level, with a specific focus on the reaction mechanism of polysulphide intermediate formation and dissolution. To achieve this, AB@S, PANI-AB@S and PEDOT:PSS-AB@S electrodes were analysed using *operando* XAS techniques as well as the electrochemical characterisations.

5.2 Material preparations

5.2.1 Synthesis of polymer additives for sulphur composites

PANI and PEDOT:PSS preparation

The polymer binders were prepared using PEDOT:PSS (1.3 wt % dispersion in water) pipetted into a sample jar and dried in oven under vacuum at 40 °C for 24 hours. PANI was synthesised by soft template method as follows; 0.02 M of aniline solution was oxidised by adding 0.01 M of iron sulphate solution dropwise. Polymerisation reaction was carried at 5 °C for 24 hours. The precipitate was washed with deionised water and methanol and resultant product was dried in vacuum oven for 24 hours at 40 °C. As-prepared materials of PEDOT:PSS and PANI were characterised using FT-IR.

Electrode preparations

The binder-free sulphur composite was prepared by mixing colloidal sulphur and AB in a mass ratio of a ratio of 60:40, followed by heating in Teflon-lined autoclave at 155 °C for 12 hours. A slurry was then prepared by dispersion in methanol by stirring for 16 hours at room temperature.

To prepare the electrodes with polymer binders, colloidal sulphur and AB were mixed in a mass ratio of 70:30 and heated in Teflon-lined autoclave 155 °C for 12 hours. This was then mixed with polymer binder (PANI or PEDOT:PSS), using a mass ratio of S/AB/polymer binder equals to 60:25:15, by dispersion in methanol and stirred for 16 hours at room temperature.

5.2.2 Electrode preparations

Slurries prepared as above methods were coated onto 12.7 mm pre-cut Al discs via spin-coating method. After coating, electrodes were dried in vacuum oven at 60°C for 4 hours and kept in an argon-filled glove box until cell assembly.

For electrodes used for *operando* measurements, pre-cut Al discs were prepared with diameter of 2 mm holes in the centre and cathode composites were spin coated and dried as described above. Cathode composite materials were then manually pasted on the 2 mm holes on the electrodes with a support of Mylar films. The resultant cathode discs were dried in vacuum oven at 60 °C for 4 hours, Mylar films were carefully removed and transferred in an argon-filled glovebox.

Coin cells were assembled in an argon-filled glove box. The construction of *operando* coin cells used in this study is essentially the same as described in **Section 2.4.2**, but CR 2320 coin cell was used instead of CR 2016 cell, together with a spring to maintain a balanced pressure in the cell. *Operando* cells were assembled using epoxy glue instead of coin cell crimper due to the failure of the coin cell crimper during beamtime preparation. Prior to *operando* cell assembly, the epoxy glue was tested to ensure no reaction with electrolyte. All coin cells prepared for in-house electrochemical measurements were assembled in CR 2016 coin cell cases utilising a cell crimper.

5.3 Material characterisations

To confirm the synthesis of PANI and PEDOT:PSS did not undergo phase changes during drying step, the as-prepared polymers were characterised using Fourier transform infrared (FTIR) spectroscopy and X-ray diffraction (XRD) techniques.

PEDOT:PSS

Figure 5-3 shows the FTIR spectrum for dried sample of PEDOT:PSS and Table 5-1 shows the peak assignments for the spectrum collected.

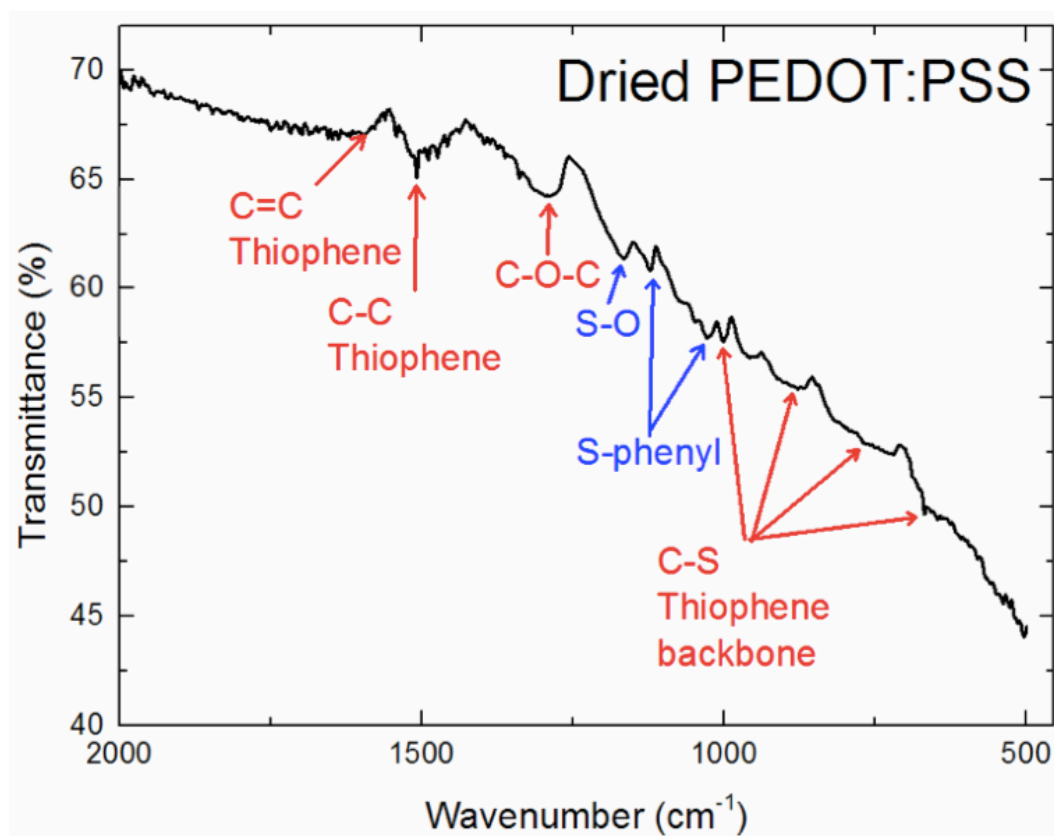


Figure 5-3. FTIR spectrum of dried PEDOT:PSS

All of the PEDOT:PSS signature peaks were observed in the dried PEDOT:PSS sample. PEDOT is recognised by C=C bond at 1585 cm⁻¹, C-C bond at 1508 cm⁻¹, C-O-C stretch at 1290 cm⁻¹, and C-S thiophene backbone located at 1001, 894, 771, 670 cm⁻¹. PSS peaks are arising from S-O bond at 1165 cm⁻¹ and S-phenyl bonds in sulphonic acid at 1122 and 1026 cm⁻¹. Those peaks agree well with previously reported values. [30][31]

Table 5-1. FTIR spectrum peak assignments for PEDOT:PSS

| Wavenumber (cm ⁻¹) | PEDOT | PSS |
|--------------------------------|------------------------------|----------|
| 1585 | C=C | |
| 1508 | C-C | |
| 1290 | C-O-C | |
| 1165 | | S-O |
| 1122 | | S-phenyl |
| 1026 | | |
| 1001 | C-S Thiophene backbone | |
| 894 | | |
| 771 | | |
| 670 | | |

The XRD patterns of PEDOT:PSS is shown in **Figure 5-4**. There were no particular sharp peaks observed in pure PEDOT:PSS sample, indicating substantial amorphous nature of PEDOT:PSS. [32]

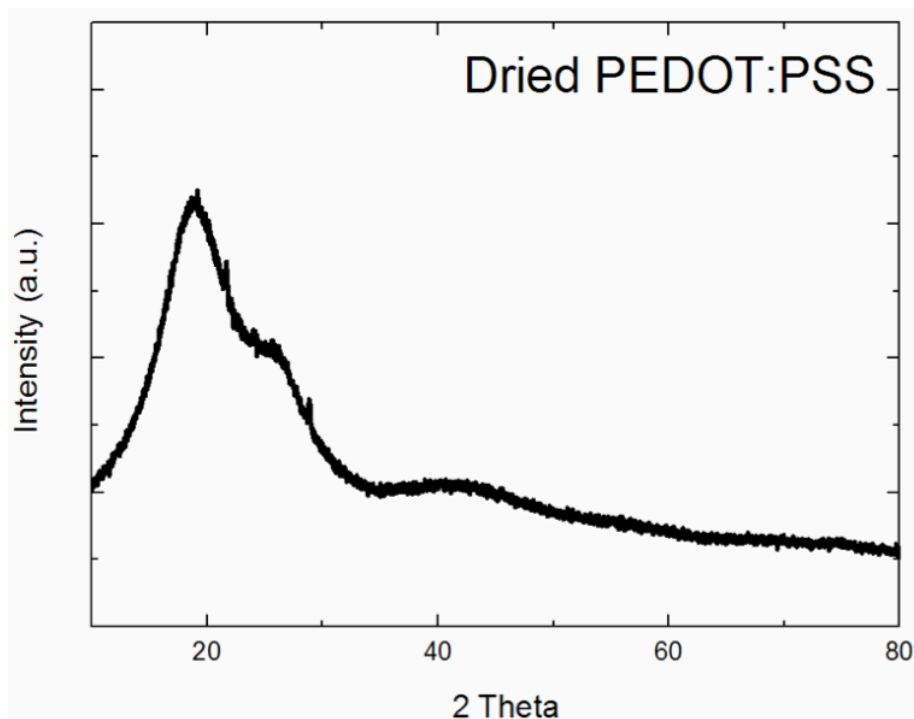


Figure 5-4. XRD spectrum of dried PEDOT:PSS.

PANI

Synthesised PANI was analysed by FTIR and presented in **Figure 5-5**, and **Table 5-2** shows the peak assignments for the spectrum.

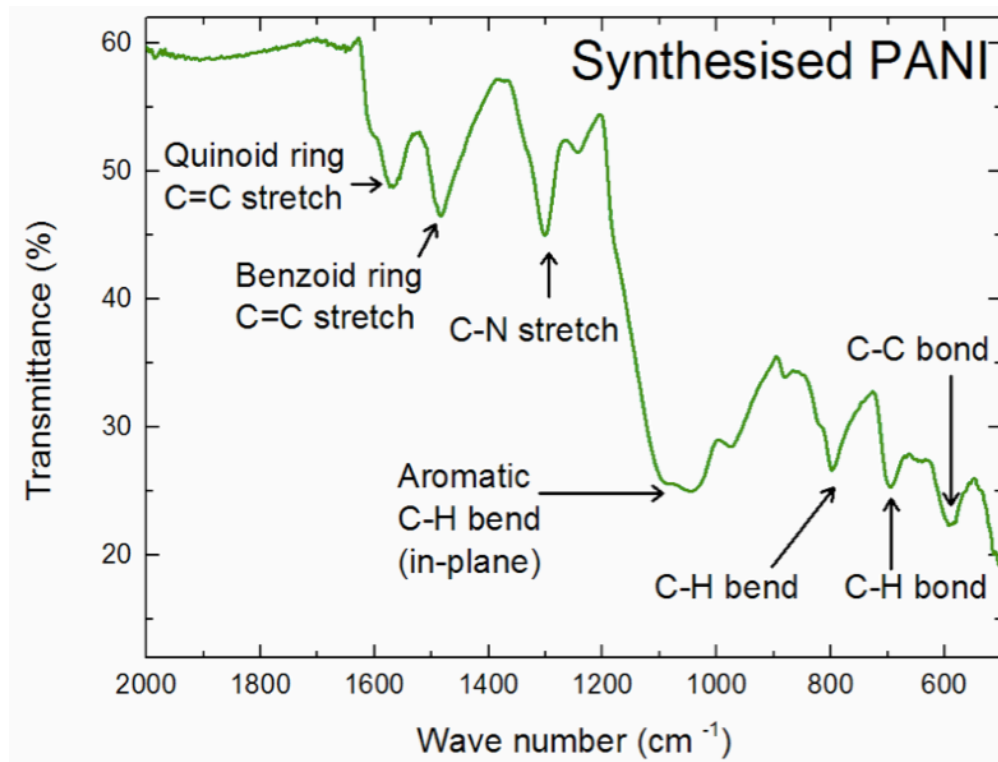


Figure 5-5. FTIR pattern of synthesised PANI.

The characteristic absorption bands of PANI are 592 cm^{-1} and 696 cm^{-1} can be ascribed to C-C and C-H bonding of aromatic ring [33], 798 cm^{-1} is a C-H stretch out of plane bending in 1,4-disubstituted benzene ring [15], broad band around 1100 cm^{-1} is a common feature of emeraldine salt which is overlapped with the aromatic C-H in-plane bending [15][34], 1301 cm^{-1} is attributed to a C-N stretching of an aromatic amine [33], two peaks at 1480 cm^{-1} and 1566 cm^{-1} can be ascribed to benzenoid and quinoid ring, respectively. [19][33][35][36]

Table 5-2. FTIR spectrum peak assignments for emeraldine PANI

| Wavenumber (cm ⁻¹) | Assignments |
|--------------------------------|----------------------------|
| 1566 | Quinoid ring-stretch |
| 1480 | Benzoid ring-stretch |
| 1301 | C-N stretch |
| 1100 | C-H bend (in plane) |
| 798 | C-H bend (out of plane) |
| 696 | C-H bond |
| 592 | C-C bond |

Figure 5-6 represents the XRD patterns of the synthesised PANI-AB@S composite and binder-free AB@S composite. For comparison, pure sulphur and acetylene black (AB) were also measured as they are present in these composites. The XRD patterns of pure AB shows a single broad peak around 26°, indicating an amorphous structure, which agrees with other reports. [37] The diffraction peaks of the AB@S and PANI-AB@S composites exist in similar patterns as pure sulphur, with an additional broad peak nearing 26°, arising from the amorphous nature of AB. The XRD pattern of PANI-AB@S composite exhibits some sharp and strong peaks throughout the entire diffraction range, indicating that the sulphur in PANI@AB@S composite exists in a well-defined crystal structure and sulphur exists in good dispersion within the PANI structure. [15][38] Similarity of the XRD patterns between AB@S composite and PANI-AB@S indicates that PANI does not affect the structure of elemental sulphur and no new phase was formed during the cathode preparation steps. [15]

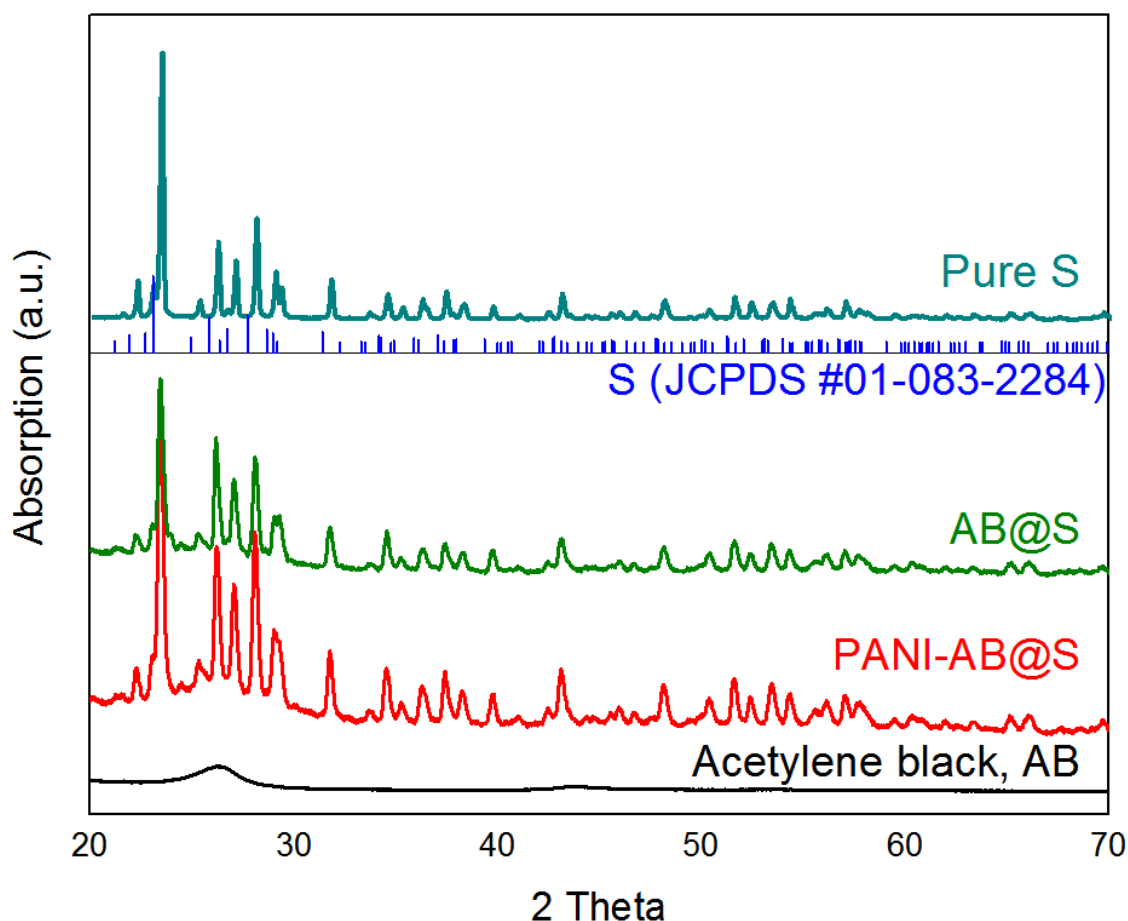


Figure 5-6. XRD patterns of pure sulphur, pure AB, PANI-AB@S, and AB@S composite.

5.4 Electrochemical measurements

In this section, coin cells were investigated electrochemically to establish the cycling performances of as-prepared electrodes.

Galvanostatic cycling was performed on the binder-free AB@S, PANI-AB@S, and PEDOT:PSS-AB@S electrodes are displayed in **Figure 5-7a-c**, respectively. All electrodes were assembled in conventional CR2016 cell assembled using a cell crimper and cycled at a rate of 0.1 C between 1.3 – 2.8 V using the electrolyte containing 1 M LiTFSI and 0.25 M LiNO₃ dissolved in DOL:DME (1:1 by volume).

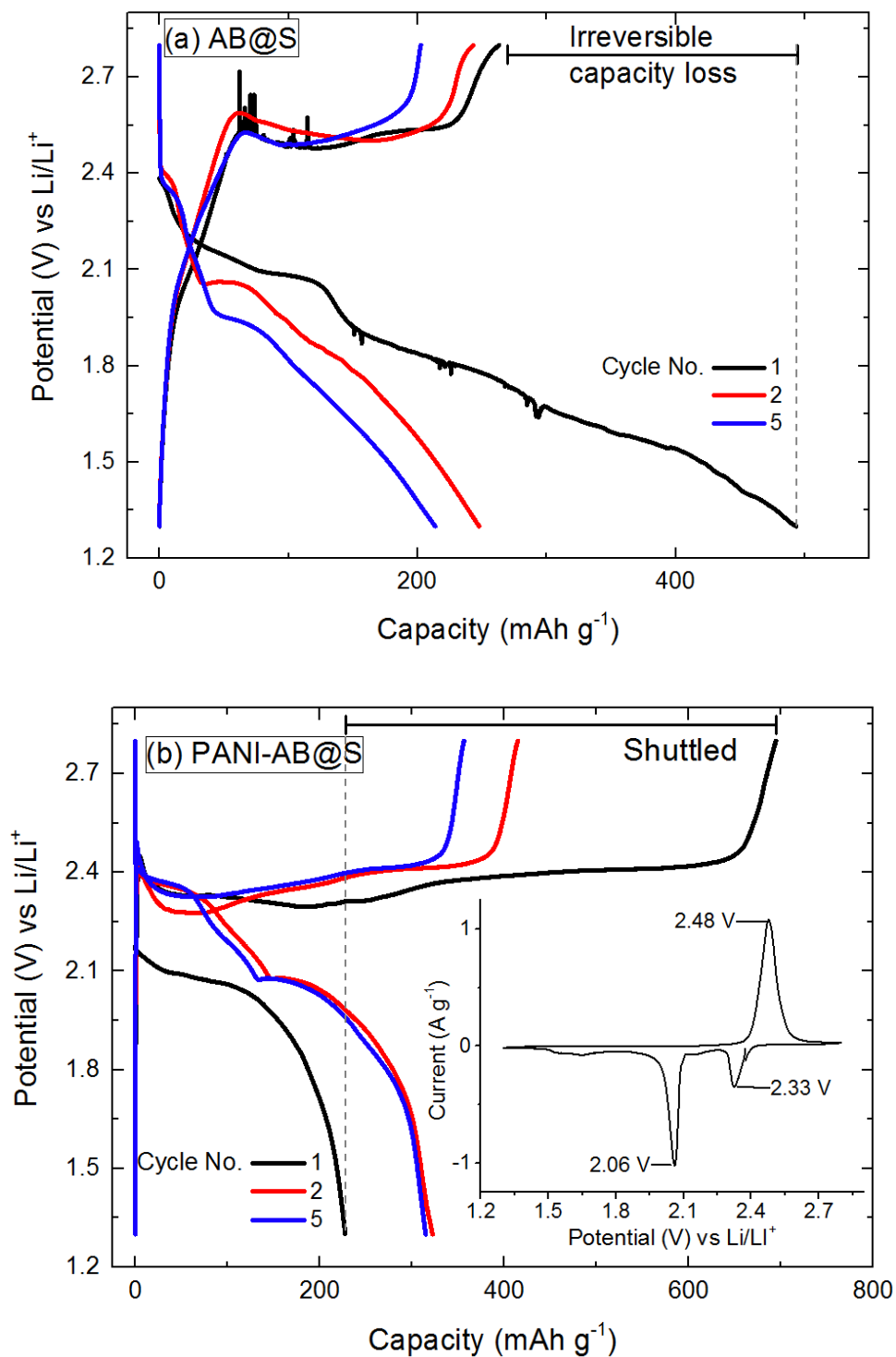


Figure 5-7. Galvanostatic cycling curves for the as-prepared electrodes cycled at a rate of 0.1 C using the electrolyte composed of 1 M LiTFSI and 0.25 M LiNO₃ in DOL:DME (1:1 by volume). (a) AB@S, (b) PANI-AB@S cells.

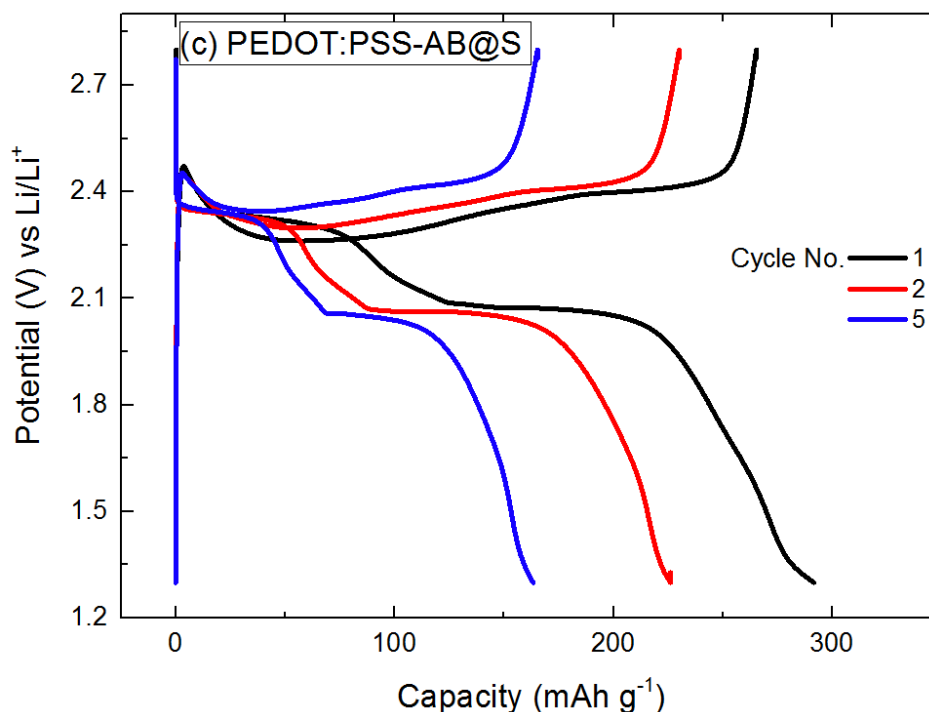


Figure 5-7. Continued. (c) PEDOT:PSS-AB@S cells.

The initial discharge capacity of the binder-free AB@S, PANI-AB@S, and PEDOT:PSS-AB@S electrodes were 493, 230, and 290 mAh g⁻¹, respectively. These values are significantly lower than those found in other samples (Chapter 3 and 4) and can be explained by the electrode design and fabrication method; PVP binder is not used, which decreased the connection between sulphur particles and conductive carbons, hence the adhesion of the electrode composite to the aluminium current collector is weak. Also, the doctor blade coating method was not applicable for this slurry composition, as the methanol is too low viscous than NMP slurry and spreads out immediately after loading onto the doctor blade machine. The spin coating method was used instead which may have decreased the electrode loading of the cell. Nevertheless, the binder-free AB@S and PEDOT:PSS-AB@S electrodes still observed the typical Li-S cell discharge and charge profiles with two discharge voltage plateaus at approximate 2.3 V and 2.1 V.

5.4.1.1 AB@S

The binder-free AB@S electrode exhibited severe voltage depression and extremely short high voltage plateau. Also, a large irreversible capacity loss is found during the

initial charging process (**Figure 5-7a**). Typically, this feature is described to the formation of a thick SEI layer, which is generated when lithium metal reacts with the polysulphides that migrated to the anode during the discharging process. It appears reasonable to believe that this was the main reason for the cell degradation, as this cathode is fabricated in the absence of a binder, therefore, the poor adhesion to the electrode material led to the dissolution of polysulphides into the electrolyte.

5.4.1.2 PANI-AB@S

PANI-AB@S cell exhibited an unusual behaviour in the initial discharge. The high voltage plateau is eliminated and only the low voltage plateau is observed at 2.08 V, followed by the extremely delayed charge ending, so-called 'shuttle' phenomenon, leading to an extremely poor Coulombic efficiency (CE) of 32 %. In the following cycling, the high voltage plateau is appeared. To confirm the accuracy of the discharge curves, CV scan was recorded at a sweep rate of 0.03 mV s⁻¹ between 1.3 – 2.8 V, and the results are shown in the inset of **Figure 5-7b**. The CV scan of this electrode exhibited two cathodic peaks at 2.33 V and 2.06 V, followed by one anodic peak at 2.48 V. These peaks are originating from the reduction and oxidation of sulphur species, which means, conducting state of PANI binder remained unchanged during the discharge and charge processes. [39] Two cathodic peaks also means that the sulphur undergoes two-step conversion reaction. Therefore, two voltage plateaus were expected for PANI-AB@S cell unlike the observed discharge/charge curve for the initial cycle.

There are three plausible explanations for the observed single plateau behaviour. (i) One possible explanation is that the high rate of severe self-discharge caused the dissolution of the sulphur into the electrolyte, forming the long-chain polysulphides in the cell before cycling, leading to the conversion reaction starting from the long-chain polysulphides to medium/short-chain polysulphides, resulting in the elimination of the high voltage plateau. (ii) Another explanation is the slow diffusion of the electrolyte throughout complex structure, limiting the utilisation of active sulphur particles. Because the molecular structure of PANI is smaller than that of PEDOT:PSS, the active sulphur and conductive carbon material can be finely surrounded by the PANI, which takes more time for the electrolyte to be soaked into the sulphur particles, hence large amount of sulphur is left unreacted in the first cycle, leading to the extremely short

high voltage plateau and low discharge capacity. (iii) There is also a possibility that the PANI is binding sulphur species tightly and does not provide sufficient spaces to form long-chain polysulphides, therefore, the long-chain polysulphide formed in the initial discharge is short-lived and immediately converted into shorter chain polysulphides soon after the ring opening of S_8 . Then, in the following charging process, the delayed charge ending is caused due to the difficulty for the short-chain polysulphides to reoxidise to the long-chain polysulphides. The extended charge ending can also be ascribed to the migration of soluble polysulphides between the cathode and anode while charging. [40][41] In the second discharge and onwards, the usual discharge voltage plateaus are observed, due to the more space gained during changing of the polysulphide chain lengths, which now have enough space to accommodate the long-chain polysulphides.

5.4.1.3 PEDOT:PSS-AB@S

In PEDOT:PSS-AB@S cell, although the accessible capacity has decreased over the cycles, two clear discharge plateaus were observed with very little or no voltage polarisation over repeated cycles, and the charging capacity is consistent with the discharge capacity. This indicates that the shuttle reaction is highly mitigated by the PEDOT:PSS binder.

5.4.2 *Operando* XAS analysis

These electrodes were further investigated using *operando* XAS technique. In this section *operando* XANES spectra were collected for as-prepared three different cathode composites and linked to the galvanostatic discharge/charge curves. Initially, the *operando* series of the binder-free AB@S cell is discussed, followed by the PANI-AB@S and PEDOT:PSS-AB@S cells. All XAS measurements displayed in this chapter were performed at beamline XMaS (BM28) at the ESRF.

For the energy calibration of spectra, pure S_8 reference compound was used and spectrum was collected using a Ketek detector. However, *operando* measurements were collected using a Vortex detector due to the failure of a Ketek detector during the beamtime experiment. The cycling rate of 0.1 C was used for the binder-free AB@S and PANI-AB@S cells, whereas slower cycling rate of 0.05 C is used for the PEDOT:PSS-

AB@S cell. Before applying the current to the measured cells, pristine spectrum was collected at OCV and labelled as “spectrum number 0” for each cell.

Spectra were recorded over the energy range of 2450 - 2520 eV, with a step size of 1.5 eV before the pre-edge (2450 – 2465 eV), 0.16 eV in the pre-edge, main-edge, and electrolyte region (2465 - 2495 eV), and 0.5 eV between 2495 – 2520 eV, with a counting time of 10 seconds per point, resulting in a total acquisition time of 43 - 44 minutes per spectrum.

5.4.2.1 Binder-free cell (AB@S)

Figure 5-8 shows the pristine spectra of the AB@S cell, together with the reference sulphur (S_8) compound. The spectrum collected at the pristine state observed a dominant peak at 2480.0 eV originating from the LiTFSI salt in the electrolyte system in which sulphur is in the form of sulphates (VI). [42] This dominant electrolyte peak is also observed in both PANI-AB@S and PEDOT:PSS-AB@S cells at the same energy position and the intensity of this peak was extremely larger than those of the electrochemically active sulphur peaks (inset **Figure 5-8**). The main focus of this XANES study is the electrochemically active sulphur region, therefore, for PANI-AB@S and PEDOT:PSS-AB@S cells, only the S K-edge energy region of the active sulphur is displayed for their *operando* spectra in **Section 5.4.1.2** and **5.4.1.3**.

Theoretically, the pristine spectra should only show a dominant peak at 2472 eV, originating from the S_8 molecule because there should be no electrochemical reaction occurring when no current is applied to the batteries. The normalised S K-edge XANES spectra collected at the pristine state of the AB@S cell is characterised by a dominant peak at 2472.2 eV and a concave shape after the main-edge at 2476.0 eV, these features are very similar to those observed in S_8 reference compound. However, an additional weak shoulder is recognised at lower energy of 2470.4 eV. This could be attributed to a weak sign of the pre-edge originating from the long-chain polysulphide, indicating the self-discharge reaction within the cell during storage.

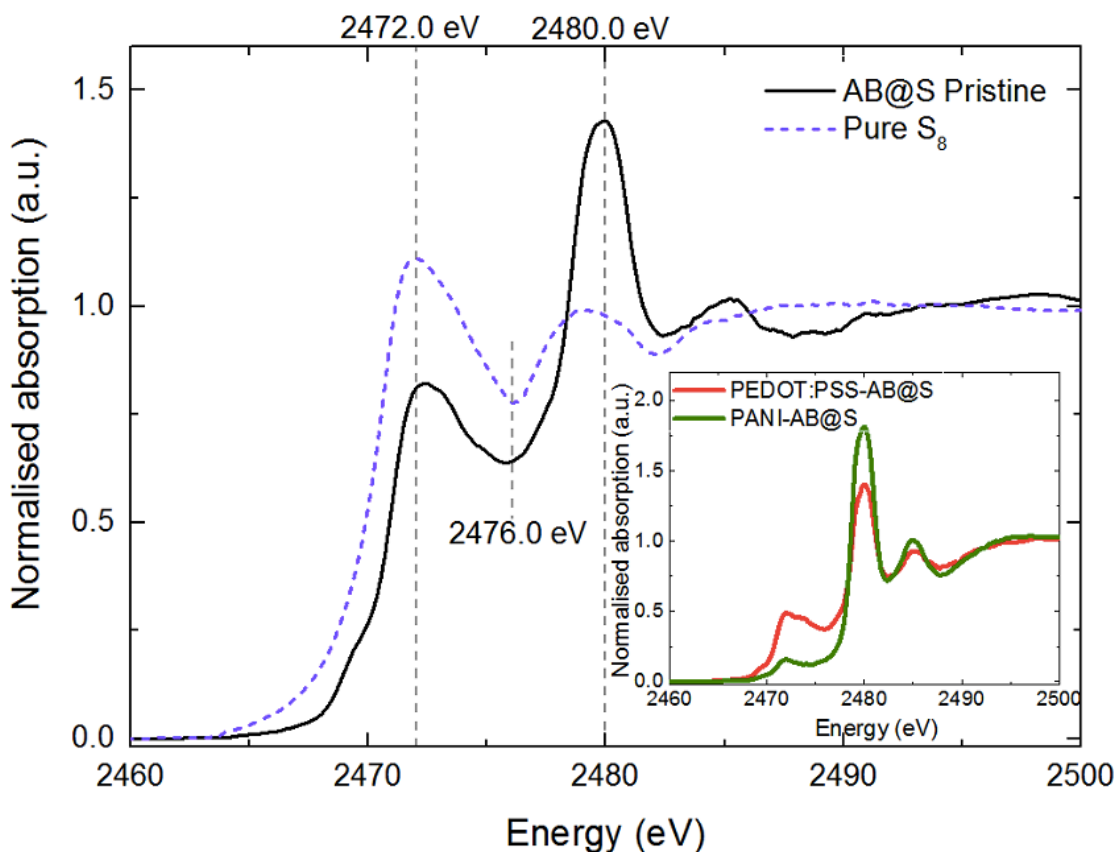


Figure 5-8. Normalised S K-edge XANES spectra of the binder-free AB@S cell in the pristine state and S₈ reference compound. The inset shows the pristine state of the PANI-@S cell and PEDOT:PSS-AB@S cell.

Following the pristine measurement, a current was applied to the cell and the subsequent of *operando* S K-edge XANES spectra were recorded during the initial cycle of this battery. The galvanostatic curve for this cell as a function of time is plotted in **Figure 5-9a**, containing two discharge voltage plateaus at around 1.95 V and 1.65 V, generally attributed to the transitions from Li₂S₈ → Li₂S₄ and Li₂S₄ → Li₂S₂₍₁₎, respectively. [43] This is consistent with the observation from the electrochemical test displayed in **Figure 5-7a**, although the voltage plateaus are approximately 0.4 V lower than those in the electrochemical test cell. This may be caused by the insufficient pressure applied to the *operando* cells, as the *operando* cells were assembled using glue, rather than a coin cell crimper. This might have caused the pressure difference between the conventional cells and *operando* cells.

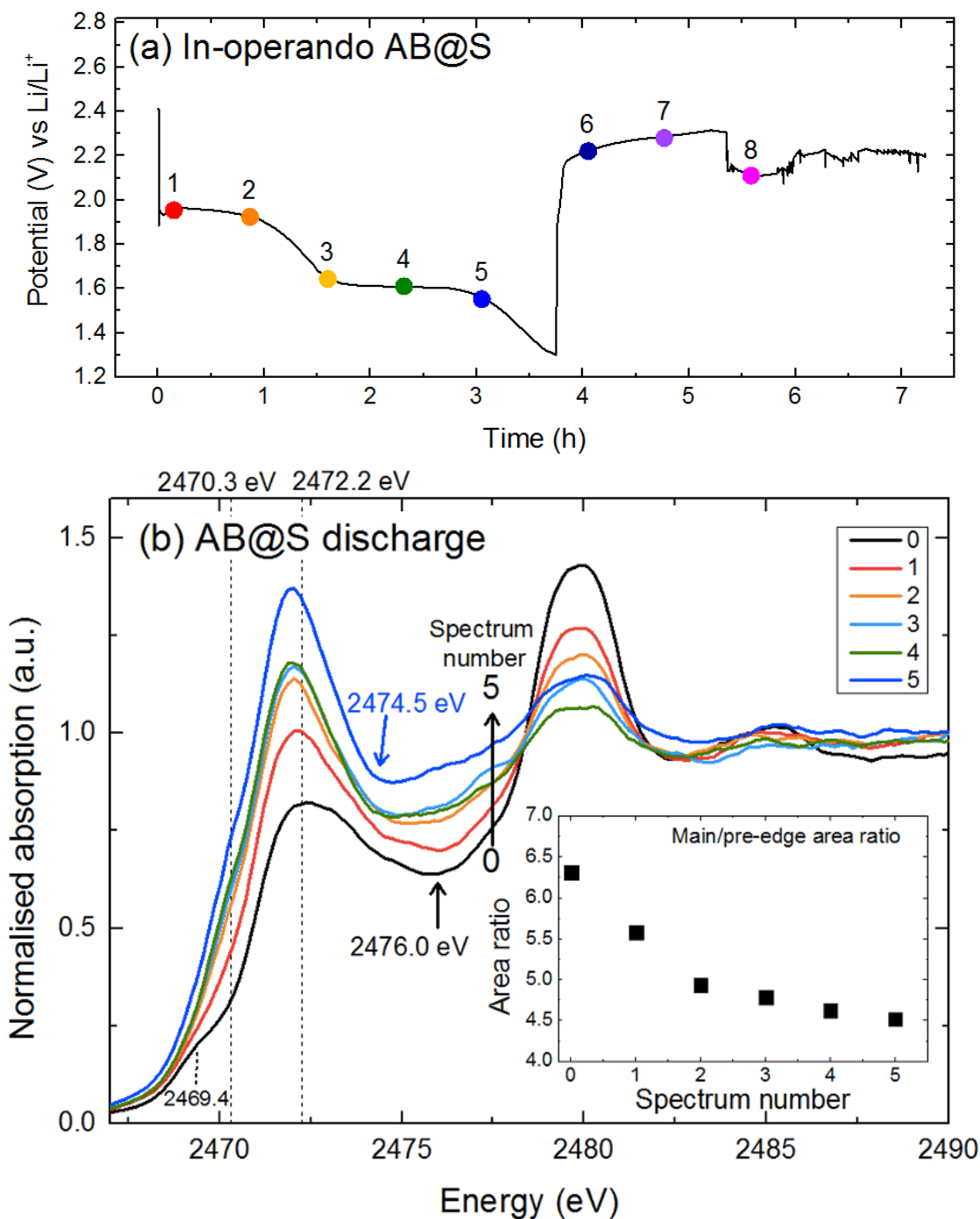


Figure 5-9. Operando XANES spectra dataset for the AB@S electrode cycled at the 0.1 C rate in LiTFSI/DOL:DME/LiNO₃ electrolyte. (a) Galvanostatic discharge/charge curve for the initial cycle with labels 1 – 8 indicating the points at which XANES spectra were started to record. (b) Normalised S K-edge spectra collected during discharge corresponding to these labels including the pristine spectrum (labelled as 0). The inset showing the calculated main/pre-edge area ratio for each spectrum.

The first *operando* spectrum is collected as soon as a current is applied to the cell (**Figure 5-9b**). There is a notable increase in the main-edge resonance in the spectrum number 1 compared to the pristine spectrum. Because the sulphur exists in high concentration (60 %) in the electrode fabricated for this study, it is reasonable to believe that the spectra are distorted by self-absorption (SA) effect, hence, a distinct increase in the main-edge intensity is originated from the dissolution and diffusion of the starting material, S₈, into the electrolyte. A weak pre-edge is recognised at the spectrum number 2 corresponding to the end of high voltage plateau. This is attributed to the formation of long-chain polysulphide. During the discharge, sulphur is reduced by ring opening of cyclo-S₈ into linear S-S chains with two ends of sulphur adjacent to Li atoms. Each of the terminal sulphur atoms have a charge of 1e⁻, which leads to a reduced binding energy of the 1s core-electrons and split the sulphur peak at 2472 eV into the pre-edge and the main-edge. [44]

The energy shift is observed in the main-edge towards slightly lower absorption energy by the value of 0.3 eV. This energy shift was the inverse trend compared to the measurements in previous chapters. Previously, the energy position of the main-edge is increased to higher absorption energy values with increasing depth of discharge, which was the indication of the shortening of the polysulphide chain length. Nevertheless, the negative shift of the main-edge energy could be arising from the error in the XAS measurement. It is worth remembering that a Vortex detector is used for this *operando* measurement instead of a Ketek detector. A Ketek detector is more suitable and advantageous for such bespoke sample environments and all measurements in the previous chapters were collected using a Keytek detector. [45]

The concave shape after the main-edge is shifted to the lower energy position and centroid at around 2475 eV in the spectrum number 2. This supports the detection of the linear-chain polysulphides. During the lower voltage plateau, corresponding to the spectrum number 3 and 4, the pre-edge and main-edge exhibit further increase in their intensities, while the main-edge energy position remains unchanged. It is suggested from the area ratio of main/pre-edge, that the average chain length of polysulphide is decreasing (inset **Figure 5-9b**), as the relative amount of terminal versus internal sulphur atoms proportionally reflects to the chain lengths of polysulphide. [46]–[49]

At the end of the low voltage plateau, both the pre-edge and the main-edge observe their maximum absorption intensity. This suggests that large amount of polysulphides are dissolved in the electrolyte. This supports the findings from the electrochemical analysis in **Figure 5-7a** that shows a large irreversible charging capacity during the first cycling. The uncontrolled dissolution of polysulphides leads to the migration of those to the anode and react with the Li metal, leading to the formation of a thick SEI layer resulting in the charging capacity loss. At the last spectrum of the discharge process (spectrum number 5 in **Figure 5-9b**), the peak position of the main-edge is observed at 2471.6 eV, evidencing that no Li_2S is formed, as the presence of Li_2S would give rise to a peak at 2473 eV.

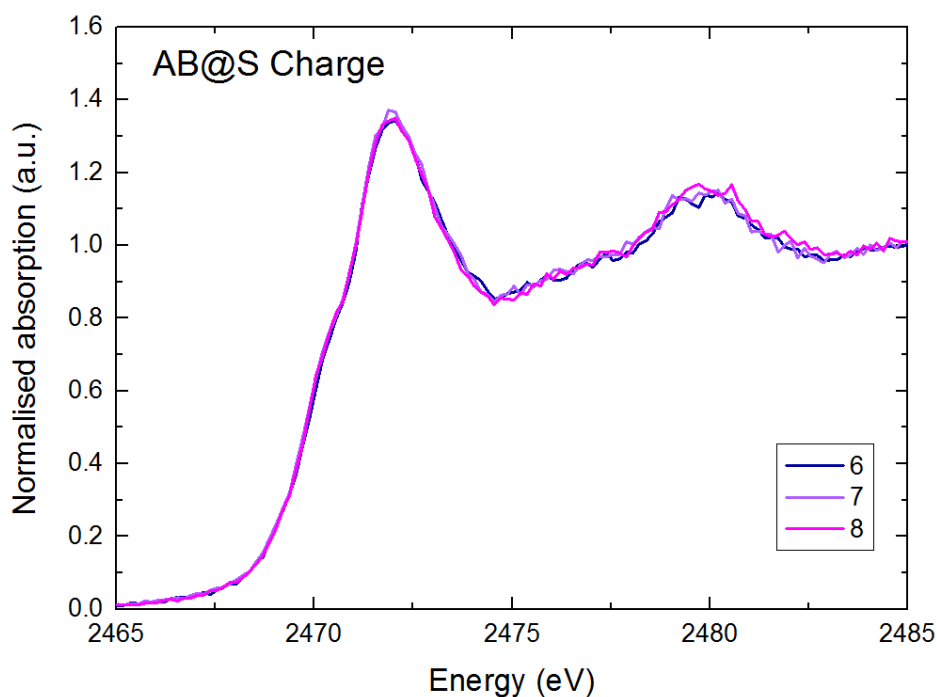


Figure 5-10. Normalised S K-edge XANES spectra set collected during the charging process of the AB@S cell.

During the following charging process, the variation in spectral shape was not observed in the S K-edge XANES spectra, as displayed in **Figure 5-10**. This indicates that the form of sulphur did not experience in any difference, suggesting the inability of the re-oxidation of polysulphides to S_8 . The voltage profile fluctuates during the charging process (**Figure 5-7a**), which is generally considered as the consumption of the

electrolyte and failure of Li⁺-ions conduction. [50] We have also noticed a major peak intensity loss in the electrolyte sulphone especially during the discharge (**Figure 5-9b**). Several explanations to this observation are possible; (i) the evaporation and leakage of the electrolyte from the cell, hence, electrolyte is decomposed which resulted in the voltage fluctuation of the cell over time, or (ii) loss of contact between the electrolyte due to the cathode cracking. As previously mentioned, the binder-free electrode is poorly adhered to the aluminium current collector and the electrode materials can easily be cracked. Both can result in the observed behaviour.

5.4.2.2 PANI-AB@S

The PANI-AB@S cell was analysed under the same conditions as the AB@S cell and a summary of the *operando* analysis is given in **Figure 5-11**.

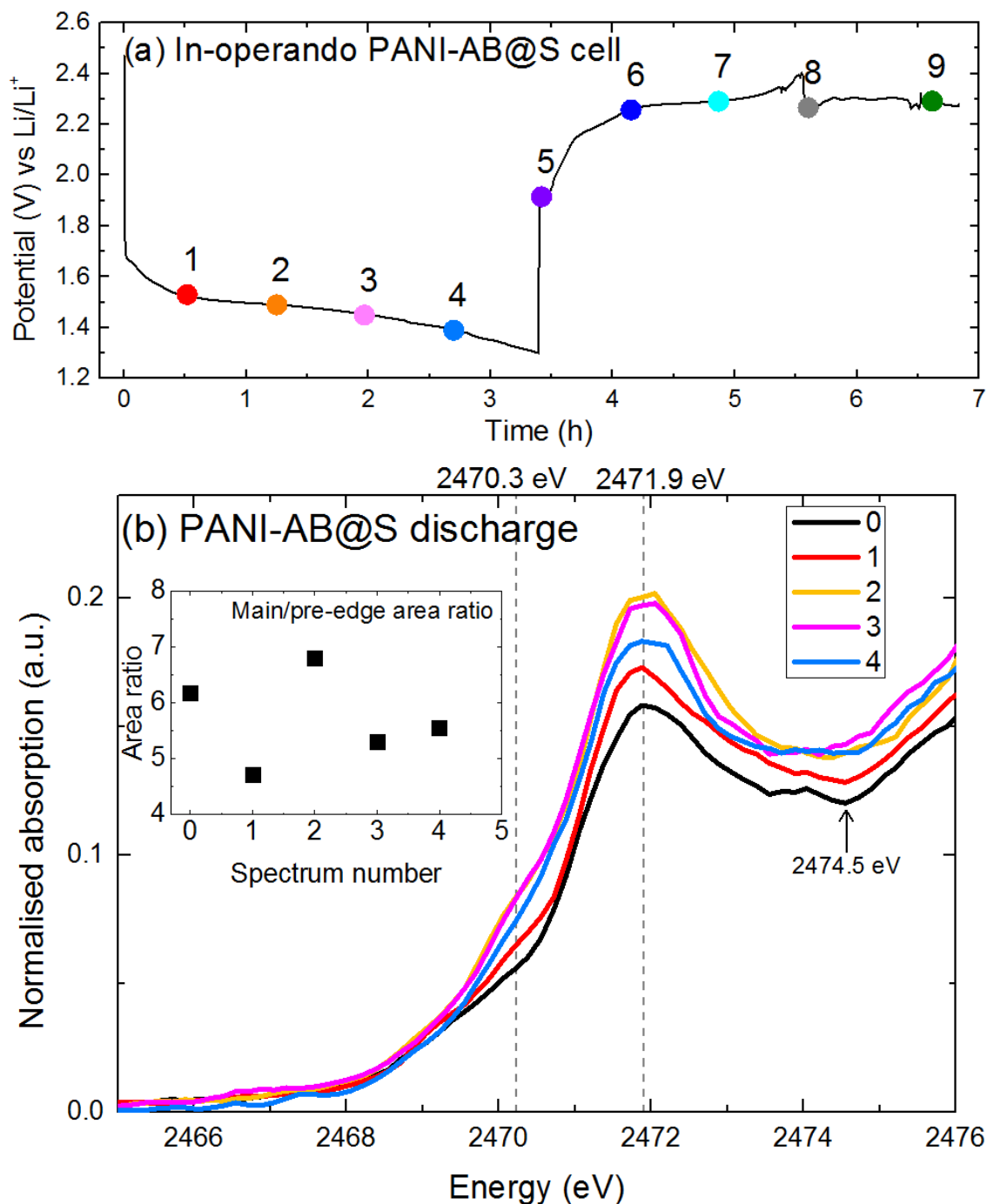


Figure 5-11. (a) *Operando* galvanostatic discharge curve of PANI-AB@S cell at a rate of 0.1 C plotted as a function of time, the dots indicate the points where the XANES spectra were collected. (b) *Operando* sulphur K-edge XANES spectra obtained during

the initial discharge process of the PANI-AB@S cell with the inset showing the calculated main/pre-edge area ratio for each spectrum.

Figure 5-11a shows the galvanostatic curves of *operando* PANI-AB@S battery as a function of time, representing that the high voltage plateau is again missing during the first discharge process and the plateau at low voltage is observed around 1.5 V. This discharge behaviour is in agreement with the one observed in the electrochemical measurement (**Figure 5-7b**), despite the fact that the low voltage plateau is observed about 0.4 V lower than that in the electrochemical test, in which, the possible reason is explained in the previous section (**Section 5.4.2.1**).

Operando XANES measurement provides some clues to this unusual single voltage plateau behaviour. The XANES spectrum at the pristine state exhibited a very weak broad signal of the pre-edge feature at around 2470.3 eV and the dominant main-edge at 2471.9 eV, accompanying the concave feature at 2474.5 eV. These are the characteristics of the long-chain polysulphide, confirming the presence of polysulphide species originating from the self-discharge reaction during the cell storage. However, the pre-edge feature is considerably smaller compared to those observed in the previous chapters where the rate of self-discharge was significantly high and resulted in elimination of the high voltage plateau. However, in this cell, the pre-edge feature at the pristine is not as strong as these cells, indicating the minor self-discharge rate. Therefore, this voltage plateau elimination behaviour may be originating from the different effects to the previous cases. Hence, the postulation (i) discussed in **Section 5.4.1.2** is likely to be eliminated.

During the discharge process, the S K-edge XANES spectra exhibits a similar trend to what was observed in the AB@S cell; start by an increase in the main-edge and pre-edge intensities from the pristine state up to spectrum number 2, indicating the dissolution of polysulphides into the electrolyte. As explained previously, the intensity increased due to the reduced SA effects by lowering the concentration of the sulphur particles at the probed area. This also suggests that the rate of self-discharge was

relatively low, as there are still active original cyclo-octasulphur (S_8) left on the cathode to be dissolved and react with the Li^+ -ions.

In the spectrum number 4, the intensity of the main-edge drops abruptly, whereas that of the pre-edge remains relatively stable. This may be a sign of the shortening of polysulphide chain lengths, where the relative population of the internal sulphur atoms are decreased while maintaining that of the terminal sulphur atoms. Nonetheless, this reaction does not reach the disproportionation of Li_2S/Li_2S because the energy position of the main-edge remains unchanged.

We have also tried to analyse the area ratio of the main/pre-edge (inset **Figure 5-11b**). However, the values fluctuate and do not show a trend which makes it very difficult to make any effective analysis. This is mainly because the spectral feature originating from the active sulphur is extremely low compared to the LiTFSI peak leading to the considerably high signal to noise ratio. To be able to clearly identify the origin of unusual discharge behaviour of this electrode, further investigation is necessary to examine the remaining possibilities discussed earlier in **Section 5.4.1.2**.

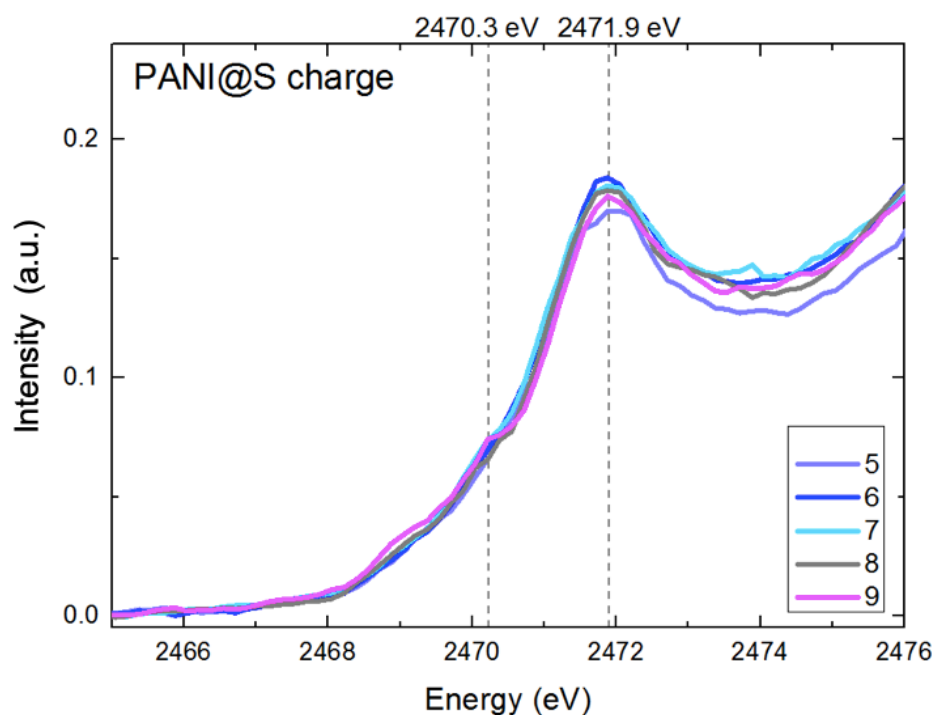


Figure 5-12. Sulphur K-edge XANES spectra obtained during the initial charge process of the PANI-AB@S cell.

Figure 5-12 shows the S K-edge XANES spectra focused on the electrochemically active sulphur species of the following charge process of the PANI-AB@S cell. Again, the voltage profile of the charging process exhibited fluctuating feature (**Figure 5-11a**), and there is no measurable difference in the S K-edge XANES spectra. The accuracy of this data during charging process is ambiguous due to the voltage fluctuation of the cell and a large signal/noise ratio of the spectra. This inferior cell behaviour is potentially caused by the insufficient cell pressure led to evaporation of the electrolyte.

5.4.2.3 PEDOT:PSS-AB@S

From the results above (AB@S and PANI-AB@S *operando* XANES), we speculated that the number of spectra obtained may be too small to clearly interpret the sulphur reaction mechanism. Therefore, for the PEDOT:PSS-AB@S cell, the C-rate is decreased to 0.05 C to allow enough time to obtain more spectra. The summary of *operando* measurement is displayed in **Figure 5-13**.

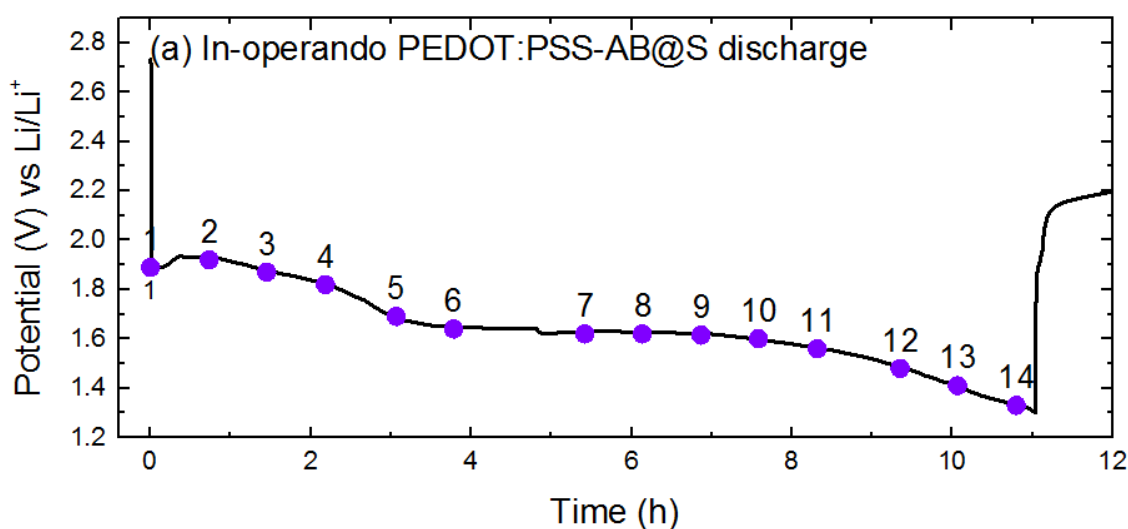


Figure 5-13. (a) Discharge curve for *operando* measurements of the PEDOT:PSS-AB@S cell at a 0.05 C rate with dots indicating the point at XANES spectra are collected.

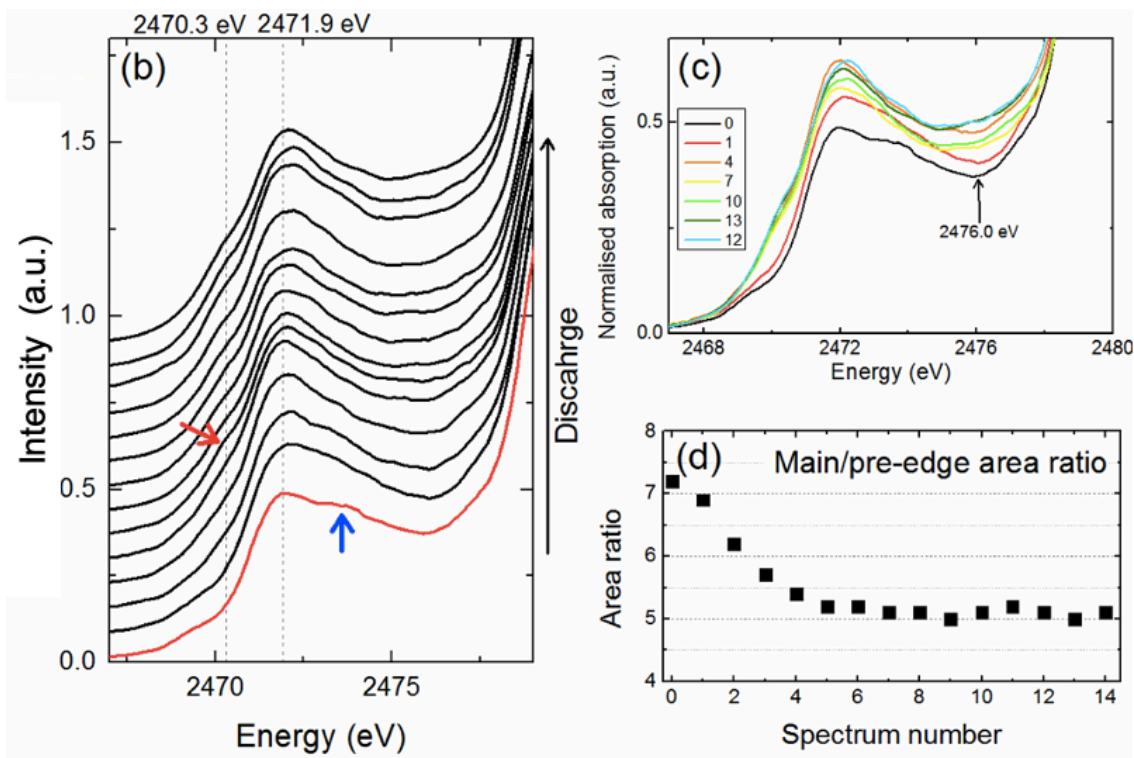


Figure 5-13. Continued. (b) S K-edge XANES spectra with offset collected during *operando* measurement, and (c) selected spectra without offset to clearly show the peak intensities. (d) Plot of the calculated main/pre-edge area ratio for each spectrum.

The discharge curve of the PEDOT:PSS-AB@S cell exhibits two plateaus as expected (**Figure 5-13a**), but again the output discharge plateaus are observed at lower potentials than those observed in **Figure 5-7c** by the value of about 0.4 V. This voltage depression behaviour in *operando* cell is consistent with the other two *operando* cells, hence it is assigned as insufficient pressure in the cell.

The pristine state is dominated by the S_8 feature (solid red line in **Figure 5-13b**), which is characterised by the main-peak at 2471.9 eV with the concave feature observed at 2476 eV. There is also a weak pre-edge sign observed in the lower energy of 2469.5 eV, suggesting the small contribution of the polysulphides, which is ascribed as the long-chain polysulphides according to the area ratio of the main/pre-edge resonance (**Figure 5-13d**). Additional to these active sulphur species, there is a broad shoulder peak detected along with the main-edge (highlighted by the blue arrow in **Figure 5-13b**). The evolution of this peak will be explained in later section.

During the discharge process, the pre-edge becomes more pronounced at spectrum number 5, indicated by the red arrow in **Figure 5-13b**, while the main-edge energy position remains unchanged. The normalised intensity of both the pre-edge and the main-edge increase, suggesting that the overall proportion of the polysulphide is increasing within the cell and polysulphides are diffusing into the electrolyte (**Figure 5-13c**). Throughout the high voltage plateau, the area ratio of the main/pre-edge observed a linear decrease from 7.2 to 5.2 (**Figure 5-13d**). These results are reflecting the reduction of polysulphide chain length. During the low voltage plateau, there is an energy shift in the absorption energy of the main-edge to a slightly higher energy value, indicating the further shortening of polysulphide chain lengths. Nonetheless, the shift in the energy position of the main-edge is very small and the energy position is still far from the Li_2S sign at 2473 eV, and the ratio of the main/pre-edge remains stable around 5 during the low voltage plateau. Therefore, no spectroscopic evidence of lithium sulphide(s) formation is provided. Even after the low voltage plateau, the XANES spectra does not recognise the Li_2S peaks (**Figure 5-13b**), indicating the absence of disproportionation reaction and deposition of Li_2S .

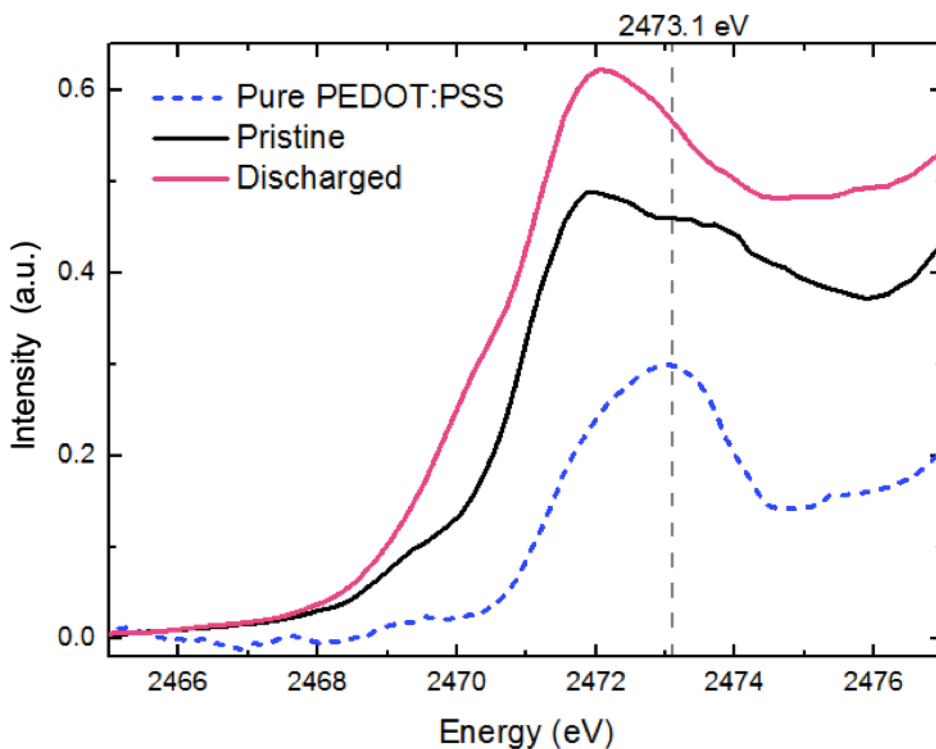


Figure 5-14. Sulphur K-edge XANES spectra of the PEDOT:PSS-AB@S cell at the pristine state and the discharged state compared with pure PEDOT:PSS reference compound.

As mentioned previously, an additional feature was observed in the pristine spectrum as a weak shoulder after the main-edge (**Figure 5-14**, black line). This is slowly diminishing during the discharge process. The energy position of this additional peak matches with that of the PEDOT:PSS reference peak, at 2473.1 eV. Therefore, this peak is assigned to the sulphur atoms present in PEDOT:PSS. The disappearance of this peak suggests that PEDOT:PSS is being consumed during the battery discharge. Therefore, the permanent effect of the PEDOT:PSS additive cannot be expected.

To conclude, the PANI additive showed the possibility of controlling the chain-lengths of polysulphides formed during the discharge. PANI could be favouring the formation of medium to short chain polysulphides due to the limited space to accommodate large compounds of long-chain polysulphides. (**Figure 5-15a**) Whereas the PEDOT:PSS additive demonstrated the prevention of cell polarisation and mitigate the shuttle reaction as well as hindering the irreversible capacity loss during charging (**Figure 5-15b**), which may be due to the support of conductive PEDOT:PSS additive. However, this effect cannot be expected to be maintained PEDOT:PSS is being consumed with increasing depth of discharge.

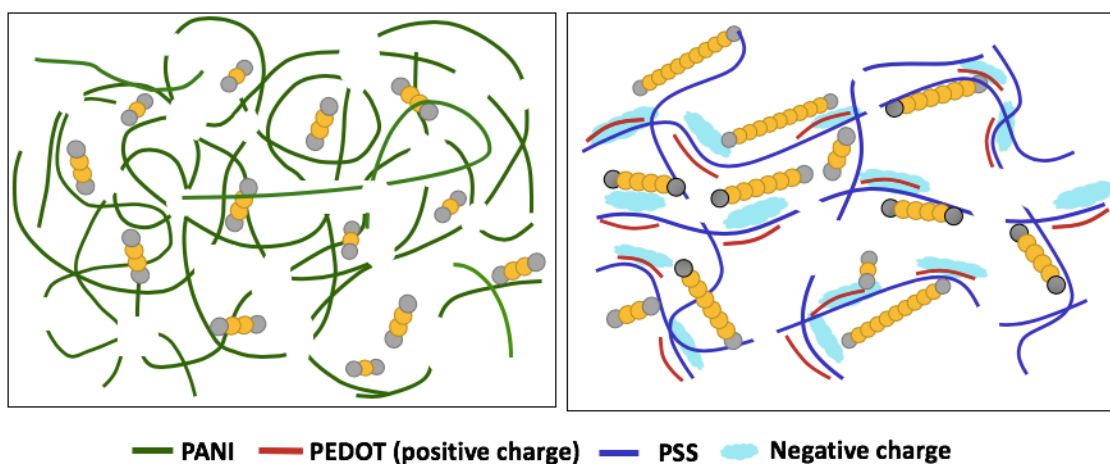


Figure 5-15. Schematic image of effects of PANI and PEDOT:PSS additives on the sulphur cathode.

5.5 Conclusions

This chapter introduced the sulphur composite cathode fabricated using electrical conducting polymers, PANI and PEDOT:PSS, as the replacement for non-conducting

and insulating PVDF binder, utilising a simple, cost-effective, and scalable method. These electrodes were investigated using an *operando* XAS technique as well as the electrochemical analysis to determine the sulphur reaction mechanisms. *Operando* XANES measurement technique used in this study was not as sophisticated as used in the previous two chapters. The scan time for each spectrum had to be longer than those collected in previous chapters because a Vortex was used for *operando* measurements due to the failure of a Ketek detector. As the conversion reaction is continuous, some polysulphide species may be too short-lived to be detectable in this measurement method. Also, the signal to noise ratio in the spectra collected using a Vortex detector was considerably higher compared to those collected using a Ketek detector. Therefore, there is a possibility that the species exist in the beginning of the spectrum collection may differ to those exist at the end of the measurement collection. Moreover, *operando* cells were assembled using an epoxy glue, which failed to supply a good pressure in the cells. Further examination is necessary to obtain more accurate results.

Of course, the binder-free AB@S, PANI-AB@S, and PEDOT:PSS-AB@S electrodes prepared in this work, will have very low mechanical strength after dissolution of sulphur on discharge, severely limiting their practical applications. Nonetheless, this study supports the further research into economical and electrochemically benign binder-free cathode as an interesting approach for rechargeable Li-S batteries for future work.

One valuable objective for future work would be to determine the behaviour of conductive polymer binders using XANES technique combined with other X-ray based investigations, such as, SAXS (small-angle X-ray scattering) and XRD. At XMaS beamline at the ESRF, it is possible to combine different characterisation methods together with XAS measurements, which would bring a significant advantage for the future research not only for the Li-S batteries, but also for various Li-ion battery systems.

5.6 References

- [1] D. Bresser, S. Passerini, and B. Scrosati, "Recent progress and remaining challenges in sulfur-based lithium secondary batteries - a review," *Chem. Commun.*, vol. 49, no. 90, pp. 10545–10562, 2013.
- [2] M. R. Kaiser, X. Liang, H. K. Liu, S. X. Dou, and J. Z. Wang, "A methodical approach for fabrication of binder-free Li₂S-C composite cathode with high loading of active material for Li-S battery," *Carbon N. Y.*, vol. 103, pp. 163–171, 2016.
- [3] K. Sun, Q. Zhang, D. C. Bock, X. Tong, D. Su, A. C. Marchilok, K. J. Takeuchi, E. S. Takeuchi, and H. Gan, "Interaction of TiS₂ and Sulfur in Li-S Battery System," *J. Electrochem. Soc.*, vol. 164, no. 6, pp. A1291–A1297, 2017.
- [4] K. Liao, P. Mao, N. Li, M. Han, J. Yi, P. He, Y. Sun, and H.S. Zhou, "Stabilization of polysulfides via lithium bonds for Li-S batteries," *J. Mater. Chem. A*, vol. 4, no. 15, pp. 5406–5409, 2016.
- [5] Y. Yang, G. Zheng, and Y. Cui, "Nanostructured sulfur cathodes," *Chem. Soc. Rev.*, vol. 42, no. 7, pp. 3018–3132, 2013.
- [6] G. Ma, Z. Wen, J. Jin, Y. Lu, K. Rui, X. Wu, M. Wu, and J. Zhang "Enhanced performance of lithium sulfur battery with polypyrrole warped mesoporous carbon/sulfur composite," *J. Power Sources*, vol. 254, pp. 353–359, 2014.
- [7] K. Park, J. H. Cho, J.-H. Jang, B.-C. Yu, A. T. De La Hoz, K. M. Miller, C. J. Ellison, and J. B. Goodenough, "Trapping lithium polysulfides of a Li-S battery by forming lithium bonds in a polymer matrix," *Energy Environ. Sci.*, vol. 8, no. 8, pp. 2389–2395, 2015.
- [8] W. Li, G. Zheng, Y. Yang, Z. W. Seh, N. Liu, and Y. Cui, "High-performance hollow sulfur nanostructured battery cathode through a scalable, room temperature, one-step, bottom-up approach," *Proc. Natl. Acad. Sci.*, vol. 110, no. 18, pp. 7148–7153, 2013.
- [9] G. Zhou, K. Liu, Y. Fan, M. Yuan, B. Liu, W. Liu, F. Shi, Y. Liu, W. Chen, J. Lopez, D. Zhuo, J. Zhao, Y. Tsao, X. Huang, Q. Zhang, and Y. Cui "An Aqueous Inorganic Polymer Binder for High Performance Lithium-Sulfur Batteries with Flame-Retardant Properties," *ACS Cent. Sci.*, vol. 4, no. 2, pp. 260–267, 2018.

- [10] Y. Yang, G. Yu, J. J. Cha, H. Wu, M. Vosgueritchian, Y. Yao, Z. Bao, and Y. Cui, "Improving the Performance of Lithium - Sulfur Batteries by Conductive Polymer Coating," *ACS Nano*, vol. 5, no. 11, pp. 9187–9193, 2011.
- [11] M. Song, Y. Zhang, and E. J. Cairns, "A Long-Life, High-Rate Lithium/Sulfur Cell: A Multifaceted Approach to Enhancing Cell Performance," vol. 13, no. 12, pp. 5891–5899, 2013.
- [12] M. R. Arcila-Velez, R. K. Emmetta, M. Karakayab, R. Podilab, K. P. Díaz-Orellanaa, A. M. Raob, and M. E. Roberts, "A facile and scalable approach to fabricating free-standing polymer - Carbon nanotube composite electrodes," *Synth. Met.*, vol. 215, pp. 35–40, 2016.
- [13] H. Wang, J. Lin, and Z. X. Shen, "Polyaniline (PANI) based electrode materials for energy storage and conversion," *J. Sci. Adv. Mater. Devices*, vol. 1, no. 3, pp. 225–255, 2016.
- [14] C. H. B. Silva, N. A. Galiote, F. Huguenin, É. Teixeira-Neto, V. R. L. Constantino, and M. L. A. Temperini, "Spectroscopic, morphological and electrochromic characterization of layer-by-layer hybrid films of polyaniline and hexaniobate nanoscrolls," *J. Mater. Chem.*, vol. 22, no. 28, p. 14052, 2012.
- [15] Y. Sun, S. Wang, H. Cheng, Y. Dai, J. Yu, and J. Wu, "Synthesis of a ternary polyaniline@acetylene black-sulfur material by continuous two-step liquid phase for lithium sulfur batteries," *Electrochim. Acta*, vol. 158, pp. 143–151, 2015.
- [16] Z. A. Boeva and V. G. Sergeev, "Polyaniline: Synthesis, properties, and application," *Polym. Sci. Ser. C*, vol. 56, no. 1, pp. 144–153, 2014.
- [17] H. D. Tran, J. M. D'Arcy, Y. Wang, P. J. Beltramo, V. A. Strong, and R. B. Kaner, "The oxidation of aniline to produce 'polyaniline': A process yielding many different nanoscale structures," *J. Mater. Chem.*, vol. 21, no. 11, pp. 3534–3550, 2011.
- [18] W. Zhou, Y. Yu, H. Chen, and F. J. Disalvo, "Yolk - Shell Structure of Polyaniline-Coated Sulfur for Lithium - Sulfur Batteries," *J. Am. Chem. Soc.*, vol. 135, no. 135, pp. 16736–16743, 2013.
- [19] L. Xiao, Y. Cao, J. Xiao, B. Schwenzler, M. H. Engelhard, L. V. Saraf, Z. Nie, G. J. Exarhos, and J. Liu, "A soft approach to encapsulate sulfur: Polyaniline

- nanotubes for lithium-sulfur batteries with long cycle life," *Adv. Mater.*, vol. 24, no. 9, pp. 1176–1181, 2012.
- [20] R. Gangopadhyay, B. Das, and M. R. Molla, "How does PEDOT combine with PSS? Insights from structural studies," *RSC Adv.*, vol. 4, no. 83, pp. 43912–43920, 2014.
- [21] Q. Zhang, Y. Wang, Z. W. Seh, Z. Fu, R. Zhang, and Y. Cui, "Understanding the Anchoring Effect of Two-Dimensional Layered Materials for Lithium-Sulfur Batteries," *Nano Lett.*, vol. 15, no. 6, pp. 3780–3786, 2015.
- [22] S. Ozaki, Y. Wada, and K. Noda, "DC Hall-effect measurement for inkjet-deposited films of poly(3,4-ethylenedioxythiophene)/poly(4-styrenesulfonate) by using microscale gap electrodes," *Synth. Met.*, vol. 215, pp. 28–34, 2016.
- [23] P. R. Das, L. Komsiyiska, O. Osters, and G. Wittstock, "Effect of solid loading on the processing and behavior of PEDOT:PSS binder based composite cathodes for lithium ion batteries," *Synth. Met.*, vol. 215, pp. 86–94, 2016.
- [24] H. Li, M. Sun, T. Zhang, Y. Fang, and G. Wang, "Improving the performance of PEDOT-PSS coated sulfur@activated porous graphene composite cathodes for lithium-sulfur batteries," *J. Mater. Chem. A*, vol. 2, no. 43, pp. 18345–18352, 2014.
- [25] A. Wang, G. Xu, B. Ding, Z. Chang, Y. Wang, H. Dou, and X. Zhang, "Highly Conductive and Lightweight Composite Film as Polysulfide Reservoir for High-Performance Lithium-Sulfur Batteries," *ChemElectroChem*, vol. 4, no. 2, pp. 362–368, 2017.
- [26] M. J. Lacey, F. Jeschull, K. Edström, and D. Brandell, "Porosity Blocking in Highly Porous Carbon Black by PVdF Binder and Its Implications for the Li-S System," *J. Phys. Chem. C*, vol. 118, no. 45, pp. 25890–25898, 2014.
- [27] K. Xi, P. R. Kidambi, R. Chen, C. Gao, X. Peng, Ca. Ducati, S. Hofmann, and R. V. Kumar, "Binder free three-dimensional sulphur/few-layer graphene foam cathode with enhanced high-rate capability for rechargeable lithium sulphur batteries," *Nanoscale*, vol. 6, no. 11, pp. 5746–5753, 2014.
- [28] L. Yan, X. Gao, J. P. Thomas, N. Jenner, H. Altounian, K. T. Leung, Y. Mengb, and Y. Lia, "Ionically cross-linked PEDOT:PSS as a multi-functional conductive binder for

- high-performance lithium–sulfur batteries,” *Sustain. Energy Fuels*, vol. 2, no. 7, pp. 1574–1581, 2018.
- [29] J. Liu, C. Xu, Z. Chen, S. Ni, and Z. Xiang, “Progress in aqueous rechargeable batteries,” *Green Energy Environ.*, vol. 3, no. 1, pp. 20–41, 2017.
- [30] Y. Liu, B. Weng, J. M. Razal, Q. Xu, C. Zhao, Y. Hou, S. Seyedin, R. Jalili, G. G. Wallace, and Jun Chen, “High-Performance Flexible All-Solid-State Supercapacitor from Large Free-Standing Graphene-PEDOT/PSS Films,” *Sci. Rep.*, vol. 5, no. October, pp. 1–11, 2015.
- [31] R. Sengupta, P. Singhai, and A.L. Verma, “A Short Review on Rubber / Clay Nanocomposites With Emphasis on Mechanical Properties,” *Engineering*, vol. 47, pp. 21–25, 2007.
- [32] C. Gao, J. Li, J. Liu, J. Zhang, and H. Sun, “Influence of MWCNTs doping on the structure and properties of PEDOT:PSS films,” *Int. J. Photoenergy*, vol. 2009, 2009.
- [33] A. Mostafaei and A. Zolriasatein, “Progress in Natural Science : Materials International Synthesis and characterization of conducting polyaniline nanocomposites containing ZnO nanorods,” *Prog. Nat. Sci. Mater. Int.*, vol. 22, no. 4, pp. 273–280, 2012.
- [34] F. Xu, G. Zheng, D. Wu, Y. Liang, Z. Li, and R. Fu, “Improving electrochemical performance of polyaniline by introducing carbon aerogel as filler,” *Phys. Chem. Chem. Phys.*, vol. 12, no. 13, pp. 3270–3275, 2010.
- [35] M. Trchová and J. Stejskal, “Polyaniline: The infrared spectroscopy of conducting polymer nanotubes (IUPAC Technical Report),” *Pure Appl. Chem.*, vol. 83, no. 10, pp. 1803–1817, 2011.
- [36] V. C. Tran, V. H. Nguyen, T. T. Nguyen, J. H. Lee, D. C. Huynh, and J. J. Shim, “Polyaniline and multi-walled carbon nanotube-intercalated graphene aerogel and its electrochemical properties,” *Synth. Met.*, vol. 215, pp. 150–157, 2016.
- [37] K. Dong, S. Wang, H. Zhang, and J. Wu, “Preparation and electrochemical performance of sulfur-alumina cathode material for lithium-sulfur batteries,” *Mater. Res. Bull.*, vol. 48, no. 6, pp. 2079–2083, 2013.
- [38] W. Li, Q. Zhang, G. Zheng, Z. W. Seh, H. Yao and Y. Cui, Understanding the Role of Different Conductive Polymers in Improving the Nanostructured Sulfur

- Cathode Performance Understanding the Role of Different Conductive Polymers in Improving the Nanostructured Sulfur Cathode Performance, *Nano Lett.*, **13**, 5534–5540, (2013)
- [39] H. Gao, Q. Lu, Y. Yao, X. Wang, and F. Wang, “Electrochimica Acta Significantly Raising the Cell Performance of Lithium Sulfur Battery via the Multifunctional Polyaniline Binder,” *electro*, vol. 232, pp. 414–421, 2017.
- [40] J. Liang, Z. H. Sun, F. Li, and H. M. Cheng, “Carbon materials for Li-S batteries: Functional evolution and performance improvement,” *Energy Storage Mater.*, vol. 2, pp. 76–106, 2016.
- [41] S. S. Zhang and D. T. Tran, “282 How a gel polymer electrolyte affects performance of lithium/sulfur batteries,” *Electrochim. Acta*, vol. 114, no. February, pp. 296–302, 2013.
- [42] A. Vizintin, L. Chabanne, E. Tchernychova, I. Arcon, L. Stievano, G. Aquilanti, M. Antonietti, T.-P. Fellingner, and R. Dominko, “The mechanism of Li₂S activation in lithium-sulfur batteries : Can we avoid the polysulfide formation ?,” *J. Power Sources*, vol. 344, pp. 208–217, 2017.
- [43] Y. V. Mikhaylik and J. R. Akridge, “Polysulfide Shuttle Study in the Li/S Battery System,” *J. Electrochem. Soc.*, vol. 151, no. 11, pp. A1969–A1976, 2004.
- [44] T. A. Pascal K.H.Wujcik, J. Velasco-Velez, C. Wu, A.A.Teran, M. Kapilashrami, J.Cabana, J. Guo, M. Salmeron, N.Balsara and D. Prendergast, “X - ray Absorption Spectra of Dissolved Polysulfides in Lithium – Sulfur Batteries from First-Principles,” *J. Phys. Chem. Lett.*, vol. 5, pp. 1547–1551, 2014.
- [45] F. T. H. E. President and F. T. H. E. President-elect, “XMAS Newsletter 2016,” vol. 10, no. 5, pp. 1–4, 2003.
- [46] R. Dominko, M. U. M. Patel, V. Lapornik, A. Vizintin, M. Koželj, N. N. Tušar, I. Arcon, L. Stievano, and G. Aquilanti, “Analytical Detection of Polysulfides in the Presence of Adsorption Additives by Operando X-ray Absorption Spectroscopy,” *J. Phys. Chem. C*, vol. 119, no. 33, pp. 19001–19010, 2015.
- [47] M. Cuisinier, P. E. Cabelguen, S. Evers, G. He, M. Kolbeck, A. Garsuch, T. Bolin, M. Balasubramanian, and L. F. Nazar, “Sulfur Speciation in Li – S Batteries Determined by Operando X - ray Absorption Spectroscopy,” *J. Phys. Chemistry Lett.*, vol. 4, pp. 3227–3232, 2013.

- [48] A. Berger, A. T. S. Freiberg, A. Siebel, R. Thomas, M. U. M. Patel, M. Tromp, H. A. Gasteiger and Y. Gorlin, The Importance of Chemical Reactions in the Charging Process of Lithium-Sulfur Batteries, *J. Electrochem. Soc.*, vol. 165, pp. A1288–A1296, 2018
- [49] J. Gao, M. a Lowe, Y. Kiya, and D. Abru, “Effects of Liquid Electrolytes on the Charge-Discharge Performance of Rechargeable Lithium / Sulfur Batteries : Electrochemical and *in situ* X-ray Absorption Spectroscopic Studies,” *J. Phys. Chem. C*, vol. 115, pp. 25132–25137, 2011.
- [50] Q. Pang, A. Shyamsunder, B. Narayanan, C. Y. Kwok, L. A. Curtiss, and L. F. Nazar, “Tuning the electrolyte network structure to invoke quasi-solid state sulfur conversion and suppress lithium dendrite formation in Li – S batteries,” *Nat. Energy*, 2018.

Chapter 6

Conclusions and Future Work

6.1 Conclusions

In this thesis, *operando* XANES technique was applied to investigate the reaction mechanism of Li-S batteries to provide a better understanding of the effect of various electrolyte systems, additives on the sulphur cathode, and electrode fabrication methods. The combination of electrochemical analysis with *operando* XAS measurements is a powerful tool to provide information about the sulphur reaction mechanisms in real-time Li-S cell operation.

Firstly, this thesis provides an overview of the fundamentals of Li-S batteries, with an emphasis on the existing issues and recent progress in various components, such as, the positive electrode, the negative electrode, and electrolytes. Secondly, experimental techniques and fabrication methods were demonstrated with an attention given to the XAS measurements. The detailed information of the preparation method of *operando* cell is provided. In order to conduct successful *operando* XANES measurements, X-ray transparent coin cell is designed to achieve both the standard electrochemical behaviour and the X-ray access to the material of interest. Our *operando* cell is specially designed to fit in the vessel chamber used at XMaS beamline (BM28) at the ESRF and capable to penetrate the beam through the X-ray window. The use of a simple but highly-effective design of the X-ray transparent coin cell allowed us to prepare numbers of backup cells, and time efficient sample changing available.

In order to understand the influence of the electrolytes on the electrochemical performances and conversion reaction mechanisms of sulphur in the Li-S batteries, *operando* XAS measurements were performed on Li-S cells with variations of the electrolyte systems. The most widely used solvent system, DOL/DME (1:1 volume ratio), tuned out to be unusable in Li-S batteries without the support of LiNO₃ or modification of LiTFSI salt to LiTDI salt. In contrast, TEGDME was found to be a flexible

choice for both LiTFSI and LiTDI salts, in the presence of LiNO₃. TMS solvent was found to achieve better electrochemical performance in the absence of LiNO₃.

Operando XANES measurements revealed that the rate of self-discharge can be mitigated by the use of the LiTDI/TMS electrolyte, and sulphur undergoes a sequential conversion reaction in this electrolyte system. On the contrary, LiTDI/TEGDME is advantageous in faster reaction kinetics of the conversion reaction favouring the reduction of long-chain polysulphides to short-chain polysulphides, and the formation of polysulphide is accompanied with the disproportionation and precipitation reaction of insoluble Li₂S₂/Li₂S. Additionally, no spectroscopic evidence of radical species was found in the electrolyte systems studied here.

To further improve the performance of Li-S batteries, metal oxides and sulphides (MX) were employed as the physical/chemical reservoir for soluble polysulphides. The S K-edge *operando* XANES measurements of the MX@S cells demonstrated that the variation of the MX additives led to different sulphur conversion mechanisms. Particularly, the TiO₂ additive demonstrated an interesting effect of accelerating the conversion reaction of linear-chain polysulphide to Li₂S. For the TiO₂@S cell, we also performed *operando* measurements of the K-edges of two elements (S and Ti) using a single test cell. This unique measurement is achieved owing to the motorised precision XYZ mount, which allowed us to reproduce the detection point precisely in-between the different energy edge measured. This analysis revealed the reversible oxidation states of the anatase-TiO₂ additive during the lithiation and de-lithiation of TiO₂@S electrode. TiO₂ behaves as a source of additional capacity to the cell, as well as accelerating the disproportionation and deposition of Li₂S on the cathode. CuO and V₂O₅ additives were found to be very effective in suppressing the self-discharge rate. A similar trend was identified between these two additives at the higher energy region of the S K-edge XANES spectra. The suppression of self-discharge is potentially due to the oxidation of active sulphur by these additives preventing the reduction reaction during cell storage. Nonetheless, more analysis is required to clearly identify the origin of these peaks.

Last but not least, the design of alternative binder materials for fabrication of the sulphur electrodes is studied. Conductive polymer binders, PANI and PEDOT:PSS were

employed as replacement of conventional binders and sulphur electrodes were fabricated via a cost-effective and environmentally benign method. Additionally, the binder-free sulphur electrode is synthesised, and they were characterised using an *operando* XAS technique. It was suggested that PANI can potentially control the chain-lengths of polysulphides. Although this architecture is not yet optimised for high-rate performance and mechanical stability is considerably low, this study opened the possibility of an interesting direction of the further research.

6.2 Future work

Our collective results did not show signs of radical polysulphides in the XANES spectra. However, S K-edge XANES analysis is not a fully suitable technique to measure the polysulphide radicals, therefore, further investigation using electron paramagnetic resonance (EPR) spectroscopy analysis is necessary for a clear detection of such species. It would also be ideal to investigate more detailed optical studies using open-cell analysis, combined with UV-VIS measurements to examine dispersion behaviour of polysulphides.

The sulphur electrodes studied in this work were fabricated via simple method to investigate the individual effect of each components. It is expected that utilisation of sophisticated materials and architectures, such as, carbon nanotubes, mesoporous carbon, and nanostructured metal oxides and sulphides would increase the battery performances. Our future work includes the use of such materials to improve the Li-S systems further.

Oxidised sulphur peaks detected at the S K-edge XANES in some of our cells are considered as potential oxidation of sulphur by metal oxide additives, and this reaction may depend on the redox potential of the metal oxide additives vs Li/Li⁺. Another possibility is that the oxidation of sulphur by LiNO₃. Further investigation is required to accurately identify the origin of these peaks. For example, XPS and FTIR measurements on the S cathode, separator, and Li anode would allow us to detect the interaction of LiNO₃ and sulphur species. It would also be interesting to conduct the 'double-edge' XAS analysis on other MXs additives to gain comparable results with the TiO₂@S cell. The combination of different synchrotron-based analysis, such as, XAS/XRD, XAS/SAXS

will provide more comprehensive pictures of the reaction mechanism, which is possible at the beamline BM28 and BM26 at the ESRF as well as at B18 at the DLS.

Appendix

A-1 List of chemicals used

The list of materials and chemicals used for fabrication, characterisation and electrochemical analysis are summarised below in **Table A-1** in alphabetical order;

Table A-1. List of chemicals and materials used

| Chemical | CAS number | Supplier |
|---------------------|---|----------------------|
| Aniline | 99.5%, 62-53-3 | Sigma-Aldrich |
| AB | Acetylene black 99.9 %, 1333-86-4 | Alfa Aesar |
| Celgard | 25 µm thick | MTI |
| Coin cell cases | CR2016 | MTI |
| CuO | Copper(II) oxide 99.999%, 1317-38-0 | Sigma-Aldrich |
| CuS | Copper(II) sulphide 99.8 %, 1317-40-4 | Alfa Aesar |
| DME | 1,2-dimethoxyethane, anhydrous 99.5% 110-71-4 | Sigma-Aldrich |
| DOL | 1, 3-Dioxolane, anhydrous 99.8 %, 646-06-0 | Sigma-Aldrich |
| Glass fibre filters | GF/F, 1825-110 | Whatman |
| Li-foil | 99.9 %, 7439-93-2 | Sigma-Aldrich |
| LiNO ₃ | Lithium Nitrate 99.99 %, 7790-69-4 | Sigma-Aldrich |
| LiTDI | Lithium 4,5-dicyano-2-(trifluoromethyl)imidazole 95%, | Alfa Aesar |
| LiTFSI | Bis(trifluoromethane)sulphonimide lithium salt 90076-65-6 | Alfa Aesar |
| Mylar film | 3.4 µm thick | Fisher scientific |
| NMP | 1-methyl-2-pyrrolidinone, anhydrous 99.5 %, 872- 50-4 | Sigma-Aldrich |
| PEDOT:PSS | Poly(3,4-ethylenedioxythiophene)- poly(styrenesulphonate) 1.3 wt% dispersion in H ₂ O, conductive grade, | Sigma-Aldrich |
| PVDF | Poly(vinylidene fluoride), 24937-79-9 | Sigma-Aldrich |

| | | |
|-----------------------------------|--|---------------|
| PVP | Polyvinylpyrrolidone, 9003-39-8 | Sigma-Aldrich |
| S₈ | Sulphur 99.998%, 7704-34-9 | Sigma-Aldrich |
| SnO₂ | Tin(IV) oxide, 18282-10-5 | sigma-Aldrich |
| TEGDME | Tetraethylene glycol dimethyl ether 99 %, 143-24-8 | Sigma-Aldrich |
| TiO₂ | Titanium(IV) oxide, anatase 99.7%, 1317-70-7 | Sigma-Aldrich |
| TMS | Sulpholane 99%, 126-33-0 | Sigma-Aldrich |
| V₂O₅ | Vanadium(V) oxide 99.99%, 1314-62-1 | Sigma-Aldrich |

A-2 Second discharge and charge cycle of TiO₂@S cell for *operando* double-edge experiment

The *operando* S K-edge & Ti K-edge XANES measurement in Section 4.4.2.1.b), was measured further until the end of second charge to investigate the reproducibility of the S and the Ti K-edge XANES feature.

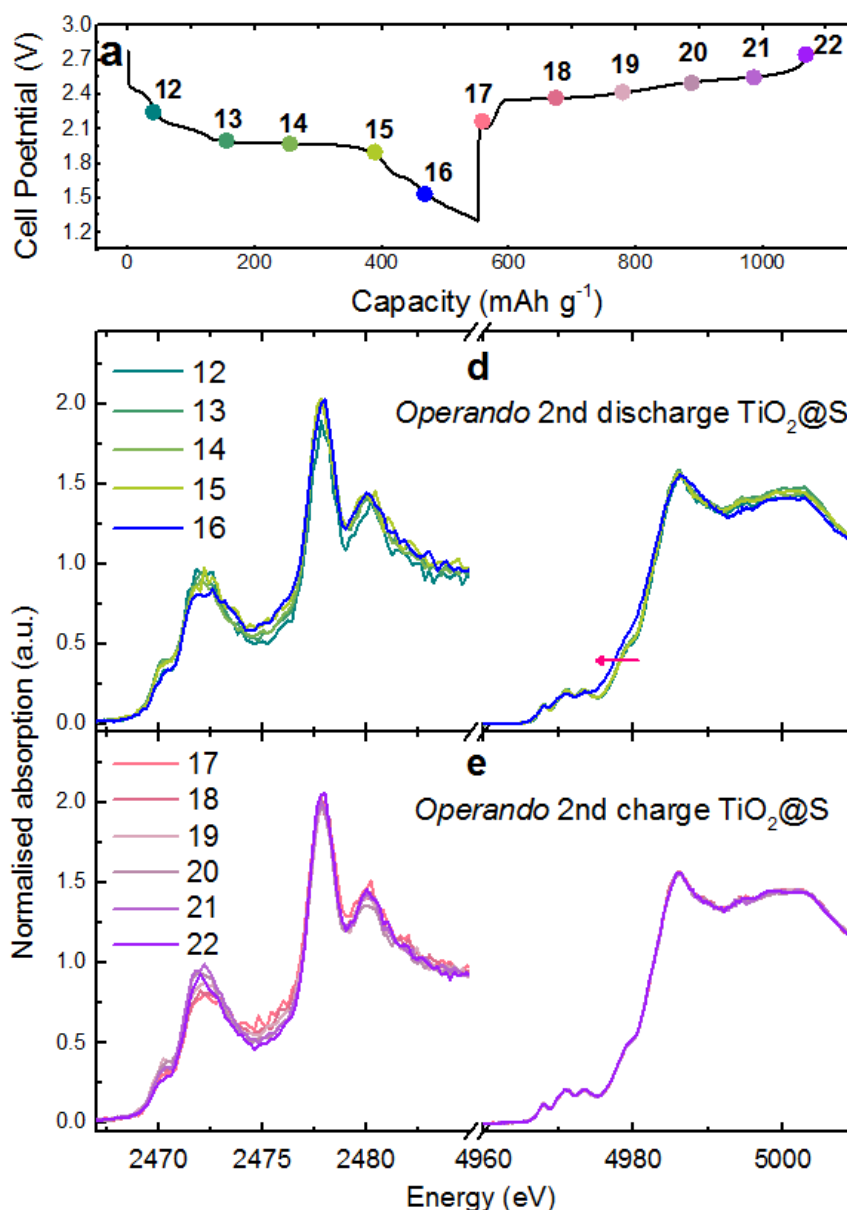


Figure A-1. *Operando* XANES measurement of the TiO₂@S cell at 0.1 C rate. (a) Voltage profile for the second discharge and charge. Normalised XANES spectra for both the S K-edge (left panels) and the Ti K-edge (right panels) for (b) the second discharge (labelled as 12 - 16), and (c) the second charge (labelled as 17 - 22).

As can be seen in **Figure A-1**, the spectral features undergo similar trend as the first cycle for both at the S and Ti K-edges. This indicates a good reproducibility of the compounds formed during the measurement of two successive cycles.

A-3 Post-mortem XAS measurements

To gain additional insights into the redox reactions and local structures, *ex situ* (post-mortem) Ti K-edge XAS measurements were performed for cycled $\text{TiO}_2@\text{S}$ cathodes and correlated these results with the electrochemical behaviour and *operando* sulphur K-edge results.

A-3.1 Sample preparation

Several $\text{TiO}_2@\text{S}$ cathodes cells were cycled in $\text{LiTfO}_4/\text{TEGDME}/\text{LiNO}_3$ electrolyte at a rate of 0.1 C and cells were disassembled to retrieve the $\text{TiO}_2@\text{S}$ cathodes. Extracted cathodes were sandwiched by Kapton adhesive foils to prevent possible side reactions in the air. Cell dissembling, and cathode packing was carried out in an argon-filled glove box. The Ti K-edge XANES and EXAFS spectra of $\text{TiO}_2@\text{S}$ cathodes extracted from coin cells were acquired in transmission detection mode at beamline B18 at the Diamond Light Source (DLS, Didcot, UK). All samples measured at this beamline were placed on a non-absorbent sample holder using Kapton adhesive foil (**Figure A-2**).

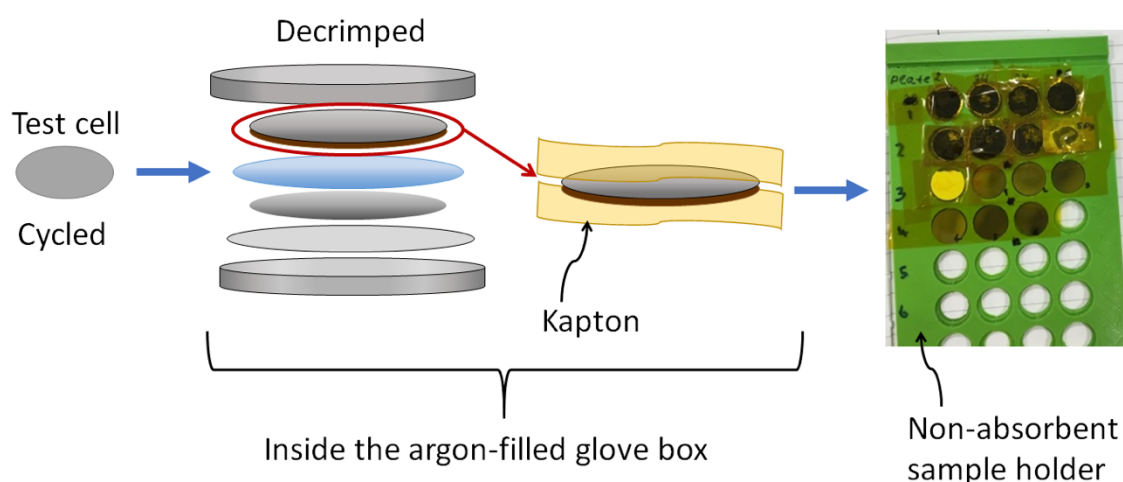


Figure A-2. Preparation steps for post-mortem samples.

A-3.2 Beamline set up

The experiment set up at the B18 (DLS) is displayed in **Figure A-3**. The ionisation chambers detectors, I_0 and I_t , were used to measure the intensities of incident beam and transmitted beam through the sample, respectively.¹² The excitation energy is adjusted using a double crystal monochromator, resulting in a spectral energy resolution of 4.98 keV.

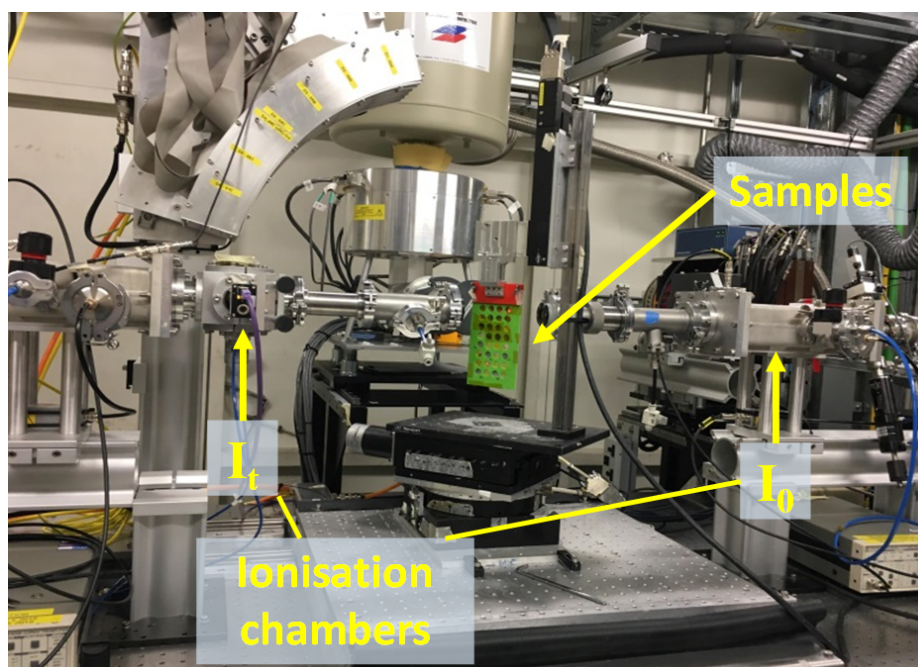


Figure A-3. Ti K-edge XAS set up at beamline B18 at DLS.

A-3.2 Results

The XANES spectra for the *ex situ* $\text{TiO}_2@\text{S}$ electrodes are represented in **Figure A-4b**, together with the anatase- TiO_2 reference spectrum. There was no significant change in the XANES region for post-mortem cathode samples, having the same number of the pre- and main-edge feature and stable energy position of the absorption edge. From the Ti K-edge XANES we do not detect the energy shift towards Ti^{3+} . Furthermore, peak intensities did not change, confirming the no change in the crystallinity. This proves that the Ti K-edge change is only observed under *operando* conditions and TiO_2 are metastable and post-mortem treatment disturbs the properties of the sample. This result highlighted the importance of the *operando* XAS measurement.

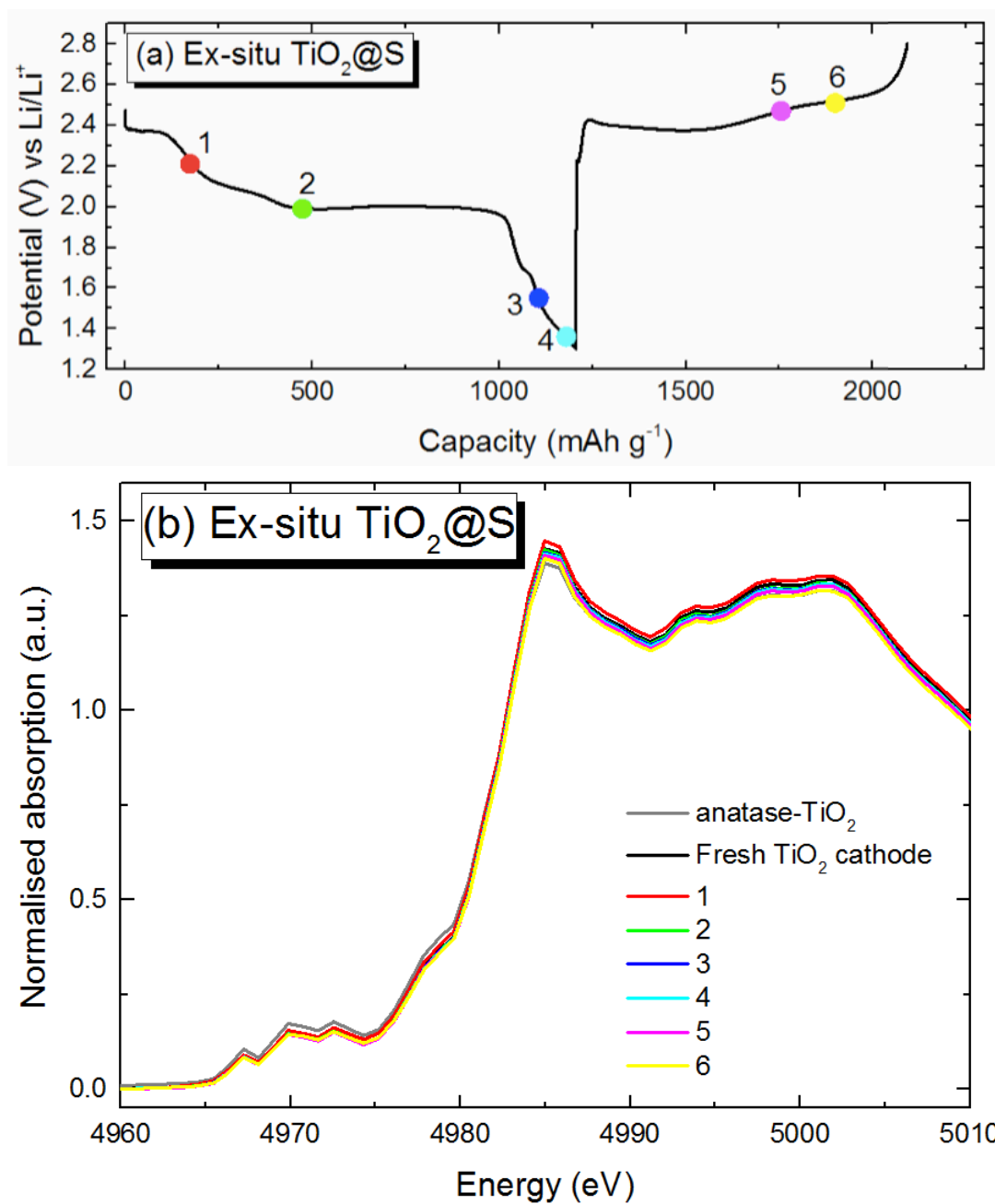


Figure A-4. (a) Typical voltage profile of $\text{TiO}_2@\text{S}$ for the first cycle with labels of various (de)lithiated states (1 - 6) for samples used in *ex situ* XAS measurements, and (b) *ex situ* Ti K-edge XANES spectra of $\text{TiO}_2@\text{S}$ cathodes.

A-4 References

- [1] [Online]. B18 Technical Information,
<https://www.diamond.ac.uk/Instruments/Spectroscopy/B18.html>. [Accessed:
23-08-2018]

- [2] A. J. Dent, G. Cibir, S. Ramos, S. A. Parry, D. Gianolio, A. D. Smith, S. M. Scott, L. Varandas, S. Patel, M. R. Pearson, L. Hudson, N. A. Krumpa, A. S. Marsch and P. E. Robbins, Performance of B18, the core EXAFS bending magnet beamline at diamond, *J. Phys. Conf. Ser.*, **430**, 012023, (2013).